Fall 2010

A geochemical investigation of heterogeneous redox reactions between Fe(II), Fe(III), and uranium

Drew Eric Latta
University of Iowa

A GEOCHEMICAL INVESTIGATION OF HETEROGENEOUS REDOX REACTIONS BETWEEN FE(II), FE(III), AND URANIUM

by

Drew Eric Latta

An Abstract

Of a thesis submitted in partial fulfillment
of the requirements for the Doctor of
Philosophy degree in Civil and Environmental Engineering
in the Graduate College of
The University of Iowa

December 2010

Thesis Supervisor: Professor Michelle M. Scherer

ABSTRACT

Iron (Fe) minerals and ferrous iron (Fe(II)) play an important role in the several natural elemental cycles, including the carbon cycle, nutrient cycles, and the cycling of metals. In this work we have characterized the reactivity structural Fe(II) in several Fe minerals and in natural soil with uranium. We have studied the reactivity of Fe(II) in solution with the Fe oxide goethite conditions relevant to many natural systems.

Green rusts are widely recognized as an intermediate phase in the Fe cycle. Here we investigate the reactivity of green rusts containing different structural anions with uranium^{VI} (U^{VI}). We have also investigated the effect of aqueous bicarbonate on U^{VI} sorption and reduction by green rusts. Our findings indicate that green rusts reduce U^{VI} to U^{IV}, and that environmentally relevant carbonate concentrations have little effect the rate and extent on this reaction.

We have also investigated U^{VI} reduction by structural Fe(II) in magnetite. Magnetite with varying stoichiometry ($x = Fe^{2+}/Fe^{3+}$) was reacted with U^{VI}. Results from x-ray absorption spectroscopy indicate that the redox properties of magnetite dictate whether magnetite reduces U^{VI}. In addition, magnetite reactivity can be "recharged" by electron transfer from aqueous Fe(II).

There is little evidence of the reactivity of structural Fe(II) towards U^{VI} in natural materials. We have characterized a naturally reduced soil and found it contains structural Fe(II) in clay minerals and a possible green rust-like phase. When this soil is exposed to U^{VI} we find that Fe(II) reduces a portion of the U added. Our work highlights the potential for abiotic reduction of U^{VI} by Fe(II) in reduced, Fe-rich environments.

We have used ^{57}Fe Mössbauer spectroscopy to study redox reactions of Fe(II) with goethite under biogeochemical conditions relevant to natural systems. When Fe(III) in goethite is substituted with aluminum or anions such as phosphate, silicate, carbonate, and natural organic matter are sorbed onto the surface of goethite, interfacial electron

transfer occurs between sorbed Fe(II) and goethite. These results indicate that electron transfer between Fe(II) and Fe oxides occurs under environmentally relevant conditions. Electron transfer was blocked by phospholipids, however, suggesting electron transfer may be inhibited under eutrophic conditions.

Abstract Approved: _____
Thesis Supervisor

_____
Title and Department

_____
Date

A GEOCHEMICAL INVESTIGATION OF HETEROGENEOUS REDOX REACTIONS BETWEEN FE(II), FE(III), AND URANIUM

by

Drew Eric Latta

A thesis submitted in partial fulfillment
of the requirements for the Doctor of
Philosophy degree in Civil and Environmental Engineering
in the Graduate College of
The University of Iowa

December 2010

Thesis Supervisor: Professor Michelle M. Scherer

Graduate College
The University of Iowa
Iowa City, Iowa

CERTIFICATE OF APPROVAL

_____

PH.D. THESIS

_____

This is to certify that the Ph.D. thesis of

Drew Eric Latta

has been approved by the Examining Committee
for the thesis requirement for the Doctor of Philosophy
degree in Civil and Environmental Engineering at the December 2010
graduation.

Thesis Committee: _____
Michelle M. Scherer, Thesis Supervisor

_____
Gene F. Parkin

_____
Timothy E. Mattes

_____
Richard L. Valentine

_____
Johna Leddy

_____
Edward J. O'Loughlin

_____
Maxim I. Boyanov

To my parents and Haylee

To keep every cog and wheel is the first precaution of intelligent tinkering.
Aldo Leopold
Round River

ACKNOWLEDGMENTS

I am very grateful to everyone that has made these last five years so enjoyable. I owe much gratitude to Michelle Scherer, for being an advisor, mentor, and role model. It has been a pleasure working with you and learning from you; thank you for encouraging me to take on the task of becoming a Ph.D., even if I was skeptical at first. I am grateful for the discussions about science, the conference trips, and the pep-talks about research and life.

A big thank-you goes out to all of my committee members, all of you have contributed to this work in some way. Thanks to Max Boyanov and Ed O'Loughlin, I'm deeply appreciative for your help with all the work in this thesis, and for the all the fruitful discussions via e-mails and in person when we have had the chance. Thanks to Rich Valentine and Johna Leddy for their instruction on the finer points of chemistry, you can count me as an appreciative student. To Gene Parkin and Tim Mattes, thanks for the ribbing about "the dark side" and for broadening my gaze beyond the world of iron. I would also like to thank Jerry Schnoor. Jerry, I appreciate your comments at my proposal defense and your condition that I take an electrochemistry class. I also cannot go without mentioning Keri Hornbuckle, as she was the first one of the CEE faculty to suggest I come to grad school here, I would probably never even have considered it if you hadn't suggested it. To all the rest of the CEE faculty: thank you for making this such a great environment to work in.

The people I've met and the friends I've made during grad school are a blessing. I don't recall a single person here that hasn't been fun to have around. Special thanks to David, Rob, Chris, Phil, Mike, and Tim and all the rest of the Scherer lab over the years, it has been very enjoyable to interact with you on both a scientific level and a personal level. And thanks to Cristina Fernandez-Baca for collecting some of the data in Chapter 5 on phosphate and Fe(II) co-sorption on goethite as part of her master's thesis work. I am

also grateful to count J.V. Loperfido and Garrett Struckhoff as friends. Garrett, without you my life would be very different now. Without you and Haley, I would never have met Haylee.

My family has always been very supportive of what I do, even when I find it hard to explain exactly what it is that I do. I thank you, Mom and Dad, for all the support growing up, and for nurturing the nascent scientist in me. Sorry for taking so many things apart and not putting them back together in working fashion.

Finally, I cannot go without expressing how grateful I am to Haylee Easton, my soon to be wife. You came into my life during a particularly dark period, and have lifted me up in so many ways. I look forward to the many adventures that life has for us in the future. I love you!

ABSTRACT

Iron (Fe) minerals and ferrous iron (Fe(II)) play an important role in the several natural elemental cycles, including the carbon cycle, nutrient cycles, and the cycling of metals. In this work we have characterized the reactivity structural Fe(II) in several Fe minerals and in natural soil with uranium. We have studied the reactivity of Fe(II) in solution with the Fe oxide goethite conditions relevant to many natural systems.

Green rusts are widely recognized as an intermediate phase in the Fe cycle. Here we investigate the reactivity of green rusts containing different structural anions with uranium^{VI} (U^{VI}). We have also investigated the effect of aqueous bicarbonate on U^{VI} sorption and reduction by green rusts. Our findings indicate that green rusts reduce U^{VI} to U^{IV}, and that environmentally relevant carbonate concentrations have little effect the rate and extent on this reaction.

We have also investigated U^{VI} reduction by structural Fe(II) in magnetite. Magnetite with varying stoichiometry ($x = Fe^{2+}/Fe^{3+}$) was reacted with U^{VI}. Results from x-ray absorption spectroscopy indicate that the redox properties of magnetite dictate whether magnetite reduces U^{VI}. In addition, magnetite reactivity can be "recharged" by electron transfer from aqueous Fe(II).

There is little evidence of the reactivity of structural Fe(II) towards U^{VI} in natural materials. We have characterized a naturally reduced soil and found it contains structural Fe(II) in clay minerals and a possible green rust-like phase. When this soil is exposed to U^{VI} we find that Fe(II) reduces a portion of the U added. Our work highlights the potential for abiotic reduction of U^{VI} by Fe(II) in reduced, Fe-rich environments.

We have used ^{57}Fe Mössbauer spectroscopy to study redox reactions of Fe(II) with goethite under biogeochemical conditions relevant to natural systems. When Fe(III) in goethite is substituted with aluminum or anions such as phosphate, silicate, carbonate, and natural organic matter are sorbed onto the surface of goethite, interfacial electron

transfer occurs between sorbed Fe(II) and goethite. These results indicate that electron transfer between Fe(II) and Fe oxides occurs under environmentally relevant conditions. Electron transfer was blocked by phospholipids, however, suggesting electron transfer may be inhibited under eutrophic conditions.

TABLE OF CONTENTS

LIST OF TABLES

LIST OF FIGURES

CHAPTER 1: INTRODUCTION

Iron Biogeochemistry

Iron is the fourth most abundant element in the Earth's crust, and the single most abundant redox active metal in the terrestrial environment. Due to this redox activity, iron plays a significant role in the chemistry of life and of environmentally relevant abiotic processes. In the geosphere, iron cycles between the reduced and soluble Fe(II) oxidation state and the oxidized and insoluble Fe(III) oxidation state. Cycling of iron oxidation states is linked to the modern cycling of globally important elements, such as carbon—including xenobiotic compounds (*1*)—nitrogen (*2*), phosphorus (*3*), and the ancient cycling of oxygen (e.g. *4*). Large quantities of Fe(II) are produced in the subsurface under anoxic conditions by the action of dissimilatory metal (or iron) reducing bacteria (DMRB or DIRB) coupled to oxidation of organic carbon (*1*). Abiotic mechanisms for the production of Fe(II) also exist, including weathering of iron bearing minerals (*5*). Weathering of iron bearing silicate minerals is the primary source of iron oxides and oxyhydroxides—called Fe oxides hereafter for the sake of brevity—in the pedosphere, and is the ultimate source for most iron in the environment. The production of aqueous Fe(II) by both abiotic and biotic processes can result in mobile Fe(II) in the subsurface depending on the geochemical conditions (i.e. anoxic conditions, neutral pH), which can interact with various mineral surfaces. The presence of mineral surfaces catalyzes the reaction of Fe(II) with environmental contaminants (e.g. *6, 7, 8*), and may be an important pathway for transformation of contaminants in the subsurface.

Interactions of Fe(II) with a variety of mineral surfaces have been studied and have typically been described using surface complexation models (i.e. *9, 10, 11*). Such methods are based on measurements in the change of solution Fe(II) concentrations in the presence of mineral surfaces, and uptake is determined by the difference between a final and initial concentration. Surface complexation models are then used based on the

formation of assumed surface and Fe complexes depending on pH. Surface complexation modeling, however, does not capture the complete range of reactions that occur between cations and mineral surfaces. In the case of divalent cations, such as Mg(II) and Fe(II), adsorption onto trivalent metal hydroxides (Fe(III), Al(III)) surfaces can induce transformation of amorphous $M(OH)_3$ precipitates and oxides to crystalline M(II)-M(III) hydroxide solids (*12, 13*). Fe(II) is known to catalyze the recrystallization of thermodynamically unstable Fe oxides such as ferrihydrite and lepidocrocite to goethite, magnetite, and green rust (*14-16*).

In addition, a growing body of research indicates that complex redox-driven dynamics occur when Fe(II) adsorbs to Fe(III) oxides. Recent experiments into secondary mineralization reactions of Fe(III) oxides in the presence of Fe(II) have shown that when ^{55}Fe radiolabeled iron oxides (goethite, lepidocrocite, and ferrihydrite) were exposed to aqueous Fe(II) that ^{55}Fe(II) was released from the underlying oxide into solution over time (*17*). Our research group and others have used Mössbauer spectroscopy to demonstrate that electron transfer between aqueous Fe(II) and solid phase Fe(III) occurs, resulting in template growth of the underlying oxide (*18-21*). In addition to electron transfer, recent work has shown a complete reworking of crystal faces of hematite occurs in the presence of dissolved Fe(II) due to a potential difference between (001) and (hk0) faces, which causes oxidation of Fe(II) at (001) faces and formation of hematite overgrowths. Oxidation of Fe(II) at the (001) face is followed by bulk electron transfer through the hematite crystal, and reductive dissolution of Fe(II) from spatially separated (hk0) crystal faces (*22, 23*).

Further work by our group and others tracking changes in aqueous Fe(II) and solid goethite isotopic composition indicates that a similar process may be happening in goethite suspensions exposed to Fe(II). Handler and colleagues have proposed that a mechanism termed the “redox-driven conveyor belt” may be responsible (*24, 25*). These results suggest that the iron oxide sorbent is not merely a static surface in the adsorption

reaction, and that Fe(II) causes time dependent changes to the Fe(III) substrate which may cause an evolution of reactivity through time. Such knowledge has necessitated the incorporation of Fe(II) to Fe(III) electron transfer into surface complexation models (*11*), and represents a step forward in prediction of iron-iron interactions in subsurface environments.

Based on this work, it is now clear that a paradigm shift is well underway in our understanding of iron oxide reactivity, and a new conceptual model of iron oxides as highly dynamic minerals is emerging. It is unclear, however, whether this conceptual model of iron oxides can be extended to the complex milieu that exists in the geosphere, as most of the spectroscopic work to date has been done under minimal complexity so that the interaction between Fe(II) and Fe(III) can be isolated. For example, it is well known that iron oxides in the environment can incorporate various cations into their structure, especially the highly abundant Al(III) cation (*26-28*). Iron oxides can also serve as an adsorbent for a multitude anions present in natural environments, such as carbonate, phosphate, silicate, and natural organic matter (*29-33*), as well as anionic contaminants such as arsenate (As(V)) and arsenite (As(III)) (*34*). Under this new paradigm it is unclear whether cation and anion sorption can still be modeled as a static process under reducing conditions in the presence of iron oxides. If the static model for iron oxide surfaces towards sorption is an invalid assumption, the fate of many inorganic contaminants, such as arsenate, chromate, and uranium will need to be reevaluated. Furthermore, little is known about the reactivity of iron oxides with structural cation substitution and sorbed with anions towards contaminants in the presence of Fe(II). The role of structural Al and sorbed anions in the reaction of Fe(II) with goethite (α-FeOOH) is explored in Chapter 5 of this thesis.

Uranium Biogeochemistry

Uranium (U) is a radioactive metal that is ubiquitous at low levels in all crustal materials (e.g. soils ~2 ppm (*35*)), however, much higher concentrations at many U.S. Department of Energy sites are a result of the technological uranium cycle. Contamination of the subsurface has resulted from both mining and further processing of uranium for nuclear technology (*36, 37*). Under atmospheric conditions (i.e. oxic and containing CO_2) uranium is oxidized to the hexavalent oxidation state, as the $U^{VI}O_2^{2+}$ cation, and is highly mobile in aqueous solution due to its strong complexing affinity for carbonate dissolved in water (CO_3^{2-}) (*38, 39*). At near neutral pH values and in low carbonate waters, UO_2^{2+} (hereafter referred to as U^{VI}) has been shown to be strongly sorbed to a variety of minerals, including both synthetic and natural iron oxides. High dissolved carbonate concentrations reduce U^{VI} sorption to iron oxides, therefore increasing its mobility in groundwater (*40-42*). The variable response of uranium to changing geochemical conditions has spurred considerable research in the laboratory and in the field into immobilizing U by reducing it to the much less soluble U^{IV} valance state, particularly when it is reduced to $U^{IV}O_2$ (uraninite) (*38, 43-46*).

Immobilization of U^{VI} by reducing it to U^{IV} is often thought of as occurring primarily due to direct enzymatic reduction by dissimilatory metal reducing microbes present in the subsurface. Microbial respiration on U^{VI} often results in the precipitation of nano-particulate uraninite (e.g., *47, 48*); however, more recent research suggests that microbial metabolism results in a more diverse array of U compounds, including mono-nuclear sorbed U^{IV}, which might be more susceptible to oxidation or remobilization (*49*). Under similar geochemical conditions, microbial respiration of Fe(III) oxides also leads to the formation of soluble Fe(II) that can sorb or precipitate as various minerals incorporating structural Fe(II), including green rusts, siderite ($FeCO_3$), magnetite (Fe_3O_4), vivianite ($Fe_3(PO_4)_2$), and Fe(II) containing clay minerals (*50-54*).

The similarity in geochemical conditions under which both dissimilatory U and Fe reduction occur suggests that abiotic reduction of U^{VI} by Fe(II) may be an important process for the immobilization of U contamination. Indeed, several studies have provided evidence that aqueous and "sorbed" Fe(II) in the presence of Fe oxides and other minerals are capable of reducing U^{VI} to U^{IV} (*55-60*). In addition, structural Fe(II) in iron minerals, including both synthetic and biogenic green rusts and magnetite, has been shown to reduce U (*54, 61, 62*). Despite evidence for reduction of U by Fe(II) in laboratory synthesized and *in vitro* biologically produced Fe(II) minerals, the role of structural and sorbed Fe(II) in *natural* soils and sediments remains unclear. Several studies have noted that sediments containing iron sulfides are capable of abiotically reducing U (*44, 63*), but a lack of significant abiotic reduction of U has been noted in non-sulfidic natural materials both containing Fe(II) as the result of microbial metabolism or to which Fe(II) has been added (*58, 64, 65*). We have explored whether this is true for a naturally reduced soil containing structural Fe(II) in Chapter 4 of this thesis.

Objectives and Hypotheses

Objectives

This thesis can be divided into two parts based on objectives. In the first part, the objective was to explore the effect of structural Fe(II) in green rust, magnetite, and soil minerals in a naturally reduced soil from Hedrick, Iowa, on the reduction of hexavalent uranium (U^{VI}). The uptake of U from solution was measured with wet chemical methods, and the extent of uranium reduction was measured using x-ray absorption spectroscopy to quantify the role of both U sorption and reduction by minerals containing structural Fe(II). In addition, Fe valance and speciation in these systems both with and without addition of U^{VI} has been measured with ^{57}Fe Mössbauer spectroscopy. Mössbauer spectroscopy provides evidence that structural Fe(II) is a reductant for U^{VI}.

The second objective of this thesis was to evaluate the role of environmentally relevant structural cation substitution and anion sorption on goethite on interfacial electron transfer between sorbed Fe(II) and Fe(III) in goethite. This work uses Mössbauer spectroscopy to evaluate whether interfacial Fe(II) to Fe(III) electron transfer occurs under more complex geochemical conditions than previously studied.

Hypotheses

1. Structural Fe(II) in green rust minerals is capable of reducing U^{VI} under a variety of conditions, including when different anions are present in the green rust structure and when U^{VI} is complexed by carbonate.
2. Reduction of U^{VI} to U^{IV} is dependent on the redox properties of magnetite (Fe_3O_4), which are determined by its stoichiometry (Fe^{2+}/Fe^{3+} content). Magnetite stoichiometry may explain the wide variation in U speciation after reaction with magnetite reported in previous studies
3. U is reduced in natural soils and sediments by structural Fe(II).
4. Sorption of Fe(II) onto goethite followed by interfacial electron transfer between sorbed Fe(II) and goethite (α-FeOOH) occurs over a wide variety of environmentally relevant conditions, including cation substation of Fe(III) by Al, and in the presence of anions (phosphate, carbonate, silicate, and natural organic matter) sorbed on goethite.
5. Electron transfer and atom exchange between aqueous Fe(II) and goethite affect the fate of metals in the environment, including reduction of U^{VI} to U^{IV}, release of metals from goethite by reductive dissolution, and Fe-isotope exchange.

Thesis Overview

The above hypotheses provide an outline of the structure of the thesis, which is organized into 5 main chapters. Each chapter contains sections detailing background

information and experimental objectives, experimental approach, results and discussion. The contents of each of the chapters are summarized below.

Chapter 2 addresses hypothesis 1. In this study, green rusts were synthesized with various anions in their structure along with several redox inactive analogues. The reaction of green rusts with uranium was assessed using aqueous chemistry and solid state uranium valence measurements with x-ray absorption spectroscopy (XAS) in collaboration with Ken Kemner, Edward O'Loughlin, and Maxim Boyanov of Argonne National Laboratory. We have found that all three forms of green rusts having different structural anions reduce U^{VI} to U^{IV}. In addition, we have found that uranium complexation by carbonate at environmentally relevant concentrations does not significantly affect U uptake or reduction by green rusts. This chapter is in preparation for submission to *Geochemical Transactions.*

Chapter 3 addresses hypothesis 2. Magnetites of known and varying stoichiometry (Fe^{2+}/Fe^{3+} content or x) were reacted with U^{VI} and the U valence state was measured using XAS. Care was taken to provide sufficient Fe(II) for reduction of all U^{VI} added for all magnetite stoichiometries, except in the case of maghemite (γ-Fe_2O_3), which is fully oxidized. We have found that for $x \geq 0.38$ magnetite reduces U^{VI} to U^{IV} in uraninite nanoparticles (UO_2 (s)). This work extends the hypothesis that contaminant reduction by magnetite is dependent on its redox properties to include U reduction (*66*). In addition, we used ^{57}Fe Mössbauer spectroscopy to measure the stoichiometry of biogenic magnetite, and to track Fe(II) oxidation by U^{VI}. This chapter is in preparation for submission to *Environmental Science & Technology.*

Chapter 4 addresses hypothesis 3. Here we have sampled soil reduced by natural processes down gradient from a spring near Hedrick, Iowa, and used wet chemical methods as well as ^{57}Fe Mössbauer spectroscopy to determine the speciation of Fe in the soil. We have concluded that the soil contains clay minerals and a possible green rust-like phase which contains structural Fe(II). We have reacted pasteurized samples of this soil

with U^{VI} and found that it is reduced by structural Fe(II) concomitant with oxidation of this Fe(II) to Fe(III). This paper is in preparation for submission to *Applied Geochemistry.*

Chapter 5 addresses hypothesis 4. We have used macroscopic measurements and the isotopic specificity of Mössbauer spectroscopy to track the speciation of Fe(II) that has been reacted with Al-substituted goethite and goethite that has been exposed to the common anions phosphate, silicate, carbonate, and natural organic matter (humic acid and phospholipids). We have found that Al-substitution and the presence of sorbed anions does not significantly change the macroscopic uptake of Fe(II). Mössbauer spectroscopy indicates that interfacial electron transfer occurs between sorbed Fe(II) and Al-substituted goethite resulting in oxidation of Fe(II) and formation of goethite. We observed similar results when anions were sorbed to goethite prior to addition of Fe(II), with oxidation of Fe(II) at the surface of goethite and resulting in the formation of goethite. Precipitation of Fe(II) from solution as vivianite partially inhibited electron transfer by sequestering Fe(II) from solution. Finally, we found that sorption of long-chain phospholipids to the surface of goethite inhibited Fe(II)-Fe(III) electron transfer, which may be an indication that electron transfer was shut down by electron-donor/acceptor separation. Our findings indicate that electron transfer between Fe(II) and goethite occurs under a variety of more complex geochemical conditions, but could be inhibited by high biomass or biofilm growth.

Chapter 6 addresses hypothesis 5. Specifically this chapter includes preliminary data on the implications of the redox driven conveyor belt that occurs when Fe oxides are exposed to Fe(II). Findings include that manganese (Mn) is released from Mn-substituted goethite during exposure to aqueous Fe(II). In addition, U^{VI} is reduced to UO_2 by Fe(II) under conditions studied in Chapter 5, but is not incorporated into goethite during atom cycling. Finally, we have developed a method that makes use of a newly acquired quadrupole-ICP-MS at The University of Iowa to measure isotope exchange between

highly enriched solutions of ^{57}Fe(II) with goethite and magnetite having a natural abundance of Fe isotopes. This new instrumentation may allow us to measure redox induced atom cycling in Fe oxides under a variety of conditions, as well as allowing measurement of low concentrations of a large number metal contaminants.

^{57}Fe Mössbauer Spectroscopy

In order to provide context for some of the discussion that appears in later chapters of this thesis, a brief overview of the background of ^{57}Fe Mössbauer spectroscopy is provided here. Mössbauer spectroscopy has become a powerful tool in environmental and geoscience for determining the speciation of iron in various solid materials. Both the valence state, and in many cases, the phase of iron can be determined with ^{57}Fe Mössbauer spectroscopy. In addition, the only requirement for determination of iron valence and coordination environment using Mössbauer spectroscopy is that the iron be in the solid phase. Because of its high sensitivity, the technique allows samples with relatively low iron content to be analyzed, and dilute phases to be quantified in mixtures. For the work presented here, Mössbauer spectra and parameters derived from fitting the spectra are used as a fingerprint for the iron species present in samples. The following is a review of ^{57}Fe Mössbauer spectroscopy based on several references (*67-70*).

In the earth's crust, there are four naturally occurring isotopes (with abundances of): ^{54}Fe (5.84%), ^{56}Fe (91.76%), ^{57}Fe (2.12%), and ^{58}Fe (0.28%). Of these isotopes, only ^{57}Fe is Mössbauer active. The Mössbauer effect uses resonant absorption of gamma-ray photons by the nucleus of a Mössbauer active nuclide, such as ^{57}Fe, to measure the energy of the transition of the ^{57}Fe nucleus from its ground state with nuclear spin I=1/2 to an excited state with nuclear spin of I=3/2. To make this measurement, a gamma-ray source is required which emits gamma photons at the required energy. In the case of ^{57}Fe the gammra-ray source is ^{57}Co, which decays by electron capture to ^{57}Fe*. ^{57}Fe* is the I=3/2 excited state of ^{57}Fe which spontaneously undergoes de-excitation to the ground

state of I=1/2 by emission of a 14.4 keV gamma photon. It is this 14.4 keV gamma photon that is utilized in ^{57}Fe Mössbauer spectroscopy, as it can go on to excite a ^{57}Fe nucleus in the ground state to the excited state. Because of the large energy of the gamma-rays emitted by ^{57}Fe*, a nucleus in the gas or liquid phase undergoes a significant amount of recoil as the gamma ray is either emitted or absorbed. This recoil causes the gamma photon to lose energy, and due to the quantized nature of the ^{57}Fe nuclear transition, resonant absorption no longer occurs. However, if both the gamma source and the absorber are placed in the solid state, the crystalline lattice is able to absorb the recoil momentum and negligible energy is lost by the gamma ray. This is the Mössbauer effect.

To observe the Mössbauer effect as described above, a ^{57}Co gamma-ray source and a suitable ^{57}Fe absorber are needed. However, resonant absorption is dependent on the energy state of the absorbing nucleus being the same as that of the emitting nucleus. As such, any nuclear environment for the ^{57}Fe nucleus absorbing the gamma-ray other than the environment the source is in will tend to place the absorber off resonance with the gamma-ray. This is because the chemical and physical environment that the nucleus is in affects its quantum state, causing slight shifts in the nuclear energy level. In order to modulate the energy such that resonant absorption occurs for different nuclear environments, the source is moved with a small velocity towards and away from the sample to impart a Doppler shift to the gamma rays. Since gamma-rays absorbed by ^{57}Fe atoms in the sample are scattered in all directions after re-emission, a drop in transmission of the gamma-rays is measured, leading to a spectrum of transmission (or absorption) vs. source velocity.

Shifts in the nuclear energy level of the iron nucleus occur as a result of varying chemical environments present in different solid state Fe materials. These shifts result in the three hyperfine interactions that can be measured using Mössbauer spectroscopy: the center shift (δ, CS), the quadrupole split or shift (Δ, QS), and the hyperfine field (H). The first of these parameters, the center shift, comes about due to the interaction of the *s*

electrons of the atom with the nucleus. When a sample is analyzed, the center shift is observed as a shift in the energy of absorption from that of the source relative to a standard (α-Fe). Measured center shifts are a combination of the interaction of electrons with the nucleus, the isomer shift, and a second-order Doppler shift due to atomic vibrations. The isomer shift is influenced by the charge density of the atom at the nucleus, which provides information as to the valence state, and local bonding environment of the Fe atoms analyzed. The difference between iron valence states is readily observed in the difference between the center shift of Fe(II) phases (≈ +1.2 mm/s) and that of Fe(III) phases (≈ +0.4 mm/s), the smaller Fe(III) center shift is due to the lower amount of electronic shielding on the nucleus.

The second hyperfine parameter that can be determined from a ^{57}Fe Mössbauer spectrum is the quadrupole split or shift. This parameter arises from the interaction of the nuclear quadrupole moment of the I=3/2 state with the electric field gradient. The I=3/2 state of the nucleus has an ellipsoidal distribution of charge. In the simple case of a perfectly symmetrical electric field, such as that in a cubic environment, no quadrupole split occurs. However, when a non-symmetrical electric field is present around the nucleus due to the crystal environment, the I=3/2 nuclear state is split into two sublevels. The splitting of the energy levels leads to a spectrum that has two absorption peaks split by an energy difference. The energy difference between these two sublevels is the quadrupole splitting parameter. Typically, Fe(III) phases without magnetic order have a lower quadrupole splitting parameter which is on the order of 0.3-0.5 mm/s than that of Fe(II) phases which ranges from approximately 1.5 to 3 mm/s.

Finally, the third hyperfine interaction is the hyperfine field interaction. Since the ^{57}Fe nucleus has a magnetic moment, the energy levels of the nucleus can be changed if a magnetic field exists in the atomic environment. In iron minerals, this magnetic field can come from magnetic ordering produced by electrons. This internal magnetic field is felt by the nucleus. Application of a magnetic field at the nucleus removes the degeneracy of

the nuclear states, causing a Zeeman splitting of the nuclear energy levels. This phenomenon produces a spectrum with 6 lines, or a 'sextet'. Many Fe(III) containing minerals order magnetically, for example, goethite orders antiferromagnetically. In addition, the quadrupole effect on the nucleus is observed for magnetically ordered iron phases, however, it manifests itself as a shift in the energy levels by a small amount, and therefore is called the quadrupole shift. The hyperfine interaction can be used together with the center shift and quadrupole shift parameters to identify the phases of iron present in a sample.

Mössbauer spectra are typically fit using a computerized algorithm to extract useful parameters. We have chosen to use the Recoil program (University of Ottawa, Ottawa, Canada). Computer fitting is an empirical procedure, and for the most part Mössbauer spectra are not derived from first principles; however, there have been recent attempts to derive Mössbauer spectra from *ab initio* models (*71, 72*). Furthermore, while the theoretical Mössbauer line is Lorentzian in shape, dynamic fluctuations in the environment surrounding the absorbing nuclear can broaden line shapes (*70, 73*). This variation can be treated by assuming a Gaussian distribution of Lorentzian lines, giving rise to a Voigt line profile (*73*). We have modeled spectra using Gaussian distributions of both the quadrupole splitting or shift parameter (Δ or QS) and the hyperfine field parameter (H).

X-ray Absorption Spectroscopy

We have also made extensive use of x-ray absorption spectroscopy to determine uranium valence states and coordination environments in collaboration with Ken Kemner, Maxim Boyanov, and Edward O'Loughlin at Argonne National Laboratory. X-ray absorption spectroscopy can be used for both valance state measurements and to characterize the structural environment of a uranium atom in liquid solution or in the solid state, and is typically done with highly brilliant and focused x-rays from a

synchrotron light source (*74*). Absorption of x-rays in matter occurs through the photoelectric effect, such that, as an x-ray is absorbed by an atom, an electron is excited from a lower energy level to a higher energy level (*75*), and these electronic transitions occur at specific energies for different elements. In x-ray absorption spectroscopy, as the energy of the photons incident upon a sample is scanned, an absorption edge is reached where adsorption goes from zero to a large value as the energy required to excite an electron in the absorbing atom to a higher level is met. In x-ray absorption near edge spectroscopy (XANES), changes in valence state of, for example, uranium, can be determined because electrons are more strongly bound to the positive nucleus in U(VI) than in U(IV). As the photon energy is increased beyond the edge, oscillations in the amount of absorption occur as an excited photoelectron from uranium interacts with the electrons of near-neighbor atoms. This gives rise to the extended x-ray absorption fine structure spectrum (EXAFS), which provides information as to the bonding environment of an atom, e.g. nearby oxygen and metal atoms (*75*).

CHAPTER 2: SORPTION AND REDUCTION OF URANIUM(VI) BY GREEN RUSTS

Abstract

Green rusts are widely recognized as an important intermediate phase in iron biogeochemical cycling. We have investigated the extent and mechanism of uranium(VI) removal in the presence of synthetic carbonate, sulfate, and chloride green rust, as well as pyroaurite, an Mg(II)-Fe(III) structural analog of carbonate green rust. The kinetics of U^{VI} removal was similar among the three green rusts and pyroaurite. The majority of U^{VI} (> 80%) was removed from solution in about an hour in batch reactors containing 1.0 g/L of green rust at pH values of 7.0 and 8.0. Sulfate and chloride green rusts completely reduced U^{VI} to U^{IV} in both TAPs buffer and 4 mM bicarbonate. Complete reduction was observed with carbonate green rust in 4 mM bicarbonate and in DI water, but only partial reduction of U^{VI} was observed in pH 8.0 TAPS buffer. No measurable reduction of U^{VI} was observed in the presence of pyroaurite. Bicarbonate concentration had little effect on the rate and extent of U^{VI} sorption and reduction at concentrations less than 10 mM. At higher concentrations (> 10 mM), U^{VI} sorption was slower, but reduction was still observed. Together, these data suggest that green rusts may be an effective sorbent and reductant for uranium near Fe-rich oxic-anoxic boundaries in natural environments.

Introduction

In the near-surface geochemical environment, blue-green colors associated with gleyed soils and sediments that change to ochre upon exposure to the air have long been thought to be due to the presence of structural ferrous and ferric iron in green rusts (*76, 77*). Green rusts are clay-like, mixed-valent iron minerals that belong to the class of minerals termed layered double hydroxides (LDH) because they are composed of sheets of Fe(II) and Fe(III) cations between a double layer of hydroxide anions (*78*). The layered double hydroxide structure of green rusts can be thought of as an $Fe(OH)_2$ sheet

where a portion of the Fe(II) atoms have been oxidized to Fe(III) creating a charge imbalance in the $Fe(OH)_2$ layer. To compensate the charge imbalance, anions, such as chloride, sulfate, and carbonate intercalate into the interlayer (*79*). Because the concentration of CO_3^{2-} is typically higher in soils and freshwater sediments than the concentrations of SO_4^{2-} and Cl^- (*77*) and a preference for CO_3^{2-} in the structure of LDH minerals over Cl^- and SO_4^{2-} (*80*), carbonate is the most likely anion to occur in green rusts found in soils and freshwater sediments. Green rusts are thermodynamically unstable and are thought to be highly reactive intermediate phases in processes as diverse as corrosion (*81*), microbial Fe redox cycling (*82*), Mars rock formation (*83*), evolution of life (*84*), and water quality control (e.g. *85, 86-89*).

Here we focus on the reaction of green rusts with U^{VI}. While green rusts have only recently been identified in nature (*90-92*), they are believed to occur widely as an intermediate species in corrosion processes (*93*) and, thus, may have a role in the migration of uranium from waste repositories. Natural green rusts have also been shown to form in soils under mildly reducing conditions that are subject to seasonal fluctuations in the water table, and represent a dynamic reactive iron species in the environment (*53*). Identification of green rusts as a common product of bacterial iron metabolism (*53, 94-98*) further suggests that the reactive minerals may be present in iron-reducing subsurface environments.

Previous studies provide some indication that green rusts are capable of reducing U(VI). Chemically synthesized sulfate green rust has been shown to reduce uranium(VI) to uranium(IV) nanoparticles in batch reactors containing deionized water (*61*). Carbonate green rust produced from the bioreduction of lepidocrocite was found to reduce U^{VI} to U^{IV} nanoparticles under similar conditions in DI water (*54*). Reduction of U^{VI} has also been noted under anoxic conditions where green rust was a corrosion product due to oxidation of iron metal, but the mechanism of reaction between the U^{VI}/Fe^0/GR is unclear (*99*). In addition, the presence of a potential “green rust-like

precipitate" in well sediments was noted by Wu et al. (*43*) during a pilot scale in-situ uranium bioremediation project where significant uranium reduction was achieved. The authors of the bioremediation study speculated that a joint biotic-abiotic uranium removal mechanism might have occurred.

There is, however, little data on whether the interlayer anion identity, or aqueous carbonate concentration influences the rate of U(VI) uptake and extent of U^{VI} reduction. Previous studies with chromate found relatively small effects of the interlayer anion on the kinetics of reduction of by green rusts (*100*), but the strong coordination of the uranyl cation by anionic ligands such as carbonate (*38*) (in contrast to the chromate anion) suggests that the interlayer anions may be of more importance in the interaction of U^{VI} with green rusts. Coordination of ligands to the UO_2^{2+} core has also been shown to have a strong influence on the rate of reduction of uranyl in aqueous solution (*101*). Here, we show that the interlayer anion (i.e., carbonate, sulfate, or chloride), as well as presence of aqueous carbonate, has little influence on the reduction of U(VI) by green rusts and that all three forms result in near-complete reduction of U(VI).

Materials and Methods

Materials Synthesis and Characterization

Sulfate and carbonate green rusts were prepared using previously described methods in an anoxic glovebox (*89*). Briefly, an 0.13 M solution of $FeCl_2 \cdot 4H_2O$ or $FeSO_4 \cdot 7H_2O$, for carbonate and sulfate green rusts, respectively, was titrated to pH 7.0 and mixed with 0.025 M $FeCl_3 \cdot 6H_2O$ titrated to pH 7.0, and the mixture was titrated to pH 8.0 for sulfate green rust and pH 8.3 for carbonate green rust at a maximum rate of 1 mL min^{-1}. The titrants were 1.0 M Na_2CO_3 and 1.0 M NaOH for carbonate and sulfate green rusts, respectively. Ferric carbonate green rust was synthesized as above and quickly oxidized with excess hydrogen peroxide (*102*). Chloride green rust was

synthesized in a similar manner as sulfate and carbonate green rusts except that the Fe(III) concentration was increased to 0.044 M for an Fe(II)/Fe(III) ratio of 3.0. Ferrous and ferric chloride salts were used in addition to a solution concentration of 0.5 M NaCl, and NaOH was used as the base.

Carbonate green rust was also synthesized in the presence of phosphate to stabilize the product from transformation to magnetite and ferrous carbonate. The method outlined in Bocher et al. (*103*) was used except that $FeCl_3 \cdot 6H_2O$ used in place of $Fe_2(SO_4)_3 \cdot 5H_2O$. Here a solution of 0.267 M $FeSO_4 \cdot 7H_2O$, 0.133 M $FeCl_3 \cdot 6H_2O$, and 2.1 mM $NaH_2PO_4 \cdot H_2O$ in 100 mL of deionized water was mixed with 100 mL of 0.466 M Na_2CO_3 and 0.8 M NaOH solution under stirring in an anoxic glovebox. All green rust solids were vacuum-filtered without washing and transferred to a sealed vessel for freeze drying. After freeze drying the solids were ground and sieved through an 0.15 mm sieve.

Pyroaurite was synthesized according to the procedure of Ferreira et al. (*104*). Here 70 mL of 0.1 M $Mg(NO_3)_2 \cdot 6H_2O$ and 0.05 M $Fe(NO_3)_3 \cdot 9H_2O$ was added dropwise under stirring to 150 mL of 2.0 M NaOH and 0.1 M Na_2CO_3 at 45 °C. After addition of the metal solution to the base solution was complete, the precipitate was aged at 85 °C for 2 h. To ensure replacement of interlayer NO_3^- with CO_3^{2-} the product was centrifuged and resuspended in 0.1 M Na_2CO_3 and stirred overnight (*105*). This solution was then washed 3 times by centrifugation. The resulting solids were freeze dried and sieved through a 0.15 mm sieve.

Freeze dried green rusts, pyroaurite, and Fe(III) oxides and oxyhydroxides were characterized using powder x-ray diffraction (pXRD) with a Bruker D-5000 diffractometer using monochromatic Cu-Kα radiation or a Rigaku MiniFlex II diffractometer using Co-Kα radiation and a Fe Kβ filter. Green rust samples were mixed with glycerol to minimize oxidation during analysis (*106*).

U^{VI} Sorption and Reduction Experiments

Experiments investigating U^{VI} sorption and reduction were carried out in an anoxic glovebox (93% N_2/7% H_2) to exclude oxygen and to maintain low atmospheric CO_2 concentrations. Sorption experiments were done at a solids loading of 1 g/L green rust in 0.1 M TAPS buffer adjusted to pH 8.0. An amount of uranyl acetate ($UO_2(CH_3COO)_2 \cdot 2H_2O$) stock solution in 0.1 M HCl was added to 75 mL of stirred buffer solution to achieve a nominal uranium concentration of 400 µM, and an initial uranium concentration sample was taken. We noted that TAPS buffer complexes U^{VI} and suppresses precipitation of U^{VI} at concentrations greater than the solubility of schoepite calculated using the speciation program Visual MINTEQ (*107*). A precipitate was visually observed after additions of U^{VI} to reactors containing DI water adjusted to a pH value of 8.0. However, U^{VI} is stable at concentrations to 500 µM in pH 8.0 TAPS solution over a time frame of at least 1 year. In some experiments, TAPS was replaced with 0.1 M PIPES buffer and 4 mM $NaHCO_3$ which was adjusted to pH 7.0. Finally, the effect of carbonate in the 0.1 M TAPS/sulfate green rust system was investigated by adding amounts of 1 M $NaHCO_3$ to TAPS buffer for HCO_3^- concentrations of 0.1 mM, 2 mM, 10 mM and 20 mM. To initiate the reaction, 75 mg of solid was added to the reactor. Aliquots for uranium analysis were removed and filtered through a 0.2 µm syringe tip filter. Samples were taken at 2, 5, 10, 20, 40, 80, 160 minutes and approximately 20-24 h.

Uranium reduction experiments were done for analysis with x-ray absorption spectroscopy and consisted of a 5 g L^{-1} suspension of solids in 60 mL of solution to which a nominal uranyl acetate spike of 500 µM was added. Various solution conditions were tested, including 0.1 M TAPS buffer (pH 8.0), 4 mM $NaHCO_3$ buffer (pH 7.0), and DI water alone. The higher solids loading and U^{VI} loading compared to the sorption experiment was used to provide sufficient solids and U mass for high quality x-ray absorption spectra. Initial U^{VI} measurements were made on a filtered aliquot of solution

prior to addition of green rust, and final aqueous U^{VI} measurements were made approximately 24 hours after initiating the reaction, using filtered aliquots of suspension.

Aqueous Uranium Measurements

Analysis of uranium was done in two ways. The method used for most experiments was a colorimetric determination of soluble uranium by 2-(2- Thiazolylazo)-p-Cresol (TAC) at a 588 nm (*108, 109*). The method of Teixeira et al. (*108*) was modified such that the sample and reagents for spectrophotometric determination were contained within a 1.5 mL micro-centrifuge tube to limit production of uranium containing waste. Briefly, 300 µL of sample was used, to which 300 µL of complexing solution (0.137 M CDTA, 0.1 M NaF, and 0.51 M 5-sulfosalicylic acid, pH 6.5), 60 µL of 0.05 M CTAB (N-cetyl-N,N,N-trimethylamonium bromide), 60 µL of 0.15 M Triton X-100, 300 µL of 1 M triethanolamine buffer at pH 6.5, and 420 µL deionized water were added. Color was allowed to develop over 2 hours and analyzed alongside standards with 10, 50, 75, 100, 150, and 200 µM U^{VI}. The detection limit was 9 µM based on repeat analysis of 11 samples of 10 µM uranyl acetate and calculated using the product of the standard deviation and Student's t-value at $p = 0.01$. The second method, used for some initial experiments, was an ion chromatographic method followed by post-column spectrophotometric determination of uranium with Arsenazo III at a wavelength of 650 nm (*110*). A Dionex DX-500 ion chromatograph equipped with a AS14 column was used with 0.05 M H_2SO_4 and 0.025 M $MgSO_4$ eluent pumped at 1 mL/min. After chromatographic separation the eluent stream was combined with 0.03 % (by weight) Arsenazo III in 1 M acetic acid from a post column reagent system operating at 60 pounds per square inch (psi). Standard solutions were prepared in 0.1 M TAPS at pH 8.0 and had concentrations of 10, 50, 100, 250, and 500 µM U^{VI}.

X-ray Absorption Spectroscopy

The U L_{III}-edge XAFS experiments were carried out at the Materials Research Collaborative Access Team (MRCAT) ID beamline, sector 10 at the Advanced Photon Source, using a previously described setup (*111*). Briefly, the beamline undulator was tapered and fixed, and the incident energy was scanned by using the Si(111) reflection of the double-crystal monochromator in quick-scanning mode (approximately 2 min per scan for the extended region and 30 s per scan for the near-edge region). The wet paste samples were mounted in drilled Plexiglas slides and sealed inside the anoxic chamber with Kapton film windows. The sealed slides were exposed to air for about 1 min while being transferred from an O_2-free transport container to the N_2-purged detector housing. Several U^{VI} and U^{IV} standards were used in the XANES and EXAFS analysis. An acidic (pH 3) solution of uranyl chloride was used as the standard for hydrated U^{VI} and a basic (pH 11) solution of U:carbonate=1:50 was used as the standard for carbonate-complexed U^{VI}. U^{IV} standards included a crystalline UO_2 purchased from Alfa Aesar and diluted 1:100 in SiO_2 (*112*), biogenic U^{IV} nanoparticles produced by *Shewanella oneidensis* MR-1 and characterized in a previous study (*47*), and U^{IV} nanoparticles produced abiotically by reduction with sulfate green rust (*61*). Linear combination spectral analysis of EXAFS data were performed using the program SIXpack (*113*).

Results and Discussion

Sorption of U^{VI} to Synthetic Green Rusts

U^{VI} Sorption Kinetics

Uranium^{VI} (U^{VI}) is rapidly removed from solution in the presence of 1 g/L sulfate, carbonate, and chloride green rusts as well as by redox inactive pyroaurite (Mg(II)-Fe(III)-CO_3 LDH) (Figure 2.1). We observed little influence of the interlayer anion on the kinetics of U^{VI} sorption to green rusts, and observed similar sorption kinetics on

pyroaurite (same structure as carbonate green rust, but Mg(II) ions replace the Fe(II) ions). Little difference in the kinetics of U^{VI} sorption was observed between pH 8.0 TAPS buffer and pH 7.0 PIPES buffer with 4 mM bicarbonate (Figure 2.1). Using a pseudo-first order kinetic model, we estimated the observed first-order rate coefficients (k_{obs}) for the initial uptake (< 20 minutes) which reveals rate coefficients at pH 7.0 and 8.0 that vary by a factor of 7 between the slowest observed rate (GR(CO_3) at pH 8.0) and the fastest observed rate (GR(SO_4) at pH 7.0) (Table 2.1). Over approximately 1 day, we noted that significant amounts of U remained in solution (48 µM) in the GR(CO_3) reactors containing pH 8.0 TAPS buffer, but was removed to below the 9 µM detection limit of the TAPS colorimetric method in all pH 7.0 PIPES and 4 mM bicarbonate buffered reactors.

The kinetics of U^{VI} uptake were also explored with carbonate green rust synthesized in the presence of phosphate. Phosphate has been shown to sorb preferentially to edge sites on green rust and to stabilize green rust from transforming to other Fe minerals (*103*). We found that phosphate reduced the rate of U^{VI} uptake from pH 8.0 TAPS buffered solution by a factor of about 2, which is within the variation in rates noted between different green rusts. The extent of uptake after 20 hours was the same as for GR(CO_3) without phosphate, with 57 µM U remaining in solution. Differences in rate could be due to differences in surface area or other factors associated with the difference in between the two synthesis methods, and for these reasons we cannot attribute any effect of sorbed phosphate to U^{VI} sorption to green rust.

Two previous studies evaluated the influence of green rust interlayer ions on chromate (*100*) and nitrate reduction (*87, 114*). The rate of Cr(VI) removal from solution has also been found to vary as a function of green rust mass loading (*85, 100*). Extrapolation of the rate data from Bond and Fendorf for Cr(VI) uptake on green rusts to 1 g/L yields rate constants on the order of 2 to 5×10^{-2} s^{-1}, which are about two orders of magnitude larger than what we have observed here for U(VI) (Table 2.1) (*100*). A study

investigating sorption of chromate on a redox-inactive calcined hydrotalcite (Mg(II)-Al(III)-CO_3 layered double hydroxide) found first-order rate constants on the order of 1 $\times 10^{-2}$ s^{-1}, potentially indicating that the rate limiting step in chromium reaction with green rusts is also the rate of uptake from solution (*115*). In a previous study, we observed similar rates of Cr(VI) reaction with carbonate green rust (*85*). In contrast to U(VI) and Cr(VI), the effect of interlayer anion on the rate of uptake of nitrate was found to be significant with rates varying up to 32-fold (Table 2.1). Differences in NO_3^- uptake rates were rationalized based on differences in the octahedral Fe(II)-Fe(III) hydroxide layer charge and the ability of NO_3^- to replace either Cl^- or SO_4^{2-} in the interlayer (*114*).

Effect of Bicarbonate

In addition to the green rust interlayer anion, we also investigated the influence of aqueous bicarbonate concentration on the uptake of uranyl from solution by sulfate green rust (Figure 2.2). Addition of 0.1 mM $NaHCO_3$ to TAPs buffer did not significantly change the rate of uranyl uptake from solution by GR(SO_4), but 2 mM bicarbonate resulted in an 2-fold increase in the rate of uranium uptake from solution. At higher carbonate concentrations (10 mM) the rate of uranium uptake was slightly inhibited, whereas at much higher concentrations (20 mM), a significant decrease in the rate of uranium uptake was observed. Results were similar in pH 8.0 buffer with 2 mM (bi)carbonate (data not shown) and in pH 7.0 PIPES buffer with 4 mM (bi)carbonate. We note that typical bicarbonate concentrations can range from around 1 to 6 mmole L^{-1} (assuming that all reported alkalinity is bicarbonate alkalinity) (*116, 117*), but bicarbonate concentrations may be greater during biostimulation of microbial activity where organic matter is oxidized to CO_2.

Potential explanations for the differences in rates of uranium sorption to green rusts and pyroaurite in the presence and absence of carbonate include differences in green rust surface charge, uranium speciation, and anion exchange. In the near-neutral to

slightly alkaline pH range green rusts likely have positively charged surfaces. The point of zero charge for the green rusts have not been reported, but the pH_{PZC} for an analogous Mg(II)-Fe(III) chloride layered double hydroxide is reported to be in the range of 10.3 - 10.8 depending on exact Mg(II)-Fe(III) composition and lies between the PZC of Fe(III) oxyhydroxides and the Mg(II) hydroxide (*118*). This positively charged surface at near-neutral pH might help explain the facile adsorption of NO_3^- and CrO_4^{2-}, but cannot be used to explain adsorption of the positively charged UO_2^{2+} and UO_2-OH species. However, adsorption of uranyl in the absence of carbonate may be made more favorable by negatively charged green rust moieties in the vicinity of structural anions.

The faster removal of U^{VI} by GR(SO_4) from pH 8.0 solution containing 2 mM $NaHCO_3$ (Figure 2.2) and by all green rusts in pH 7 solution containing 4 mM $NaHCO_3$ (Figure 2.1) may be due to the favorable uptake of negatively charged uranyl carbonate species by a positively charged green rust surface. The predicted speciation for uranyl in these solutions was calculated with Visual MINTEQ (*107*) and uranyl species are predominantly in the form of the negatively charged $(UO_2)_2CO_3(OH)_3^-$ $UO_2(CO_3)_2^{2-}$, and $UO_2(CO_3)_2^{4-}$. At low carbonate concentrations from 0.1 mM and 2 mM $(UO_2)_2CO_3(OH)_3^-$ is the predominant uranyl species. Increasing the carbonate concentration to 10 and 20 mM results in the formation of the tris-carbonato uranyl complex ($UO_2(CO_3)_3^{4-}$). In addition, at high carbonate loadings, surface complexation of carbonate on the green rust surface might be expected to give a negative charge to the surface. A negatively charged green rust surface is less likely to sorb the negatively charged uranyl tris-carbonato complex, which likely accounts for the reduced extent of U uptake in the 20 mM bicarbonate reactor.

In addition to the carbonate complexation of U^{VI} in these systems, we have found that TAPS may be complexing U^{VI}. We observe that concentrations of up to 500 µM UO_2^{2+} are soluble in pH 8.0 TAPS buffer at a time scale of over a year. These concentrations of U^{VI} are over the solubility limit of schoepite ($UO_3 \cdot 2H_2O$) expected

from solubility constraints (pK_{s0}(schoepite) = 5.994 using the software package Visual MINTEQ (*107*)). Precipitation of U^{VI} is observed after adding a stock of uranyl acetate to control reactors adjusted to pH 8.0 in the absence of TAPS. This suggests that TAPS is forming a stable complex with the uranyl cation, thus the effect of U^{VI}-TAPS complexation as well as complexation of the underlying surface by this organic buffer may also have a role in reducing the extent of uranium uptake by GR(CO_3) in TAPS buffer relative to the PIPES buffer with 4 mM bicarbonate. PIPES buffer has been considered as a non-complexing buffer (*119*). With no carbonate present, soluble uranyl will likely exist as positively charged hydroxylated species or as a U^{VI}-TAPS complex with unknown characteristics.

In addition to the potential for surface complexation of carbonate on GR(SO_4) and GR(Cl) when carbonate is added to a suspension of these green rusts, anion exchange between the SO_4^{2-} or Cl^- in the interlayer and the aqueous carbonate ion can occur, as carbonate is favored over sulfate or chloride in the interlayer (*120*). At low carbonate loadings, interlayer exchange of sulfate for carbonate may reduce the concentration of carbonate in solution available for complexation of U^{VI}, leading to the observed increase in the rate of U uptake from solution in the case of 2 mM bicarbonate relative to the higher carbonate loadings (Figure 2.2). At low carbonate loadings, uptake of CO_3^{2-} into the interlayer may also help bring UO_2-CO_3 complexes in contact with the green rust surface and allow for sorption to occur, a phenomenon which may be inhibited at higher loadings due to increased formation of negatively charged U^{VI}-CO_3 complexes and charging of the green rust surface by negatively charged bicarbonate and carbonate anions.

Uranium Reduction by Green Rusts

To determine whether the sorbed uranium was reduced by chloride, sulfate, and carbonate green rusts, we used x-ray absorption spectroscopy. Previous work has shown

that sulfate green rust reduces U^{VI} to $U^{IV}O_2$ uraninite nanoparticles in deionized water containing no carbonate (*61*). X-ray absorption near edge spectroscopy (XANES) at the U L_3-edge indicates that no reduction of U^{VI} occurs in the presence of pyroaurite – the Mg(II)-Fe(III) analogue of GR(CO_3) (Figure 2.3). Similar results were also observed for fully ferric green rust, in which all the Fe(II) has been oxidized but the LDH structure is maintained (*102*).

In contrast to pyroaurite, both sulfate and chloride green rusts in TAPs buffer reduced most of the 500 µM U^{VI} added within about four days, consistent with the previous report of reduction of U^{VI} by sulfate green rust, which occurred in about a day (*61*). Interestingly, the addition of bicarbonate at pH 8.0 at concentrations of 2 and 20 mM had no observable effect on the extent of reduction of U^{VI} to U^{IV} in 5 g/L GR(Cl) and GR(SO_4) suspensions (Table 2.2). It is important to note that bicarbonate may have influenced the rate of reduction, but our XAS measurements were made between 3 and 4 days after sample preparation which appears to have been enough time for nearly complete reduction to occur in both the absence and presence of bicarbonate.

Carbonate green rust in pH 8.0 TAPS buffer, on the other hand, did not fully reduce U^{VI} to U^{IV} after 3 to 4 days. The uranium oxidation state lies between that of the U^{VI} and U^{IV} standards (Figure 2.3). The amount of reduction observed in TAPS buffer ranged from 45 to 70% (note there is a ±10-15% variability in XANES measurements) based on three samples measured during two different beam runs (45% reduction shown in Figure 2.3). Addition of 2 mM $NaHCO_3$ to pH 8.0 TAPS and GR(CO_3) suspension resulted in an extent of uranium reduction that was similar to GR(SO_4) and GR(Cl) suspensions containing 2 mM bicarbonate (Figure 2.4).

Our findings of incomplete reduction of U^{VI} by GR(CO_3) are not consistent with previous work which reported complete reduction of U^{VI} by carbonate green rust formed from reduction of lepidocrocite by *Shewanella putrefaciens* CN32 (*54*). To investigate why, we ran several additional experiments evaluating the effect of freeze-drying,

phosphate incorporation, and the TAPs buffer. We have investigated whether freeze drying carbonate green rust during preparation caused a change in its ability to reduce U^{VI}. We note that other researchers have suggested that freeze drying green rust changes its reactivity (*121*). When fresh GR(CO_3) was resuspended in TAPS buffer it reduced 35% of the uranium added (Table 2.1). This result is consistent with the freeze dried experiment (within XANES analytical error), suggesting that freeze drying didn't have a measureable effect on U reduction.

Due to our observation that TAPS buffer appears to complex U^{VI} we have also investigated the role of buffer in U reduction by carbonate green rust. In the absence of TAPs, in both deionized water alone and 4 mM $NaHCO_3$ as a pH 7.0 buffer, nearly complete reduction of U^{VI} to U^{IV} was observed, with > 85% of the U in the products as U^{IV} (Figure 2.4). In addition, when both fresh GR(CO_3) harvested by filtration and freeze-dried GR(CO_3) were reacted with U^{VI} at pH 8.0 in the absence of buffer 85% to 100% U^{IV} was observed in the products. Green rust stabilization by phosphate during synthesis also had no observable effect on U^{VI} reduction by GR(CO_3) suspended in TAPS, as 50% of the U^{VI} added has been reduced to U^{VI} (Table2.2, Figure 2.4).

Our observation of partial U reduction by synthetic GR(CO_3) in the pH 8.0 TAPS system and nearly complete reducution in systems where TAPS was omitted indicates that the complexation of U^{VI} by TAPS may have an effect on U speciation in the carbonate green rust system. However, complete reduction of U^{VI} to U^{IV} was observed in the GR(Cl) and GR(SO_4) systems in the presence of TAPS. These results indicate that in comparison to sulfate and chloride green rusts U^{VI} reduction by carbonate green rust may be more variable depending on the conditions studied. We caution against the use of TAPS buffer in uranium work because of its complexing ability towards UO_2^{2+}. Finally, we note that freezed dried GR(CO_3) was unstable over time in DI water, PIPES, and bicarbonate buffers, and underwent a visible transformation to black solid (most likely magnetite). The same green rust was stable for a much longer period of time in TAPS

buffer. Complexation of U^{VI}, however, may be applicable to systems with high concentrations of natural organic matter or under high bacterial growth conditions with production of extra-cellular material.

Conclusions

Our study indicates that U^{VI} uptake in the presence of green rusts with the commonly occurring interlayer anions (Cl^-, SO_4^{2-}, and CO_3^{2-}) is relatively fast and similar for the green rusts with different anions. Similar rates of uranium uptake from solution by redox-active green rusts and redox inactive Mg-Fe(III) pyroaurite indicate that sorption is likely the rate-limiting step in the reaction of U^{VI} with these materials. Our results indicate that solution (bi)carbonate has relatively little effect on U^{VI} sorption at lower concentrations, but as concentrations increase to 20 mM total (bi)carbonate sorption of U^{VI} from solution is decreased. Our results with synthetic green rust confirm those of previous studies that sulfate green rusts are effective reductants of U^{VI}, and further shows that both chloride and carbonate green rusts reduce U to U^{IV} (*54*, *61*). As carbonate is present in most natural waters, it is also of significance that we observed reduction of U^{VI} -carbonate complexes by all three forms of green rust.

We caution that use of organic buffers such as TAPS may lead to erroneous results due to their metal complexing ability, and suggest if these organic buffers are to be used they should be checked for metal complexing ability prior to their use in experiments. The reduced extent of U^{VI} reduction by carbonate green rust in the presence of TAPS may indicate that this material is more susceptible to solution composition changes that may change it effectiveness as a reductant for U and possibly other oxidized contaminants. This is potentially important, as carbonate green rust will be the most likely to form under fresh-water conditions with relatively low sulfate concentrations.

Table 2.1. Pseudo first-order rate constants (k_{obs}, s^{-1}) for contaminant sorption/reduction by synthetic green rusts.

	UO_2^{2+} pH 7.0[a]	**UO_2^{2+} pH 8.0[b]**	**CrO_4^{2-} pH 7.0[c]**	**NO_3^- pH 7.5[d]**
GR(Cl)	$(9.0 \pm 3) \times 10^{-4}$	$(8.8 \pm 0.3) \times 10^{-4}$	$(12.6 - 366) \times 10^{-4}$ [e]	$(3.08 \pm 1.04) \times 10^{-4}$ [f]
GR(SO_4)	$(15 \pm 2) \times 10^{-4}$	$(8.3 \pm 2.7) \times 10^{-4}$	$(6.10 - 181) \times 10^{-4}$ [e]	$(0.095 \pm 0.038) \times 10^{-4}$ [g]
GR(CO_3)	$(10 \pm 2) \times 10^{-4}$	$(2.0 \pm 0.2) \times 10^{-4}$	$(19.2 - 239) \times 10^{-4}$ [e]	-
Pyroaurite	$(7.1 \pm 2) \times 10^{-4}$	$(6.7 \pm 0.2) \times 10^{-4}$	-	-

[a] pH 7.0, 0.1 M PIPES, and 4 mM $NaHCO_3$. Error term: ± 1 standard deviation.

[b] pH 8.0, 0.1 M TAPS. Error term: ± 1 standard deviation.

[c] pH 7.0, 0.005 M MOPS

[d] pH 7.5, pH Stat

[e] (*100*), 0.125 g L^{-1} to 0.5 g L^{-1} green rust loading

[f] (*114*)

[g] (*87*)

Table 2.2. Uranium redox speciation after reaction with green rusts under several conditions as determined by x-ray absorption near-edge spectroscopy (XANES).

Iron Mineral	Solution Conditions	pH	U^{IV}/U_{Total}
GR(Cl) – freeze dried	TAPS buffer	8.0	100 %
	TAPS/2 mM $NaHCO_3$	8.0	93 %
	TAPS/20 mM $NaHCO_3$	8.0	100 %
GR(SO_4) – freeze dried	TAPS buffer	8.0	100 %
	TAPS/2 mM $NaHCO_3$	8.0	100 %
	TAPS/20 mM $NaHCO_3$	8.0	100 %
GR(CO_3) – freeze dried	TAPS buffer	8.0	45 to 70 % [a]
	TAPS/2 mM $NaHCO_3$	8.0	50 %
	4 mM $NaHCO_3$	7.0	95 %
	DI water	~8.0	100 %
GR(CO_3) + PO_4 – freeze dried	TAPS buffer	8.0	50 %
GR(CO_3) – fresh filtered precipitate	TAPS buffer	8.0	35 %
	DI water	~8.0	85 %

[a] Range of three samples of carbonate green rust prepared at two different dates and analyzed during two beam runs.

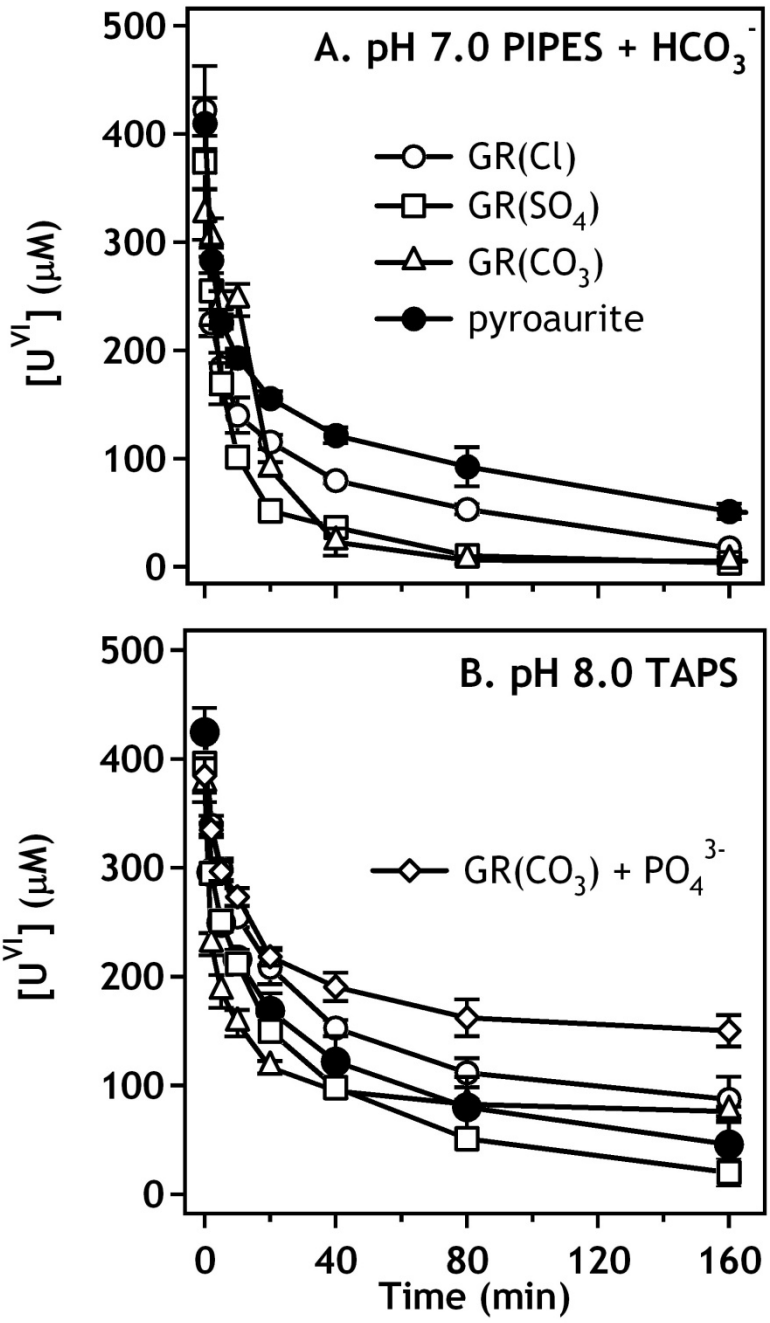

Figure 2.1. Uranium uptake by sulfate green rust ($GR(SO_4)$), carbonate green rust ($GR(CO_3)$), chloride green rust (GR(Cl)), and pyroaurite (Mg(II)-Fe(III) layered double hydroxide) in the presence of pH 7 PIPES buffer with 4 mM $NaHCO_3$ (**A**) and pH 8 TAPS (**B**). $GR(CO_3) + PO_4^{3-}$ refers to carbonate green rust synthesized in the presence of phosphate anion, which is sorbed to the green rust during synthesis. Error bars represent one standard deviation of triplicate reactors.

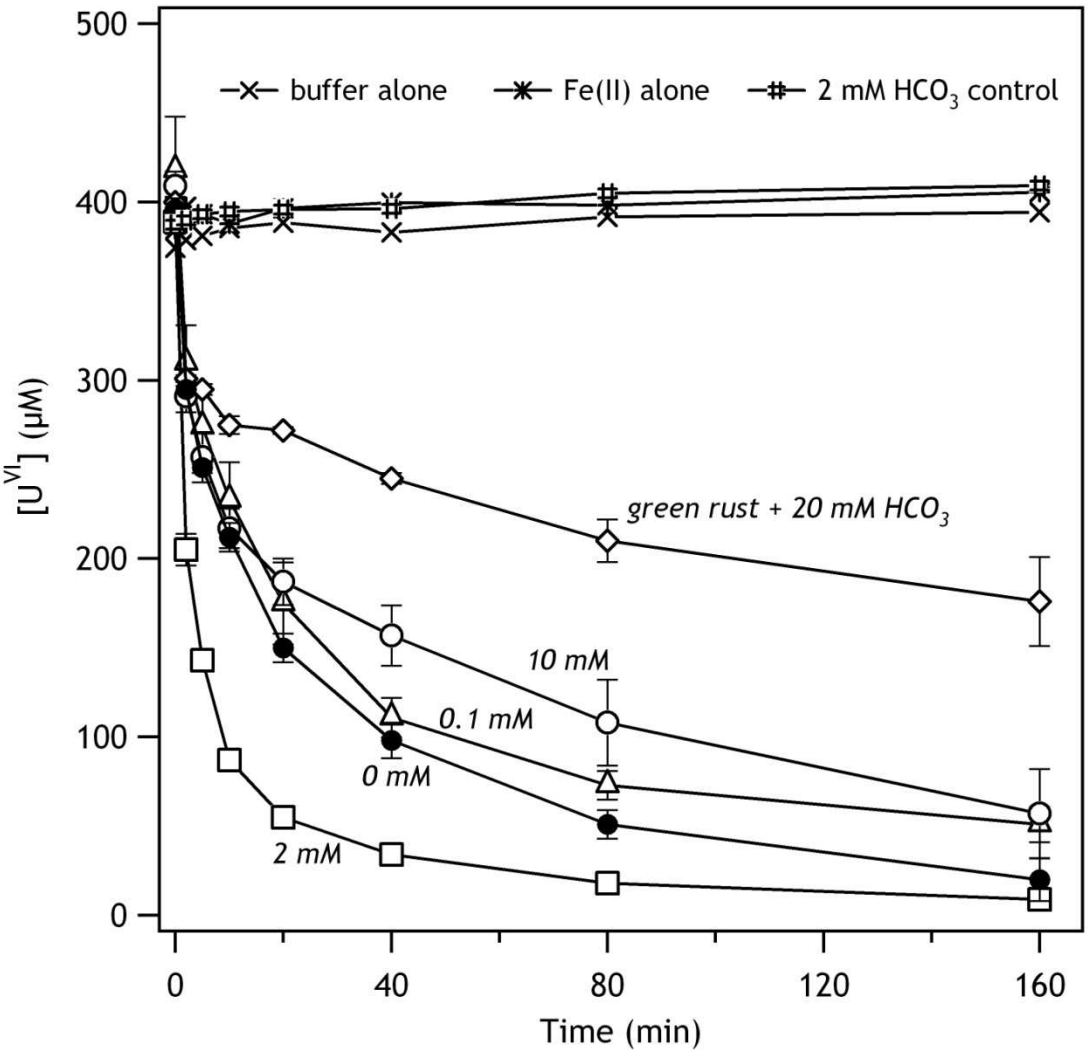

Figure 2.2. Effect of aqueous carbonate concentration on uptake of U^{VI} from solution in the presence of sulfate green rusts. Each reactor contained 1 g L^{-1} of sulfate green rust in 0.1 M TAPS pH 8.0 buffer solution. The buffer control represents a reactor with no green rust or bicarbonate. This control highlights the ability of TAPS to complex UO_2^{2+}, as this solution is supersaturated with respect to solid U^{VI}. No removal of uranium was seen in a reactor containing 0.5 mM Fe(II) with 400 μM U^{VI} under the experimental conditions tested.

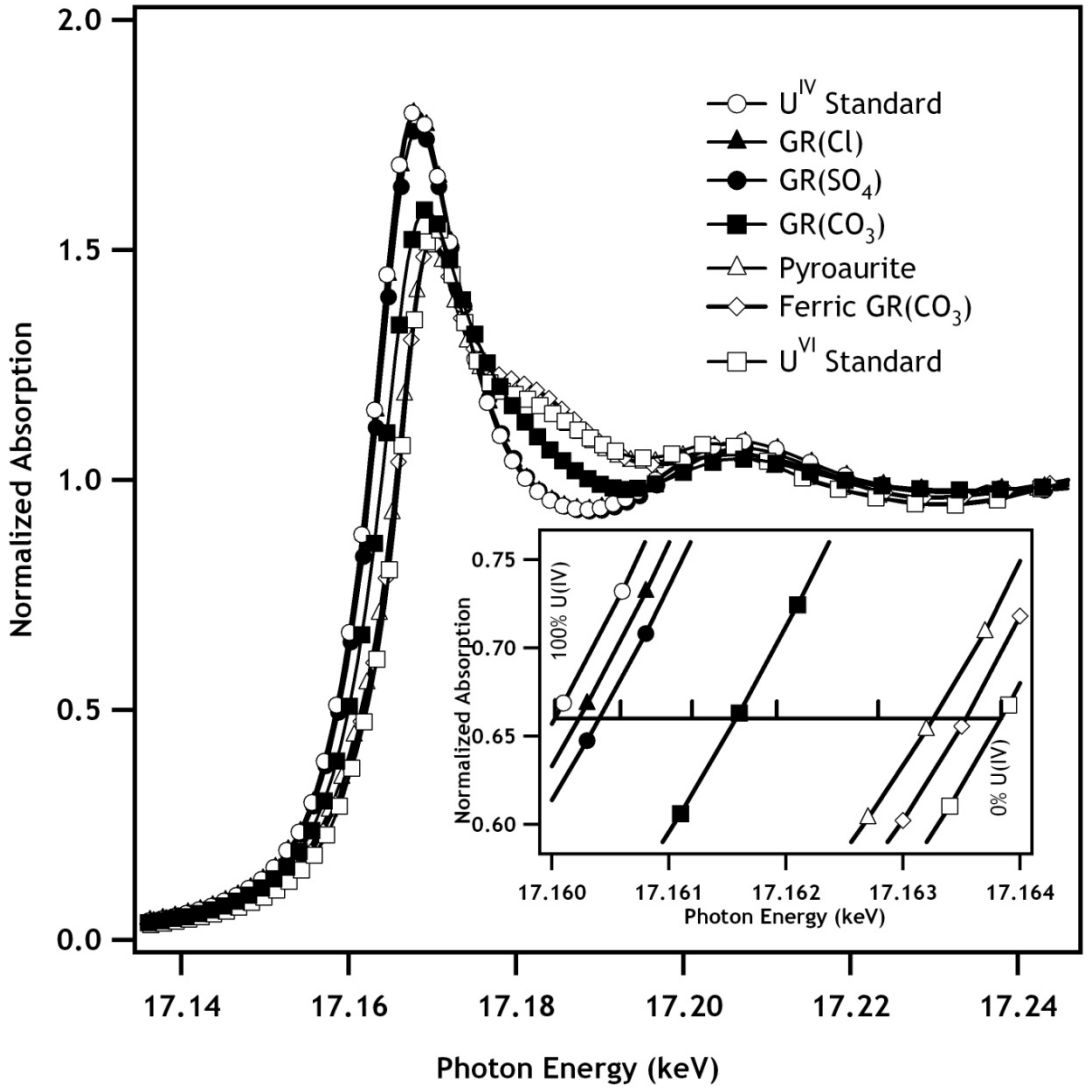

Figure 2.3. Uranium speciation after reaction with green rusts and pyroaurite. The spectra are U-L_3 XANES spectra of 5 g/L synthetic green rust samples and pyroaurite reacted with 500 uM U^{VI} in pH 8.0 TAPS. Inset: The relative position of the absorption edge of the uranium reacted with the green rust and pyroaurite samples. The scale between 0 % U^{IV} and 100% U^{IV} is marked with 20% increments on a non-linear scale.

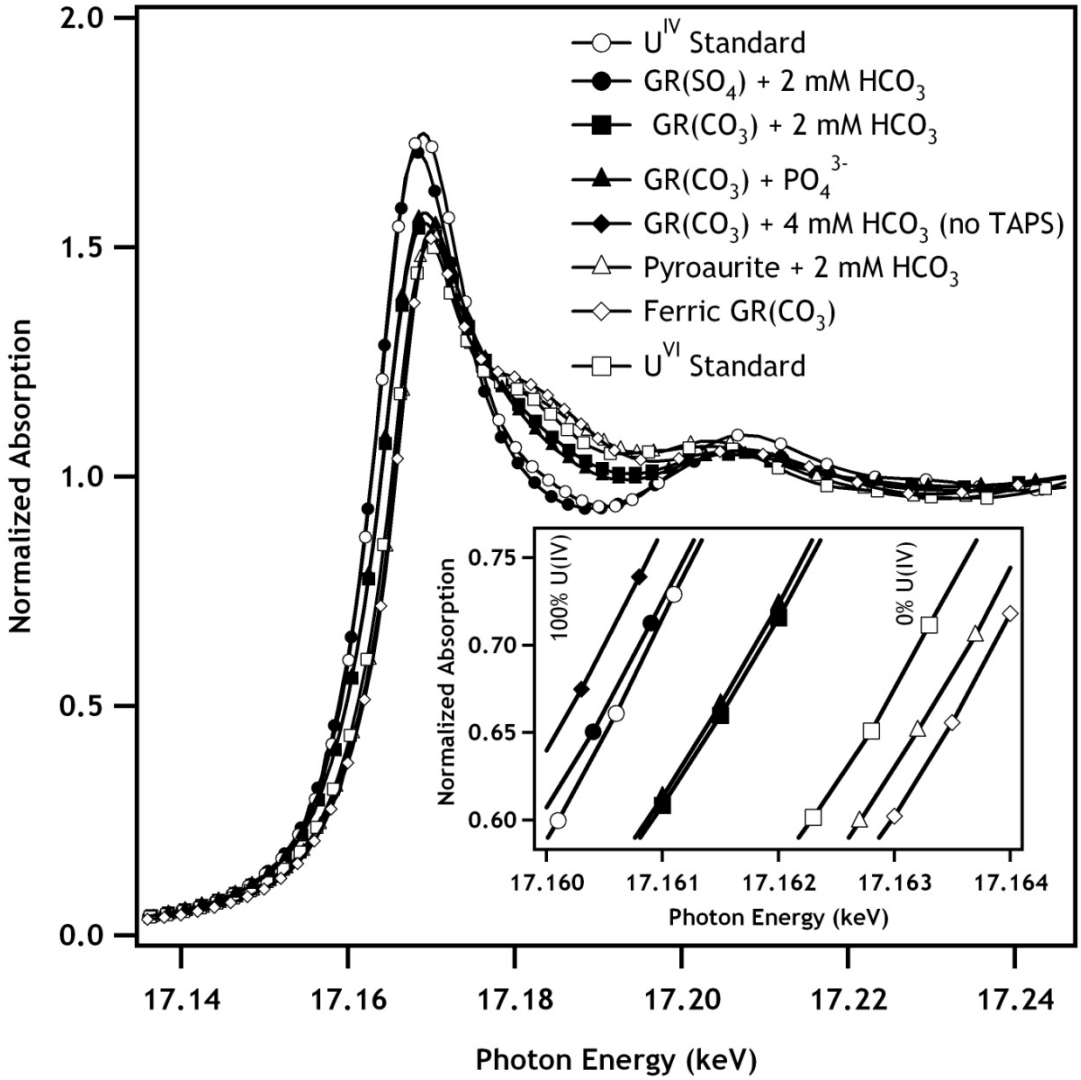

Figure 2.4. Effect of bicarbonate on the reaction of U^{VI} with green rusts and pyroaurite. The spectra are U-L_3 XANES spectra of 5 g/L green rusts and pyroaurite reacted with 500 uM U^{VI} in pH 8.0 TAPS and 2 mM bicarbonate. Also included are GR(CO_3) synthesized in the presence of phosphate (PO_4^{3-}), and GR(CO_3) in 4 mM bicarbonate buffer without TAPS with a pH value of 7.0 reacted with U^{VI}. Inset: The relative position of the absorption edge of the uranium reacted with the green rust and pyroaurite samples.

CHAPTER 3: REDOX SPECIATION OF URANIUM REACTED WITH MAGNETITES OF VARYING STOICHIOMETRY

Abstract

The current DOE strategy for treatment of radionuclide and heavy metal contamination in the subsurface relies heavily on in situ immobilization and stabilization. It is well-established that hexavalent uranium (U^{VI}) can be enzymatically reduced by a variety of microbial species, as well as abiotically reduced by many reduced iron minerals. Of the reduced iron minerals, magnetite is of significant interest because of its formation from many Fe^{III} minerals as a result of dissimilatory iron reduction. Magnetite is also a significant corrosion product of iron metal in suboxic and anoxic conditions, and will likely play a significant role in corrosion of iron waste containers holding uranium-containing spent nuclear fuel. In previous work, discrepancies exist regarding the extent of U^{VI} reduction by magnetite. Here, we demonstrate that the Fe^{2+} content of magnetite may explain the observed discrepancies in the literature, along with other differences such as solution composition, pH, and surface area. We observed that varying the initial Fe^{II} content in the magnetite significantly influenced the extent of U^{VI} reduction by magnetite. Stoichiometric and partially oxidized magnetites with an Fe^{2+}/Fe^{3+} ratio (x) greater than 0.38 reduced U^{VI} to U^{IV} in UO_2 (uraninite) nanoparticles, whereas with more oxidized magnetites ($x < 0.38$) and maghemite ($x = 0$) only sorbed U^{VI} was observed. We further show that aqueous Fe^{II} is capable of recharging the reducing capacity of these oxidized magnetites, presumably by Fe(II) reduction of the oxidized magnetite as we have previously demonstrated. Mössbauer spectroscopic results provide direct evidence that the reduction of U^{VI} to U^{IV} is coupled to oxidation of Fe^{II} in the magnetite. The stoichiometry of a biogenic magnetite produced from the reduction of lepidocrocite was found to be $x = 0.43$. Uraninite is formed from reduction of U^{VI} in a heat-killed suspension of the biogenic magnetite, consistent with our chemically synthesized

magnetites. Our results suggest that magnetite stoichiometry and the presence of aqueous Fe^{II} are important when evaluating the potential for reduction of U^{VI} in the subsurface.

Introduction

Magnetite is expected to play an important role in several aspects of the technological and natural uranium (U) cycle. The stimulation of metal reducing microbial communities has been considered and implemented as a strategy to immobilize sub-surface U contamination resulting from U processing (*43, 45, 122*), and plays a key role in the U.S. Department of Energy's program to manage legacy uranium contamination. Immobilization of U by microbial metal metabolism is thought to occur via direct enzymatic reduction of the more soluble U^{VI} species to the less soluble $U^{IV}O_2$ (e.g., *47, 48*) and via indirect reduction of U^{VI} to U^{V} and U^{IV} species by sorbed and structural Fe^{II} (*58-60*). Dissimilatory metal reducing organisms reduce several iron oxides (Fe-oxides) to magnetite (*123, 124*). Magnetite is also a common iron corrosion product from iron canisters used to contain uraniferous wastes in both short-term storage and long-term geological repositories (*125, 126*).

Magnetite (Fe_3O_4), is a mixed valence mineral containing both Fe^{2+} and Fe^{3+} ideally in a 1:2 ratio (Fe^{2+}/Fe^{3+}). Removal of all Fe^{2+} from the structure of magnetite by oxidation or dissolution results in the formation of the Fe^{3+} only mineral, maghemite (γ-Fe_2O_3) (*127*). Partially oxidized magnetites can exist between the end-members of magnetite and maghemite, and can be referred to by their Fe^{2+} content, which we denote *x*, where *x* is defined as:

$$x = \frac{Fe^{2+}}{Fe^{3+}} \quad (2.1)$$

Magnetite and maghemite crystallize with an inverse spinel structure, with magnetite having 2 Fe atoms in octahedral coordination (one Fe^{2+} and one Fe^{3+} atom) and one Fe^{3+} atom in a tetrahedral coordination site. Partially oxidized magnetite and maghemite contain cation vacancies in octahedral sites as Fe^{2+} is removed in order to

maintain charge balance (*14, 128*). The Fe^{2+} content of magnetites has considerable influence on their properties, such as conductivity/resistivity, and redox potential. A slight change in stoichiometry has been found to have a great effect on the conductivity (inversely, resistivity) of magnetite samples (*129, 130*). Several studies highlight the significant variation in redox potential with varying Fe^{2+} content (*66, 127, 131*). It is of note, however that the variation in redox potential is more gradual than the change in resistivity with *x*. Recent work by our group has highlighted the importance of magnetite Fe^{2+} content on contaminant reduction (*66, 132*). This work found that the rate of nitrobenzene reduction can be modeled as a function of the redox potential difference between magnetite and several substituted nitrobenzenes (*66*).

Previous reports investigating the reduction of U^{VI} by magnetite show results varying from complete reduction of U^{VI} to U^{IV} to no observed reduction (*54, 55, 58, 62, 133-136*). The majority of studies have found that in the presence of magnetite, U added to solution is reduced to a mix of valence states (U^{VI}, U^{V}, and U^{IV}). The reduction of U^{VI} to a mixture of valence states has been seen under various solution conditions and pH values. One study found that a magnetite synthesized via oxidation of $FeSO_4$ reduced U^{VI} to a mixture of U valence states in both pH 5 and pH 7 solutions (*126*). In contrast to the relatively stable aqueous U concentration over time, the amount of reduced U associated with the magnetite increased with time over a period of 3 months at the expense of U^{VI}, suggesting a slow continued redox reaction. Over a similar time span, the partial reduction of U^{VI} (as determined by EXAFS) by a commercially purchased magnetite at acidic pH has been reported, although only a small shift in U 4f XPS binding energies occurred, indicating reduction of only a portion of the total U in the samples (*135*). Time-dependent U^{VI} reduction by sectioned single crystals of magnetite with near stoichiometric Fe^{II} contents under acid conditions has also been observed. In that study, the presence of U^{IV} as UO_{2+x} was supported with SIMS depth profiling of the magnetite (*62*). Under slightly alkaline conditions (pH ~8.0) in the presence of 1 mM (bi)carbonate,

magnetite produced by oxidation of $FeSO_4$ reduced about half of the added U^{VI} to U^{IV} (*55*). Finally, a recent study observed reduction of U^{VI} to U^{V} in unbuffered pH 3.2 – 4.7 solutions with XPS and EXAFS. The stoichiometry of the magnetite, produced by oxidation of $FeSO_4$ by nitrate, was measured by XPS and found to be near stoichiometry (*137*).

In contrast to the large number of studies reporting partial U reduction by magnetite, relatively few works have concluded that magnetite reduces U completely to U^{IV}. Instantaneous reduction of U^{VI} by biogenic magnetite is mentioned in a study that uses bicarbonate extraction as a proxy for U reduction; however, the authors of this study did not provide data or conduct spectroscopic studies to confirm the nature of the reduced U product (*58*). Similarly, O'Loughlin et al. provided evidence using XANES and EXAFS that microbially produced magnetite reduces U^{VI} to U^{IV} in nanoparticulate uraninite (UO_2) (*54*). The stoichiometry of the biogenic magnetites was not measured in either of the two studies. In addition, the origin of the magnetite used in the different studies varies significantly, with some researchers using commercially purchased magnetite and others using laboratory synthesized magnetite produced under various conditions both in the presence and absence of oxygen. The Fe^{II} content of the magnetite used has often not been measured.

No reduction of U^{VI} by magnetite has been observed in two studies. Dodge et al. (*133*) synthesized magnetite in the presence of U^{VI} by oxidation of $FeSO_4$ under normal atmospheric conditions and in the presence of KNO_3 in solution. The valence state of U was measured with x-ray photoelectron spectroscopy (XPS) and x-ray absorption near-edge spectroscopy (XANES) and both were consistent with U^{VI}. The second study investigating U interaction with commercially purchased magnetite was used in the presence and absence of $H_2(g)$. This study was conducted in carbonate containing solution with near-neutral to alkaline pH and noted a lack of U reduction in an anoxic environment in the absence of $H_2(g)$. In the presence of $H_2(g)$, uranium was reduced,

although it is unclear whether the H_2 reduced U^{VI} directly, or reduced the magnetite (*134*).

We have previously found that the Fe^{2+} content (stoichiometry) of magnetite dramatically influences the rate of reduction of nitroaromatic compounds(*66, 132*). The stoichiometry of magnetite has also been suggested to be an important factor in the reduction of U^{VI} (*137*). Here we have evaluated the hypothesis that magnetite Fe^{2+} content is important for U^{VI} reduction under near neutral pH conditions in the presence and absence of the strongly U^{VI} complexing (bi)carbonate anion. We show that a dramatic shift from sorbed U^{VI} to U^{IV} in uraninite nanoparticles occurs between an *x* of 0.33 and 0.38, both in the presence and absence of (bi)carbonate.

Materials and Methods

Magnetite Synthesis and Characterization

Magnetite was synthesized according to previously published methods (*66, 132, 138*). Briefly, the solids were prepared by precipitating magnetite with NaOH from a solution containing a 1 to 2 ratio of Fe^{II} and Fe^{III}. Partially oxidized magnetite was made by adding hydrogen peroxide (approximately 30 % H_2O_2) to oxidize Fe^{2+} to Fe^{3+}. Maghemite was produced by oxidation of magnetite in air at 200 °C. Magnetite stoichiometry was characterized by acidic dissolution (x_d) in 5 M HCl followed by measurement of aqueous Fe^{II} colorimetrically by 1,10-phenanthroline complexation with Fe^{III} masking by F^- (*138, 139*). Total Fe was measured after reduction of Fe^{III} by hydroxylamine hydrochloride. The magnetite stoichiometry was also measured by Mössbauer spectroscopy (x_{MS}) (*138*). The specific surface area was obtained via N_2 adsorption BET analysis and was found to be 63 ± 7 m^2 g^{-1} which correlated well with the particle size measured by transmission electron microscopy (TEM) of 20 nm.

Uranium Uptake and Reduction Experiments

Uranium uptake by magnetites with various stoichiometries was measured in 5 g L^{-1} suspensions in either 50 mM 3-(N-morpholino)propanesulfonic acid buffer (MOPS, pKa = 7.2) or in 2 mM $NaHCO_3$ buffer, with both adjusted to an initial pH of 7.2. Experiments were done inside an anoxic glovebox with a 93% N_2/7% H_2 atmosphere. Uranium was added as U^{VI} in the form of uranyl acetate ($UO_2(CH_3COO)_2 \cdot 2H_2O$) dissolved in 0.1 M HCl to a nominal concentration of 500 µM U^{VI}. Initial U concentrations were measured prior to addition of magnetite and final concentration were measured after 24 hours of reaction time, prior to them being sent off for x-ray absorption spectroscopic measurements. U concentration in solution was measured using the TAC colorimetric method described in Chapter 2.

Fe^{II} Uptake Experiments

Fe^{II} uptake experiments on partially oxidized magnetite (x = 0.28) were done by adding an aliquot of $FeCl_2$ stock to 60 mL of MOPS buffer. In one experiment, 11 mM of Fe^{II} was added based on the total amount of Fe^{II} needed to bring the partially oxidized magnetite to x = 0.50. In addition, a second experiment was done with 5.7 mM aqueous Fe^{II} to see if partial restoration of magnetite stoichiometry induced U^{VI} reduction. The experiment with 11 mM aqueous Fe^{II} addition was done with and without removal of the aqueous Fe^{II} by decanting the supernatant. The amount of Fe^{II} in solution was measured prior to addition of 5 g L^{-1} partially oxidized magnetite, and was measured again after 20 hours prior to addition of U^{VI}. Aqueous Fe^{II} was measured using the 1,10-phenanthroline method described above. The amount of Fe^{II} removed from solution was used to calculate the stoichiometry of the magnetite prior to U^{VI} addition, and was based on mass balance considerations (*132*).

X-ray Absorption Spectroscopy

The U L_{III}-edge XAFS experiments were carried out at the Materials Research Collaborative Access Team (MRCAT) ID beamline, sector 10 at the Advanced Photon Source, using a previously described setup (*111*). Briefly, the beamline undulator was tapered and fixed, and the incident energy was scanned by using the Si(111) reflection of the double-crystal monochromator in quick-scanning mode (approximately 2 min per scan for the extended region and 30 s per scan for the near-edge region). The wet paste samples were mounted in drilled Plexiglas slides and sealed inside the anoxic chamber with Kapton film windows. The sealed slides were exposed to air for about 1 min while being transferred from an O_2-free transport container to the N_2-purged detector housing. Several U^{VI} and U^{IV} standards were used in the XANES and EXAFS analysis. An acidic (pH 3) solution of uranyl chloride was used as the standard for hydrated U^{VI} and a basic (pH 11) solution of U:carbonate=1:50 was used as the standard for carbonate-complexed U^{VI}. U^{IV} standards included a crystalline UO_2 purchased from Alfa Aesar and diluted 1:100 in SiO_2 (*112*), biogenic U^{IV} nanoparticles produced by *Shewanella oneidensis* MR-1 and characterized in a previous study (*47*), and U^{IV} nanoparticles produced abiotically by reduction with sulfate green rust (*61*). U^{VI} sorbed to goethite was used as a standard for Fe-oxide sorbed U^{VI}, this sample contained 250 µM U^{VI} in a suspension of 1.5 g L^{-1} of goethite buffered at pH 7.4 with 0.1 M TAPS and 2 mM $NaHCO_3$. Linear combination spectral analysis of EXAFS data were performed using the program SIXpack (*113*).

Magnetite Oxidation by U^{VI} Experiment

We also conducted experiments to link Fe^{2+} oxidation in magnetite to the reduction of U^{VI}. These experiments were conducted in 50 mM pH 7.2 MOPS buffer with a solids loading of 1.5 g L^{-1} nearly-stoichiometric magnetite with x_d = 0.49 and x_{MS} = 0.45. A spike of 500 µM U^{VI} was added from the uranyl acetate stock, and the reactors were re-adjusted to pH of 7.2. After 20 hours, the solution was filtered to collect the

solids onto a 0.45 µm filter. The solids were then mounted between two pieces of Kapton tape for the Mössbauer spectroscopy measurements.

Biogenic Magnetite

Biogenic magnetite was provided by Edward O'Loughlin at Argonne National Laboratory and prepared from the bioreduction of lepidocrocite by *Shewanella putrefaciens* CN32 as described previously (*123*). The cultures were allowed to reduce the lepidocrocite for 3 days after inoculation. The suspension was then pasteurized for 1 h at 70° C. The material was not washed to remove cell debris in order to avoid dissolution of Fe^{2+} from the magnetite.

Mössbauer Spectroscopy

Transmission Mössbauer spectroscopy was used to measure the stoichiometry of biogenic magnetite and synthetic magnetite used in the Fe^{2+} oxidation experiment. Mössbauer spectroscopy was done with a variable temperature He-cooled system with a 1024 channel detector. A ^{57}Co source (~ 50 mCi) embedded in Rh was used and was maintained at room temperature. All center shifts reported are calibrated relative to an α-Fe foil at room temperature. Samples are kept anoxic by mounting them between pieces of adhesive Kapton tape, and minimizing the time they are exposed to air prior to mounting them in the spectrometer cryostat.

Collected Mössbauer spectra have been fit using the Recoil software package (University of Ottawa, Ottawa, Canada) using extended-Voigt based fitting (*138*). The relative peak areas of the sextets have been constrained to the ideal 3:2:1:1:2:3 ratios. Center shift (CS), quadrupole shift (QS), and hyperfine field (H) parameters have been allowed to float during the fitting procedure. Sextets were fit with two hyperfine field components which had individual Gaussian distributions of hyperfine field parameters and relative areas that were allowed to float in order to achieve the best fit to the observed spectra.

Results and Discussion

Uranium Reduction as a Function of Magnetite Stoichiometry

Based on our previous observations that reduction rates of nitro-aromatic compounds were dependent on the Fe^{II} content of magnetite (*66, 132*) we have investigated the effect of magnetite stoichiometry on uranium reduction. We determined the oxidation state of U in the solids by x-ray absorption near edge spectroscopy (XANES) (Figure 3.1). The edge position of the U^{IV} standard (biogenic nano-uraninite) lies to the left of the U^{VI} standard (U^{VI} sorbed to goethite) as shown in Figure 3.1. The resonance feature in the spectra beyond the absorption edge (denoted by the vertical arrow) is indicative of the axial uranium-oxygen bonds (Oax) of uranyl. The XANES results indicates that all of the U^{VI} added to the 5 g/L magnetite suspension in pH 7.2, 2 mM $NaHCO_3$ buffer is reduced by stoichiometric magnetite (x = 0.50), as well as by partially oxidized magnetite with x = 0.48 and 0.42. In contrast, for oxidized magnetites with x < 0.42, little to no reduction was observed within the error of the XANES measurement (which is approximately 10%). The position of the absorption edge and the presence of the resonance feature above the absorption edge indicate that the majority of the U in these oxidized magnetite samples remains in the +6 valence state as the uranyl cation.

We conducted linear combination (LC) fitting of the XANES spectra using the U^{IV} and U^{VI} end-members to determine an estimate of the proportion of the two U valence states as a percentage of the total uranium in the samples. The percentage of U^{IV}/U_{Total} as a function of initial magnetite stoichiometry is shown in Table 3.1 and Figure 3.2. A marked shift in the amount of reduction is observed between x = 0.42 and x = 0.33, from 84% reduction of the total U is reduced to U^{IV} for x = 0.42 to only 13% reduced for x = 0.33. This abrupt change in reactivity as a function of x occurs in both a 2

mM bicarbonate buffer and in 50 mM MOPS buffer at pH 7.2, despite a difference in starting U^{VI} speciation in the two buffer solutions. In the bicarbonate buffer 500 µM uranium remains in solution, most likely as uranyl carbonate complexes., whereas in the 50 mM MOPS buffer U^{VI} precipitation as a colloid of schoepite ($UO_3 \cdot 2H_2O$) is expected based on the solubility product for schoepite (pK_{s0}(schoepite) = 5.994). Indeed, a precipitate was visually observed after adding a stock of uranyl acetate to 50 mM MOPS buffer without magnetite. We also note that the amount of U^{VI} reduction to U^{IV} is concomitant with an decrease in solution U after reaction with magnetite, consistent with the difference in solubility of UO_2 and sorbed U^{VI} (*40*, *46*, *58*, *140*).

It is unclear whether the marked shift from sorbed U^{VI} to reduced U^{IV} products as a function of *x* is thermodynamically or kinetically limited. The abrupt shift from mostly U^{IV} to mostly U^{VI} as a function of *x* may be kinetically controlled, as XANES measurements were made after about a week. Previous results for non-stoichiometric magnetites indicate that reduction of nitrobenzene compounds is slow for $x < 0.42$, with half-lives for reduction of 3.8 days for $x = 0.36$ and 90 days for $x = 0.31$, showing the extent of contaminant reduction by magnetite of varying *x* can be dictated by kinetics (*66*). However, it is unlikely that predictions for the rates of reduction of nitroaromatic compounds can be extended to predict rates of U^{VI} reduction by magnetite due to the significant difference between UO_2^{2+} and the nitro group of nitroaromatic compounds and differences between the sorptive behavior of UO_2^{2+} and non-sorptive behavior of the nitroaromatics studied.

We used thermodynamic parameters to see if the reduction of U by magnetite with different redox properties can be predicted. We have compared the measured electrochemical open circuit potential (E_{OCP}) for these magnetites (*66*) with several redox couples between predicted U^{VI} species in 2 mM bicarbonate solution at pH 7.2 and UO_2(am) (amorphous UO_2) (Figure 3.3). No clear correlation between the observed amount of reduction and the redox couples for reduction of U^{VI} carbonate complexes to

U^{IV} and the magnetite E_{OCP} exists. The most abundant species predicted to exist in solution in the bicarbonate buffer (using the Visual MINTEQ database (*107*)) is the $(UO_2)_2CO_3(OH)_3^-$ species (~78%). Reduction of this species is favorable over all the redox potentials presented by the magnetites in this study. Interestingly, however, the range of redox potentials for the reduction of amorphous UO_3 to either UO_2(am) or crystalline uraninite (UO_2(cr)) encompasses the E_{OCP} of magnetites with *x* values near where the shift from all U^{VI} to all U^{VI} occurs. We note that such a UO_3 type precipitate is formed in the MOPS buffer system, and that nano-crystalline UO_2 is the product (discussion below). This appears to suggest that thermodynamics may play a role in determining whether magnetite reduces U in these systems, although it doesn't explain why similar results are seen in the two different buffers, as carbonate would inhibit the precipitation of U^{VI} as a schoepite (UO_3) phase.

We have also explored whether aqueous Fe^{II} can serve to recharge the U^{VI} reducing capacity of oxidized magnetite with respect to U^{VI} reduction, as we have previously shown for nitrobenzene reduction (*132*). We started with 5 g L^{-1} of $x = 0.28$ oxidized magnetite and added two different amounts of Fe^{II} (5.7 and 11 mM) to the oxidized magnetite suspension. In the 5.7 mM and 11 mM suspensions, 5.1 mM and 8.0 mM Fe^{II} were removed from solution by reaction with the oxidized magnetite, respectively. We have previously shown that ET occurs between sorbed Fe(II) and magnetite, and leads to reduction of octahedral Fe^{3+} in the magnetite to Fe^{2+} (*132*). The Fe^{II} uptakes measured are equivalent to increasing the magnetite stoichiometry from an *x* of 0.28 to *x*'s of 0.38 and 0.44. The addition of U^{VI} to these recharged magnetites results in nearly complete reduction to U^{IV}, with over 95% of the total U as U^{IV} for the 11 mM Fe^{II} (Figure 3.2, Table 3.1), and 84% reduction for the 5.7 mM addition. Removal of the aqueous phase Fe^{II} had no effect on the ability of the magnetite to reduce U^{VI}, as one sample with 11 mM added Fe^{II} was magnetically separated and resuspended in fresh buffer containing U^{VI} and no Fe^{II}.

Uranium Products

The abrupt shift between U^{IV} products for magnetite with $x \geq 0.42$ and U^{VI} for lesser Fe^{II} contents is also reflected in the EXAFS spectra (Figure 3.4). The results for the magnetites with differing Fe^{2+} contents are compared with a bulk uraninite standard and a maghemite sample with no Fe^{2+}. The coordination of the U in the maghemite sample is consistent with a Fe-O-U surface complex similar to those observed for U^{VI} adsorption onto hematite and goethite (*141, 142*). Surface complexation of U^{VI} as the uranyl cation is evident in the EXAFS spectra with the U-Oax bond at 1.4 Å, and an equatorial uranium-oxygen bond (U-Oeq) at 2.0 Å. As Fe^{2+} content in the magnetite is increased to an *x* of 0.33, the EXAFS spectra indicate that U coordination in these samples is similar to that of the maghemite sample, and indicates that the solid phase U in these samples remains sorbed as U^{VI}. As with the XANES data, there is a shift from U^{VI} to U^{IV} products in the EXAFS data when *x* is decreased to 0.42 from 0.33. The peak at 3.6 Å in the samples with $x \geq 0.42$ is indicative of U-U bonding and is consistent with the formation of the U^{IV} product uraninite (UO_2(s)). The reduction of the intensity of this U-U peak in the Fourier transform data is consistent with the presence of nanoparticulate uraninite (*54*).

Previous work suggests that a mixed U^{V}/U^{VI} phase can form when magnetite is reacted with U^{VI} (*137*). In the previous report, magnetite stoichiometry was determined by fitting x-ray photoelectron spectroscopy spectra of the Fe 2p peak, and taking the ratio of Fe^{2+} to total Fe. The reported ratio of Fe^{2+} to total Fe was between 0.27 and 0.34 with an average of 0.29 for both unreacted samples and samples reacted with U^{VI}. This range corresponds to values of *x* (Fe^{2+}/Fe^{3+}) of approximately 0.37 to 0.52, and an average *x* of 0.41 close to our *x* of 0.42.

There are several differences between our study and the previous one observing the presence of U^{V} are the solution conditions, magnetite specific surface area/particle size, and synthesis methods. In our study, the pH was buffered with MOPS or 2 mM

$NaHCO_3$ at a value of 7.2, whereas in the previous study the initial pH of the solution was much lower (pH = 3.2 – 4.7) and rose with time, likely due to dissolution of Fe^{II} from the magnetite (*137*). Magnetite specific surface areas in our work have an average of 63 ± 7 $m^2 g^{-1}$ (*66*), and are nearly 5 times higher than the 13.5 ± 0.1 $m^2 g^{-1}$ reported by Ilton and co-workers. A similar magnitude difference is seen in the powder x-ray diffraction determined crystallite sizes. We also note that the methods of synthesis of the magnetites are quite different, with the magnetite in this study synthesized by precipitation of magnetite from an Fe^{2+} and Fe^{3+} containing solution at pH 10.0 whereas that of the previous study was prepared by oxidation of Fe^{2+} containing solution with nitrate. However, a hypothesis that the synthesis method changes the properties of the magnetite, such as inducing a core-shell structure, with an enriched Fe^{3+} layer at the surface can be discarded on the basis of the Fe^{2+} to total Fe ratios being near $x = 0.41$ in XPS measurements, which are inherently surface-sensitive (*137*).

Of the differences between the previous study and our study, we believe that solution conditions and surface area loading provide the addition explanation for the differences. For most of our experiments our magnetite surface area loading is approximately 5 times greater than that in the previous work, with 320 $m^2 L^{-1}$ and 68 $m^2 L^{-1}$, respectively (*137*). Even at our lowest mass loading of 1.5 g L^{-1}, the surface area loading is higher than the highest in the previous study. In addition, the value of x is greater in our 1.5 g L^{-1} suspension resulting in a higher amount of available Fe^{2+}. Solution pH will also greatly affect the redox potential (E_h) imposed by magnetite in suspension, with the potential increasing with increasing pH (*127*). The lower initial pH of the previous study would likely have poised the redox potential of the system at a higher E_h, perhaps resulting in conditions where U^{VI} reduction to UO_2 is unfavorable.

Stoichiometric Oxidation of Magnetite by U^{VI}

We have used Mössbauer spectroscopy to track the oxidation of Fe^{2+} in a 1.5 g L^{-1} suspension of magnetite in 50 mM MOPS (pH 7.2) after addition of 500 µM U^{VI}. The spectrum of unreacted magnetite is shown as the top spectrum in Figure 3.5, and consists of two magnetically ordered sextets. The outer sextet corresponds to tetrahedrally coordinated Fe^{3+} and octahedrally coordinated Fe^{3+} not paired with Fe^{2+} ($^{Oct,Tet}Fe^{3+}$) in the magnetite lattice. The inner sextet corresponds to octahedrally coordinated Fe^{2+} and Fe^{3+} which appears as an $^{Oct}Fe^{2.5+}$ sextet due to fast electron hopping between Fe^{2+} and Fe^{3+} (*132, 138; and references therein*). The magnetite used had an *x* from dissolution measurements of 0.49 and the *x* determined from Mössbauer fitting was 0.45 (Figure 3.6). The total Fe^{2+} content of the reactor was therefore 6.39 mM and the Fe^{3+} content 13.0 mM. If the U^{VI} is assumed to be completely reduced to U^{IV}, 1000 µM e^- equivalents are required. Thus, after reaction with U^{VI}, 5.39 mM Fe^{2+} and 14.0 mM Fe^{3+} should be present for a final $x = 0.39$.

The Mössbauer spectrum indicates that the only phase present after reaction is magnetite. Visual inspection of the Mössbauer spectrum of the reacted magnetite reveals that some of the $^{Oct}Fe^{2.5+}$ is lost with concomitant increase of the $^{Oct,Tet}Fe^{3+}$ sextet, confirming that Fe^{2+} has been oxidized to Fe^{3+} within the magnetite. We have fit the spectrum of the oxidized magnetite to determine the amount of oxidation of Fe^{2+} in the magnetite that has occurred during the reduction of the added U (Figure 3.6, Table 3.2). Using the results from the fitting procedure, the $x_{Mössbauer}$ after oxidation of Fe^{2+} by U^{VI} is 0.38. The measured value of *x* closely matches the *x* of 0.39 we have calculated based on the amount of added U^{VI} indicating complete reduction U^{VI} to U^{VI}. Our result indicates that reduction of U^{VI} occurs as a result of electron transfer from structural Fe^{2+} in magnetite. Our observation is consistent with the previous observation of reduction of U^{VI} to U^{IV} coupled to Fe^{2+} oxidation on the surface of freshly cleaved single crystal

magnetite with a near-stoichiometric Fe^{2+}/total Fe ratio but at a much lower pH value of 4.1 (*62*).

Biogenic Magnetite Stoichiometry and Reaction with U^{VI}

We have also investigated the stoichiometry and reactivity of magnetite produced from lepidocrocite reduction by *Shewanella putrefaciens* CN32. In order to examine the reactivity of the magnetite produced by bioreduction, and not the ability of the bacteria to reduce U^{VI}, the suspension has been heat-killed by pastuerization. In previous studies, magnetite produced by bacterial reduction of iron oxides has been shown to reduce U^{VI} to U^{IV} (*54, 58*); however, neither study determined the stoichiometry of the solid produced by bacterial reduction.

Here we have used Mössbauer spectroscopy to determine the Fe^{2+}/Fe^{3+} ratio of biogenic magnetite (Figure 3.6, Table 3.2). Upon inspection, magnetite is the only phase present in the sample. In order to determine the value of *x* of this magnetite, we have used the same fitting procedure as for the synthetic magnetites and fitted parameters are reported in Table 3.2. The *x* of the biogenic magnetite was found to be 0.43, indicating that it is partially oxidized, most likely due to incomplete reduction at the time the sample was heat-killed. Our observation of the bioreduced magnetite stoichiometry is slightly less than what was observed with the x-ray magnetic circular dichroism studies of bioreduced magnetite stoichiometry (*143, 144*). We note that care was taken to sample the reduction process early to avoid the formation of ferrous hydroxyl carbonate (*145*), which probably resulted in the partially oxidized nature of the magnetite.

We have reacted the $x = 0.43$ biogenic magnetite with 500 μM U^{VI} for comparison to our continuum of magnetites with varying Fe^{2+} content. Analysis of the XANES spectrum reveals that when U^{VI} is reacted with the biogenic magnetite in 2 mM bicarbonate buffer the majority of the added U is reduced to U^{IV} (Figure 3.1). However, data from the linear-combination XANES analysis indicates that only 63% of the total U

was reduced to U^{IV} by the biogenic magnetite in 2 mM bicarbonate suspension, whereas only 33% of total U was reduced to U^{IV} in the MOPS suspension (Table 3.1). EXAFS analysis of the biogenic magnetite reacted with U^{VI} in the bicarbonate buffer indicates that a portion of the reduced U in the sample has U-U coordination at approximately 3.8 Å indicative of nanoparticulate uraninite (Figure 3.2).

We speculate that the difference between the amount of reduction by the biogenic magnetite relative to the synthetic magnetite may be due to the presence of cell debris in the suspension, which could act as a secondary sink for uranium in these samples and make it unavailable for reduction by the magnetite. As we have noted above, in the MOPS suspension U^{VI} precipitation is expected and is observed. Binding of this U^{VI} precipitate to cell debris may have or formation of U^{VI}-biomass complexes may have occluded a part of the added U^{VI} from contact with the magnetite and limited reduction.

Conclusions

Magnetite Fe^{2+} content (stoichiometry) controls whether U^{VI} is reduced to U^{IV} under near-neutral conditions with low bicarbonate concentrations. In addition, our work suggests that biogenic magnetite with a defined *x* of 0.43 reduces U^{VI} to U^{IV}, indicating that biogenic magnetites may follow similar trends as synthetic magnetites. Much of the variation in magnetite reactivity in past studies may be explained by differences in magnetite stoichiometry. The fact that U^{VI} reduction occurs for partially oxidized magnetite also raises an important question relevant to sub-surface uranium remediation, that is: to what extent will magnetite buffer U^{IV} redoxidation by O_2, NO_3^-, NO_2^-, etc? Work with bioreduced sediments containing reduced uranium indicates that exposure to atmospheric concentrations of O_2 and to dissolved NO_3^- or NO_2^- results in oxidation of U^{IV} to U^{VI} (*146-148*). However, it is not known to what extent solid Fe^{2+} can buffer the redoxidation of U^{VI}, though our results suggest that magnetite may have some ability to do so.

The recharge of structural Fe^{2+} in magnetite by aqueous Fe^{II}, is an important process in mediating its reactivity with contaminants, shown for U^{VI} here and nitroaromatic compounds previously (*66*, *132*). Solid state cycling of structural Fe^{2+} to Fe^{3+} in magnetite may also be an important process for the electron transfer mechanisms that have been hypothesized to occur between sediment dwelling bacteria and inorganic electron acceptors at a distance (*149*, *150*). This phenomenon, termed the "biogeobattery model," is hypothesized to occur over large distances (meter scale) (*150*), and may ultimately drive the fate of iron and uranium redox cycling in the subsurface.

Table 3.1. Summary of results from magnetite/U^{VI} experiments in this study.

$x = Fe^{2+}/Fe^{3+}$	$[U]_{initial}$ (µM)	$[U]_{final}$[a] (µM)	% U^{IV}/U_{Total}[f] (from XANES)
2 mM $NaHCO_3$ buffer			
0.50 - Magnetite	405	< 9	99
0.48	558	< 9	87
0.43 - Biogenic[b]	435	< 9	*63*
0.42	358	< 9	84
0.33	512	52	13
0.28	493	46	12
0.22	550	84	12
0.17	541	38	7
0 - Maghemite	522	52	4
50 mM MOPS buffer			
0.50 - Magnetite	380	< 9	95
0.48	480	< 9	86
0.43 - Biogenic[b]	398	24	*33*
0.42	375	< 9	88
0.33	541	< 9	9
0.28	554	22	11
0.22	504	< 9	3
0 - Maghemite	525	< 9	0
0.28	353	< 9	17
0.28 → 0.44[c]	289	< 9	99
0.28 → 0.44[d]	343	< 9	96
0.28 → 0.38[e]	286	< 9	84

[a] = $[U]_{final}$ was measured after approximately 24 hours reaction. Samples with $[U]_{final}$ < 9 µmoles/L have final solution uranium concentrations below the detection limit of the colorimetric uranium analysis method used in this study, which was determined to be 9 µmoles/L.

[b] = Fe^{2+}/Fe^{3+} ratio determined by Mössbauer spectroscopy.

Table 3.1—continued

[c] = Non-stoichiometric magnetite with x = 0.28 reacted with 11 mM aqueous Fe^{II}. The magnetite sorbed 1.59 mmoles g^{-1} Fe^{II}. The final x of 0.44 is calculated based on the formulae given in the Supporting Information of Gorski and Scherer (*132*), and is based on the amount of Fe^{II} removed from solution.

[d] = Same as [e] above but with the aqueous Fe^{II} removed prior to addition of U^{VI}. The magnetite sorbed a similar quantity of Fe^{II} (1.62 mmoles g^{-1}).

[e] = x = 0.28 magnetite reacted with 5.7 mM aqueous Fe^{II}. The magnetite removed 1.03 mM Fe^{II} from solution. The final value of x is 0.38.

[f] =$U^{IV}/(U^{IV}+U^{VI})$ ratios are obtained by linear combination analysis of the U XANES spectra. U^{VI} endmember: U^{VI} sorbed to goethite; U^{IV} endmember: biogenic nanoparticulate uraninite.

Table 3.2. Mössbauer parameters at 140 K for magnetite before and after reaction with U^{VI}, and for biogenic magnetite.

	$^{Oct}Fe^{2.5+}$				$^{Oct,Tet}Fe^{3+}$				
Sample	**CS (mm/s)**	**ε (mm/s)**	**H (T)**	**Area (%)**	**CS (mm/s)**	**ε (mm/s)**	**H (T)**	**Area (%)**	$x_{Mössbauer}$ [b]
Unreacted Magnetite[a]	0.74	-0.02	46.0	62.3	0.38	0.001	49.3	37.7	0.45
Magnetite + 500 µM U^{VI}	0.75	-0.01	46.6	54.8	0.38	-0.001	49.2	45.2	0.38
Biogenic Magnetite	0.77	-0.01	46.3	60.3	0.38	-0.003	50.3	39.8	0.43

[a] Magnetite $x_d = 0.49$. [b] $x_{MS} = ½ (^{Oct}Fe^{2.5+})/(½\ ^{Oct}Fe^{2.5+} + {}^{Oct,Tet}Fe^{3+})$

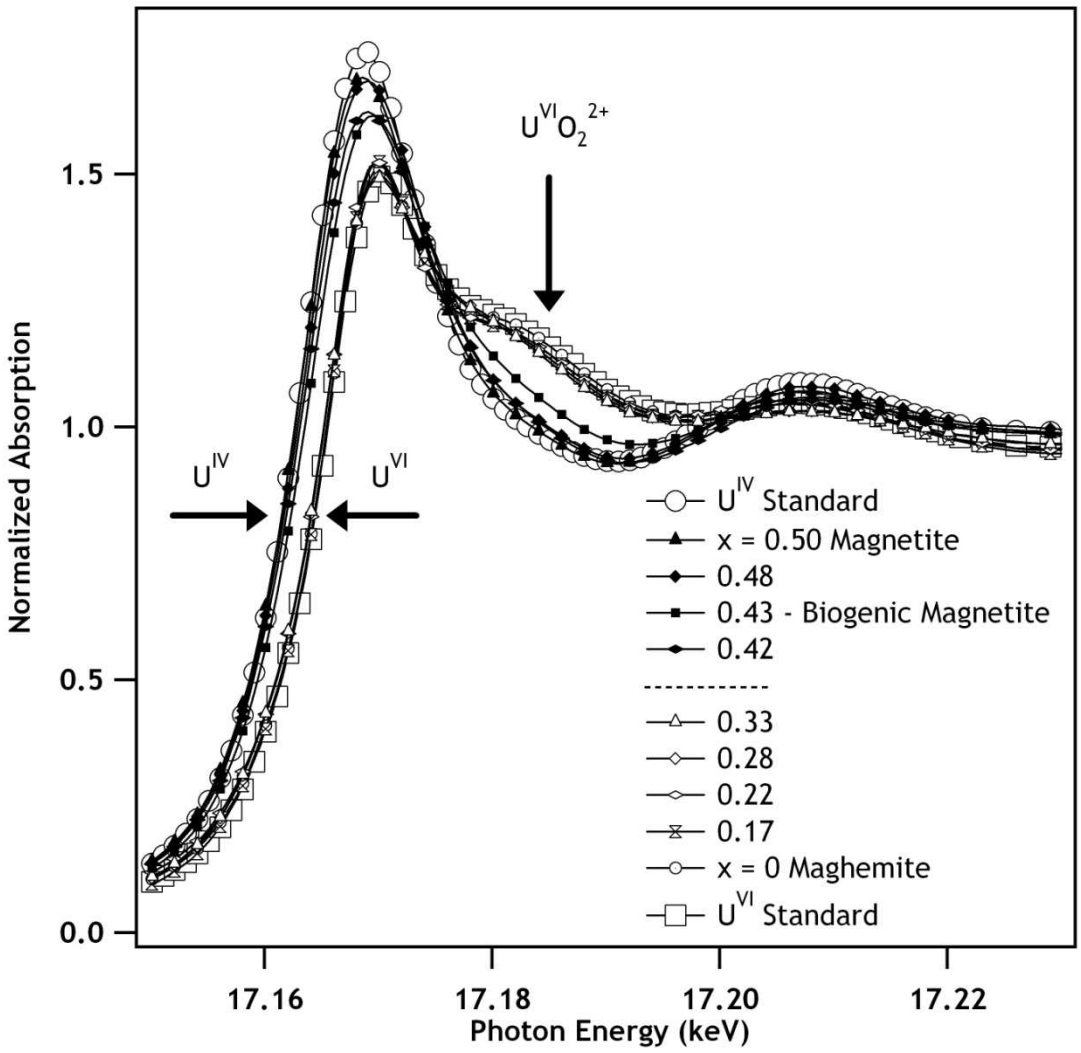

Figure 3.1. XANES spectra indicating reduction of U^{VI} to U^{IV} by synthetic magnetites containing varying Fe^{2+} contents in pH 7.2, 2 mM bicarbonate. The arrows denote the important features of the spectra and are discussed further in the text.

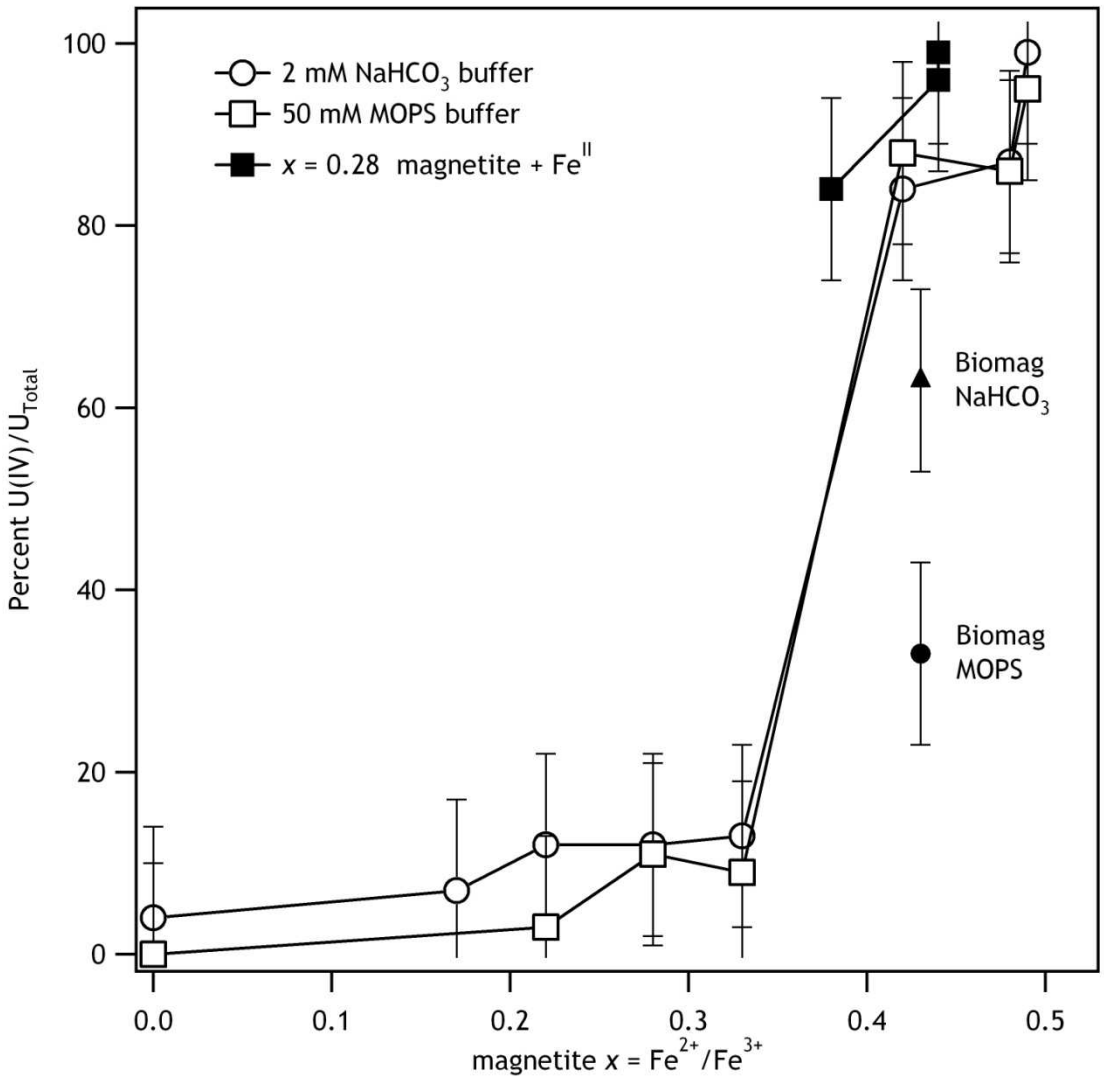

Figure 3.2. Percent U^{IV}/U_{Total} after reaction of U^{VI} with magnetites with varying stoichiometry. The percent U^{IV}/U_{Total} was determined using linear combination fitting of U XANES spectra with U^{VI} sorbed to goethite and biogenic nanoparticulate uraninite end-members.

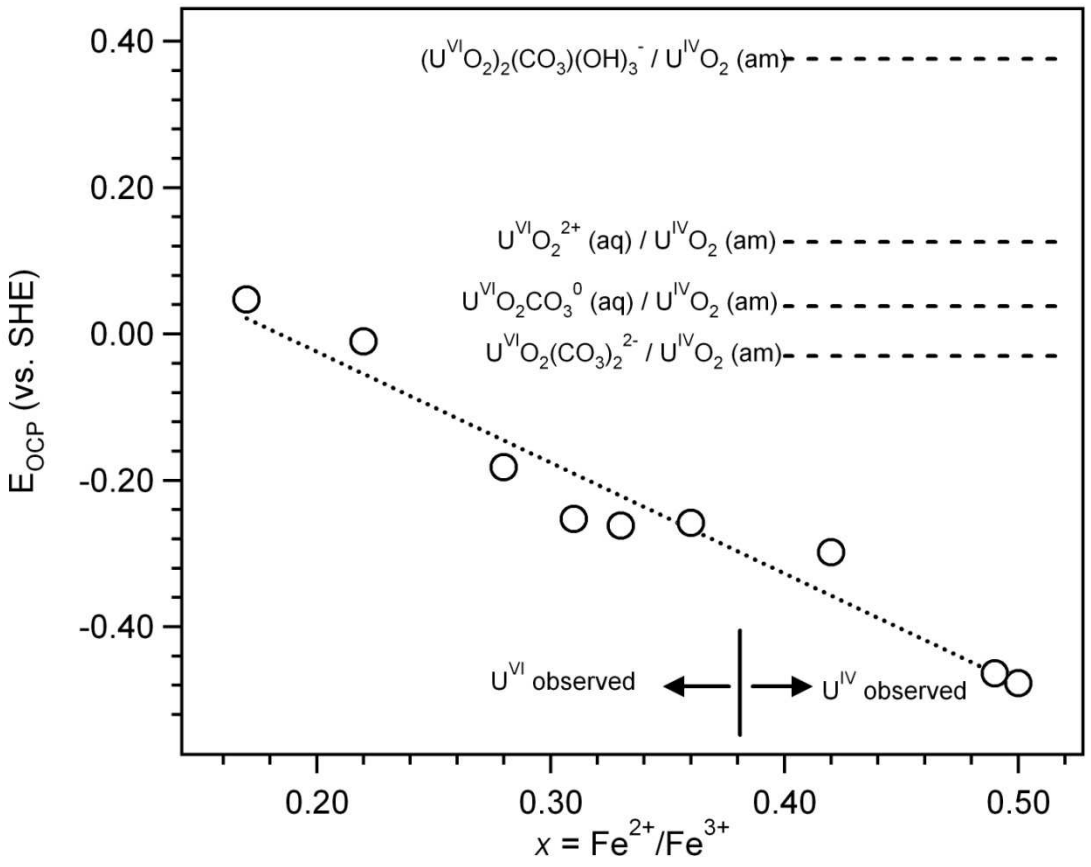

Figure 3.3. E_{OCP} of magnetites with varying *x* compared to several $U^{VI}/U^{IV}O_2$ couples derived from thermodynamic data (*66*). The reduction potential for the U^{IV} species are calculated based on 500 µM U^{VI} of each component present, and with 2 mM bicarbonate buffer at pH 7.2. UO_2(am) and UO_2(cr) represent end-members for UO_2 thermodyanmic data. Thermodynamic data are from Ref. (*151*).

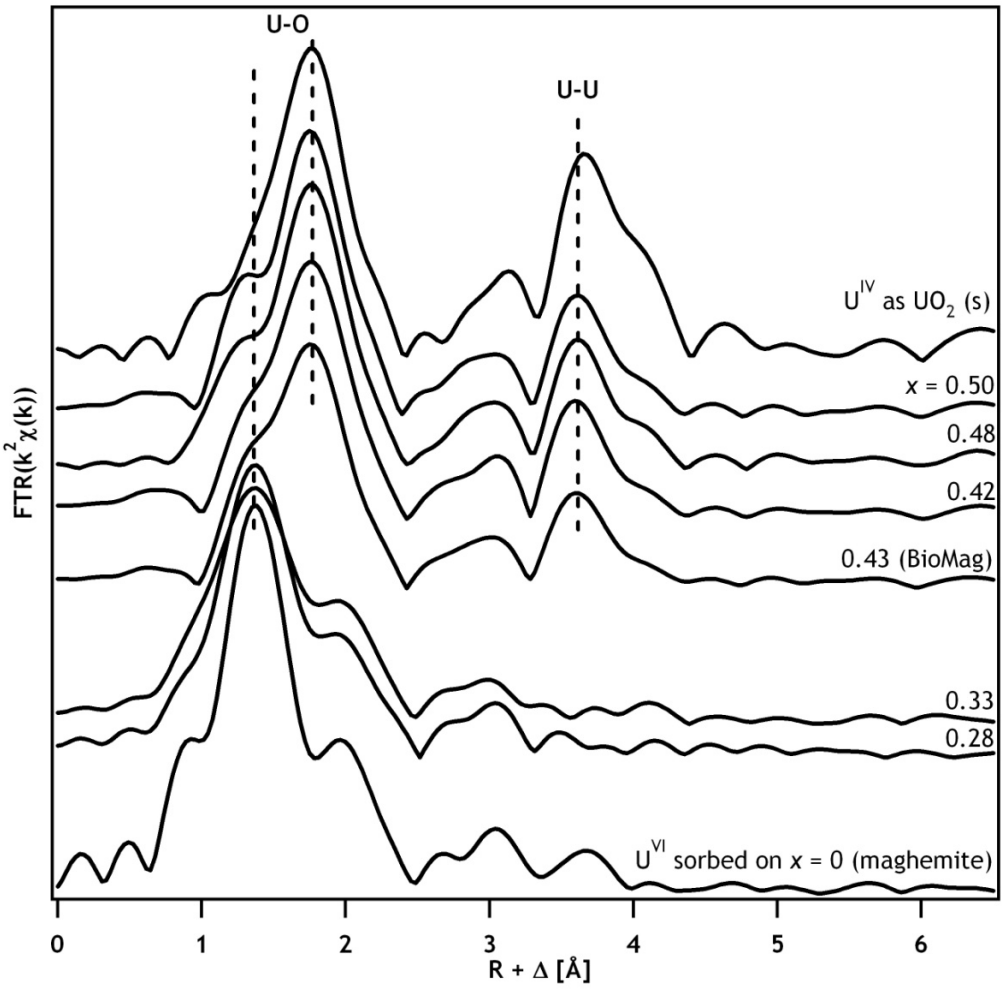

Figure 3.4. Reduction of U^{VI} by near-stoichiometric magnetite results in the formation of a U^{IV} precipitate with a structure like that of uraninite (UO_2) with considerable U-U coordination. Transition between U^{IV} products and more oxidized U products occurs at stoichiometries of $x < 0.42$. The reduced intensity of the 3.5 to 4.2 Å feature in the U/magnetite EXAFS is a result of reduced U-U coordination at the particle surface suggesting formation of uraninite nanoparticles.

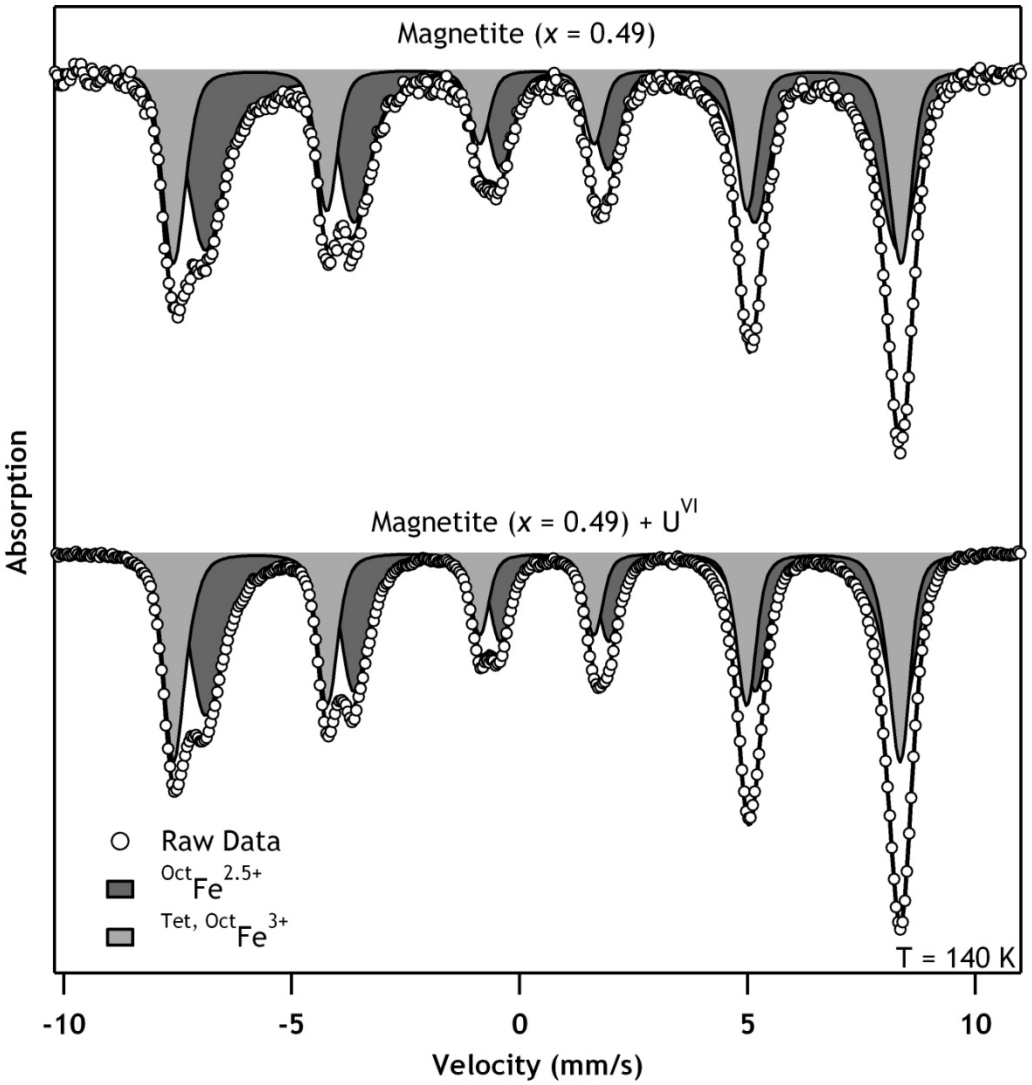

Figure 3.5. Oxidation of 1.5 g/L magnetite with $x = 0.49$ ($x_{MS} = 0.45$) by 500 µM U^{VI} to magnetite with $x_{MS} = 0.38$. The value of x_{MS} after oxidation agrees well the value of x calculated for oxidation of 1 mM of Fe^{2+} in magnetite by U^{VI} of $x = 0.38$. If the value of $x_{MS} = 0.45$ is used, the expected value of x after Fe^{2+} oxidation by U^{VI} is calculated to be $x = 0.35$. These values are consistent with results from XANES and EXAFS that indicate that U^{VI} exposed to nearly-stoichiometric magnetite is reduced to U^{IV}.

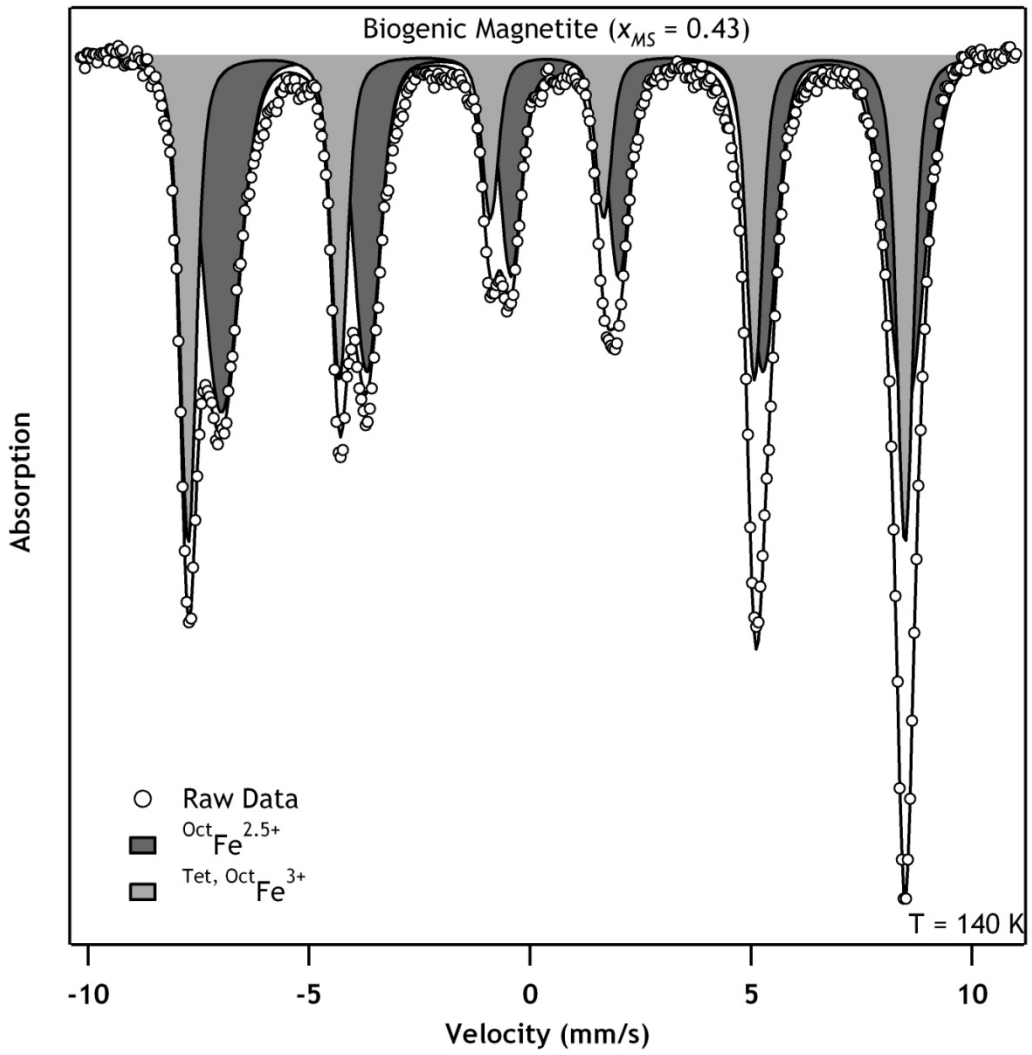

Figure 3.6. Mössbauer spectrum of unwashed biogenic magnetite produced via the reduction of lepidocrocite by *S.* putrefaciens CN32. Fitting of the Mössbauer spectrum indicates that the *x* value of this magnetite is 0.43.

CHAPTER 4: ABIOTIC REDUCTION OF URANIUM BY FE(II) IN SOIL

Abstract

Structural Fe(II) has been shown to reduce several oxidized environmental contaminants, including nitrate, chlorinated solvents, and hexavalent chromium and uranium. Studies investigating reduction of hexavalent uranium (U(VI)) by soils and sediments, however, suggest that abiotic reduction of U(VI) by Fe(II) is not significant, and that direct enzymatic reduction of U(VI) by metal reducing bacteria is required for U(VI) immobilization as U(IV). Here we present evidence for abiotic reduction and immobilization of U(VI) by structural Fe(II) in a redoximorphic soil collected from a hillside spring in Iowa. We demonstrate oxidation of Fe(II) in the soil after reaction with U(VI) by Mössbauer spectroscopy and reduction of U(VI) by the pasteurized soil using X-ray absorption spectroscopy (XAS). XAS indicates that both U(IV) and U(VI) or U(V) in a non-uranyl (UO_2^{2+}) geometry are present after interaction with the Fe(II) containing soil. Little U(VI) reduction is observed by soil that has been exposed to air and oxidation of Fe(II) to goethite has occurred. Soil characterization based on chemical extractions, Mössbauer spectroscopy, and XAS indicate that the majority of Fe(II) in the soil is structural in nature, existing in clay minerals and possibly a green rust-like phase. These data provide compelling evidence for abiotic reduction of U(VI) by structural Fe(II) from soil near Fe-rich oxic-anoxic boundaries in natural environments. Our work highlights the potential for abiotic reduction of U(VI) by Fe(II) to occur in reduced, Fe-rich environments.

Introduction

Uranium (U) is a radioactive metal present in the environment as result of release from both natural and anthropogenic sources. Although small concentrations of U are ubiquitous in all crustal material (e.g. soils - *35*), the primary source of subsurface U

contamination is mining for weapons production and nuclear power generation (*36, 37*). Releases of stored U-containing waste can also occur from accidents such as the one that occurred at the Hanford Site in Washington in 1951 where approximately eight metric tons of caustic aqueous sludge containing dissolved U leaked from an underground storage tank (*152*). Considerable effort continues both to characterize existing wastes (*153*) and to explore methods and mechanisms for subsurface immobilization of U (*43-45*).

The mobility of uranium once it is released into the environment is strongly dependent on its oxidation state. Under oxidizing conditions, U exists as the hexavalent uranyl cation ($U(VI)O_2^{2+}$), hereafter referred to as U(VI). Under environmental conditions, the presence of (bi)carbonate strongly influences the speciation of U, resulting in formation of U(VI)-carbonate complexes (*38, 39*). At low (bi)carbonate concentrations and near-neutral pH's values U(VI) has been found to strongly sorb to the surfaces of both synthetic and natural iron oxides. An increase in bicarbonate concentration results in decreased sorption to iron oxides due to both formation of U(VI)-carbonate complexes and competitive adsorption above approximately pH 6.0, thus increasing U(VI) mobility (*40-42*). The variability in U(VI) sorption under changing environmental conditions has spurred considerable research into immobilizing U by reducing it to U(IV) in uraninite ($UO_2(s)$) , which is significantly less soluble than U(VI) species (*38, 46*)

Reduction of U(VI) can occur directly from biological reduction by metal and sulfur reducing bacteria that couple organic carbon oxidation to U(VI) reduction or indirectly by Fe(II) produced from microbial respiration of Fe(III) oxides. Direct microbial respiration of soluble U(VI) results in the formation of nano-particulate uraninite in both synthetic and natural materials (e.g., *47, 48*). Under similar geochemical conditions, microbial respiration of Fe(III) oxides also leads to the formation of soluble Fe(II) that can sorb or precipitate as various minerals incorporating structural Fe(II),

including green rusts, siderite ($FeCO_3$), magnetite (Fe_3O_4), vivianite ($Fe_3(PO_4)_2$), and Fe(II) containing clay minerals (*50-54*).

Both sorbed Fe(II) and Fe(II)-bearing minerals have been shown to reduce U(VI). The formation of a surface complex (>S-Fe(II)-OH) has been correlated with the rate of U(VI) reduction at pH 7.5. Diffuse-reflectance FTIR spectroscopy provided evidence for U products with a valence state lower than U(VI) (*154*). Reduction of U(VI) by Fe(II) has been shown spectroscopically in systems with Fe(II) sorbed on goethite (α-FeOOH), Fe(II) sorbed to corundum (α-Al_2O_3), and Fe(II) sorbed to montmorillonite clay(*55-57*). Several studies have inferred similar reduction of U(VI) by Fe(II) sorbed on iron oxides by tracking aqueous and bicarbonate extractable U (*58-60*).

U(VI) has also been shown to be reduced by structural Fe(II) in Fe(II) bearing minerals. Complete reduction of U(VI) to uraninite nano-particles has been observed in the presence of synthetic sulfate green rust, biogenic carbonate green rust, and biogenic magnetite (*54, 61*). Similarly, U(VI) is reduced to U(IV) by natural, single crystal magnetite (*62*). Other authors have reported varying degrees of U(VI) reduction by synthetic magnetites (*134, 135, 137*). This variation is likely due to varying Fe(II) contents of the synthetic magnetites studied, as the Fe(II) content of magnetite recently has been shown to have a strong influence on its redox properties (*66, 132*). Reduction of U(VI) to the intermediate valence state of U(V) has been reported for heterogeneous reduction of U(VI) on Fe(II)-bearing micas (*155, 156*). Structural similarities between phyllosilicate micas and clay minerals suggest that Fe(II) bearing clay minerals may also be capable of reducing U(VI). However, a recent report suggests that, akin to magnetite, the redox behavior of clay minerals may depend on the structural Fe(II) content of the solids (*157*).

Despite extensive experimental evidence for reduction of uranium by synthetic and model Fe(II)-bearing minerals and sorbed Fe(II), the role of Fe(II) in U(VI) reduction in *natural* soils and sediments remains unclear. A study using sediments from an aquifer

contaminated with landfill leachate in Norman, Oklahoma, saw abiotic U(VI) reduction by a dark-colored clayey sediment in heat-killed laboratory experiments. Sediments from this aquifer were noted to contain iron sulfides (*63*), consistent with the recent observation that both U(IV) and U(VI) were associated with framboidal pyrites in U contaminated Rifle, Colorado, sediment (*44*). In non-sulfidic natural materials, U(VI) reduction by Fe(II) adsorbed to naturally occurring goethite and hematite in sediment samples was observed, but was limited to less than 30% of the total added U(VI) (*58*). Despite some evidence for U(VI) reduction by sorbed Fe(II) and Fe(II) containing minerals, two studies investigating U(VI) reduction in sediments contaminated by uranium mill tailings (San Juan River, New Mexico, and Rifle, Colorado, sediments) have concluded that despite the presence of Fe(II) as a result of microbial Fe(III) reduction, samples that were heat-killed to stop metabolic processes did not reduce U(VI) to U(IV). Based on this evidence it was concluded that in situ abiotic U(VI) reduction by Fe(II) in natural soils and sediments is unlikely (*64, 65*). Here we present evidence for abiotic reduction and immobilization of U(VI) by structural Fe(II) in a redoximorphic soil collected from a hillside spring in Iowa. We discuss soil characterization based on chemical extractions, Mössbauer spectroscopy, and x-ray absorption spectroscopy and the presence of structural Fe(II) in clay minerals, as well as the potential presence of a green rust-like phase. Our results indicate that structural Fe(II) may be important for in-situ reductive uranium immobilization.

Materials and Methods

Soil Sampling and Characterization

Soil samples were obtained approximately 1 m downhill from a perennial hillside spring located near Hedrick, Iowa (41° 15’ N, 92° 20' W). Generally, the landscape is that of the Southern Iowa Drift Plain, characterized by a dissected glacial till plain forming numerous hills and interconnected drainages, with hilltops mantled by Late-Pleistocene

loess deposits (*158*). The spring is located on the backslope of a ravine under predominantly oak forest adjacent to the South Skunk River, a tributary of the Mississippi River. The soil at the sampling site is continuously saturated due to the perennial nature of the spring.

The soil profile sampled near the spring can be described as an A-Bg-C soil profile. The soil profile consists of the following horizons: A – 0 to 0.15 m; very dark grayish brown (Munsell color 10YR 3/2); silty clay loam; massive structure; many fine roots; common reddish brown (5YR 4/4) iron accumulation mottles; wavy, gradual boundary. Bg1 – 0.15 m to 0.25 m; brownish yellow (10YR 6/8) to strong brown (7.5YR 5/8); silty clay loam; massive structure; few fine roots; common reddish brown (10YR 6/8) and grayish green (5G 5/2) mottles; wavy, gradual boundary. Bg2 – 0.25 m to 0.30 m; grayish green (5G 4/2); silty clay loam; massive structure; few reddish brown (10YR 6/8) mottles; common carbonate pebbles and cobbles. C – 0.3 m to bottom of sampling depth (0.5 m); dark grey (N 4/1); silty clay loam; massive structure, smooth, gradual boundary. Groundwater flow was apparent along the stone line in the Bg2 horizon and the water table rose to the level of the land surface when left undisturbed. We suspect that the stone line is an erosional lag feature sourced from nearby limestone outcrops, and the soil parent material colluvium and alluvium from upslope.

Soil samples were collected with a soil sampling auger and split core soil sampling tubes driven into the soil horizon of interest. The soil core tubes were sealed with plastic caps to minimize exposure to air and to prevent drying. After transport, the soil samples were transferred to an anoxic glovebox and stored capped until used for analysis or experiments. Samples for analysis and experiments were taken from the inside of the core to minimize sampling of partially oxidized material on the ends during the 4 hours of exposure to air during handling and transport.

For characterization of clay minerals, samples of the soil matrix were size fractionated to less than 2 µm based on calculations from Stokes' law for settling time.

The less than 2 µm fraction was centrifuged, resuspended in deionized water, dropped onto glass XRD slides, and dried under air. The oriented clay mounts were analyzed with a Rigaku MiniFlexII diffractometer using Co radiation with a Fe Kβ filter with and without expansion with ethylene glycol. Semi-quantitative powdered x-ray diffraction analysis of the clay minerals was done according to the method of Biscaye (*159*). Based on this analysis, illite is the dominant clay mineral in the Hedrick soil, comprising roughly half of the clay-size fraction; smectite (~30%) and kaolinite (~20%) make up the remaining half.

Chemical Extractions

Chemical extractions by citrate-bicarbonate (CB) and dithionite-citrate-bicarbonate (DCB) were performed following the procedure of Feder et al. (*160*). To prepare the CB reagent, a solution of 0.267 M sodium citrate and 0.117 M sodium bicarbonate was prepared from deoxygenated deionized water. For soil extractions, several grams of grayish green soil were homogenized by mixing and 500 mg of soil was added to 50 mL of citrate-bicarbonate buffer in serum vials. DCB extractions were done similarly, but 1.0 g of sodium dithionite was added to a second vial containing the grayish green soil. Finally, a third reactor was prepared with 500 mg soil in 50 mL of 5 N HCl. The serum vials were capped, shaken vigorously to break up soil aggregates, and placed on an end-over-end rotator for mixing inside an anoxic glovebox. During initial experiments samples from the extractions were taken at 18 h and 14 days, in a second experiment samples were taken at 1, 3, 8, 24, 48 and 72 h. Soil suspensions were filtered through a 0.2 µm filter before Fe analysis.

For comparison to the soil Fe extractions, we also extracted carbonate green rust, ferrihydrite, lepidocrocite, goethite, hematite, two nontronites, an illite clay, and a bioreduced nontronite with CB, DCB, and 5 N HCl. These extractions were done in triplicate reactors in which 36 mg of solid were added to 18 mL of CB, DCB, and 5 N

HCl, with all other procedures the same as used for the soil. The carbonate green rust and bioreduced nontronite extractions were done inside an anoxic glovebox, and all others were done under normal atmosphere. Total Fe of the clay minerals was determined from an HF/HCl extraction to dissolve the silicate structure. Here 3 mL of 70% concentrated HCl/30 % HF mixture were added to 60 mg of the clay which was allowed to dissolve for 2 days. After dissolution, the mixture was made up to 100 mL and dissolved Fe was measured colorimetrically with the 1,10-phenanthroline method at a light wavelength of 510 nm. Ferrous iron was analyzed in the presence of Fe(III) with fluoride as a Fe(III) masking agent (*139*). Total Fe was measured in a separate sample by reduction of Fe(III) to Fe(II) by hydroxylamine hydrochloride, and Fe(III) was calculated by the difference between total Fe and Fe(II).

Mineral Synthesis and Characterization

Synthetic carbonate green rust was prepared using previously described methods in an anoxic glovebox (*89*). Briefly, an 0.13 M solution of $FeCl_2 \cdot 4H_2O$ was titrated to pH 7.0 and mixed with 0.025 M $FeCl_3 \cdot 6H_2O$ titrated to pH 7.0, and the mixture was titrated to pH 8.3 with 1.0 M Na_2CO_3 at a maximum rate of 1 mL min^{-1}. The iron oxides goethite, hematite, lepidocrocite, and ferrihydrite were synthesized according to procedures provided in Schwertmann and Cornell (*161*). Freeze dried green rusts and Fe(III) oxides and oxyhydroxides were characterized using powder x-ray diffraction (pXRD) with a Bruker D-5000 diffractometer using monochromatic Cu-Kα radiation or a Rigaku MiniFlex II diffractometer using Co radiation and a Fe Kβ filter. Green rust samples were mixed with glycerol to minimize oxidation during analysis (*106*).

Nontronites from The Clay Minerals Society Source Clays Repository (nontronites NAu-1 and NAu-2) were used as representative Fe-bearing clay mineral samples for extraction procedures. Nontronites were ground and sieved through an 0.15 mm mesh sieve, but otherwise used as received. In addition, an Fe-bearing illite was

obtained from Ward's Natural Science and treated in a manner similar to that of the nontronites. The bioreduced nontronite was provided by Edward O'Loughlin at Argonne National Laboratory and was prepared by incubating NAu-2 in the presence of *Shewanella putrefaciens* CN32 (ATCC BAA-453), a dissimilatory Fe(III)-reducing bacterium. Briefly, suspensions consisting of 1 g of NAu-2 per L of sterile M1 medium (*162*) with 20 mM lactate were placed in sterile 60-mL serum bottles which were then sealed with rubber septa and aluminum crimp caps and sparged with sterile Ar. The suspensions were inoculated with 1×10^8 cells mL^{-1} of *S. putrefaciens* CN32, cultured as described in O'Loughlin et al. (*53*), and incubated at 30 °C in the dark until Fe(II) production ceased. The bioreduced clays were centrifuged, washed once, freeze dried, and stored as a powder.

U(VI) Sorption and Reduction Experiments

Experiments investigating U(VI) sorption and reduction were carried out in an anoxic glovebox (93% N_2/7% H_2) to exclude oxygen and to maintain low atmospheric CO_2 concentrations. Solutions containing 50 g/L soil were prepared with 1 mM $NaHCO_3$ and the pH was adjusted to 7.6 using 1 M HCl or 1 M NaOH. The soil samples in suspension were pasteurized at 70 °C for 1 h in a water bath. After pasteurization, U(VI) was added as uranyl acetate in 0.1 M HCl, and the concentration of dissolved U(VI) was measured in a filtered aliquot. Several soil samples were also exposed to citrate-bicarbonate extractant for 72 hours, washed 2 times with DI water, centrifuged, resuspended in 1 mM $NaHCO_3$ at pH 7.6, and pasteurized prior to addition of U(VI).

Dissolved U(VI) was quantified using colorimetric determination at 588 nm with the 2-(2- Thiazolylazo)-p-Cresol (TAC) method (*108, 109*). Briefly, 300 µL of sample was mixed with 300 µL of complexing solution (0.137 M CDTA, 0.1 M NaF, and 0.5 M 5-sulfosalicylic acid, pH 6.5), 60 µL of 0.05 M CTAB (N-cetyl-N,N,N-trimethylamonium bromide), 60 µL of 0.15 M Triton X-100, 300 µL of 1 M

triethanolamine buffer at pH 6.5, and 420 µL deionized water in a 1.5 mL micro-centrifuge tube. Color was allowed to develop over 2 hours and analyzed alongside standards with 10, 50, 75, 100, 150, and 200 µM U(VI). The detection limit was 9 µM based on repeat analysis of 11 samples of 10 µM uranyl acetate and calculated using the product of the standard deviation and student's t-value at $p = 0.01$.

X-ray Absorption Spectroscopy

The U L_{III}-edge XAFS experiments were carried out at the Materials Research Collaborative Access Team (MRCAT) beamline, sector 10 at the Advanced Photon Source, using a previously described setup (*111*). Briefly, the beamline undulator was tapered and fixed, and the incident energy was scanned by using the Si(111) reflection of the double-crystal monochromator in quick-scanning mode (approximately 2 min per scan for the extended region and 30 s per scan for the near-edge region). The wet paste samples were mounted in drilled Plexiglas slides and sealed inside the anoxic chamber with Kapton film windows. The sealed slides were exposed to air for about 1 min while being transferred from an O_2-free transport container to the N_2-purged detector housing. Several U(VI) and U(IV) standards were used in the XANES and EXAFS analysis. An acidic (pH 3) solution of uranyl chloride was used as the standard for hydrated U(VI) and a basic (pH 11) solution of U:carbonate=1:50 was used as the standard for carbonate-complexed U(VI). U(IV) standards included a crystalline UO_2 purchased from Alfa Aesar and diluted 1:100 in SiO_2 (*112*), biogenic U(IV) nanoparticles produced by *Shewanella oneidensis* MR-1 and characterized in a previous study (*47*), and U(IV) nanoparticles produced abiotically by reduction with sulfate green rust (*61*). Linear combination spectral analysis of EXAFS data were performed using the program SIXpack (*113*).

Mössbauer Spectroscopy

Soil samples were analyzed using ^{57}Fe Mössbauer spectroscopy using the instrumentation described in Larese-Casanova and Scherer (*19*). Mössbauer spectra were

taken of the untreated grayish green soil extracted from the core tubes and a parallel sample which was allowed to oxidize in air for several weeks. Samples for Mössbauer analysis were mounted in the spectrometer between pieces of Kapton tape to minimize exposure to oxygen.

Mössbauer analysis of soil samples before and after reaction with U(VI) was done after suspension of 180 mg of homogenized soil in 18 mL of 1 mM $NaHCO_3$ adjusted to a pH value of 7.6. U(VI) acetate was added to the suspension for a nominal U(VI) concentration of 500 µM. After 2 days reaction, the samples were filtered and the filtered sample was mounted between pieces of Kapton tape prior to analysis. Fitting of all samples was done in the Recoil software package using a Voight-based lineshape with a fixed linewidth (HWHM = 0.97 mm/s) (*73*).

Results and Discussion

Evidence for Abiotic U(VI) Reduction by Hedrick, Iowa Soil

We exposed several soil samples from the Hedrick site to aqueous U(VI) to evaluate whether the Fe(II) containing grayish green soil from near Hedrick, Iowa, could reduce U(VI). To minimize microbial U(VI) reduction while also minimizing thermal alteration of the soil Fe(II) species, we heat-killed the soil samples by pasteurization (rather than autoclaving). We measured the uptake of U(VI) from solution, as well as the oxidation state of solid phase U and Fe by x-ray absorption near edge spectroscopy (XANES) (Figure 4.1 and Table 4.1). Uptake measurements indicated that total uranium was rapidly lost from solution with complete removal observed within 24 hours (data not shown).

The U L_3-edge XANES spectra in Figure 4.1 can be interpreted using the edge position (horizontal arrows in Figure 4.1 and Figure 4.2) and intensities of spectral features (vertical arrow). The edge position (horizontal arrows) is a measure of the

average oxidation state of the U atoms in the sample, with the U(IV) standard (uraninite) to the left of the edge position of the U(VI) standard (aqueous uranyl ion). The resonance feature beyond the absorption edge (vertical arrow in Figure4.1) comes from the axial oxygen coordination (Oax) of the uranyl ion (*54*). Based on the XANES spectra, it is evident that some reduction of U(VI) by the Hedrick soil occurred. This can be seen in the shift in the absorption edge to a lower energy (horizontal arrows in Figure 4.1 and Figure 4.2). Edge positions of the Hedrick soil spectra were refined against linear combinations of spectra collected for U(IV) and U(VI) standards (Figure 4.2 and Table 4.1). We note that the absolute determination of valence state in the XANES measurement is approximately ±10 %. The XANES edge for U reacted with the Hedrick soil falls about midway between the U(VI) and U(IV) standards indicating that ≈ 50% of the U(VI) has been reduced to an overall valence state between U(VI) and U(IV). Further indication of reduction of U(VI) to a lower valence state or a change in U(VI) coordination involving reduced U-Oax bonding is the loss in intensity of the post-edge resonance feature (vertical arrow) in the Hedrick soil sample.

In an attempt to isolate whether the Fe in the grayish green soil was responsible for the U(VI) reduction, we conducted several controls. For the first control, we attempted to remove the reactive Fe from the grayish green soil by extracting the soil with citrate-bicarbonate, washing it to remove the citrate-bicarbonate, and reacting it with U(VI). In previous studies, citrate-bicarbonate has been used as a measure of labile Fe in samples, as well as a method to dissolve green rusts (*28, 160*). The citrate-bicarbonate extracted soil reduced ≈ 30% of the U(VI) which was slightly less than the ≈ 50% reduction observed by the grayish green soil (Figure 4.2 and Table 4.1). For the citrate-bicarbonate extracted soil sample, we also observed a loss in intensity of the post-edge resonance feature indicative of some loss of U-Oax bonding, due to reduction or change in U(VI) coordination (vertical arrow; Figure4.1). Less reduction of U(VI) after some Fe was extracted by citrate-bicarbonate suggests that some easily dissolved Fe phase may be

responsible for a portion of the U(VI) reduction. On the other hand, the continued reduction of U(VI) reduction after citrate-bicarbonate extraction indicates that additional reductants besides citrate-bicarbonate extractable Fe(II), such as unextracted Fe(II) or other reductants are present in the soil and capable of reducing U(VI).

For the second control, we allowed the grayish green soil to oxidize in air for several weeks before reacting it with U(VI). For the air-oxidized soil, XANES edge-position measurements indicate that only ≈ 10% of the U(VI) was reduced which is significantly less that the 50% reduction observed by the untreated soil (Figure 4.2 and Table 4.1). The XANES specta of the air-oxidized soil also has a post-edge feature similar to that of the uranyl standard (Figure 4.1), indicating that uranyl U-Oax coordination is preserved in this sample. Significantly less U(VI) reduction by the air-oxidized soil indicates that Fe(II) and other reductants have been removed. It is also interesting to note that about 10% less uptake of U was observed on the air-oxidized soil than the untreated soil indicating that reduction in the grayish green soil is important in decreasing the solution concentration of uranium below the concentration for sorptive processes.

To evaluate the uranium products formed after reduction by the Hedrick soil samples, we also collected U L_3-edge EXAFS spectra (Figure 4.3). A two-shell numerical analysis of the uranium-oxygen bonding environment in U(VI) spiked soil samples was done to quantitatively determine the contribution of axial and equatorial U-O bonding (U-Oax and U-Oeq, respectively). Both the untreated Hedrick soil and the citrate-bicarbonate extracted soil sample have similar spectral features. In all of the samples, there is no indication of U-U coordination at 3.6 Å, suggesting that the products of U(VI) reduction are not uraninite. In the air-oxidized soil sample reacted with U(VI), the EXAFS spectrum is consistent with UO_2^{2+} complexed to a metal-oxide surface site, such as U(VI) complexed on a goethite surface as shown in Figure 4.3.

In both the untreated and citrate-bicarbonate extracted soil samples where significant U(VI) reduction was observed in XANES spectra, EXAFS spectra show loss of the U-Oax component. The fitted U-Oax shell distance is 1.80 Å, consistent with U(VI) in a uranyl geometry. Using the loss in U-O_{ax} signal as a measure of how much U(IV) formed, we can estimate the fraction of U existing in the U(IV) valence state (i.e., U(IV)/U_{Total}) from the EXAFs data (Table 4.1). Interestingly, there is a significant difference between the U(IV)/U_{Total} estimated from the EXAFs data compared to the U(IV)/U_{Total} obtained from linear combination XANES data. If we were to allow for the presence of a U(V) component in the system, the difference between the XANES and EXAFS U(IV)/U_{Total} would be even larger because in the XANES analysis the relative U(IV) content will be lower.

We speculate that the difference between the XANES and EXAFS determined U(IV)/U_{Total} is due to a portion of the oxidized U present in a non-uranyl geometry. Whereas the presence of a U(IV) compound is required to fully explain both the XANES and EXAFS spectra, several different forms of oxidized U can be suggested for the oxidized non-uranyl phase. The presence of a non-uranyl oxided U phase can result from the formation of a non-uranyl U(VI) mineral (*163*) or the stabilization of pentavalent uranium (U(V)) in a uranium mineral or on the surface of another mineral (*156, 164*). We can discount the formation of a U(V)-carbonate mineral in the EXAFS spectrum as there is no indication of the U-O_{ax} component at 1.9 Å (*165*). The tentative U(V) could be in a structure such as an U(V)-U(VI) mineral (*164*). A lack of a shoulder in the XANES post-edge was observed for the synthetic U(V)-U(VI) mineral. The U-O_{ax} peak in the EXAFS appears smaller than what would be expected from a linear combination of U(V) and U(VI) in a uranyl geometry. In fact, XRD of the U(V)-U(VI) compound indicated that the 33% U(V)/(U(V)+U(VI)) fraction has 2 U(V)-O_{ax} distances of 2.06 Å and 4 U(V)-O_{eq} distances of 2.41 Å. Signals from the 2.06 Å shell would likely not contribute to the U-

O_{ax} peak in the EXAFS spectrum, but would shift the equatorial shell to smaller distances which is consistent with what we observe.

Taken together, the XANES and EXAFS data suggest that upon addition of U(VI) to the grayish-green reduced Hedrick soil samples U(VI) is reduced. The reduced U product is made up of a mixture of U(IV) and either U(VI) or possibly U(V) in a non-uranyl phase. The formation of the non-uranyl phase was not observed in the U(VI) sorbed onto air-oxidized Hedrick soil, further suggesting that the change in XAS spectra are result of U(VI) reduction.

To evaluate potential reductants present in the Hedrick soil, we used Mössbauer spectroscopy to determine whether U(VI) reduction was coupled to oxidation of Fe(II) in the soil. Mössbauer spectra of the soil with and without addition of U(VI) are shown in Figure 4.4. After reaction with 500 µM U(VI), a decrease in the amount of Fe(II) present in the Mössbauer spectra of the soil from 41% to 35% was observed (Fe(II) doublet D_1 – Table 4.3) with a concomitant increase of the Fe(III) fraction of the soil from 59% to 65% (Fe(III) doublet D_3 – Table 4.3)). The Mössbauer spectra indicate that approximately 6% of the Fe in the soil was oxidized from Fe(II) to Fe(III) after reaction with U(VI). Measurements of the Fe content by dissolution in 5 M HCl indicate that 1.2 mM Fe(II) and 0.7 mM Fe(III) was present. Thus, the 6% oxidation indicated by Mössbauer spectroscopy corresponds to oxidation of 110 µM Fe(II), and a reduction of an equivalent of 55 µM U(VI) to U(IV), which is 11% of the total U(VI) added. The lower amount of reduction in the Mössbauer experiment relative to the XANES data shown in Figure 4.1 and 4.2 is likely due to the decrease in solids loading to 10 g/L in the Mössbauer experiment compared to the 50 g/L in the XANES experiment. The reduced solids loading was necessary to observe a change in the Mössbauer spectra collected. At higher solids loadings, the change in relative area between Fe(II) and Fe(III) would not be detectable with any degree of confidence.

Our results provide compelling evidence that U(VI) reduction by Hedrick soil was coupled to Fe(II) oxidation and suggests that abiotic reduction of U(VI) may be a viable pathway for in situ uranium immobilization, despite recent findings that have indicated that reduction of U(VI) under Fe(III)-reducing conditions is due exclusively to direct enzymatic reduction (*58, 63, 65*). Reduction of U(VI) was not observed in heat-killed sediment samples (*63*) or was minimally observed in heat-killed samples that had been incubated with Fe reducing organisms or amended with Fe(II) (*58*). It is unclear why U(VI) is reduced in our soil samples and was not observed in previous experiments. We can speculate that it may be due to the formation of different Fe(II) containing phases, such as green rust and Fe(II) containing clay minerals, as opposed to Fe(II) adsorbed onto surface sites, but clearly more work is needed to determine the relative role of abiotic and biotic reduction of U(VI) under environmentally relevant conditions.

Identification of the Structural Fe(II) in the Hedrick, Iowa Soil

Selective extraction with citrate-bicarbonate

We characterized the soil using chemical extractions, Mössbauer spectroscopy, and XAS in an attempt to identify the soil Fe(II) component that was responsible for U(VI) reduction by the grayish green redoximorphic soil from Hedrick, Iowa. Based on the color of the soil and recent reports that green rusts can reduce U(VI) to U(IV) and form in redoximorphic soils (*61, 91*), we hypothesized that fougerite, a naturally-occurring green rust mineral was present in the soil and was responsible for the U(VI) reduction.

We chose a citrate-bicarbonate extraction because it has been shown to rapidly and completely dissolve synthetic green rusts and is considered a measure of the more labile Fe phases in a soil sample (*28, 160, 166*). Dithionite-citrate-bicarbonate (DCB) extraction was selected to estimate the total amount of crystalline Fe oxides (*28, 167*). In

addition, we measured the total amount of Fe extracted by 5 N HCl or concentrated HF/HCl. The mass of Fe dissolved during each extraction is summarized in Table 4.2.

The total Fe extracted from the three soils samples with 5 N HCl ranged from 13.4 to 23.4 g Fe/kg soil (38.3 to 66.9 g Fe_2O_3/kg soil) indicating that the soil has an Fe content typical for the Coppock series soil type mapped by the USDA-NRCS (*168*). The amount of citrate-bicarbonate extracted Fe in the soil samples was 4.60, 7.30, and 7.33 g Fe/kg soil after about one day (18 or 24 hours). The mass of Fe extracted by citrate-bicarbonate corresponds to 20, 42, and 55% of the total Fe present in the grayish green Hedrick soil samples. The variability of the Fe content was likely due to variability in its distribution through the soil.

To evaluate what phases are likely to be dissolved by citrate-bicarbonate, we measured the dissolution of several Fe oxides and clay minerals commonly found in soils. Of the Fe oxides we tested (hematite, goethite, ferrihydrite, lepidocrocite), only ferrihydrite was significantly dissolved by citrate-bicarbonate (Table 4.2). The dissolution of the soil samples, however is much faster than the dissolution of ferrihydrite, suggesting that the extracted phase is not ferrihydrite. Further evidence indicating citrate-bicarbonate is not extracting ferrihydrite is that significant Fe(II) is measured in the soil extract. At the start of the extraction, the ratio of Fe(II) to Fe(III) is 2.93 and then decreases to about 0.82 after 8 hours (Table 4.4). Dissolution of ferrihydrite would result in mostly Fe(III) and a much lower Fe(II) to Fe(III) ratio. Citrate-bicarbonate extraction of a Hedrick soil sample (#3) was slower than the carbonate green rust, but still quite rapid with about 39% of the total Fe extracted within three hours. It is important to note that the soil was added as large chunks, which were dispersed by vigorous hand shaking (which likely would act to slow the dissolution rate of the soil sample), relative to synthetic green rust which was added as a fine powder (< 150 μm).

Although it is reasonable to eliminate the Fe oxides as a source of the citrate-bicarbonate extracted Fe, the clay minerals are more difficult to rule out. We observed

negligible dissolution from the Fe(III) end-member smectites (nontronites NAu-1 and NAu-2), as well as an Fe(II)-bearing illite (despite the presence of Fe(II) in Mössbauer spectra of the illite tested - data not shown). Citrate-bicarbonate could, however, significantly dissolve both a biologically reduced smectite (bioreduced NAu-2), as well as smectites reduced by dithionite (Figure 4.5 and Table 4.2). Almost 7.5% of the total Fe was extracted from the bioreduced smectite with relative proportions of Fe(II) and Fe(III) of 60% and 40% resulting in an Fe(II) to Fe(III) ratio of 1.5.

Chemical reduction of the nontronite and illite samples by dithionite in the citrate-bicarbonate medium also resulted in significant dissolution of Fe (about 25% for NAu-1 and NAu-2 and 5.5% for illite) (Table 4.2). Some of the dissolved Fe, however is likely from the presence of up to 10% goethite, which is evident in Mössbauer spectra of both the illite and the NAu-1 nontronite (data not shown). Since goethite is dissolved by DCB, we suspect that little of the Fe dissolved from the illite (the dominant clay mineral in the soil) was removed from the structure of the mineral by DCB dissolution, but significant amounts of Fe were dissolved from both nontronites by DCB extraction.

Clearly our results indicate that identifying green rusts in soils by selective extraction with citrate-bicarbonate alone is not possible. We show here that reduced Fe clays, such as Fe(II) bearing smectites can also be dissolved by citrate-bicarbonate. In previous work where citrate-bicarbonate extraction was used for green rust identification, there was not a significant amount of silicated Fe in the soil, including clay minerals, as estimated by total Fe minus dithonite-citrate-bicarbonate extracted Fe (*160*). Up to 65% of the Fe in the Hedrick soil can be attributed to silicate Fe, based on the total Fe minus DCB Fe estimate. The presence of a significant silicate Fe fraction makes it more difficult to use citrate-bicarbonate extraction as a selective extraction for green rust. Although we show that citrate-bicarbonate is not specific to green rust, it is nonetheless still useful as a means to distinguish between crystalline Fe oxides and more labile Fe

such as green rusts and Fe(II) bearing clays, particularly if the kinetics of dissolution are measured, as green rusts dissolve much faster.

Mössbauer spectroscopy.

To further characterize the Fe in Hedrick, soil sample, we collected Mössbauer spectra of three soil samples at 77, 13, and 4 K. All three spectra had similar features, and one is shown in Figure 4.6. At 77 K, the spectra from the grayish green soil consisted of two Fe(II) doublets and one Fe(III) doublet. The Fe(II) doublet comprising about 31% of the spectral area (D_1: center shift, CS = 1.26 mm/s and quadrupole splitting, QS = 2.91 mm/s), as well as the Fe(III) doublet compromising about 66% of the area (D_3: CS = 0.47 mm/s and QS = 0.47 mm/s and 0.68 mm/s), both have fitted Mössbauer spectral parameters that are consistent with literature values for synthetic carbonate green rust and naturally occurring fougerite (*169, 170*) (D_1 and D_3 in Figure 4.6 and Table 4.3). The second, smaller Fe(II) doublet comprises about 3% of the spectra and is quite wide with CS = 1.46 mm/s and QS = 3.30 mm/s. The Fe(II) and Fe(III) doublets were observed in all three soil samples analyzed and compromised between 22 and 33% and 59 to 66% of the total spectra area respectively. One of the three soil samples had an Fe(III) sextet compromising about 14% of the spectral area with parameters consistent with goethite (data not shown).

Additional spectra were collected at lower temperatures (13 and 4 K) to see if the Fe in the soil sample would magnetically order at lower temperatures. At 13 K, there was no indication of magnetic ordering and the spectrum was almost identical to the 77 K spectrum. At 4 K the spectrum of the Hedrick soil sample could not be quantitatively modeled with a unique set of parameters (collapsed feature in Figure 4.6). Qualitatively, however, the spectrum is similar to the 77 and 13 K spectra in that it consists of several magnetically unordered Fe(II) and Fe(III) doublets (D_1 and D_3). The 4 K spectrum also

contains a collapsed feature that is likely due to magnetic ordering of some of the Fe in the sample.

Based on the Mössbauer spectra at different temperatures, we can rule out ferrous Fe containing minerals, such as siderite, ferrous hydroxide, and magnetite. The wide quadrupole splitting of the Fe(II) doublet (D_1) observed in the soil spectra (QS = 2.85 mm/s) eliminates siderite ($FeCO_3$) which has quadrupole splitting of QS = 1.80 mm/s at 77 K (*171*). The lack of magnetic ordering (splitting of an Fe(II) doublet to an octet) at 13 K also excludes siderite since it is expected to order below its Néel temperature of 38 K (*171*). A similar argument can be used to eliminate ferrous hydroxide, since it is expected to magnetically split to an octet below 34 K (*172*, *173*). Ferrous iron from magnetite is also not a candidate since at temperatures below its Curie temperature of 850°C, it is a sextet (*174*). Vivianite ($Fe_3(PO_4)_2 \cdot 8H_2O$) is more difficult to eliminate because it does indeed have Mössbauer parameters that are similar to what we observed for the soil (CS = 1.22 mm/s, QS = 2.93 mm/s and CS = 1.17 mm/s, QS = 2.47 mm/s) (*175*). Results from an x-ray photoelectron spectroscopy scan, however, revealed no evidence for any substantive phosphorus (P 2s, P 2p) suggesting that vivianite is unlikely (data not shown).

The contribution of frozen, aqueous Fe(II) to the Mossbauer signal at low temperatures can also be excluded because significant Fe(II) is present in the room temperature Mössbauer spectra of the Hedrick soil samples (data not shown). The relatively high citrate-bicarbonate extractable Fe(III) content of these samples argues against the majority of the signal coming from Fe(II) sorbed onto crystalline oxides as sorbed metals are extracted by citrate-bicarbonate (*28*), and our results indicate that even ferrihydrite is poorly dissolved by citrate-bicarbonate. We also consider it unlikely that sorbed Fe(II) would give the soils their grayish-green color, as this color is due to Fe(II)-Fe(III) intervalance charge transfer in a solid (*106*). Although we cannot completely rule out sorbed Fe(II) on the basis of Mössbauer spectroscopy, our Fe K-edge EXAFS results

indicate that most of the iron in the samples is structural in nature, and is discussed in further detail below.

Although we can reasonably eliminate many of the Fe(II) containing iron minerals, it is much more challenging distinguish among Fe(II) in clay minerals and Fe(II) in green rust. A comparison of the center shift and quadrupole splitting parameters of green rusts, fougerite, and reduced clay minerals, including Fe(II) containing smectites and illites, is shown in Figure 4.7 (*176-178*). The center shift of reduced smectites ranges from 1.2 to 1.3 mm/s and the quadrupole splitting from 2.5 to over 3.0 mm/s. These reduced clay mineral Fe(II) parameters overlap those of doublet D_1, precluding us from distinguishing green rust from reduced Fe in clay minerals on the basis of Mössbauer spectroscopy alone. This is especially the case for the Hedrick soil which contains significant amounts of smectitic and illitic clay minerals (based on XRD).

We note that in-situ Mössbauer measurements of fougerite have a reported center shift of 1.03 to 1.07 mm/s, which is much lower than the ≈ 1.21 mm/s typical of synthetic green rusts and other reports of fougerite (*91, 160, 170*). Others have previously questioned these low center shift values and suggested that they were due to inappropriate fitting of the spectra (*102*). We have re-fitted the data from Feder and co-workers and get similar low values, and we suspect that the discrepancy is more likely due to the higher temperature of in-situ experiment (~283 K) relative to the 78 K spectra in previous studies of green rust. Center shifts are well known to decrease with increasing temperature due to the second-order Doppler shift term (*70*), and we have observed shifts to as low ≈ 1.1 mm/s in room temperature spectra of synthetic carbonate green rust. We have excluded these data from Figure 4.7 due to the effect of temperature on Mössbauer parameters.

Fe K-edge EXAFS

In addition to Mössbauer spectroscopy, we have measured Fe speciation in the Hedrick soil using Fe K-edge EXAFS (Figure 4.8). To quantify the Fe-bearing phases present we conducted a linear combination fitting procedure of the soil using several Fe containing clay minerals, iron oxides, and green rusts as reference spectra. The spectrum of the grayish-green Hedrick soil can be fit with several different combinations of clay minerals including a combination of 59% Fe-bearing illite, 23% bioreduced NAu-1 nontronite, and 5% each of unaltered and reduced NAu-2 nontronite. The same 60% contribution of illite to the spectrum can be mimicked by a combination of kaolinite, hectorite, and montmorillonite, indicating the EXAFS analysis cannot be used to determine the exact nature of the Fe in clay minerals. We note that although during the linear-combination fitting of the spectrum we have included green rust as a potential phase, it is rejected during the fitting procedure.

In a previous study, Fe-EXAFS was used to determine the presence of a green rust type Fe(II)-Fe(III) precipitate in a natural sample (*179*) with an order of magnitude higher total Fe-content (~200 g Fe/kg for their sediment vs. ~ 20 g Fe/kg for our soil samples). Some difference was observed in EXAFS spectra of laboratory synthesized green rust and that of the natural material, which they attributed to the affects of small size or differences in Fe(II)/Fe(III) content. Differences in Fe(II)/Fe(III) content may explain our results, also, as the ratio in our soil samples is approximately 0.5, which is more oxidized than our green rust standard. To date, no EXAFS analysis has been done on green rusts with varying Fe(II)/Fe(III) ratios, although green rusts can be synthesized with variable Fe(II)/Fe(III) ratios ranging from 3:1 to 0 (*102, 180*). The wide range of Fe(II)/Fe(III) ratios for green rusts affects their structure due to the smaller size of the Fe(III) cation and deprotonation of OH^- to O^{2-} upon oxidation of Fe(II). This structural change is readily apparent in x-ray diffraction patterns of synthetic green rusts (*102*). Due to structural similarities between octahedral Fe in green rusts and in the octahedral sheet

of reduced 2:1 clay minerals, a future study investigating different valence states of the two may provide useful information for Fe-phase identification in reduced sediments and soils.

Goethite forms from air oxidation

One compelling line of evidence to indicate that the soils contain some green rust is the visually and spectroscopically observed oxidation of the grayish green soil by oxygen in air. Exposing the soil to air results in a color change from grayish green (5G 4/2 to 5G 5/2) to light olive brown (2.5Y 5/6) over several days. Mössbauer spectra of the air-oxidized soil reveals an Fe(II) and Fe(III) doublet at room temperature, with a broad Fe(III) sextet appearing as the temperature is lowered to 77 and 13 K (Figure 4.9). The Fe(III) sextet comprises about 40% of the spectral area at 77 and 13 K and has Mössbauer parameters consistent with goethite (CS = 0.49 mm/s, ε = -0.11 mm/s, and H = 48.1 T). The Fe(III) doublet (CS = 0.45 mm/s and QS= 0.51 mm/s) comprises most of the spectral area at room temperature (87%), but decreases to about half of the spectral area at the lower temperatures. The last feature is an Fe(II) doublet comprising 6% of the spectral area with parameters similar to D_1 (CS = 1.24 mm/s and QS= 2.90 mm/s) (Table 4.3). Spectral parameters at 77 and 13 K of the Fe(III) sextet of the oxidized soil (Figure 4.9 and Table 4.3) are consistent with poorly crystalline, nanometer sized goethite (*128, 181*) or aluminum-substituted goethite (*182*).

Slow oxidation of green rust to goethite upon exposure to air is similar to previous observations of green rust oxidation in a carbonated medium (*169*). The amount of goethite formed via oxidation of green rust phase can be estimated as approximately 44% (based on relative area of the sextet in the Mössbauer spectra). The percentage of total Fe oxidized to goethite is within the range we measured for total Fe extracted by citrate-bicarbonate (20 to 55%). It is unlikely that oxidation of structural Fe(II) in clay minerals would result in the formation of goethite. Studies done on Fe-containing smectites

indicate that structural Fe in these minerals can be reduced and reoxidized in a quasi-reversible process without the formation of secondary Fe oxides (*183*). It is also improbable that large amounts of Fe(II) from inside the clay mineral structure could diffuse out of the structure to form goethite upon oxidation. We can also exclude oxidation of sorbed Fe(II) to form goethite as a mechanism based on our Fe-EXAFS results, which indicate that the majority of Fe(II) in these samples is structural in nature. The absence of ferrihydrite in our low temperature Mössbauer spectra (13 K and 4 K) rules out recrystallization of ferrihydrite to goethite (*128*). Taken together, these results are a compelling argument to indicate that that the goethite originated from green rust in the soil.

Identification of green rust by XRD, Raman spectroscopy, and transmission electron microscopy/selected area electron diffraction (TEM-SAED) was also attempted. No peaks were detected in the XRD pattern that were characteristic of green rust, most likely due to the dilute nature of green rust in these samples (< 1% of the total mass). Raman spectroscopy of the soil samples was attempted to look for the peaks at approximately 425 and 520 cm^{-1} diagnostic for green rusts (*170*). We did observe shoulders in the Raman spectra against a strong background at wave numbers near those for green rust, however, definitive peaks were not observed. Hexagonal shaped particles were also observed in TEM images of the soil, which are a characteristic of green rust particles, but other minerals present in the soil, such as kaolinite have hexagonal morphology (*184*). Selected area electron diffraction (SAED) revealed diffraction rings with a similar *d*-spacing as one of green rusts, but the (*110*) rings (d = 1.58 Å) of carbonate green rust are similar to those to those of quartz (d = 1.54 Å).

Conclusion

The redox state of soils is expected to be strongly coupled to the biogeochemical cycling of trace elements, nutrients, and important environmental contaminants, such as

radionuclides. Our work demonstrates that in soils and sediments which have conditions favorable for the formation of structural Fe(II), and possibly the green rust mineral fougerite, U(VI) can be removed from solution and reduced as a result of abiotic processes. Reduction of U(VI) is coupled to the oxidation of Fe(II) to Fe(III) in the soil sample. Our data suggest that structural Fe(II) may be important for the reduction of U(VI) in contaminated soils and sediments. Manipulation of site conditions favorable for the production of structural Fe(II) rather than aqueous Fe(II) by microbial metabolism may be an important remediation strategy.

Characterization of the structural Fe in the soil from Hedrick, Iowa, indicates the presence of several forms of Fe(II) that could be responsible for the abiotic reduction of U(VI). Based on wet chemical extractions and Mössbauer spectroscopy, we have identified the presence of a labile Fe(II) phase that oxidizes to goethite on exposure to air. We also identified Fe(II) in clay minerals most likely as Fe(II) in smectite or illite using Fe-edge EXAFS that is consistent with semi-quantitative clay mineral analysis by pXRD . Our data are also consistent with a portion of the labile Fe in the soil being the green rust mineral, fougerite. Our lines of evidence for fougerite include (*i*) significant percent of Fe extracted with citrate-bicarbonate with Fe(II)/Fe(III) ratios consistent with green rusts, (*ii*) Mossbauer spectral parameters consistent with fougerite and green rusts, and (*iii*) air oxidation to goethite. Fougerite has been previously found in redox active soils and sediments and was named for its occurrence in soil near Fougères, France (*91*). Green rusts have also been found in deeper subsurface groundwater (*185*), suggesting their presence may be important for remediation of contaminants in aquifer environments.

Our critical evaluation of both the citrate-bicarbonate extraction and use of Mössbauer spectral parameters as means for identifying fougerite confirm that neither are sufficient for positive identification. We found that citrate-bicarbonate extraction is not specific to green rusts and fougerite as it dissolves a small amount of ferrihydrite over

long time scales and removes both Fe(II) and Fe(III) from a bioreduced clay mineral. It is, however, useful as a means to distinguish between crystalline Fe oxides and more labile Fe such as green rusts and Fe(II) bearing clays, particularly if the kinetics of dissolution are measured. Analysis of the literature data for Mössbauer parameters for green rusts, fougerite, and Fe(II) bearing clays suggests that Fe(II) in reduced clays cannot be distinguished from fougerite based on Mössbauer alone.

Table 4.1. Comparison of the percent $U(IV)/U_{Total}$ estimated from Uranium L_3-edge XANES and EXAFS results from reduction of U(VI) by pasteurized Hedrick soil samples.

Sample	% $U(IV)/U_{Total}$ – XANES	% $U(IV)/U_{Total}$ – EXAFS[a]
Hedrick grayish green soil	50	80
Extracted grayish green soil[b]	32	57
Air oxidized grayish green soil	9	0

[a] = Percent $U(IV)/U_{Total}$ estimated based on $U\text{-}O_{axial}$ content of U L_{III}-EXAFS spectra using a two-shell numerical fitting procedure.

[b] = Extracted with citrate-bicarbonate.

Table 4.2. Results from chemical extraction of Fe from soils and synthetic Fe minerals in g Fe/kg solid[a].

Citrate-Bicarbonate													
Time (hour)	Soil Sample 1	Soil Sample 2	Soil Sample 3	GR (CO_3)	Ferri-hydrite	Lepido-crocite	Goethite	Hematite	Illite	NAu-1	NAu-2	Bioreduced NAu-2
1			2.91 *(21.8)*	466 *(106)*	2.00 *(0.45)*	0.460 *(0.08)*	0 *(0.00)*	0.314 *(0.04)*	0.050 *(0.02)*	0.036 *(0.02)*	0.154 (0.08)	12.7 *(5.11)*
3			5.17 *(38.8)*		3.91 *(0.88)*	0.891 *(0.15)*	0 *(0.00)*	0.341 *(0.04)*	0.043 *(0.02)*	0.238 *(0.11)*	0.208 *(0.10)*	15.6 *(6.27)*
8			5.86 *(43.9)*		4.12 *(0.93)*	1.12 *(0.19)*	0 *(0.00)*	0.361 *(0.05)*	0.078 *(0.04)*	0.198 *(0.09)*	0.198 *(0.10)*	13.6 *(5.47)*
16					9.50 *(2.15)*	2.17 *(0.37)*	0.007 *(0.00)*					
18	4.60 *(19.6)* †	7.30 *(41.8)*										
24			7.33 *(54.9)*					0.415 *(0.05)*	0.208 *(0.10)*	0.558 *(0.26)*	0.494 *(0.24)*	18.5 *(7.46)*
48			6.34 *(47.5)*					0.474 *(0.06)*	0.164 *(0.08)*	0.533 *(0.25)*	0.558 *(0.27)*	
72			5.43 *(40.6)*		13.0 *(2.94)*	4.61 *(0.79)*	0.252 *(0.00)*		0.272 *(0.13)*	0.567 *(0.26)*	0.550 *(0.27)*	
7 days					34.2 *(7.74)*	1.90 *(0.32)*	0.084 *(0.00)*		0.302 *(0.15)*	0.545 *(0.25)*	0.511 *(0.25)*	
14 days	7.59 *(32.4)*	10.0 *(57.3)*			58.9 *(13.3)*	2.80 *(0.48)*	0.560 *(0.02)*		0.321 *(0.16)*	1.02 *(0.47)*	0.975 *(0.48)*	
DCB Fe[b]	8.10 *(34.6)*	6.42 *(36.8)*	n.m.	n.m.	446 *(101)*	595 *(102)*	579 *(82.6)*	730 *(94.0)*	2.09 *(5.54)*	61.7 *(28.6)*	51.7 *(25.2)*	n.m.
Total Fe[c]	23.4	17.4	13.4	438	442	586	701	777	37.6	215	205	248

Table 4.2—continued

[a] numbers in parantheses are % of Fe extracted based on total Fe.

[b] Dithionite-citrate-bicarbonate extractable Fe after 18 – 32 hours.

[c] Total Fe is defined as the 5 N HCl extractable iron for the soil samples, GR(CO_3), ferrihydrite, goethite, and hematite; and for illite and nontronites total Fe was determined by dissolution in concentrated HCl/HF solution.

n.m = not measured

Table 4.3. Mössbauer spectral parameters for the Hedrick soil sample, fougerite, and carbonate green rust.

Sample	T (K)	Component	CS (mm/s)	QS or ε (mm/s)	H (T)	Area(%)
Grayish green Soil[a]	77	D_1 - Fe(II) doublet	1.26	2.91	-	31
		Fe(II) doublet	1.46	3.30	-	3
		D_3 - Fe(III) doublet	0.47	0.47	-	66
			0.47	0.68		
	13	D_1 - Fe(II) doublet	1.26	2.92	-	29
		Fe(II) doublet	1.48	3.34	-	6
		D_3 - Fe(III) doublet	0.49	0.47	-	58
			0.48	0.68	-	
Fougerite ref. (*170*)	77	D_1 - Fe(II) doublet	1.25	2.87	-	50.7
		D_3 - Fe(III) doublet	0.45	0.54	-	49.3
Carbonate GR ref. (*169*)	77	D_1 - Fe(II) doublet	1.27	2.92	-	49
		D_2 - Fe(II) doublet	1.28	2.69	-	17
		D_3 - Fe(III) doublet	0.47	0.43	-	34
Air Oxidized Soil[b]	298	Fe(II) doublet	1.19	2.65	-	13
		Fe(III) doublet	0.38	0.51	-	87
	77	Fe(II) doublet	1.24	2.90	-	6
		Fe(III) doublet	0.45	0.51	-	54
		Fe(III) Sextet	0.48	-0.13	48.1	40
	13	Fe(II) doublet	1.20	2.91	-	7
		Fe(III) doublet	0.46	0.49	-	49
		Fe(III) sextet	0.49	-0.11	49.5	44
Unreacted Soil[c]	77	D_1 - Fe(II) doublet	1.27	2.93		41
		D_3 - Fe(III) doublet	0.47	0.48	-	59
			0.47	0.39	-	
Soil reacted with U(VI)[c]	77	D_1 - Fe(II) doublet	1.27	2.95		35
		D_3 - Fe(III) doublet	0.46	0.50	-	65
			0.46	0.51	-	

[a] Spectra for the soil sample are shown in Figure 4.5.

[b] Spectra for the air oxidized soil are shown in Figure 4.6.

[c] Spectra for the comparison between the U(VI) reacted soil and the unreacted soil are shown in Figure 4.3.

Table 4.4. Fe(II) and Fe(III) (in g/kg) and Fe(II)/Fe(III) ratio extracted by citrate-bicarbonate for synthetic Hedrick grayish green soil sample 3.

Time (h)	Fe(II), g/kg	Fe(III), g/kg	Fe(II)/Fe(III)
1	2.17	0.74	2.93
3	2.89	2.28	1.26
8	2.65	3.22	0.82
24	2.33	5.00	0.47
48	2.69	3.65	0.74
72	2.49	2.94	0.85

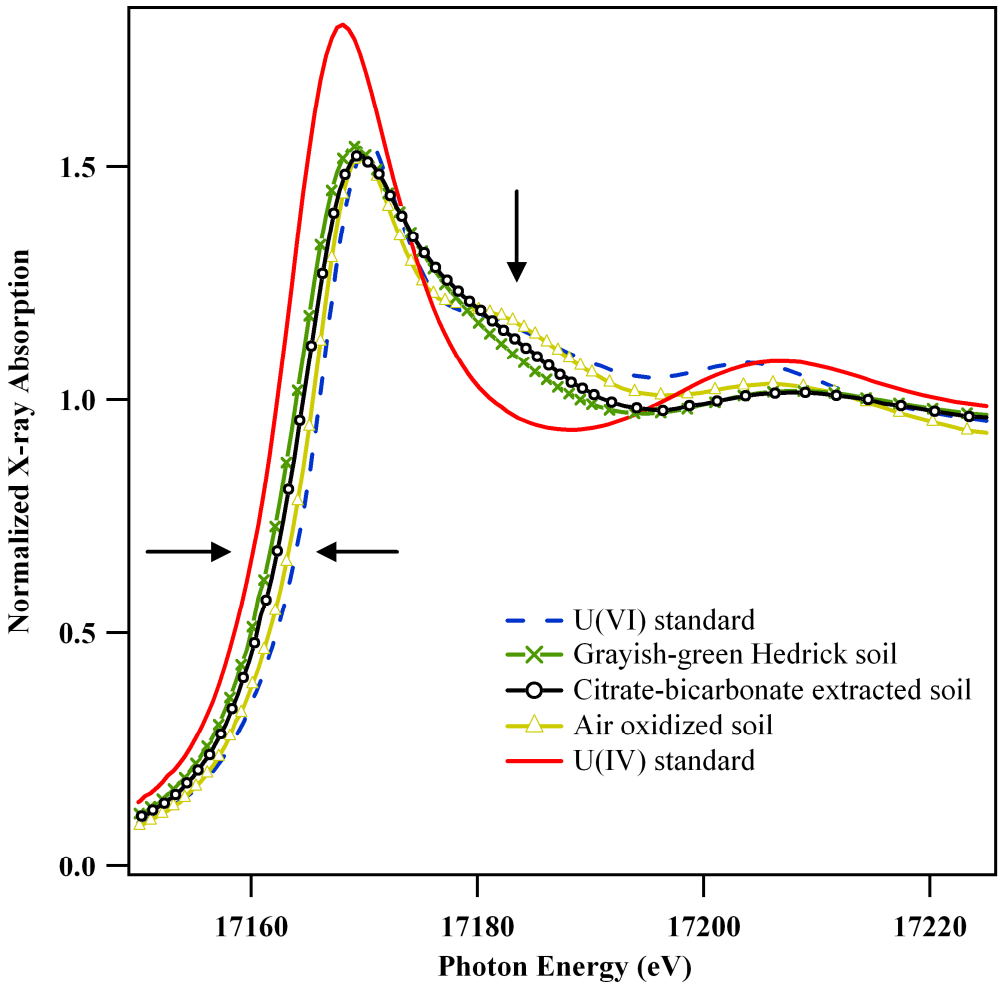

Figure 4.1. Uranium L_3-edge XANES spectra of pasteurized grayish-green Hedrick soil, citrate-bicarbonate extracted and washed soil, air-oxidized soil, U(VI) standard (aqueous UO_2^{2+}-CO_3), and U(IV) standard (uraninite). The position of the absorption edge is indicated by the horizontal arrows. The resonance feature above the absorption edge is indicated by the vertical arrow. Reactors contained 50 g/L soil, 1 mM $NaHCO_3$ at pH 7.6, and 500 µM U(VI).

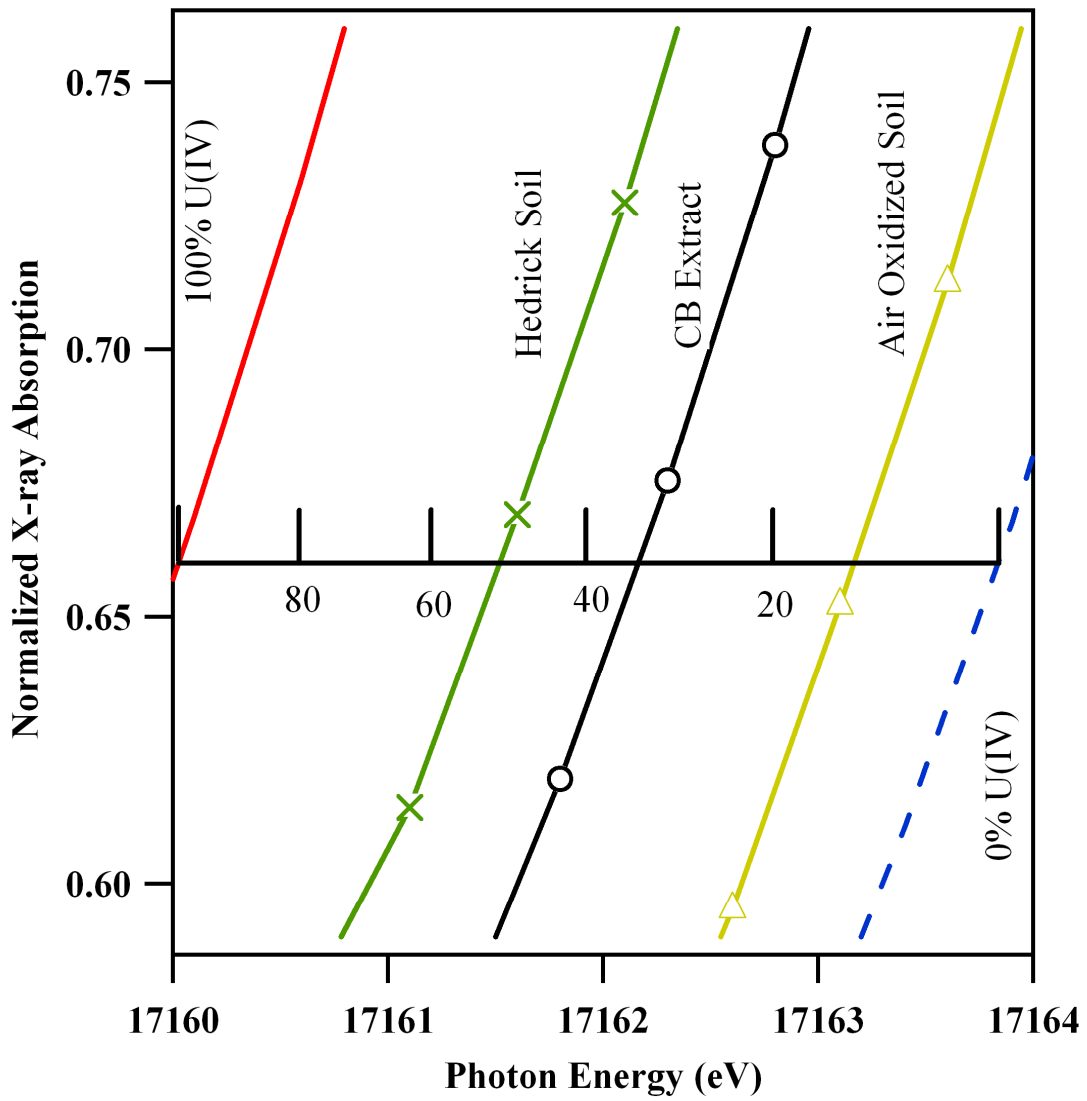

Figure 4.2. Percentage of U(IV) in pasteurized grayish-green Hedrick soil, air-oxidized soil, and citrate-bicarbonate extracted soil estimated from U L_3-edge XANES absorption edge positions and linear combinations between the U(IV) and U(VI) standards.

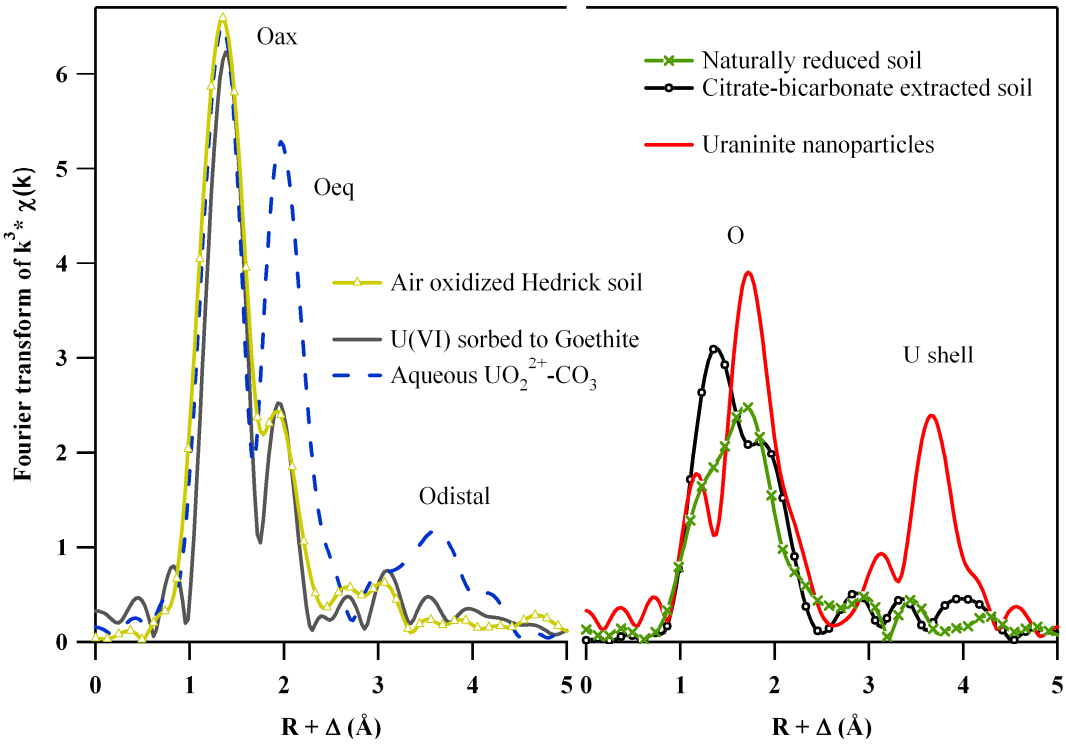

Figure 4.3. Uranium L_3-EXAFS of 50 g/L suspensions of the pasteurized soil samples. Attenuation of the Fourier transform intensity of the untreated grayish-green soil and the citrate-bicarbonate treated soil indicates a loss of axial U-O coordination. This suggests that a portion of the uranium is not in an uranyl (UO_2^{2+}) coordination. The EXAFS spectrum of the air-oxidized soil is similar to that of uranyl bound to goethite.

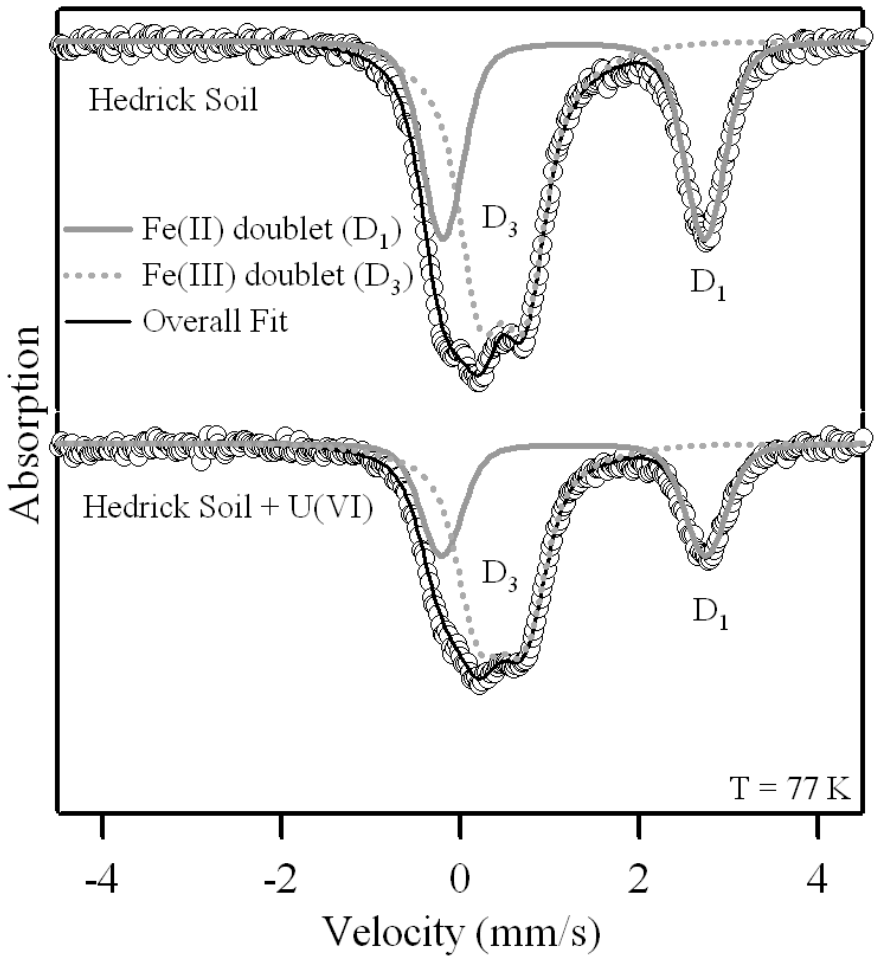

Figure 4.4. Mössbauer spectrum of Hedrick Soil before and after being exposed to 500 µM U(VI). After exposure the relative area of the Fe(II) doublet (D_1) is reduced from 41% of the total area to 35%, confirming that U(VI) reduction is coupled to oxidation of Fe(II) in the soil.

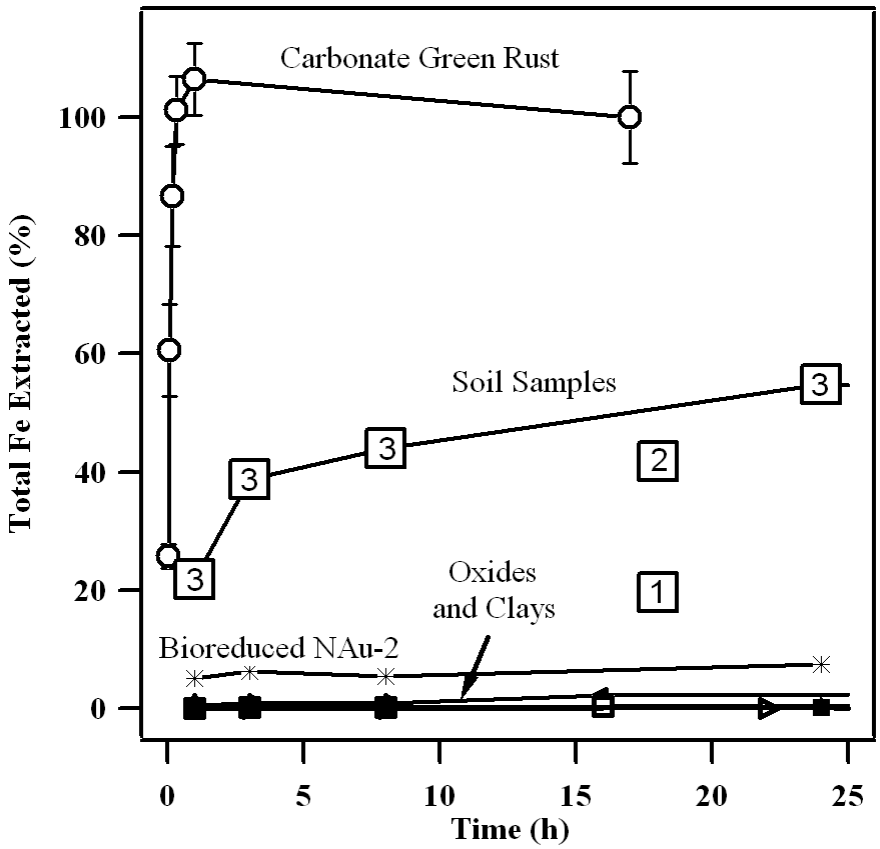

Figure 4.5. Chemical extractions using citrate-bicarbonate with various iron oxides (goethite (△), ferrihydrite (◁) lepidocrocite (□), and hematite (◇)), carbonate green rust (○), reference nontronite clays (NAu-1 (■) and NAu-2 (▲)), illite (●), bioreduced nontronite (*), and Hedrick grayish green soil (□, with numbers).

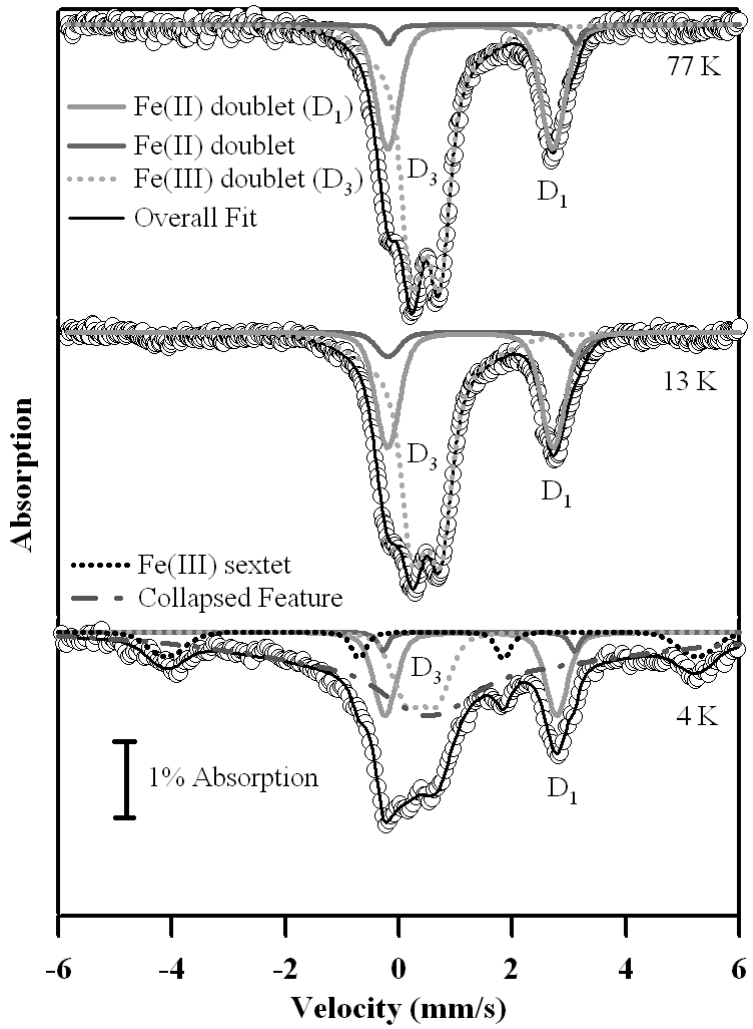

Figure 4.6. Temperature dependent Mössbauer spectra of grayish green Hedrick soil sample collected from a redoximorphic feature near a hillside spring in Iowa. The 77 and 13 K spectra were collected at a reduced velocity scale to increase the signal to noise ratio in the region of interest, and the outer peaks of the sextet are cropped. Mössbauer spectral parameters are reported in Table 4.3.

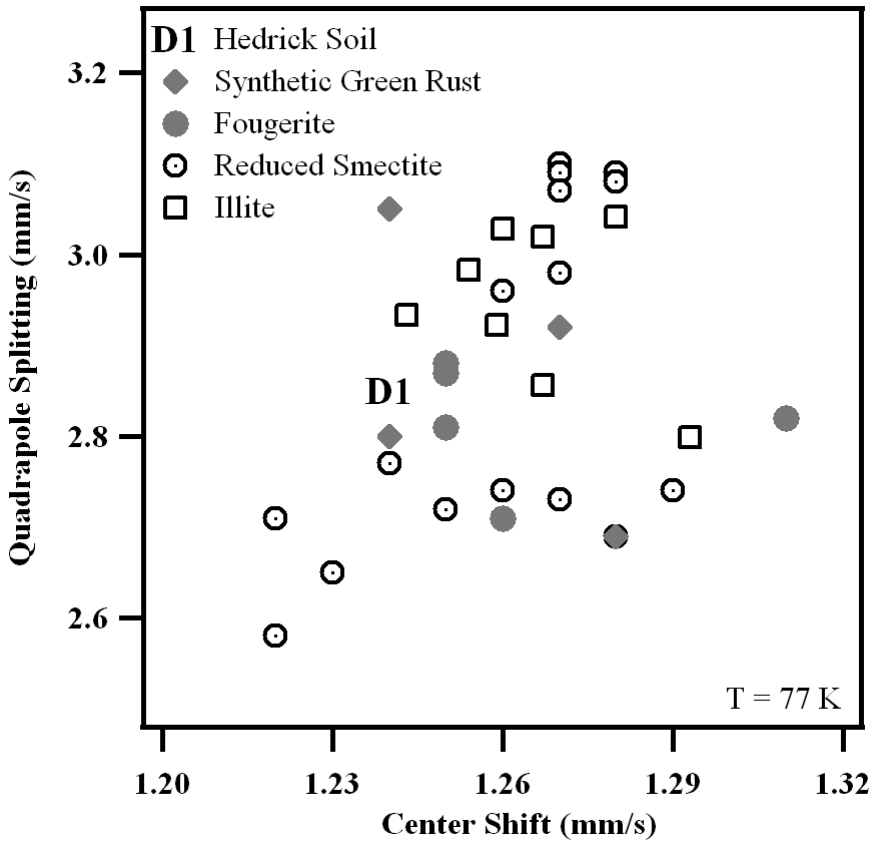

Figure 4.7. Comparison of hyperfine interaction parameters among Hedrick soil Fe(II) doublet (D_1), fougerite (*91*), synthetic carbonate green rust (*102*, *169*, *186*), and various clay minerals (*176-178*).

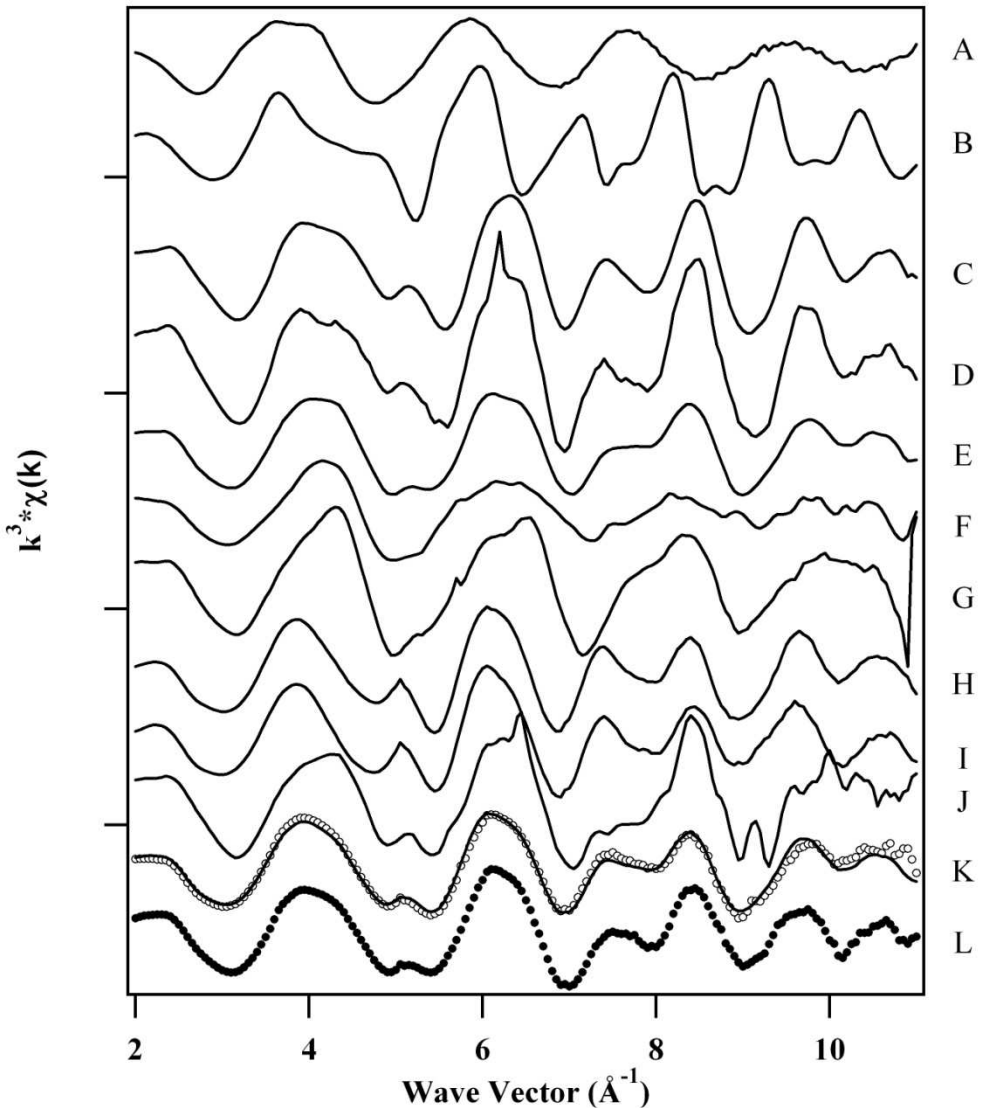

Figure 4.8. Fe K-edge EXAFS of the grayish green Hedrick soil sample. (A) Sorbed Fe(II), (B) carbonate green rust, (C) NAu-1 Nontronite, (D) NAu-2 Nontronite, (E) Illite, (F) Kaolinite, (G) Montmorillonite, (H) Bioreduced NAu-1, (I) Bioreduced NAu-2, (J) Hectorite, (K) Hedrick soil (open circles) and linear combination fit (solid line), (L) citrate-bicarbonate extracted Hedrick soil. Linear combination fitting of the Hedrick soil spectrum with laboratory prepared standards reveals approximately 60% of the iron in illite and 25% in reduced NAu-1 smectite, consistent with the clay mineralogy of the soil. The Fe EXAFS indicates structural Fe(II) and Fe(III) in clay minerals contribute to the majority of the spectrum.

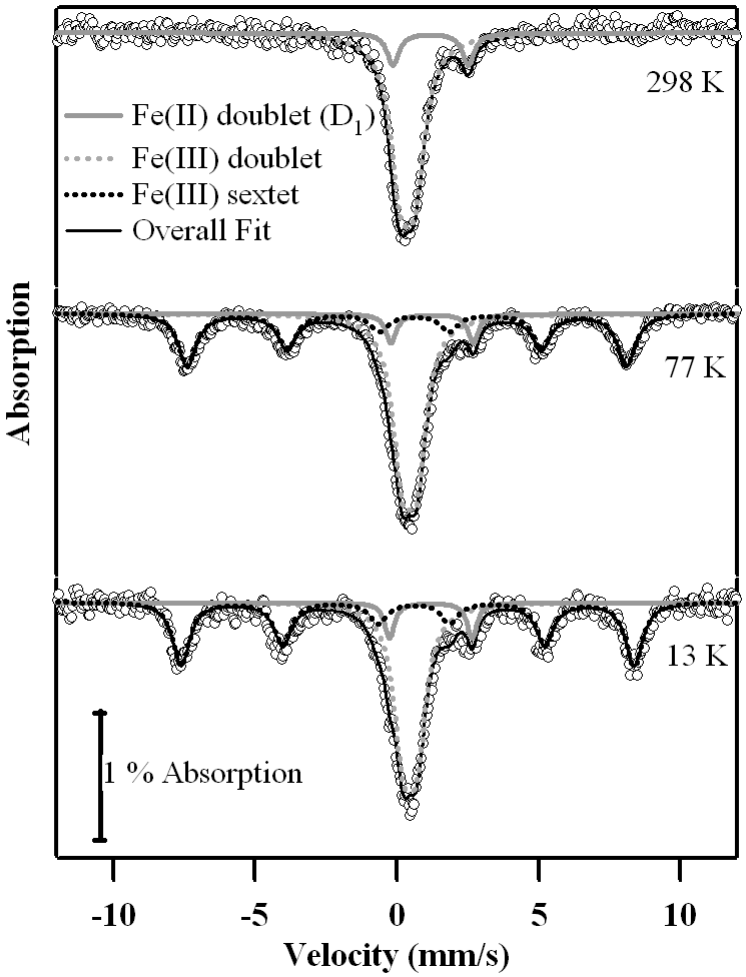

Figure 4.9. Temperature dependent Mössbauer spectra of air-oxidized Hedrick soil from a grayish green redoximorphic feature. A large proportion of the Fe(II) present in the unoxidized spectra (Figure 4.5) has been oxidized to produce an Fe(III) sextet consistent with goethite. Mössbauer spectral parameters are shown in Table 4.3.

CHAPTER 5: EFFECT OF CATION SUBSTITUTION AND ANION SORPTION ON ELECTRON TRANSFER BETWEEN FE(II) AND GOETHITE

Abstract

The reaction of Fe(II) with Fe(III) oxides and hydroxides is complex and has been shown to include sorption of Fe(II) to the oxide, electron transfer between sorbed Fe(II) and Fe(III), reductive dissolution, and mineral transformation. Much of the work investigating electron transfer between Fe(II) to Fe(III) oxides has been done under relatively simple aqueous conditions in organic buffers to control pH and background electrolytes to control ionic strength. In nature, however, iron oxides such as goethite are subjected to a complex biogeochemical milieu which includes significant amounts of structural cation substitution by Al(III) and the presence of sorbed anions such as phosphate, carbonate, silicate, and natural organic matter. We used ^{57}Fe Mössbauer spectroscopy to explore whether Al substitution and sorbed anions (PO_4^{3-}, CO_3^{2-}, SiO_4^{4-}, humic acid, and phospholipids) inhibit electron transfer between aqueous Fe(II) and Fe(III) goethite. We have found Fe(II) is oxidized to Fe(III) by goethites with Al-substitution up to 9.4%, forming goethite, as has been previously observed for pure goethite. Electron transfer between aqueous Fe(II) and goethite also occurred in the presence of sorbed PO_4^{3-}, CO_3^{2-}, SiO_4^{4-}, and humic acid. In addition, electron transfer via dissolution of vivianite and sorption of Fe(II) on the surface of goethite also occurs when vivianite is precipitated in the presence of goethite. Fe(II) to Fe(III) electron transfer was only inhibited after sorbing a long-chain phospholipid to the surface of goethite and found it stops Fe(II) to Fe(III) electron transfer. Our work indicates that interfacial electron transfer between Fe(II) and Fe(III) in goethite is a robust process under a wide variety of geochemical conditions, but that it may be inhibited at high biomass concentrations or in the presence of extracellular polymeric substances and biofilms.

Introduction

Redox reactions between Fe(II) and Fe(III) oxides are important drivers of groundwater geochemistry. Cycling between oxidized and reduced iron species is important to several elemental cycles in the environment, including the carbon cycle, nutrient cycles, and contaminant transformation (*7, 61, 187-189*). In the past, Fe(II) interactions with minerals, including iron oxides, have been described using surface complexation models which do not consider the potential for redox reactions to occur between Fe(II) and the mineral (*8-10*). Surface complexation models fail to capture the range of complexity that occurs when Fe(II) reacts with iron oxyhydroxides and oxides (hereafter referred to as Fe oxides). For example, Fe(II) is known to catalyze the recrystallization of thermodynamically unstable Fe oxides such as ferrihydrite and lepidocrocite to goethite, magnetite, and green rust (*14-16*). In addition, several recent studies have shown Fe(II) is oxidized to Fe(III) at the surface of goethite, hematite, ferrihydrite, and non-stoichometric magnetite in a templated oxidation reaction to form a new layer of the underlying oxide in a reaction involving no net reduction of Fe(III) (*18-23, 132, 190*).

Based on studies tracking the exchange of Fe isotopes between aqueous solution and solid Fe oxides (*17, 24, 25*), in concert with the studies that show Fe(II) oxidation by Fe(III) oxides, a new conceptual model for the reaction between aqueous Fe(II) and Fe oxides has been proposed (*22-24*). The model suggests that the interaction of aqueous Fe(II) with Fe(III) in iron oxides can be thought of as “redox driven conveyor belt,” where sorption of Fe(II) is followed by electron transfer to the oxide, producing an Fe(III) atom template on the surface of the oxide with a similar character as the underlying oxide, the electron transferred to the oxide is conducted through the oxide, reduces an Fe(III) atom elsewhere in the Fe oxide crystal to Fe(II), which is followed by detachment of this Fe(II) atom from the oxide into solution.

Despite the now extensive evidence that interfacial electron transfer occurs between sorbed Fe(II) and Fe oxides, there is little evidence as to whether this phenomenon might occur in the complex biogeochemical milieu found in nature. We note that these studies have all been done in relatively pure systems in electrolyte solutions with the pH fixed by potentiometry or organic buffers and using pure oxide materials (*18-21, 132, 190*); however, in natural systems Fe oxides frequently contain other cations that substitute for Fe(III) in their structure (*26-28*). The most abundant and frequently studied of the cations that can substitute for Fe(III) in iron oxides is aluminum (as the Al(III) cation) (*26, 27*). Research on both natural and synthetic aluminum substituted goethites (Al-goethites), suggests that approximately 33% of the Fe(III) in goethite can be replaced by Al (Al/(Al+Fe)) (*191*). This phenomenon is not entirely unexpected. In the environment, the release of aluminum during mineral weathering is likely to occur simultaneously with iron release. In addition, the relatively small difference in cation size for Al(III) and Fe(III) (53 pm vs. 65 pm) and the structural similarity between diaspore (α-AlOOH) and goethite (α-FeOOH) can be used to account for the common substitution of Fe(III) by Al(III) in goethite.

In addition to the common cation substitution of goethite by Al, Fe oxides are good sorbents for a variety of anions present in the environment including phosphate, carbonate, silicate, and natural organic matter (*29-33*). Phosphate (PO_4^{3-}) has been the subject of a large number of studies, due to its importance in determining soil fertility (*32, 33, 192-194*). Phosphate is known to form inner-sphere coordination complexes with goethite, but the exact coordination geometry is a subject of debate, with both a protonated monodentate surface complex (*195, 196*) or a deprotonated bidentate surface complex proposed (*33*). The adsorption of the phosphate anion, which has weak acid properties, changes the surface charging characteristics of goethite suspensions and the point of zero charge shifts (pH_{PZC}) from pH 8.1 to 5.1 after adsorption of phosphate (*197*). The shift in pH_{PZC} results in the occurrence of a less protonated, thus more

negative, surface at lower pH's than pure goethite. By extension, this more negative surface has a greater affinity for cations. This result is seen in work by Stachowicz et al. (*34*), where both Ca^{2+} and Mg^{2+} both have lower pH edges of adsorption to goethite in the presence of phosphate than in its absence.

Here we have investigated whether Fe(II) to Fe(III) interfacial electron transfer happens between Fe(II) and goethite under environmentally relevant conditions of Al-for-Fe substitution in goethite and in the presence of sorbed anions (phosphate, silicate, carbonate, and natural organic matter (humic acid and phospholipids)). We have used the isotope specificity of ^{57}Fe Mössbauer spectroscopy to track whether added ^{57}Fe(II) is oxidized by Mössbauer spectroscopy invisible ^{56}Fe goethite. We have also investigated macroscopic uptake of Fe(II) from solution by Al-substituted goethites and goethite with sorbed phosphate to explore whether inferences can be drawn between the macroscopic sorption data and spectroscopic data.

Materials and Methods

Goethite Synthesis

For goethite samples synthesis from naturally abundant iron with less than 5% aluminum substitution (samples denoted Gt, 2Al-Gt, and 4Al-Gt) a solution of $Al(NO_3)_3$ was added to a solution of 5 M KOH to create soluble aluminate $Al(OH)_4^-$ (0.313 M) in 1.88 M KOH. Aliquots of this aluminate solution were added to enough 5 M KOH to make a total final concentration of 0.3 M KOH, and 50 mL of 1 M $Fe(NO_3)_3$ was added. A dark reddish brown Fe(III) precipitate formed, and the solution was diluted to 1 L. The 1 L bottles were placed in an air oven at 70 °C for 2 weeks. After 2 weeks, the samples were removed from the oven and the supernatant was discarded. The precipitates were washed once with 1 M KOH to remove any Al precipitates and centrifuged. The pellet of goethite was resuspended in DI water and adjusted to a pH of approximately 9.0 with 1 M HCl to increase flocculation, and washed three times by centrifugation. The pellet was

dried overnight at the synthesis temperature in an oven and ground to a powder with a mortar and pestle.

For fractions of Al (Al/(Al+Fe)) in solution greater than 0.15 in 0.3 M KOH, hematite was formed along with goethite, and higher base concentration was needed to prevent the crystallization of hematite over goethite (*198*). A similar procedure was followed for the 10% Al-substituted goethite (denoted 10Al-Gt) sample, but the final base concentration of 0.3 M KOH was replaced with 1 M KOH and the suspension was heated at 60 °C for 4 weeks. The lower temperature also ensured the formation of goethite instead of hematite. Addition of Fe(II) to a suspension of this 10% Al-substituted goethite revealed formation of a black precipitate, likely magnetite, indicating partially uncrystallized ferrihydrite. Similar results were indicated by dithionite-citrate-bicarbonate (DCB) dissolution. This uncrystallized material was removed by dissolving it in 0.5 M HCl for 2 hours prior to measure Fe(II) sorption isotherms.

Goethite with and without aluminum substitution was also synthesized from Mössbauer spectroscopy invisible ^{56}Fe in order to investigate electron transfer dynamics between Mössbauer active ^{57}Fe and the underlying goethite. The synthesis parameters and properties are outlined in Table 5.1. Goethite was synthesized by dissolving $^{56}Fe(0)$ powder (Chemgas, Inc., 99.77%) in 25 mL of 1 M HCl. The resulting 200 mM $^{56}Fe(II)$ containing solution was oxidized to $^{56}Fe(III)$ with excess H_2O_2. For ^{56}Fe Al-goethite, an $AlCl_2$ solution of the same concentration as used in the naturally abundant Al-goethite synthesis was used instead of $Al(NO_3)_3 \cdot 9H_2O$ to minimize the presence of redox active nitrate in the reactors. An aliquot of aluminate solution was added to a polypropylene bottle to set the Al content of the synthesis batches to 0.27 and 0.44 based on the Al/(Al+Fe) ratio. A solution of 5 M KOH was added to bring the final base concentration to 1 M, while accounting for the neutralization of the HCl from the dissolution procedure. At this point the deionized H_2O was added to bring the total volume of the bottle to 87.5 mL and 12.5 mL 200 mM $^{56}Fe(III)$ was added for a total of 100 mL of solution. The

precipitate was aged at 60 °C in an oven for 3 months in order to insure complete conversion of the Fe(III)/Al precipitate to goethite. This procedure was done in parallel with naturally-abundant Fe(0) powder for Mössbauer analysis. After 3 months the goethite was processed by washing once with 1 M KOH, then 3 times with DI water, dried, and ground to a powder. A similar procedure was followed for Al-free ^{56}Fe goethite, but the aluminate solution was omitted and the final KOH concentration was 0.3 M.

Goethite Characterization

Several methods were used to characterize the goethite and Al-goethites synthesized, including wet chemical methods and solid-state methods. The wet chemical methods used to characterize the goethite and Al-goethite were reductive dissolution in dithionite-citrate-bicarbonate solution and proton-promoted dissolution in 8 M HCl. Solid state methods included scanning electron microscopy (SEM), powder x-ray diffraction (pXRD), and Mössbauer spectroscopy. The aluminum content of Al-goethites was measured by dissolving it in 8 M HCl overnight at 70 °C, and measuring Al and Fe using ICP-OES or ICP-MS. Al contents as Al/(Al+Fe) of the naturally abundant Fe goethites used in this study were 2.2% (referred to as 2Al-Gt), 4.4% (4Al-Gt), and 9.9% (10Al-Gt). The Al contents of the ^{56}Fe Al-goethites used in this study were 5.4% and 9.4%, these are referred to as "5Al-^{56}Gt" and " 9Al-^{56}Gt", respectively.

In addition, proton promoted kinetic dissolution experiments were done at room temperature (22 °C) and the congruency of Al and Fe dissolution were measured using ICP-MS (Figure 5.1). The reductive dissolution rate of goethite and Al-goethite was measured using a dithionite-citrate-bicarbonate solution (DCB) of 0.27 M sodium citrate, 0.12 M sodium bicarbonate, and 0.12 M sodium dithionite with a pH value of 7.3 (*160, 199*). Dissolution kinetics in DCB were measured using triplicate reactors containing 10 mg solids and 20 mL DCB. Fe(II) concentration was measured using the 1,10-

phenanthroline method (*139*). Initial rates were determined by fitting the initial linear portion of the dissolution curve and are shown with the raw data in Figure 5.3.

All of the goethites used in the study have been characterized with powder x-ray diffraction (pXRD) to determine if phases other than goethite were present (Figure 5.2). All data was collected using a Rigaku Mini FlexII diffractometer using Co K-alpha radiation with a K-beta filter made from Fe. No secondary phases were noted in any of the goethites used. In order to discuss the goethite crystal structure, we have chosen to use the Pbnm space group indexing, as it can be used to directly compare our results to the majority of the work investigating Al-substitution in goethite. Some more recent work uses the Pnma space group (*128*). The Pbnm space group (*abc*) can be translated to the Pnma space group with the following transformation: (*abc*) → (*bca*). Using the pXRD patterns we measured the full width at half maximum (FWHM) of (111) and (110) planes of the goethite crystal lattice using the Jade 6 software package (Materials Data, Incorporated, USA). The FWHM of these planes was used in the Scherrer equation to calculate the mean crystallite dimension. The *c*-dimension of the Al-goethite unit cells was calculated using the whole-pattern fitting procedure in the Jade 6 software package, and used to estimate the aluminum content of these goethites (*191*).

The goethites used in this study were also imaged with scanning electron microscopy (SEM) (Hitachi S-4800). This was used to provide images of the morphology of the goethite particles, and to check for secondary phases that may have been missed by low concentration in pXRD (Figure 5.4). Particles were suspended in deionized water (DI), sonicated briefly with a probe sonicator, and dropped onto aluminum sample stubs. Accelerating votages of 1.0 – 5.0 kV gave high quality images without the need to sputter coat with Au or carbon. In experiments where Fe(II) uptake by goethite in the presence of phosphate was examined for precipitation of vivianite, aliquots of solution were centrifuged and the pellet was washed 3 times in DI water and dropped onto Al sample stubs without sonication.

Transmission Mössbauer spectroscopy was done with a variable temperature He-cooled system with a 1024 channel detector. A ^{57}Co source (~ 50 mCi) embedded in Rh was used and was maintained at room temperature. All center shifts reported are calibrated relative to an α-Fe foil at room temperature. Samples are kept anoxic by mounting them between pieces of adhesive Kapton tape, and minimizing the time they are exposed to air prior to mounting them in the spectrometer cryostat. Collected Mössbauer spectra have been fit using the Recoil software package (University of Ottawa, Ottawa, Canada) using Voigt based fitting. The relative peak areas of the sextets have been constrained to the ideal 3:2:1:1:2:3 ratios. Center shift (CS), quadrupole shift (QS), and hyperfine field (H) parameters have been allowed to float during the fitting procedure. Mössbauer spectroscopy was used characterize the goethites used and check for Fe containing impurities in samples containing ^{57}Fe. Also, ^{56}Fe goethite and Al-goethite samples were checked for the presence of significant ^{57}Fe at 15K, and found to be lacking of measurable quantities of the Mössbauer active isotope.

Fe(II) Uptake Experiments

Fe(II) uptake experiments on pure goethite and Al-goethites were done in an anoxic glovebox (93% N_2/7% H_2) outfitted with a palladium catalyst to remove trace oxygen. Fe(II) uptake was measured in triplicate reactors containing 15 mL of 25 mM 4-(2-Hydroxyethyl)piperazine-1-ethanesulfonic acid, N-(2-Hydroxyethyl)piperazine-N′-(2-ethanesulfonic acid) (HEPES) buffer adjusted to pH 7.5 with KOH and containing 25 mM KBr as a background electrolyte. Fe(II) was added from a stock of $FeCl_2$ in 0.1 M HCl to make nominal solution concentrations of 0.1, 0.25, 0.5, 1, 2, 4 and 5 mM Fe(II). After the intial concentration of Fe(II) was measured, 30 mg of pure or Al-goethite was added for a solids loading of 2 g/L. Reactors were placed on an end-over-end rotator and sampled after 20 hours of reaction. Final Fe(II) samples were filtered through a 0.22 µm nylon filter and acidified with 5 M HCl prior to analysis with 1,10-phenanthroline.

Experiments were repeated under similar conditions with 2 g/L ^{56}Fe goethite and ^{56}Fe Al-substituted goethite using ^{57}Fe(II) to track Fe(II) sorption and electron transfer with Mössbauer spectroscopy. A stock of ^{57}Fe(II) was made by dissolving 63.5 mg ^{57}Fe(0) (Chemgas, Inc., 97.82% ^{57}Fe purity) in 2 mL 1.6 M HCl in a sealed serum bottle at 70 °C for 2 weeks. After all of the ^{57}Fe(0) was dissolved, 8 mL of DI water was added inside an anoxic glovebox to bring the final volume to 10 mL and a final HCl concentration of approximately 0.1 M.

Fe(II) Uptake in the Presence of Phosphate

We have measured the uptake of Fe(II) in the presence of phosphate anion over a range of pH values (pH edge). In these experiments, 15 mL of 10 mM KCl electrolyte solution was used without an organic buffer. An aliquot of 10 or 100 mM KH_2PO_4 was added to the electrolyte solution and the initial phosphate concentration was measured prior to addition of 30 mg goethite. The pH was adjusted to the desired value with 0.1 M KOH and 0.1 M HCl. Phosphate was allowed to sorb to the goethite overnight, the pH of the solution was remeasured, and the amount of phosphate sorbed was measured after filtering the solution through a 0.22 µm filter. Fe(II) was then added from a stock of $FeCl_2$ in 0.1 M HCl, and the pH was readjusted back to the equilibrium value after PO_4^{3-} sorption. Since Fe(II) sorption to goethite is rapid at near neutral pH, the initial concentration of Fe(II) was determined by adding the same volume aliquot of $FeCl_2$ to reactors without goethite. After 20 more hours of reaction, the final aqueous Fe(II) and PO_4^{3-} concentrations were measured after filtration of the samples. In addition, we measured a phosphate sorption isotherm in the absence of Fe(II) at pH 7.5 in 10 mM KCl by varying the initial concentration of PO_4^{3-}.

Phosphate was measured using a reduced volume modification of the Standard Methods procedure 4500-P.E. Ascorbic Acid Method such that 1 mL sample and 0.16 mL of the combined reagent solution were used. The combined reagent solution as made

by adding 2.5 mL of 5 N H_2SO_4, 0.25 mL of 4.1 mM potassium antimonyl tartrate ($K(SbO)C_4H_4O_6 \cdot 1/2H_2O$), 0.75 mL of 32 mM ammonium molybdate ($(NH_4)_6Mo_7O_{24} \cdot 4H_2O$) solution, and 1.5 mL 0.1 M ascorbic acid ($C_6H_8O_6$), in that order.

Fe(II) to Fe(III) Electron Transfer in the Presence of Sorbed Anions

We have investigated the effect of sorbed anions on electron transfer between Fe(II) and Fe(III) in goethite. The anions studied include phosphate (PO_4^{3-}), bicarbonate (HCO_3^-), natural organic matter (Aldrich humic acid - NOM), silicate (SiO_4^{4-}), and a phospholipid (1,2-dioleoyl-sn-glycero-3-phosphate or DOPA, Avanti Polar Lipids). Experiments were done using 12.5 mL of 10 mM KCl solution and 25 mg ^{56}Fe goethite for a solids loading of 2 g L^{-1}, except for the DOPA experiment, which was done in 25 mM HEPES buffer containing 25 mM KBr to adjusted to pH 7.5 be comparable with previous experiments investigating phospholipid sorption on metal oxides (*200*, *201*). At higher phosphate and ^{57}Fe(II) concentrations, 6 mL of 10 mM KCl solution was used with 12 mg ^{56}Fe goethite. This was done to reduce the overall mass of ^{57}Fe present during Mössbauer spectroscopy. The DOPA suspension was pre-processed by sonication in a bath sonicator at room temperature for 2 hours.

The speciation of Fe(II) was tracked with Mössbauer spectroscopy by adding aliquots of ^{57}Fe(II) to suspensions containing anions and goethite that had been pre-equilibrated. Experimental conditions, including anion concentrations and Fe(II) concentrations are summarized in Table 5.3.

Results and Discussion

Goethite Properties

The goethites used in this study range from having no aluminum substitution to almost 10 mole% Al substitution on an Al/(Al + Fe) basis. The aluminum contents are

shown in Table 5.1, along with other characteristics we have measured. The goethites are referred to as Gt when they contain no aluminum substitution, as 2Al-Gt for 2.2% Al-substitution, 4Al-Gt for 4.4% Al-substitution, and 10Al-Gt for 9.9% Al-substitution. We also have synthesized goethite with and without Al out of ^{56}Fe, which is invisible to Mössbauer spectroscopy in order to track the speciation of added ^{57}Fe(II) in these systems. The ^{56}Fe goethites used in this study that have no aluminum substitution are referred to as ^{56}Gt (Batches 1 and 2), 5Al-^{56}Gt which contains 5.4% Al-substitution, and 9Al-^{56}Gt which contains 9.4% Al-substitution.

One of the most curious of properties of aluminum substituted goethite is the fact that as aluminum substitution increases, morphology of the particles changes and the crystallinity increases for similar synthesis methods using moderate temperatures and high base concentration. Qualitatively, inspection of scanning electron microscope (SEM) images indicates at the highest aluminum substitution (10Al-Gt) the length of goethite particles decreased (Figure 5.4). The particles also transition from a lath-like morphology made up of aggregates of goethite crystals to increasingly single crystalline particles with a reduced length to width ratio.

In addition to visual observation of goethite morphology, the unit cell dimensions and crystallinity of goethite can be measured by using powder x-ray diffraction (pXRD) and the Scherrer equation (*202*) (Figure 5.2). The difference in cation size between Al(III) and Fe(III) (53 pm vs. 65 pm) causes decreasing the unit-cell size of Al-goethite, which varies directly with increasing aluminum substitution (*26, 191*). We used the *c*-dimension of the goethite unit cell (Pbnm space group) to estimate the Al-content of the goethites (*191*). The pXRD determined Al-contents are compared to the dissolution determined Al-contents in Table 5.1. The pXRD determined Al content can be used to differentiate goethites that vary in their Al content by 2.6 % (*191*). In all cases, the pXRD determined Al-content of the goethites is consistent with the trend observed from the acid dissolution, and within the 2.6% error of the method.

The breadth of the diffraction peaks in the pXRD data gives information about the size of coherently diffracting domains in the particles, this size is termed the mean crystallite dimension ($MCD_{(hkl)}$). These coherently diffracting domains can be thought of as small crystallites that make up a larger goethite particle. Goethite particles containing no aluminum (Gt) have sizes measured from SEM images of 124 ± 44 nm across (n=15) (a- and b-direction) and approximately 1 µm long (c-direction). The particle sizes from SEM images are much larger than those estimated from the pXRD data ($MCD_{(110)}$) derived from the Scherrer equation of 58.3 nm (Table 5.1). This can be interpreted as indicating that there are many different crystal domains in the a- and b-directions of the unsubstituted goethite crystals (*203*). In fact, a recent study using electron microscopy to reconstruct the 3-D structure of goethite found that an unsubstituted goethite had a highly imperfect structure with many internal voids (*204*).

As aluminum substitution increases, the $MCD_{(110)}$ increases, indicating an increase in crystallinity and coarsening of domains in the a- and b-directions. For example, the average width of goethite particles with 4.4% Al-substitution (4Al-Gt) is 125 ± 49 nm (n=15), which closely matches the pXRD $MCD_{(110)}$ of 106 nm. This quantitative change in the pXRD determined crystal parameters along with less difference between imaged particle size and pXRD domain size suggests that crystallinity of the goethite increases as aluminum substitution increases. In the aluminum goethites synthesized, a similar comparison for the crystallinity of goethites in the c-direction, which is parallel to the long direction of goethite, is not as useful. This is because no reflections consisting of just the (00*l*) plane are available from the pXRD data, and $MCD_{(111)}$ is influenced greatly by the width of the goethite domains.

Dissolution of Al-Substituted Goethites

We have studied both the proton-promoted and reductive dissolution of the aluminum substituted goethites used in this study. We used 8 M HCl to dissolve the

goethites to measure the congruency of Fe and Al release from the solid phase due to proton-promoted dissolution (Figure 5.1). The dissolution of Al from the all of the solids tested is slightly incongruent, indicating preferential release of Al from the Al-substituted goethites. Several possible mechanisms may cause the incogruency of Al dissolution. One mechanism is preferential release of Al during the dissolution, perhaps due to zonation of Al incorporation of the goethite towards the surface or at domain boundaries or due to faster detachment of Al than Fe from the surface of the goethite particles. In addition, a secondary phase with greater Al-content might also be dissolving at a faster rate that majority of the Al-goethite. We note, however, that lattice parameters of the studied goethites found using pXRD indicate that Al is incorporated into the structure, and that there are no crystalline Al-containing phases, nor is there evidence from the pXRD patterns to indicate that there is more than one phase of goethite (Figure 5.2).

Reductive dissolution of goethite and Al-substituted goethite was measured by monitoring Fe(II) release during exposure to dithionite-citrate-bicarbonate solution (DCB) (Figure 5.3). The overall rate of goethite dissolution followed the trend Gt ≈ 2Al-Gt > 4Al-Gt > 10Al-Gt. Normalizing the dissolution of the Al-goethites to specific surface area, results in rates within a factor of 3 (inset, Figure 5.3). These rates ($3 - 8 \times 10^{-10}$ moles m^{-2} s^{-1}) are two orders of magnitude slower than those found previously for dissolution of Al-substituted goethites in DCB solution and by dithionite in pH 5.5 EDTA solution (~10^{-8} moles m^{-2} s^{-1}) (*205*, *206*). In the first case, the pH of the DCB solution is not given, and in the second case the pH of the solution was 5.5, which may account for the faster rate of dissolution in that study. In a recent study, the rate of wüstite (FeO) dissolution was suggested to be an upper limit for Fe oxide reductive dissolution, due to constraints on rate detachment of Fe(II) from the surface of the oxide (*207*). Our results are in close agreement with the rate of dissolution of Fe(II) from FeO when extrapolated to pH 7.3 (rate ~ 2×10^{-10} moles m^{-2} s^{-1}). This suggests that the rate limiting step in reductive dissolution of Al-goethites in the presence of a ligand (citrate in our study) may

be detachment of Fe(II) from the surface of the goethite or that Al and Fe(II) detactment occur at equivalent rates.

Fe(II) uptake by Goethite and Al-Goethite

In order to compare the macroscopic Fe(II) uptake behavior of the Al-substituted goethite with that of unsubstituted goethite, we collected Fe(II) uptake data at a pH value of 7.5 in 25 mM HEPES/25 mM KBr buffer (Figure 5.5). We have compared the results of this study with those previously reported by our group for a pure, micron-sized goethite (*20*). It is notable that the results from this study for goethite match well (within 1 standard deviation) with the previous report. When Al is added to the goethite structure, on a per-gram basis the amount of Fe(II) taken up from solution by the Al-goethite is slightly less than that of the unsubstituted goethite (Figure 5.5A). When the uptake is normalized to the specific surface area of the goethites measured by N_2 BET adsorption, the Fe(II) uptake is similar for Gt, 2Al-Gt, and 4Al-Gt. The uptake of Fe(II) by the 10Al-Gt is higher than the lower Al goethites on a surface area basis. This difference is not large, with the uptake about 3 times greater at the highest Fe(II) loading. We note that Fe(II) recovery by dissolving whole reactors with an addition of concentrated HCl resulted in 99 ± 4% recovery of the added Fe(II) (99 % confidence interval), proving that there was no net oxidation of Fe(II).

Initially, we hypothesized that Al-goethite would take up less Fe(II) from solution. This hypothesis was based on several studies reporting reduced Fe(II) uptake by Al-oxide suspensions relative to their isostructural Fe-oxide counterparts, (for example, γ-AlOOH (boehmite) and γ-FeOOH (lepidocrocite)) (*9, 18, 208*). In the case of lepidocrocite it is important note that Fe(II) adsorption onto lepidocrocite can catalyze its transformation to magnetite and goethite (*17, 209*), which in the case of its transformation to magnetite would act as a sink for aqueous Fe(II) uptake and increase its measured affinity for Fe(II). Our results, however, do not suggest that there is a large

difference in the uptake of Fe(II) from solution between unsubstituted and Al-substituted goethite.

Since electron transfer occurs between sorbed Fe(II) and Fe(III) in goethite (*18, 21*), the uptake of Fe(II) from solution is not a "sorption isotherm" in the classical sense that it reflects binding of an Fe(II) cation to a static surface site (e.g. *10*). Although recent work has suggested modified sorption models incorporating electron transfer can be used to model this data (*11*). In addition, the majority of Fe(II) is recovered by dilution or extraction by 0.4 M HCl in similar experiments (*20, 210*), which contrasts with hematite where Fe(II) cannot be recovered by dilution due to Fe(II) doping in the structure (*19, 22, 190*). It is unclear what the nature of this Fe(II) lost from solution is in goethite suspensions, as Fe(II) is not observed in Mössbauer spectra of ^{57}Fe(II) reacted with goethite at low Fe(II) loadings (*18, 20*). We note, however, that Fe(II) is recovered to 99 ± 4% at the 99% confidence interval, when the whole suspension is dissolved by 6 M HCl, suggesting no net oxidation of Fe(II) by oxygen or other oxidants.

Electron transfer between Fe(II) and Fe(III) in Al-Substituted Goethite

We have used the isotope specificity of ^{57}Fe Mössbauer spectroscopy to probe whether sorbed Fe(II) is oxidized via electron transfer to Fe(III) in Al-substituted goethite. Two Al-substituted goethites were synthesized from Mössbauer invisible ^{56}Fe in Al containing solutions and have Al-contents of 5.4 and 9.5 mole % Al (Table 5.1) and are termed 5Al-^{56}Gt goethite and 9Al-^{56}Gt, respectively. In addition, an Al-free goethite was synthesized in a similar manner (^{56}Gt). In order to investigate whether electron transfer occurred between aqueous Fe(II) and Fe(III) in Al-substituted goethite we reacted 1 mM and 3 mM aqueous ^{57}Fe(II) with 2 g L^{-1} suspensions of ^{56}Fe goethite and Al-goethite in pH 7.5, 25 mM HEPES, and 25 mM KBr buffer. Mössbauer spectra are shown in Figure 5.6 for 1 mM ^{57}Fe(II) and Figure 5.7 for 3 mM ^{57}Fe(II). In these

suspensions, Fe(II) uptake was similar to that found for both micron and nanometer sized goethite, and was 0.13, 0.14, and 0.11 mmoles g^{-1} for the ^{56}Gt, 5Al-^{56}Gt, and 9Al- ^{56}Gt at 1 mM Fe(II) loading, respectively (Table 5.2). Addition of 3 mM Fe(II) resulted slightly higher uptake of Fe(II) for the Al-substituted goethites, and the Fe(II) uptake was 0.14, 0.23, and 0.16 mmoles g^{-1}, for the ^{56}Gt, 5Al-^{56}Gt, and 9Al-^{56}Gt (Table 5.2). The lack of an increase in Fe(II) uptake by the ^{56}Gt goethite in the 3 mM ^{57}Fe(II) loading experiment is likely due to a second batch of goethite being used for that experiment. This second batch of ^{56}Fe goethite had a slightly higher $MCD_{(110)}$ and $MCD_{(111)}$ indicating it likely has a reduced surface area.

After reaction with ^{57}Fe(II), the Mössbauer spectra consist of mostly Fe(III), indicating that the added ^{57}Fe(II) has been oxidized and resides in the solid phase. The spectra unequivocally indicate that for all three goethithes, including the 5.4% and 9.4% Al-substituted goethite that the sorbed ^{57}Fe(II) transferred an electron to the underlying goethite thus becoming oxidized (Figure 5.6 and Figure 5.7). This electron transfer has resulted in the formation of ^{57}Fe goethite on the surface. The Fe(III) has a sextet with overall parameters similar to a goethite sextet. The oxidation of sorbed Fe(II) on the surface of goethite is consistent with the previous findings of our group and others (*18, 20, 21*).

In addition to the sextet, peaks belonging to a small doublet are observed, as has been reported for hematite at high Fe(II) loadings and for goethite at similar Fe(II) loadings as were used in this study (*19, 211*). The concentrations of Fe(II) used in our Mössbauer isotope study are above where we see a bend in the Fe(II) sorption isotherms consistent with the transition from monolayer Fe(II) coverage to formation of Fe(II) polymers on the surface of the goethite, based on a surface site density of about 5 μmoles sites m^{-2} (*30*). Little difference is observed in the spectra when comparing between the 1 and 3 mM ^{57}Fe(II) loadings. Close inspection of the spectra indicate that there may be more than one sextet present, as peak 6 (the furthest to the right) has a shoulder on the

high velocity side and the 5th peak appears as the sharpest peak perhaps resulting from overlap of the two sextets here.

In order to determine if there is any evidence for the presence of a stable sorbed Fe(II) phase formed on the goethite, we have used Mössbauer spectral fitting to deconvolute the spectra. Fits of the spectra collected at 77 K of the ^{56}Fe goethites exposed to 3 mM Fe(II) are shown in Figure 5.8 and spectral parameters derived from the fitting are reported in Table 5.4. The fits reveal the presence of two ordered sextets, an Fe(II) doublet, and a broad, partially ordered or collapsed feature for all three goethite samples. In the ^{56}Gt, one sextet (Sextet 1) has parameters similar to those of goethite with a center shift (CS) of approximately 0.47 mm s^{-1}, a quadrupole shift parameter (QS = 2ε) of -0.25 mm s^{-1}, and a hyperfine field of 48.9 T. These parameters are typical of magnetically ordered, antiferromagnetic goethite. The 5Al-^{56}Gt and 9Al-^{56}Gt exposed to 3 mM ^{57}Fe(II) have slightly different parameters for this left-most sextet (Sextet 1), with CS values of 0.47 mm s^{-1}, but QS values of -0.46 mm s^{-1} and -0.47 mm s^{-1}, respectively. The hyperfine field of Sextet 1 of the ^{57}Fe(II) sorbed onto and oxidized by these Al-goethites is 48.4, and 48.0 T for the 5Al-^{56}Gt and 9Al-^{56}Gt samples, respectively, and is consistent with the reduction of the hyperfine field experienced by the ^{57}Fe nucleus as Al is substituted into the goethite structure (*212-214*). The QS parameters for Sextet 1of the Al-goethites are beyond the range typically reported for goethite and Al-substituted goethite (*212-214*). The second sextet (Sextet 2) has CS parameters of near 0.5 mm s^{-1}, QS parameters on the order of 0.10 mm s^{-1}, and a hyperfine field similar to Sextet 1 for all three goethites reacted with ^{57}Fe(II) (Table 5.4). These parameters are closer to those of lepidocrocite, but lepidocrocite has a Néel temperature near or lower than 77 K, which means it is unlikely to be magnetically ordered at this temperature (*128, 215*). As such, formation of lepidocrocite in these experiments can be ruled out. We note that such an anomalously high QS parameter was found for one of three sextets when ^{57}Fe(II) was sorbed to goethite with a natural abundance of ^{57}Fe, under conditions where the amount of ^{57}Fe

sorbed was roughly equal to the amount of ^{57}Fe in the goethite (*21*). In that report, however, these parameters were deemed to be consistent with those of goethite.

In addition to the two magnetically ordered sextets, the spectra of ^{57}Fe(II) oxidized by sorption to the ^{56}Fe goethite and Al-goethites contain a doublet. This doublet is consistent with octahedral Fe(II) with CS parameters near 1.3 mm s^{-1} and quadrupole splitting (QS) parameters approximately 2.5 -2.7 mm s^{-1} (*174*), and is similar to the parameters for Fe(II) sorbed onto oxide minerals and clays that have been previously reported (*18, 19, 216, 217*). This Fe(II) doublet is distinct from frozen aqueous Fe(II) which has CS values near 1.4 mm s^{-1} and QS values near 3.2 mm s^{-1}, and is also different from that of solid ferrous hydroxide ($Fe(OH)_2$) at 77 K with a CS and QS of 1.3 and 3.1 mm s^{-1}, respectively (*217, 218*). There is apparent loss in the area of this doublet when the temperature is lowered from 77 K to 15 K (Figure 5.6 & Figure 5.7), but the loss in area can be attributed to further ordering of the overlapping collapsed feature as the temperature is lowered. Homogeneous ferrous hydroxide precipitation can also be ruled out on the basis of the solubility of $Fe(OH)_2$. At pH 7.5 and an ionic strength of 25 mM the solubility of $Fe(OH)_2$ is 13.8 mM (pK_{sp} = 12.89) (calculated using Visual MINTEQ (*107*)). Further evidence that this doublet is due to a solid-associated Fe(II) species is the Mössbauer spectrum of the 3 mM ^{57}Fe(II) sample reacted with ^{56}Fe goethite and then exposed to air for a month prior to reanalysis (Figure 5.9). This spectrum shows no evidence of a Fe(II) doublet similar to those in Figure 5.6, Figure 5.7, and Figure 5.8, indicating that the Fe(II) has been oxidized by exposure to air.

As well as the two component sextet and the Fe(II) doublet the spectra contain a broad, collapsed feature we have fit with a magnetically collapsed sextet. This phase makes up a significant portion of the area in the samples (~30%). We cannot attribute this phase to a specific iron oxide due to its broad hyperfine field distribution and lack of significant features. In addition to oxidation of the sorbed Fe(II) phase after exposure to air, the oxidation has removed the collapsed feature present in the goethite + 3 mM Fe(II)

sample. We speculate that this phase may be formed via electron injection or delocalization in the goethite newly formed by oxidation of the ^{57}Fe(II) and exposed to atom exchange (*24*).

Larese-Casanova and Scherer concluded that Morin transition suppression in ^{57}Fe hematite exposed to ^{56}Fe(II) was due to delocalization of an electron in the bulk of the hematite structure (*190*). This result was based on work showing Morin transition suppression in M(IV) doped hematites, which to maintain charge balance contain Fe(II), and also on *ab initio* modeling of electron transfer in hematite, which suggests that electron hopping in hematite is on the order of or faster than the measurement window of Mössbauer spectroscopy (*219-221*). There is no work published to date using *ab initio* molecular methods to model electron transfer in goethite, as there is for hematite (*221-224*). We speculate that a similar electron delocalization process may be happening for the newly formed goethite produced from ^{57}Fe(II), giving the collapsed feature observed in Figure 5.9. We further speculate that exposure to air would have removed this phase due to reduction of O_2 by these electrons.

The electronic properties of goethite and hematite are similar. Goethite and hematite have similar band gaps (2.10 eV for goethite and 2.20 eV for hematite (*128*)). Goethite and hematite have been noted to have greatly different electrical conductivities of ~10^{-9} and ~10^{-4} Ω^{-1} cm^{-1} near room temperature, respectively (*223, 225*). This difference might be due to the fact that hematite conductivity is measured for single crystals, whereas goethite conductivity has been measured for powders. A study that measured conductivity of hematite and goethite powders found room temperature direct current conductivities that were much closer than previous found with both on the order of 10^{-7} Ω^{-1} cm^{-1} (*226*), perhaps suggesting that the two have more similar conductivities/resitivities than previously thought.

The production of Fe(II) in the goethite structure by cation doping is less studied than for hematite. Two isotope Mössbauer studies with ^{119}Sn and ^{57}Fe indicate that

Sn(IV) doping did not cause reduction of Fe(III) to Fe(II), but rather the charge balance was maintained by cation vacancies in the goethite structure (*227*). In contrast, the conductivity of Ti-doped goethite was found to be increased relative to unsubstituted goethite, and this increased conductivity was quenched upon exposure to air (*225*). This conductivity increase was attributed to production of Fe(II) in the goethite structure by Ti(IV) doping.

Effect of Phosphate on Fe(II) Uptake by Goethite

In addition to Al-substituted goethites, we have also investigated the effect of sorbed phosphate (referred to as P) on the uptake of Fe(II) from solution, and Fe(II) to Fe(III) interfacial electron transfer. We initially hypothesized that a shift in the pH of Fe(II) sorption might occur because the point of zero charge (pH_{PZC}) has been measured to be lowered by phosphate sorption (*33*). In addition, the presence of phosphate in solution has been observed to increase both Mg^{2+} and Ca^{2+} sorption on the surface of goethite (*34*), and a significant change in Fe(II) sorption with pH has been noted to occur in the presence of various carbonate concentrations (*228*). Here we have exposed 2 g L^{-1} suspensions of goethite in 10 mM KCl electrolyte to 0.1, 0.2 and 0.5 mM phosphate overnight (20 hours) and then added 0.1 or 0.5 mM Fe(II) and measured its uptake at various pH values (pH edges) (Figure 5.10).

Our results indicate that the presence of sorbed phosphate does not greatly change the pH edges for Fe(II) uptake by goethite (Figure 5.10). The pH of 50% Fe(II) uptake at a concentration of 0.1 mM is approximately 6.0 with and without 0.1 and 0.5 mM P present. The pH of 50% Fe(II) uptake is higher at around 7.0 when the Fe(II) loading is increased to 0.5 mM in the absence and presence of 0.2 mM P. We note that this behavior has been observed in previous reports investigating Fe(II) uptake by goethite (*10*). It was also noted in that report that increased As(III) (AsO_3^{3-}) sorption occurred as increased Fe(II) was added to the goethite and 1.0 mM As(III) system, but recent work suggests

that this may be due to the oxidation of As(III) to As(V) in the presence of Fe(II) and goethite (*211*).

Fe(II) – Fe(III) Electron Transfer in the Presence of Anions

Sorbed Phosphate

To investigate whether Fe(II) to Fe(III) electron transfer occurs between sorbed Fe(II) and goethite in the presence of sorbed phosphate we have sorbed phosphate to 2 g L^{-1} ^{56}Fe goethite and reacted this phosphated goethite with ^{57}Fe(II). We have used ^{57}Fe Mössbauer spectroscopy to determine whether electron transfer occurred between the ^{57}Fe(II) and the goethite in the presence of sorbed phosphate. Figure 5.11 shows a typical phosphate adsorption isotherm on goethite at pH 7.5. We note that on a surface-area normalized basis, the goethite (^{NA}Fe) used to collect this data sorbs about 3 µmoles P m^{-2}, similar to the 2.5 µmoles P m^{-2} maximum sorption density reported previously (*30, 32, 229*). This maximum sorption density is a function of pH, as phosphate is more strongly bound to the positively charged goethite surface at low pH (*32*).

The first experiment investigating ^{57}Fe(II) to ^{56}Fe goethite electron transfer was done at a phosphate loading of 0.51 mM in the presence of 2 g L^{-1} ^{56}Fe goethite at a pH value of 7.5 (denoted Mid P/Low Fe(II) - details in Table 5.3). Prior to addition of ^{57}Fe(II), 0.18 mM P was sorbed (0.34 mM P remained in solution). This corresponds to surface saturation of the goethite by phosphate shown in Figure 5.11. In order to reduce the possibility of vivianite ($Fe_3(PO_4)_2 \cdot 8H_2O$) precipitation only 0.125 mM ^{57}Fe(II) was added. At these concentrations of Fe(II) and P the solubility of vivianite (pK_{sp} = 33.04) is exceeded at pH 7.5 (equilibrium concentrations are [Fe(II)] = 0.046 mM, [$PO_{4\text{-Total}}$] = 0.036 mM) (*230*). The Fe(II) uptake in the system was 0.112 mM, or 90% removal from solution, and addition of Fe(II) resulted in further uptake of 0.017 mM P. The Mössbauer spectra at temperatures from 250 K to 13 K are shown in Figure 5.12.

The Mössbauer spectra of the Mid P/Low Fe(II) experiment are consistent with the oxidation of ^{57}Fe(II) by Fe(III) in the underlying goethite. The spectra are dominated by a sextet similar to that of goethite, and also contain a doublet consistent with Fe(II). These results show that although a significant amount of phosphate has sorbed to the goethite that electron transfer between the sorbed ^{57}Fe(II) and the ^{56}Fe goethite occurs. In addition, the ^{57}Fe(II) that has been oxidized to Fe(III) has undergone templated growth on the goethite to produce a neo-formed ^{57}Fe goethite phase. Our results indicate, (*i*) that sorbed phosphate does not block interfacial electron transfer between aqueous and sorbed Fe(II) and Fe(III) in goethite, and (*ii*), that goethite is the oxidized product of this Fe(II)-Fe(III) interfacial electron transfer *despite* the presence of phosphate. Phosphate is known to favor the production of lepidocrocite over goethite during oxidation of Fe(II) (*231, 232*).

The phosphated ^{56}Fe goethite exposed to ^{57}Fe(II) has similar Mössbauer features as the ^{56}Fe Al-substituted goethites exposed to ^{57}Fe(II). We have fit the Mössbauer spectrum of the ^{56}Fe goethite exposed to 0.5 mM P and 0.1 mM ^{57}Fe(II) collected at 77 K with two sextets, an Fe(II) doublet, and a collapsed feature. The two sextets have similar parameters as the spectra of the Al-substituted goethites (Table 5.5), as does the collapsed feature, although this feature can be fit with a wide range of potential parameters without significantly changing the goodness of fit. The Fe(II) doublet has slightly higher CS and QS parameters (1.36 mm s^{-1}, 2.92 mm s^{-1}), which are consistent with average parameters for vivianite (*233*), suggesting that vivianite may have precipitated in this system. Vivianite precipitation is consistent with homogeneous controls done in the absence of goethite. Aqueous concentrations of 0.51 mM P and 0.13 mM Fe(II) resulted in loss of 0.08 mM P and 0.03 mM Fe(II) from solution, likely due to precipitation of vivianite.

We also investigated whether the precipitation of vivianite would shut down electron transfer between ^{57}Fe(II) and ^{56}Fe goethite. To do this, we added a higher concentration of phosphate (0.988 mM) to a 2 g L^{-1} suspension of ^{56}Fe goethite prior to

addition of 1.5 mM ^{57}Fe(II) (denoted High P/High Fe(II) in Table 5.4). Prior to addition of the ^{57}Fe(II) 0.12 mM P was removed from solution by sorption to the goethite, which is consistent with saturation of the goethite surface with P as in the 0.51 mM P experiment. After 2 hours of equilibration of the goethite/1 mM P suspension, 1.52 mM ^{57}Fe(II) was added and suspension was reacted for 4 hours prior to filtering and collection of Mössbauer spectra. Addition of Fe(II) resulted in further removal of P (0.92 mM P removal or 93%), and the majority of Fe(II) (1.22 mM Fe(II) removal or 80%) from solution.

Results from Mössbauer spectroscopy of this High P/High Fe(II) experiment indicate that precipitation of vivianite occurs, partially inhibiting interfacial electron transfer between Fe(II) and goethite (Figure 5.13). As the analysis temperature is lowered, a sextet is apparent in the spectra, indicating that some Fe(II) to Fe(III) electron transfer has occurred and has resulted in the formation of ^{57}Fe goethite. The majority of the ^{57}Fe in the system (84%), however, remains as ^{57}Fe(II) bound in precipitated vivianite and appears to be unavailable for electron transfer over the time scale of this experiment. Fitting of the spectrum at 77 K confirms that the Fe(II) in the system is vivianite, as the two Fe(II) doublets have parameters similar to those of vivianite (Table 5.5, Figure 5.13). In addition, the sextet (16% of the total area) has parameters similar to those of goethite, which confirms again that oxidation of some of the ^{57}Fe(II) in the system has formed goethite.

In order to determine whether the precipitation of vivianite in High P/High Fe experiment was due to surface precipitation on the goethite or that vivianite precipitated homogeneously from solution we have examined the solids with SEM. We found that vivianite precipitated homogeneously from solution forms large (1-10 μm) prismatic crystals and star-shaped clusters of these crystals (Figure 5.14, top image). In the High P/High Fe experiment we noted the presence of crystals with a similar morphology as

those formed homogeneously, suggesting that homogeneous precipitation rather than surface precipitation was how vivianite formed in this system.

Finally, we have investigated whether solid state electron transfer could occur between ^{57}Fe(II) in vivianite and Fe(III) in goethite. In order to do this, we devised an experiment such that nearly all the ^{57}Fe in the system was present as Fe(II) in vivianite prior to the addition of ^{56}Fe goethite. In this experiment (^{57}Vivianite + ^{56}Goethite, Table 5.4) we added equal portions of 1.5 mM P and Fe(II) and adjusted the pH to a value of 9.51 to precipitate vivianite. Precipitation of vivianite reduced the aqueous Fe(II) concentration to 0.04 mM. After the precipitation of vivianite, ^{56}Fe goethite was added to the solution to test whether Fe(II) in vivianite is capable of solid state electron transfer from Fe(II) to solid Fe(III) in goethite. We have hypothesized that under these conditions that we should observe one or more of three possible outcomes in the Mössbauer spectra: (i) solid state electron transfer happens between ^{57}Fe(II) in vivianite and ^{56}Fe(III) in goethite. This would result in the production of an Fe(III) doublet in vivianite, a result observed when vivianite is oxidized by O_2 (*175, 234*), (ii) solid state electron transfer does not occur, and the low solubility of vivianite at pH 9.5 prevents significant dissolution of Fe(II) resulting in the observation of Fe(II) only, or (iii) dissolution of Fe(II) from vivianite results in sorption of Fe(II) to goethite and interfacial electron transfer between Fe(II) and goethite, resulting in the presence of a goethite sextet in the spectrum. The results from this experiment are shown in Figure 5.15.

The Mössbauer spectra of the ^{57}Fe vivianite exposed to ^{56}Fe goethite indicate that solid state electron transfer is not occurring between the Fe(II) in the vivianite and the Fe(III) in the goethite. No Fe(III) doublet is observed in the Mössbauer spectrum, but rather, a pair of Fe(II) doublets similar to vivianite and two sextets similar to those found in the systems where ^{57}Fe(II) is reacted with ^{56}Fe goethite are present. The Mössbauer spectra from 250 K to 15 K indicate that ^{57}Fe(II) has been oxidized by Fe(III) in goethite forming the sextet in Figure 5.15. The amount of ^{57}Fe(II) oxidized in this sample is much

greater than the extra 0.03 mM Fe(II) sorbed (2%) upon addition of the goethite to the ^{57}Fe vivianite suspension. The large amount of goethite formed from oxidation of the ^{57}Fe(II) relative to the extra Fe(II) removed from solution after addition of the goethite to the vivianite suspension suggests that Fe(II) from the vivianite is dissolving and ^{57}Fe is re-precipitating forming goethite after being oxidized by the Fe(III) in the ^{56}Fe goethite. The cycling of ^{57}Fe between vivianite raises questions about whether atom exchange akin to the atom exchange that occurs between aqueous Fe(II) and goethite (*17*, *24*, *25*) is happening between solid vivianite and goethite via aqueous Fe(II). The large proportion of goethite in this system indicates that Fe atom cycling may be occurring, but further isotope tracking studies will be needed to determine this conclusively.

Other Environmentally Relevant Anions

We have also tested whether electron transfer occurs between Fe(II) and goethite in the presence of other common groundwater anions, including sorbed bicarbonate (4mM HCO_3^-), silicate (1 and 10 mM SiO_4^{4-}), and natural organic matter (20 mg/L Aldrich humic acid or NOM). These experiments were conducted near pH 7.5 in the presence of 1 mM ^{57}Fe(II) and 2 g L^{-1} ^{56}Fe goethite, and with several concentrations of anions (Table 5.3). We note that the amount of the anions sorbed to the goethite was not measured. Several studies, however, have shown that these anions sorb onto goethite (*29-31*). Previous research has suggested that silicate adsorption on goethite results in the formation of Si polymers at high concentrations of silicate (*31*).

The Mössbauer spectra in Figure 5.16 collected at 77 K indicate that in the presence of 4 mM bicarbonate, 1 mM silicate, 10 mM silicate, and 20 mg/L NOM electron transfer occurs between ^{57}Fe(II) and ^{56}Fe goethite. In general, these spectra are all very similar to the spectrum collected with 1 mM ^{57}Fe(II) in the absence of anions, and are also similar to those collected in the presence of phosphate. The spectra contain two sextets similar to goethite and a small Fe(II) doublet. In all cases, the results of the

experiments indicate that electron transfer occurs between ^{57}Fe(II) and Fe(III) in ^{56}Fe goethite and results in the formation of goethite templated onto goethite. Therefore, we can conclude that, at the concentrations studied, sorbed anions do not inhibit Fe(II)-Fe(III) electron transfer in goethite.

Of significant interest are silicate and NOM, as their effect on atom exchange between Fe(II) and several oxides has recently been measured for several oxides, including ferrihydrite, lepidocrocite, schwertmannite, jarosite, and hematite (*235, 236*). In the case of ferrihydrite, lepidocrocite, schwertmannite, and jarosite the presence of adsorbed Si and NOM decreased both the rate and extent of isotope exchange between aqueous Fe(II) and ^{55}Fe-labeled oxide (*236*). Atom exchange also occurs between aqueous Fe(II) and hematite in the presence of silicate, though the extent of atom exchange is relatively small for hematite in both the presence and absence of Si, and only comprises several atomic layers of the hematite (*235*). While adsorbed Si and NOM decrease the extent of isotope exchange, some isotope exchange in the presence of Si is consistent with our results that show ^{57}Fe(II) is oxidized by ^{56}Fe(III) in goethite and formation of ^{57}Fe containing goethite. Our results indicate that electron transfer between aqueous Fe(II) and the underlying oxide may be still be invoked to explain isotope exchange between Fe(II) and Fe-oxides.

Phospholipids and Electron Transfer Distance

Finally, we have investigated the effect of sorbed phospholipids on electron transfer between ^{57}Fe(II) and ^{56}Fe goethite. Phospholipids are biomolecules that make up the cell membranes in living organisms (*237*), and have recently been shown to form supported bilayers and multi-layers on metal oxide particles (*200, 201*). In addition, the phosphate end of phospholipids can undergo inner sphere complexation with iron oxides during bilayer formation (*238*). Phospholipid bilayers and multilayers can be several nanometers to tens of nanometers in thickness on the surface of the oxide (*200*). This

large distance provides a means to probe whether electron transfer between Fe(II) and goethite can be shut off due to distance, as electron transfer rate is dependent on electron donor-electron acceptor separation (*239, 240*).

In order to explore the potential for electron transfer blocking by sorbed layers of phospholipids, we have sorbed a phospholipid (1,2-dioleoyl-sn-glycero-3-phosphate or DOPA, Avanti Polar Lipids) onto goethite and interrogated whether electron transfer occurs between ^{57}Fe(II) and goethite. In this experiment, approximately 1 mM DOPA was sorbed to a suspension of 2 g L^{-1} goethite overnight and 1 mM ^{57}Fe(II) was added to the suspension. Mössbauer spectra were collected on the filtered suspension and are shown in Figure 5.17.

The Mössbauer spectra indicate that electron transfer between ^{57}Fe(II) and ^{56}Fe goethite does not occur in the presence of DOPA phospholipids (Figure 5.17). The spectra are solely comprised of an Fe(II) doublet, showing that none of the added ^{57}Fe(II) has been oxidized by goethite. Based on previous work with phospholipids showing adsorption onto metal oxides resulting in formation of supported bilayers (*200, 201*), we speculate that adsorption of DOPA to goethite occurs leading to formation of a thick capping layer over the surface of goethite which inhibits electron transfer between Fe(II) and Fe(III) in goethite. Other mechanisms are also possible, as Fe(II) might also form a complex with the phosphate ends of the DOPA, or be sequestered into suspended phospholipid micelles, thus making it unavailable for electron transfer.

The observation that phospholipids inhibit electron transfer between Fe(II) and goethite has interesting implications for interactions between Fe(II), Fe(III) oxides, and microbes responsible for Fe(III) reduction. Recent work has shown that large molecules in bacterial extracellular polymeric substances (EPS) preferentially adsorb to goethite (*241*). In addition, the presence or absence of EPS and high biomass levels also appears to influence the rate of Fe(III) reduction and ferrous products resulting from dissimilatory iron reduction of lepidocrocite (*123*). It is possible that the slowed production of Fe(II) in

the high biomass and EPS systems in could have resulted from inhibited electron transfer reactions between Fe(II) and lepidocrocite, between reduced electron shuttles such as AQDS and the lepidocrocite, or even perhaps by limiting direct contact between the bacteria and lepidocrocite. Inhibition of electron transfer between aqueous Fe(II) and iron oxides by bacterial EPS might be important to consider in high productivity systems, such as during subsurface biostimulation efforts.

Conclusion

Our work extends the concept that interfacial electron transfer occurs between Fe(II) and Fe(III) oxides to a variety of environmentally relevant conditions. We have shown that interfacial electron transfer between Fe(II) and Fe(III) occurs when Fe(III) in the goethite structure is replaced by the redox inactive Al(III) cation. We have also shown that sorption of anions such as phosphate, silicate, and NOM onto goethite does not inhibit Fe(II) to Fe(III) oxide electron transfer. In all cases, oxidation of the sorbed Fe(II) to Fe(III) results in the templated formation of goethite on goethite. We have observed that interaction between solid Fe(II) in vivianite and goethite occurs via solution and results in electron transfer between sorbed Fe(II) and goethite, rather than solid state oxidation of Fe(II) in vivianite. Our results suggest that interfacial electron transfer between Fe(II) and Fe(III) is robust over a wide range of oligotrophic geochemical conditions. We note that electron transfer between Fe(II) and goethite is inhibited by putative adsorption of long-chain phospholipids onto the surface of goethite. Blocking of interfacial electron transfer may be important under eutrophic geochemical conditions were large amounts of biomass or biofilms are produced, such as during subsurface biostimulation with various organic electron donors. Further work will be needed to evaluate the extent to which cation substitution in goethite and sorbed anions affect Fe cycling and atom exchange, although it appears we can speculate that very little exchange occurs in the phospholipid system.

Table 5.1. Properties of pure and Al-substituted goethites used in this study (± 1 standard deviation, when given).

	Synthesis Parameters					Solid properties					
Sample ID	Initial Al/(Al+Fe)	[KOH] (M)	Temp. (°C)	Aging Time (week)	Al/(Al+Fe)[a]$_{solid}$ x 100%	$MCD_{(110)}$[b] (nm)	$MCD_{(111)}$[c] (nm)	Length (nm) (n = 15)	Width (nm) (n =15)	pXRD Al Content[d]	BET Surface area (m^2/g)
Gt	0	0.3	70	2	0	58.3	40.1	982 ± 392	124 ± 44	2.4	37
2Al-Gt	0.07	0.3	70	2	2.15 ± 0.02[e]	65.0	92.2	1500 ± 855	120 ± 66	2.8	14
4Al-Gt	0.15	0.3	70	2	4.43 ± 0.09[e]	73.5	103	1180 ± 506	125 ± 49	5.3	20
10Al-Gt	0.44	1.0	60	4	9.85 ± 0.03[e]	106	217	416 ± 153	158 ± 99	12	7.9
Small Batch ^{56}Fe Al-Goethites											
^{56}Gt (Batch 1)[f]	0	0.3	70	2	0	47.6	32.1	n.m.[i]	n.m.[i]	2.1	n.m.[i]
^{56}Gt (Batch 2)[g]	0	0.3	70	2	0	99.7	67.4	n.m.	n.m.	1.2	n/m
5Al-^{56}Gt	0.27	1.0	60	14	5.41[h]	56.9	38.0	993 ± 370	109 ± 28	7.5	n/m
9Al-^{56}Gt	0.44	1.0	60	14	9.44[h]	98.2	59.4	569 ± 180	103 ± 29	12	n/m

[a] = Percent (%) aluminum substitution determined by dissolution in HCl and titration by ICP-OES.

[b, c] = Mean crystallite dimensions determined from pXRD data of the breadth of the (110) and (111) reflections of goethite.

Table 5.1—continued

[d] = Powder XRD determined Al content using the equation described in Ref. (*191*). The method has a 95% CI of ±2.6 % Al.

[e] = Mean and 1 standard deviation of triplicate reactors of 10 mg of goethite dissolved in 8 M HCl.

[f] = Used for 1 mM ^{57}Fe(II) experiment, all phosphate experiments, and phospholipid experiment.

[g] = Used for 3 mM ^{57}Fe(II) experiment, and all other anion experiments (NOM, SiO_4^{4-}, CO_3^{2-}).

[h] = Average of duplicates of 10 mg goethite dissolved in 8 M HCl.

[i] = not measured.

Table 5.2. Experimental conditions for Fe(II) to goethite and Al-goethite electron transfer experiments.

Experiment ID	[Fe(II)], initial (mM)	[Fe(II)], final (mM)	Fe(II) uptake (mmoles/g)[b]	pH, initial	pH, final	Mössbauer spectroscopy figure
			~1 mM ^{57}Fe(II)			
^{56}Gt	1.06	0.795	0.132	7.46	7.44	Figure 5.6
5Al-^{56}Gt	0.977	0.700	0.138			Figure 5.6
9Al-^{56}Gt	1.07	0.848	0.112			Figure 5.6
			~3 mM ^{57}Fe(II)			
^{56}Gt	3.23	2.96	0.135	7.49	7.46	Figure 5.7
5Al-^{56}Gt	3.63	3.17	0.232	7.50	7.45	Figure 5.7
9Al-^{56}Gt	3.13	2.81	0.160	7.51	7.46	Figure 5.7

Note: All experiments were preformed in 25 mM HEPES buffer with 25 mM KBr background electrolyte.

Table 5.3: Experimental conditions for Fe(II) to goethite electron transfer experiments in the presence of sorbed anions.

Experiment ID	Solution Conditions	[Anion], initial (mM)	Anion Uptake after Sorption (mM)[a]	Total Anion Uptake (mM)[b]	[Fe(II)], initial (mM)	Fe(II) uptake (mM)	pH, initial[c]	pH, final	Mössbauer spectroscopy figure
Mid P/Low Fe(II)	10 mM KCl	0.51	0.175	0.192	0.125	0.113	7.51	7.64	Figure 5.12
High P/High Fe(II)	10 mM KCl	0.988	0.121	0.920	1.52	1.22	7.52	7.51	Figure 5.13
^{57}Fe Vivianite +^{56}Fe Goethite	10 mM KCl	1.52	0.698	1.09	1.51	1.50	9.51	9.40	Figure 5.15
Bicarbonate	10 mM KCl	4.0	n.m.[d]	n.m.[d]	1.16	0.266	7.54	7.28	Figure 5.16
Natural Organic Matter (NOM)	10 mM KCl	20 mg L^{-1}	n.m.[d]	n.m.[d]	1.14	0.263	7.48	7.02	Figure 5.16
Low Silicate	10 mM KCl	1.0	n.m.[d]	n.m.[d]	1.14	0.191	7.46	7.17	Figure 5.16
High Silicate	10 mM KCl	10.0	n.m.[d]	n.m.[d]	1.38	0.303	7.52	6.84	Figure 5.16
Phospholipid (DOPA)	25 mM HEPES/25 mM KBr	1.0	n.m.[d]	n.m.[d]	~1	~0.7	7.51	7.51	Figure 5.17

[a] Anion uptake from solution by 2 g L^{-1} goethite after equilibration but prior to addition of ^{57}Fe(II).

[b] Total anion uptake from solution by 2 g L^{-1} goethite after addition of ^{57}Fe and a period of equilibration.

[c] pH after re-adjustment following the spike of ^{57}Fe(II) to solution.

[d] not measured

Table 5.4. Mössbauer parameters derived from fitting of spectra collected at 77K for ^{56}Fe goethite and Al-goethite reacted with 3mM ^{57}Fe(II).

Component	CS[a] (mm s^{-1})	QS[b] (mm s^{-1})	H[c] (Tesla)	std(H)[d] (T) or std(QS)[e] (mm s^{-1})	Area (%)
		Goethite			
Sextet	0.48	-0.24	49.5	0.77	100
		^{56}Gt + 3 mM ^{57}Fe(II)			
Sextet 1	0.47	-0.25	48.9	0.79	43
Sextet 2	0.53	0.14	49.5	1.06	24
Collapsed Feature	0.44	-0.14	29.3	14.4*	28
Fe(II) Doublet	1.26	2.66	-	0.36	4
		5Al-^{56}Gt + 3 mM ^{57}Fe(II)			
Sextet 1	0.47	-0.46	48.4	1.23	30
Sextet 2	0.50	0.06	48.7	1.38	31
Collapsed Feature	0.37	-0.18	30.8	14.5*	34
Fe(II) Doublet	1.25	2.53	-	0.48	5
		9Al-^{56}Gt + 3 mM ^{57}Fe(II)			
Sextet 1	0.47	-0.48	48.0	1.35	30
Sextet 2	0.50	0.06	48.1	1.46	30
Collapsed Feature	0.38*	-0.18*	30.7	14.5*	33
Fe(II) Doublet	1.26	2.64	-	0.57	7
		^{56}Gt + 3 mM ^{57}Fe(II) Oxidized in Air 1 month			
Sextet 1	0.47	-0.40	48.9	0.93	53
Sextet 2	0.52	0.02	49.1	0.99	44

* Denotes that the parameter was fixed during the fitting procedure to obtain resonable values for the Mössbauer hyperfine parameters.

[a] Center shift.

[b] Quadrupole splitting for doublets and quadrupole shift parameter for sextets.

[c] Hyperfine field.

[d,e] Standard deviation of the Voigt profile for the hyperfine field or quadrupole splitting parameters, respectively.

Table 5.5. Mössbauer parameters derived from fitting spectra recorded at 77 K for ^{56}Fe goethite with sorbed anions reacted with ^{57}Fe(II).

Component	CS[a] (mm s^{-1})	QS[b] (mm s^{-1})	H[c] (Tesla)	std(H)[d] (T) or std(QS)[e] (mm s^{-1})	Area (%)
^{56}Fe Goethite + 0.51 mM Phosphate + 0.13 mM ^{57}Fe(II)					
Sextet 1	0.47	-0.42	48.8	0.98	33
Sextet 2	0.50	0.10	49.1	0.93	30
Collapsed Feature	0.43	-0.42	30.5	14.5*	32
Fe(II) Doublet	1.36	2.92	-	0.53	6
^{56}Fe Goethite + 1.0 mM Phosphate + 1.5 mM ^{57}Fe(II)					
Fe(II) Doublet 1	1.30	2.64	-	0.35	38
Fe(II) Doublet 2	1.36	3.23	-	0.29	46
Sextet	0.47	-0.10	48.7	2.5	16
^{57}Fe Vivianite + ^{56}Fe Goethite					
Fe(II) Doublet 1	1.30	2.62	-	0.28	20
Fe(II) Doublet 2	1.34	3.23	-	0.23	25
Sextet	0.48	-0.15	49.0	1.77	19
Collapsed Feature	0.5*	-0.58	21.9	13.3	36
Vivianite[f]					
Fe(II) Doublet 1	1.33	3.14	-	-	-[f]
Fe(II) Doublet 2	1.27	2.54	-	-	-[f]

* Denotes that the parameter was fixed during the fitting procedure to obtain resonable values for the Mössbauer hyperfine parameters.

[a] Center shift.

[b] Quadrupole splitting for doublets and quadrupole shift parameter for sextets.

[c] Hyperfine field.

[d,e] Standard deviation of the Voigt profile for the hyperfine field or quadrupole splitting parameters, respectively.

[f] Ref (*233*), relative areas not reported.

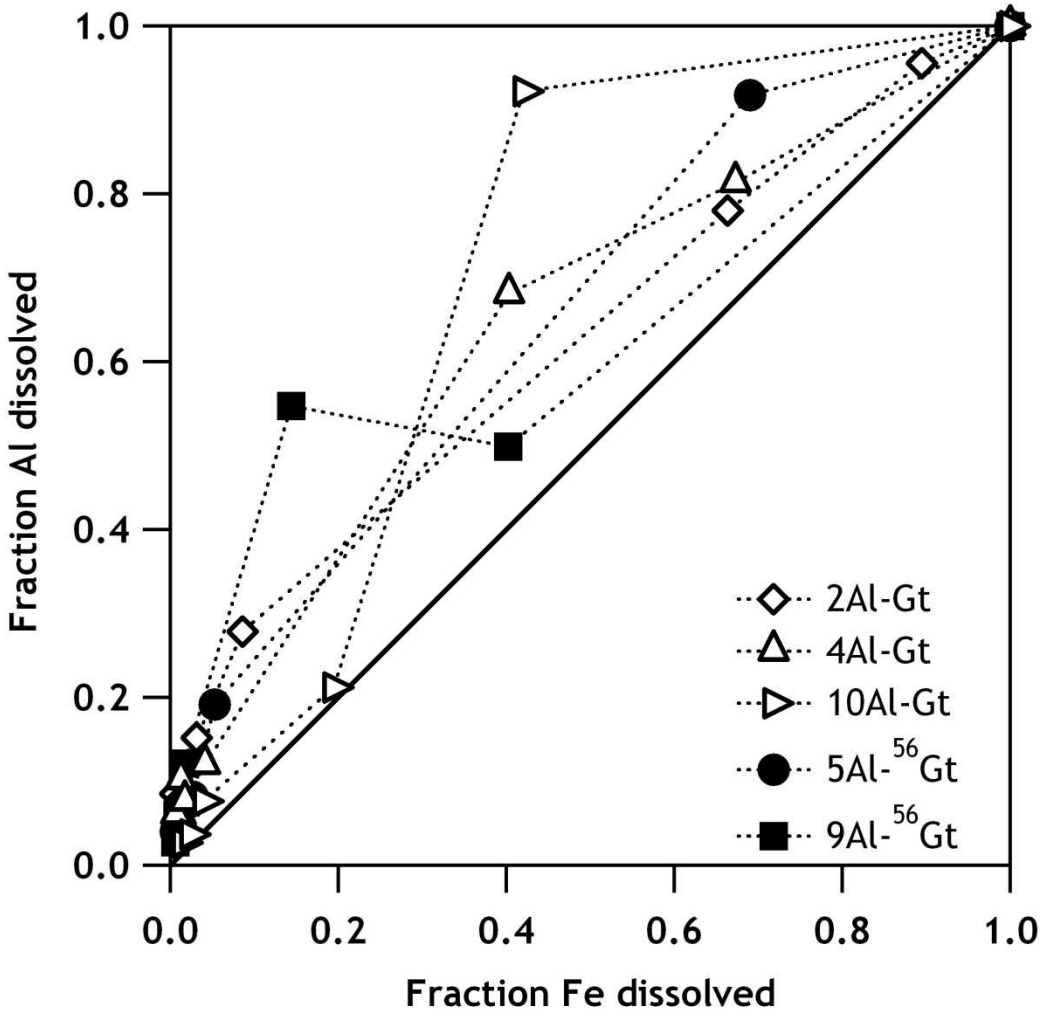

Figure 5.1. Dissolution of Al-goethites used in this study in 8 M HCl indicating that dissolution of Al is not completely congruent with Fe dissolution. Congruent dissolution is represented by the solid line. This non-congruent release of Al is most likely due to enrichment of the particles with Al on the surface or at domain boundaries that dissolve most readily.

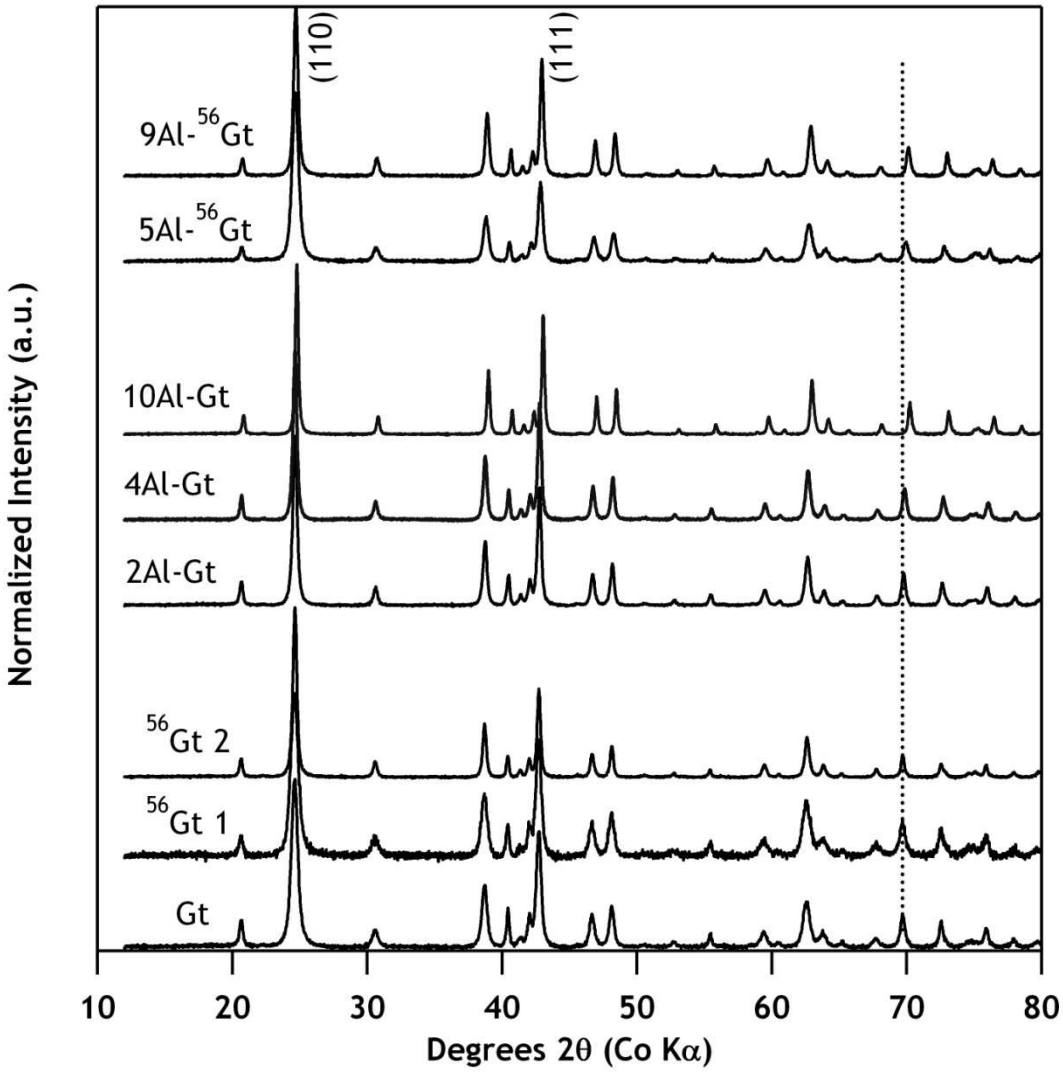

Figure 5.2. Powder x-ray diffraction patterns of the goethite and Al-goethite used. The dotted vertical line is shown as a visual reference to the change in goethite crystal properties upon aluminum substitution. This shift indicates that Al(III) is included in the goethite lattice (*191*).

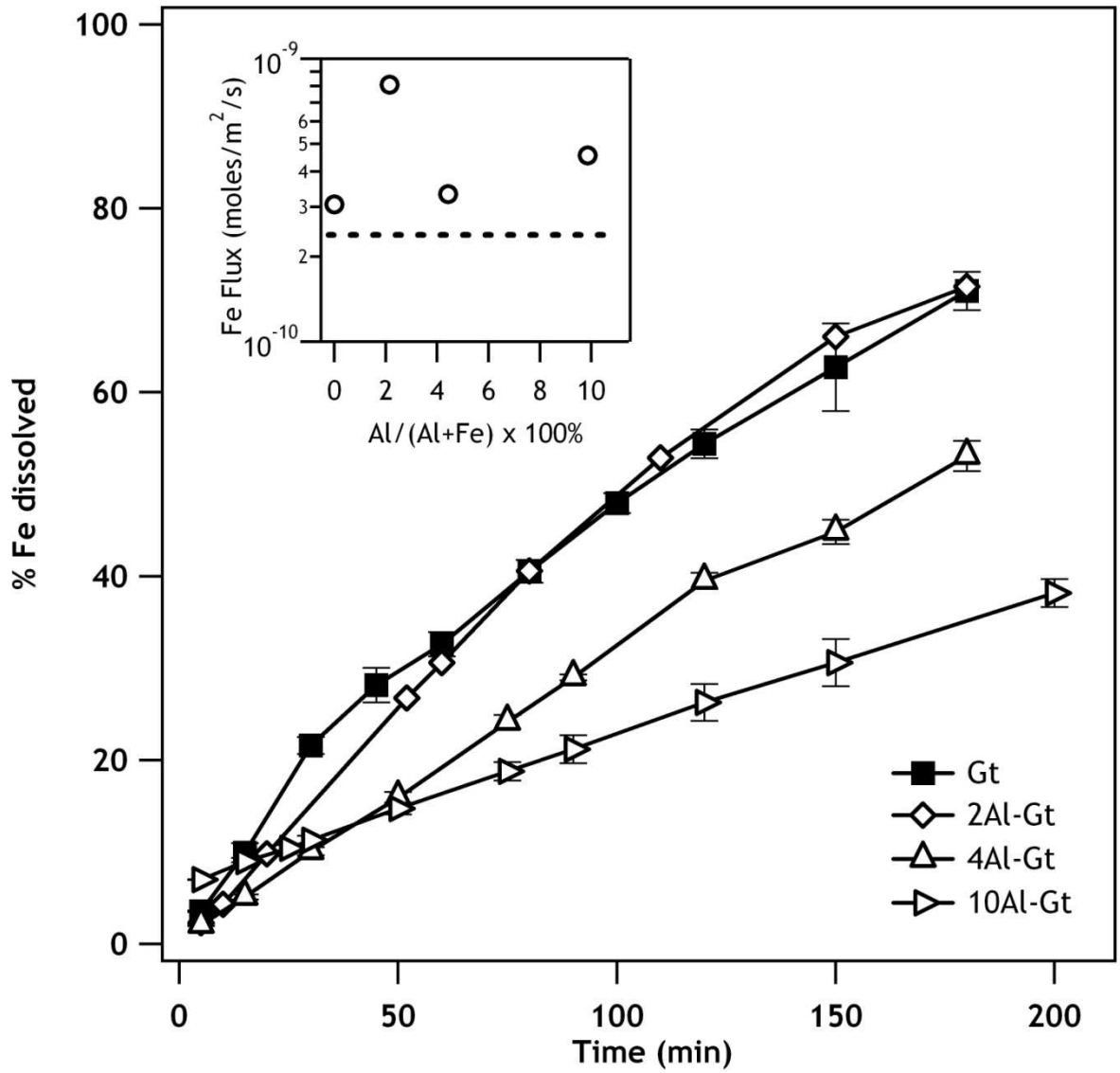

Figure 5.3. Dissolution of goethites and Al-goethites in dithionite-citrate bicarbonate (DCB) solution. Inset: Flux of Fe(II) from the goethites in moles m^{-2} s^{-1}. The dash line represents the upper limit of for the rate of dissolution of Fe(II) from FeO extrapolated to pH 7.3 (*207*).

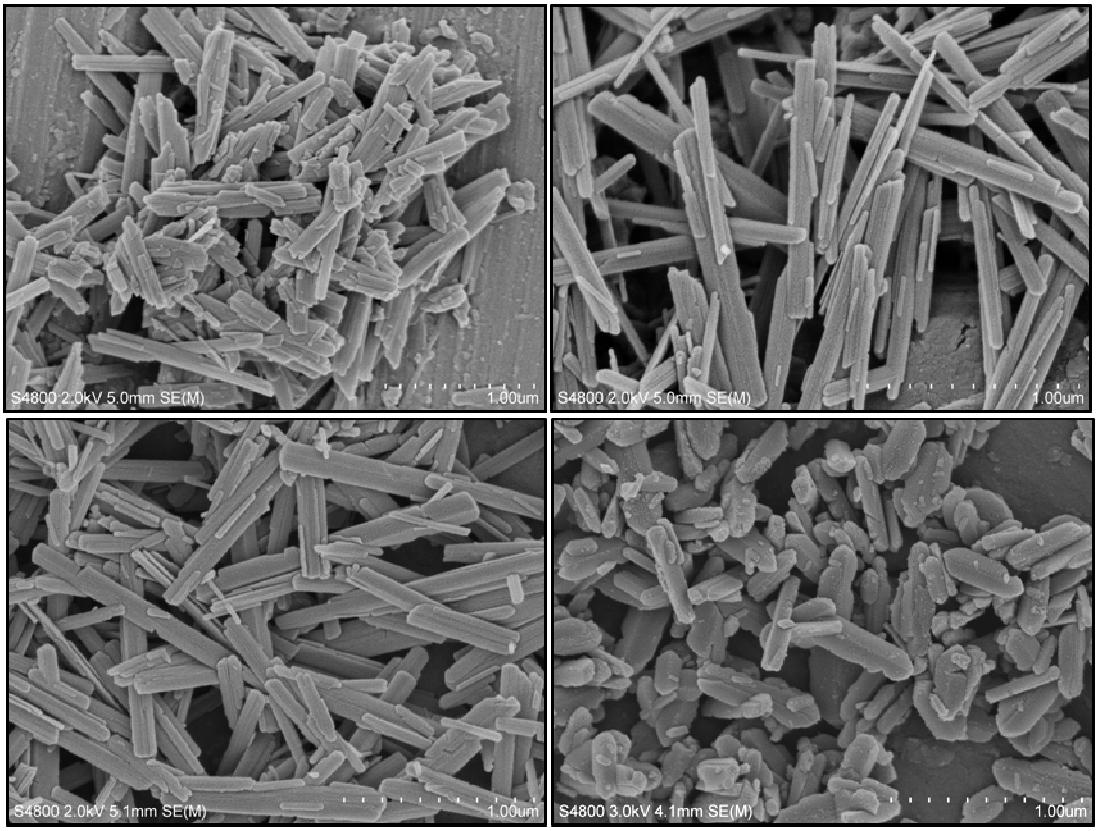

Figure 5.4. Scanning electron micrographs (SEMs) of (clockwise from top left) Gt, 2Al-Gt goethite, 4Al-Gt goethite, and 10Al-Gt showing the change in morphology of the goethite particles with increasing aluminum content. The scale bar in the SEM images represents 1 µm.

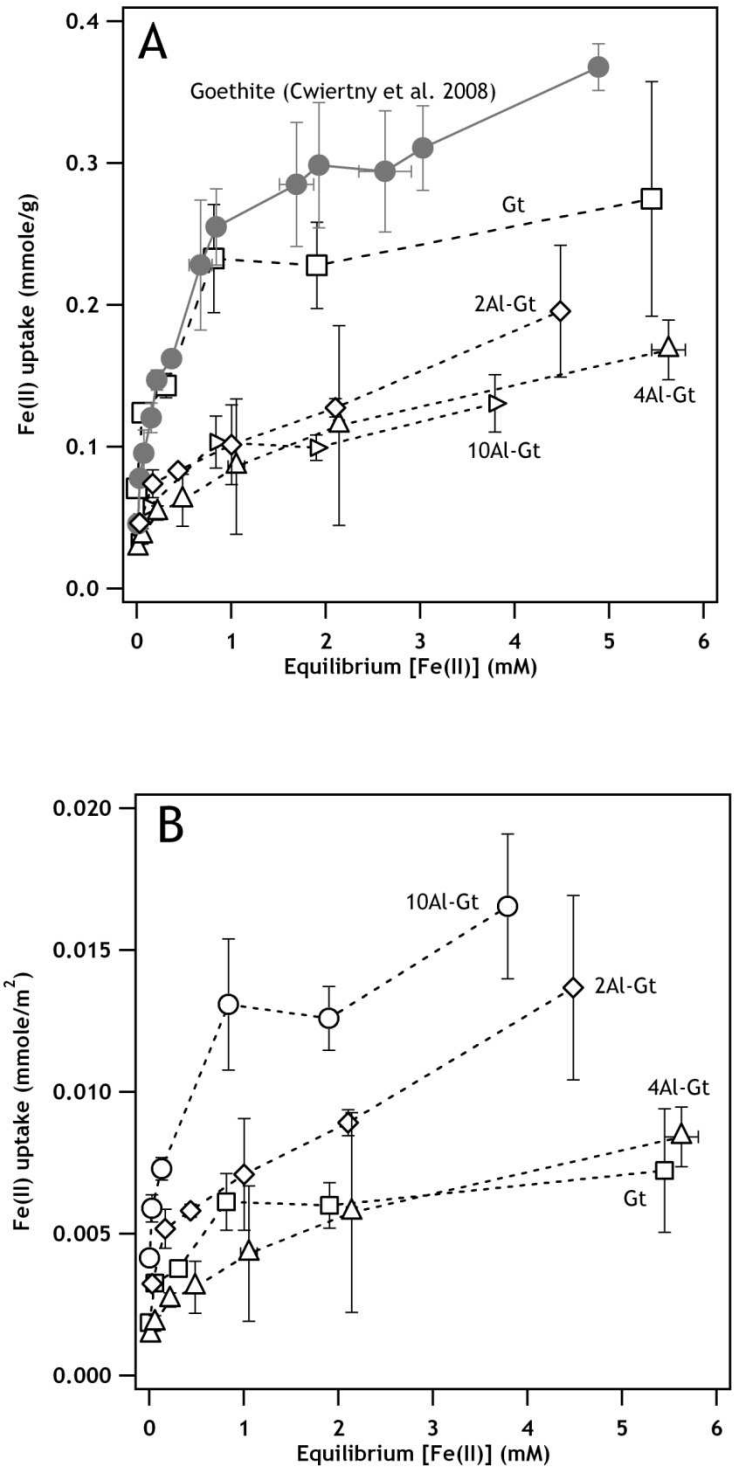

Figure 5.5: Uptake of Fe(II) from solution by goethite and Al-substituted goethites on a mass basis (A) and a surface area basis (B). The grey circles represent data from Ref (*20*).

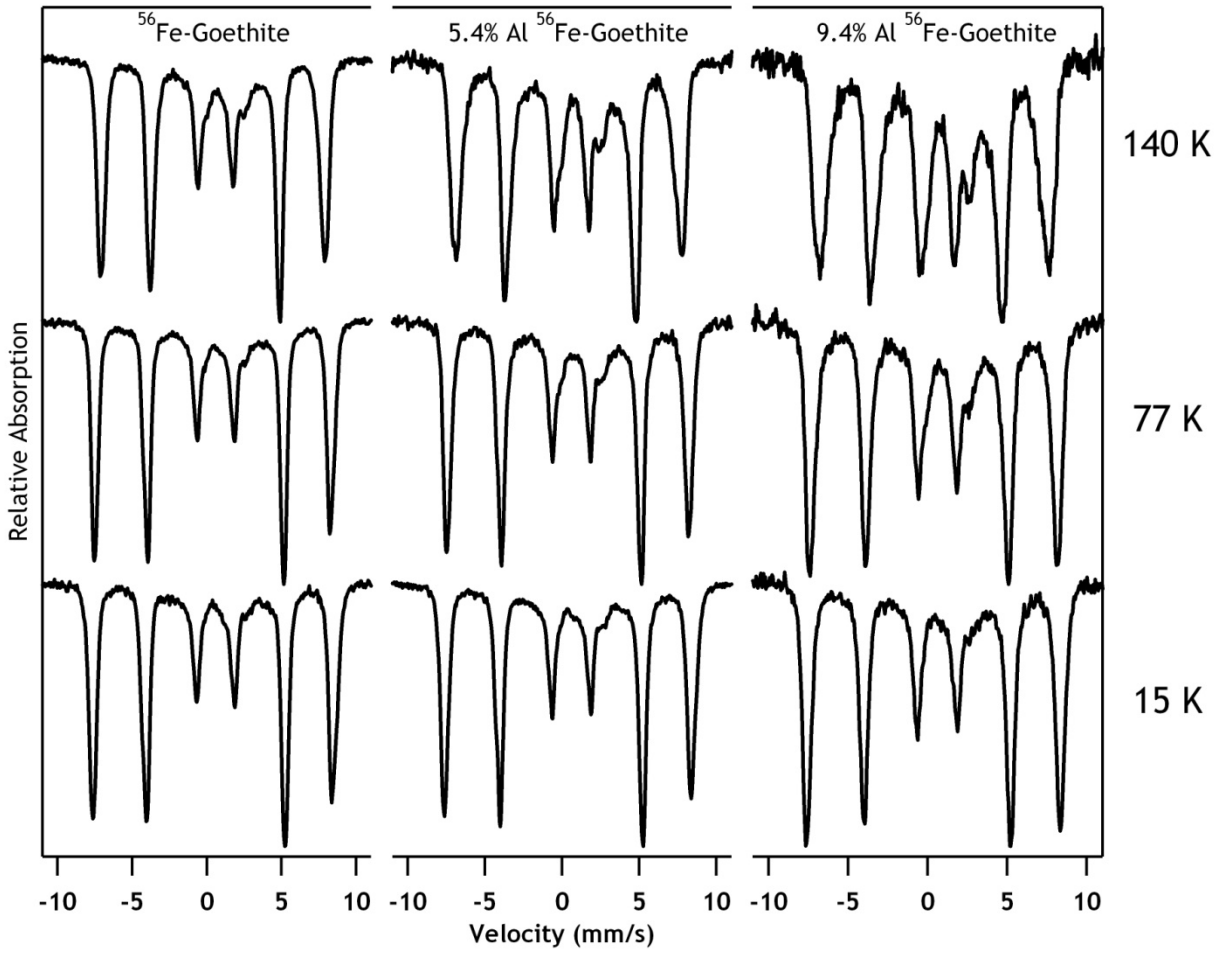

Figure 5.6. Temperature profiles of Mösssbauer spectra of ^{56}Gt (pure ^{56}Fe-goethite), 5Al-^{56}Gt (5.4% Al-substituted), and 9Al-^{56}Gt (9.4% Al-substituted) ^{56}Fe goethites reacted with 1 mM ^{57}Fe(II). The suspensions had an Fe(II) uptake of 0.13, 0.14, and 0.11 mmoles g^{-1} respectively. Reactions were carried out in a 2 g L^{-1} suspension of goethite in 25 mM HEPES and 25 mM KBr buffer at a pH value of 7.5.

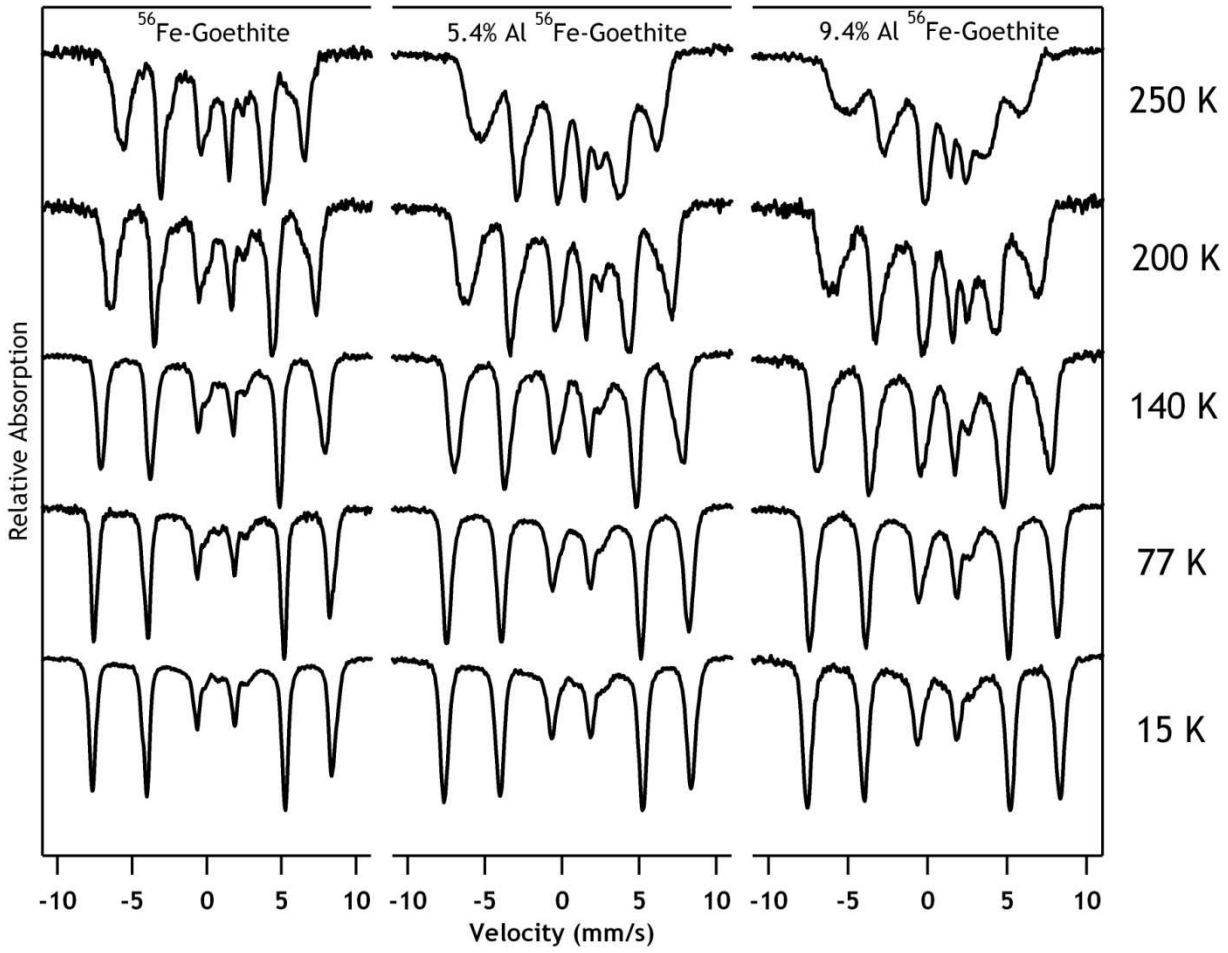

Figure 5.7. Temperature profiles of Mösssbauer spectra of ^{56}Gt, 5Al-^{56}Gt (5.4% Al-substituted), and 9Al-^{56}Gt (9.4% Al-substituted) ^{56}Fe goethites reacted with 3 mM ^{57}Fe(II). The suspensions had an Fe(II) uptake of 0.14, 0.23, and 0.16 mmoles g^{-1}, respectively. Reactions were carried out in a 2 g L^{-1} suspension of goethite in 25 mM HEPES and 25 mM KBr buffer at a pH value of 7.5

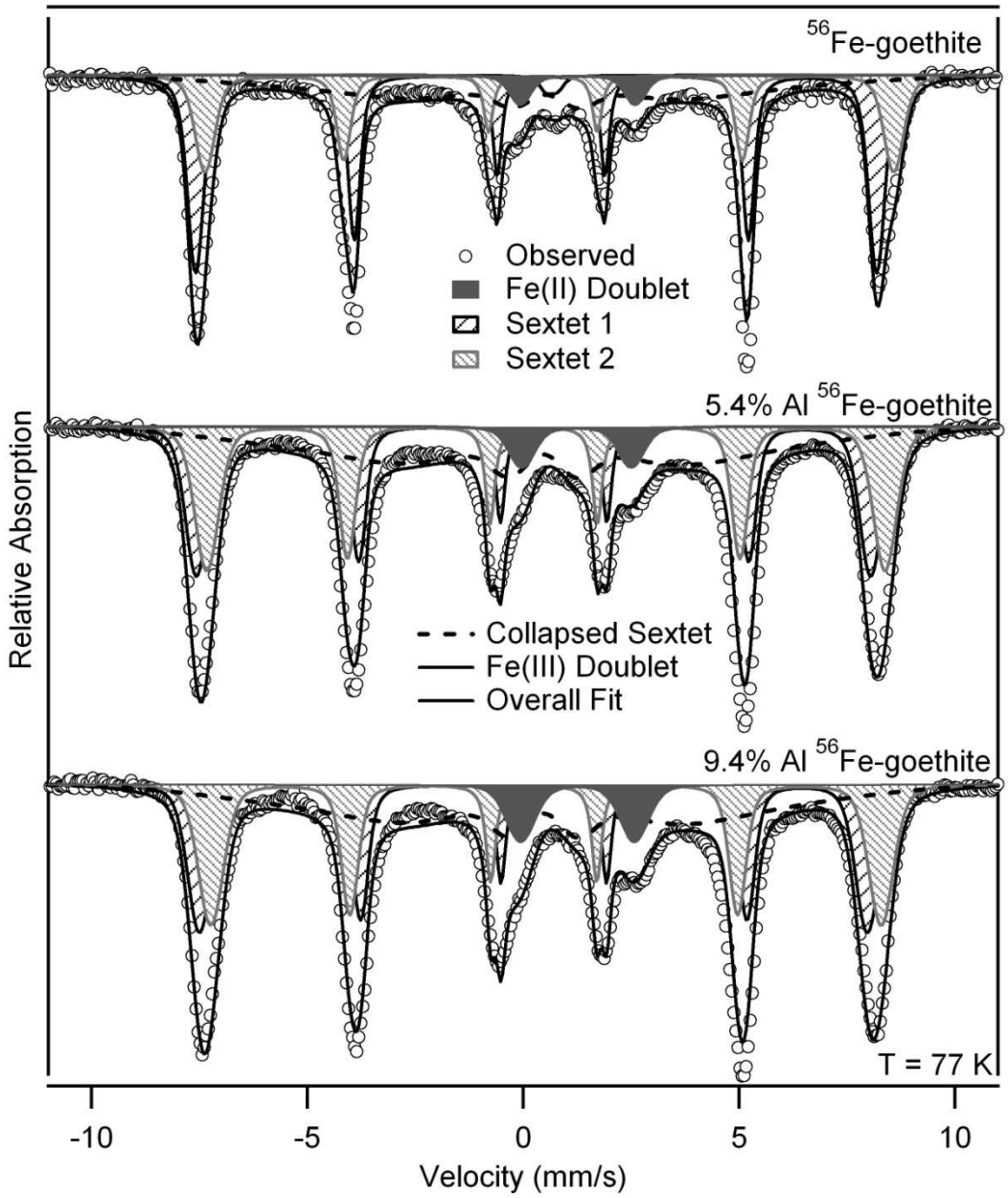

Figure 5.8. Mössbauer spectra of ^{56}Fe goethites and Al-substituted goethites (^{56}Gt, 5Al-^{56}Gt, and 9Al-^{56}Gt) after reaction with ^{57}Fe(II). Spectra were collected at 77 K. We have fit the spectra with two sextets and an Fe(II) doublet, as well as a collapsed feature. Spectral parameters are reported in Table 5.4.

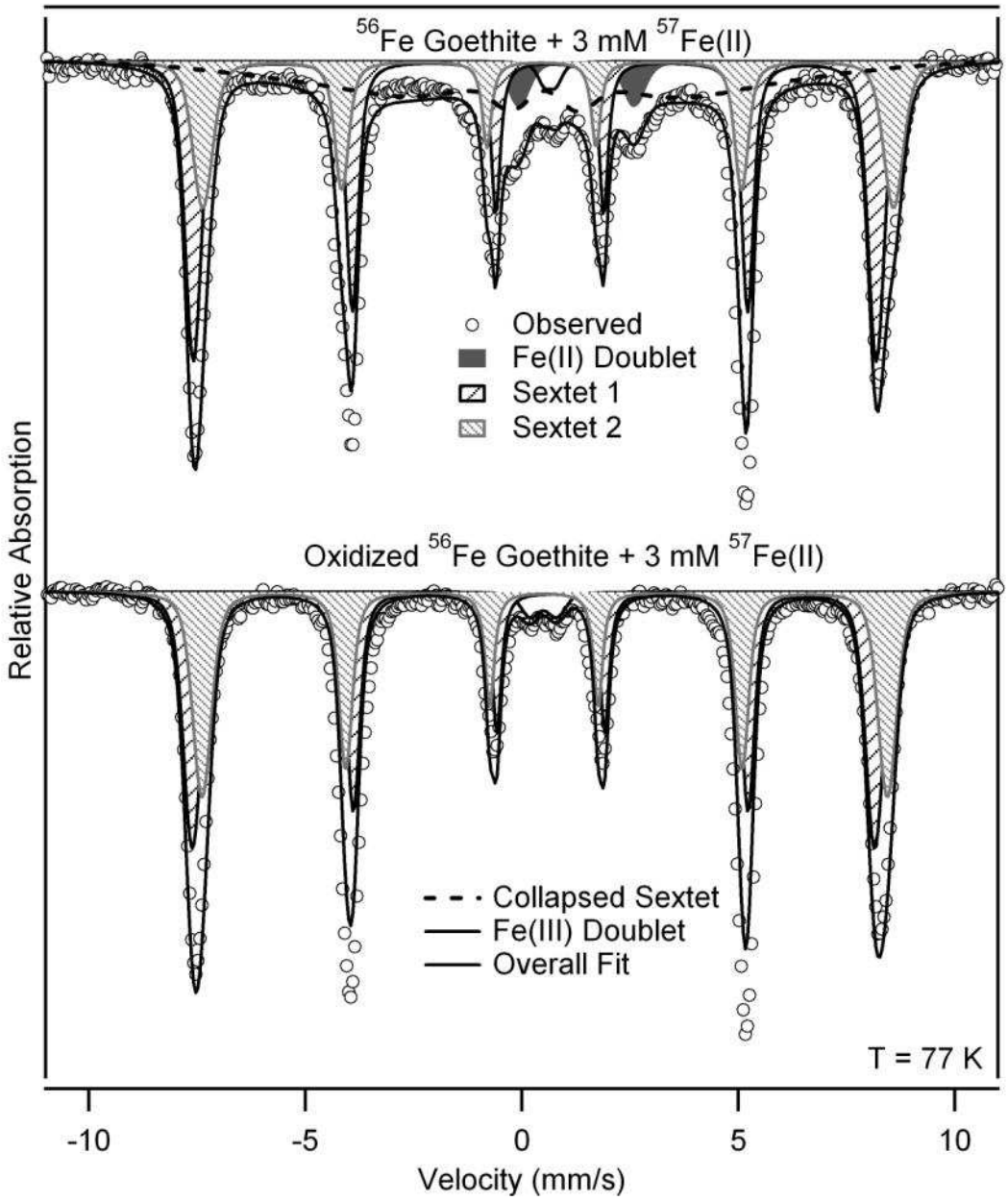

Figure 5.9. Mössbauer spectrum of ^{56}Fe goethite reacted with 3 mM ^{57}Fe(II) collected at 77 K compared to the spectrum of the same goethite after oxidation in air for 1 month.

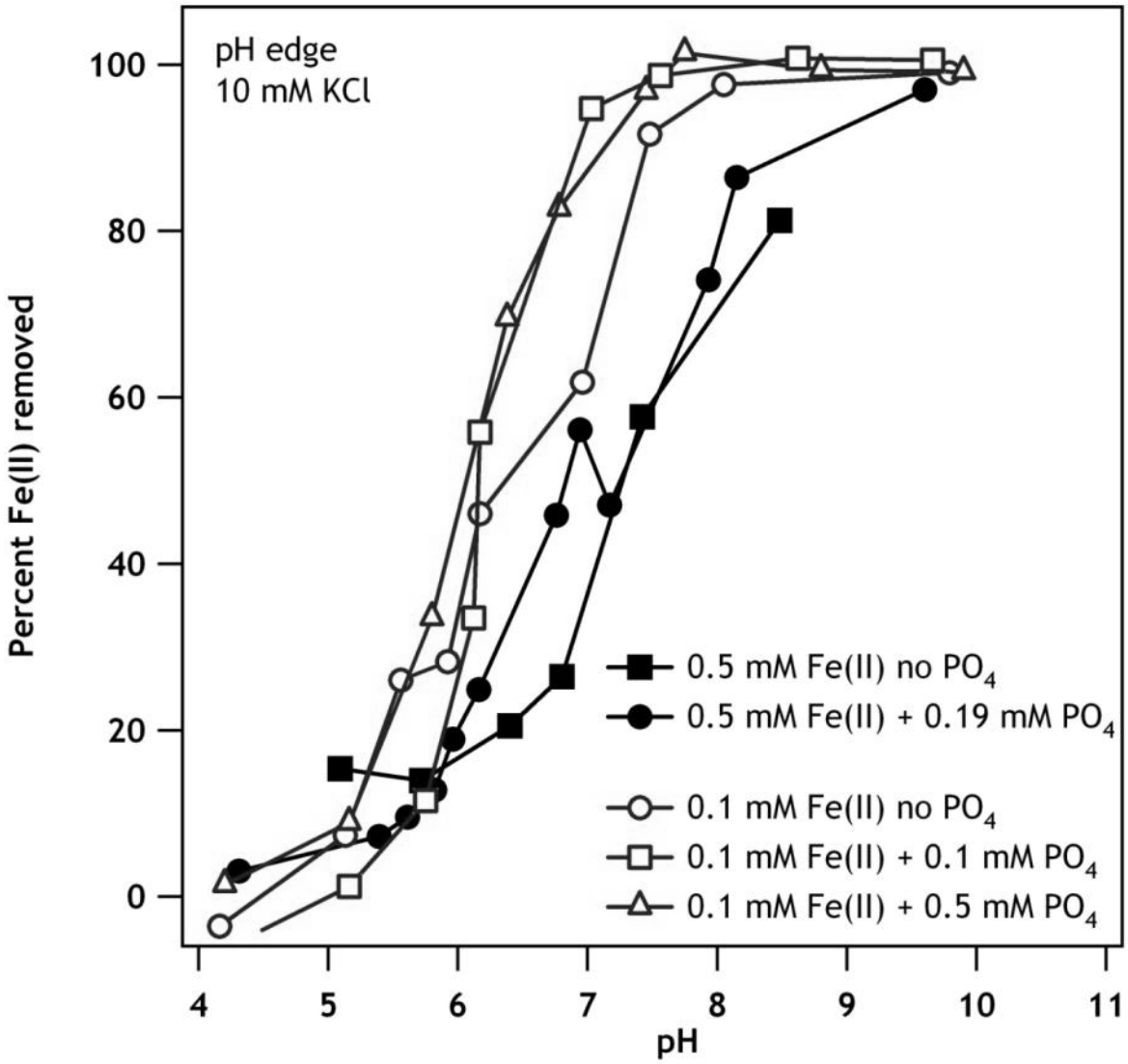

Figure 5.10. pH edges for uptake of 0.1 and 0.5 mM Fe(II) by goethite in the presence of 0.1, 0.19, and 0.5 mM phosphate (PO_4).

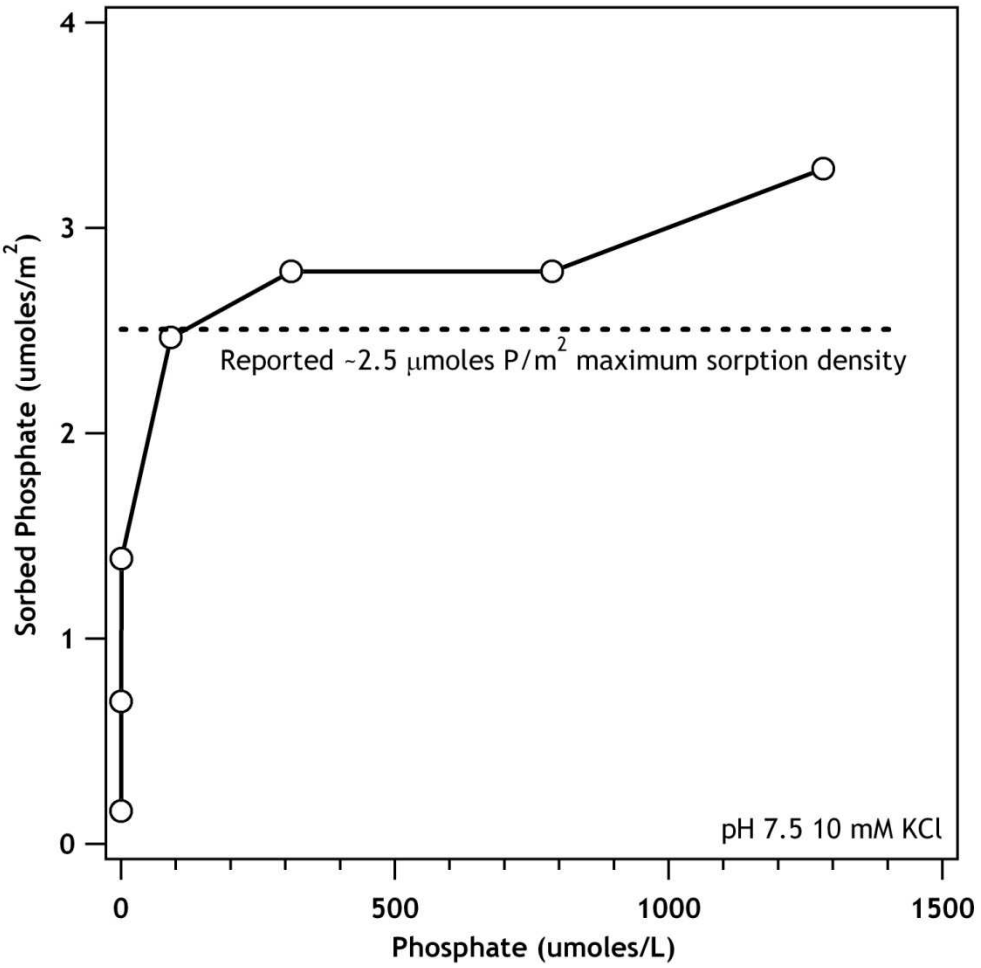

Figure 5.11. Phosphate sorption onto goethite at a pH value of 7.5 in 10 mM KCl background electrolyte (no added Fe(II)). The maximum sorption density of phosphate has been reported to be approximately 2.5 μmoles P m^{-2} (*32, 229*).

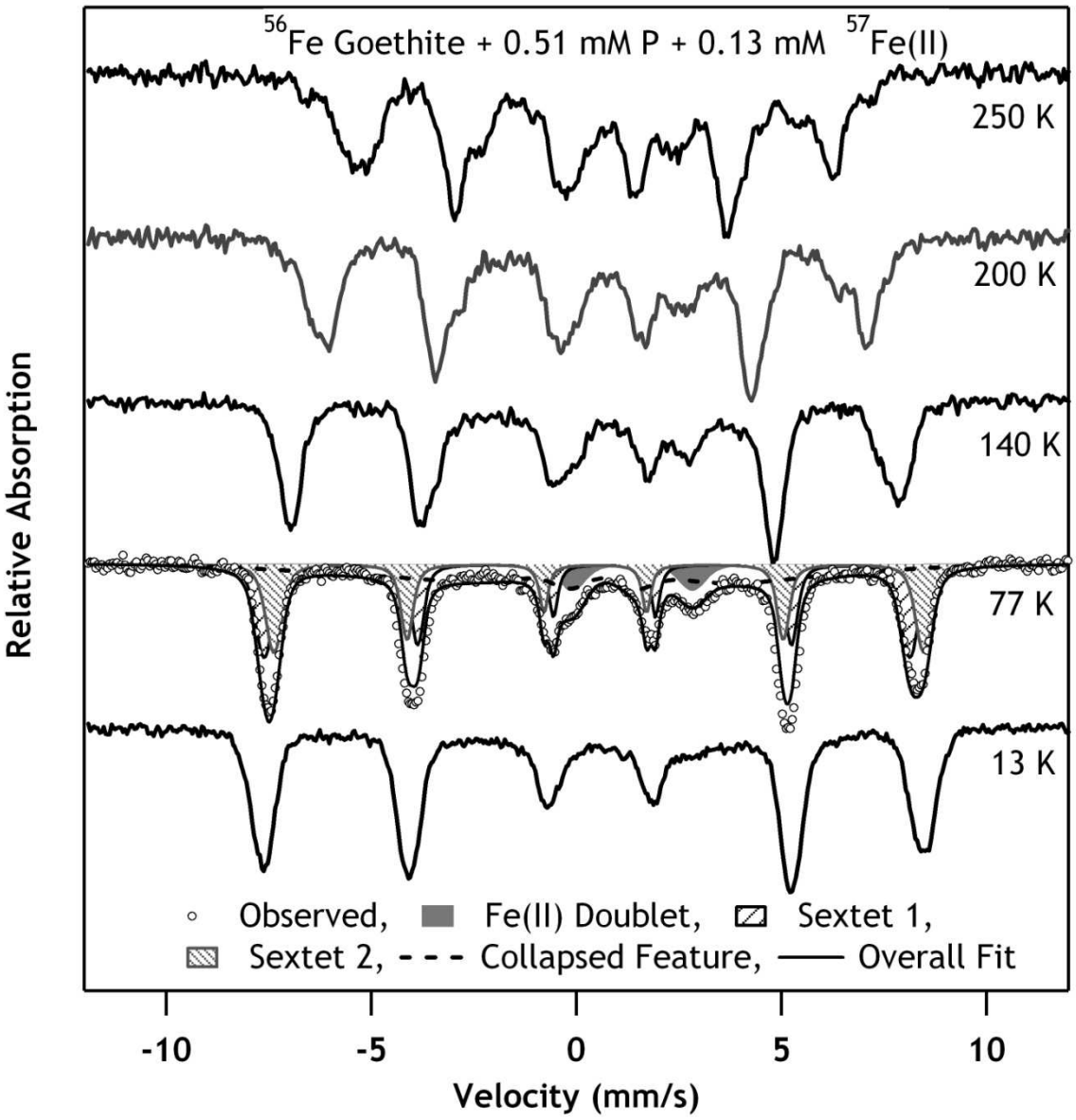

Figure 5.12. Temperature profiles of Mösssbauer spectra of ^{56}Fe goethite reacted with 0.51 mM P and 0.13 mM ^{57}Fe(II). Reactions were carried out in a 2 g L^{-1} suspension of goethite in 10 mM KCl background electrolyte (further solution details are in Table 5.4). We have fit the 77 K spectra with two sextets and an Fe(II) doublet, as well as a collapsed feature. Spectral parameters are reported in Table 5.5.

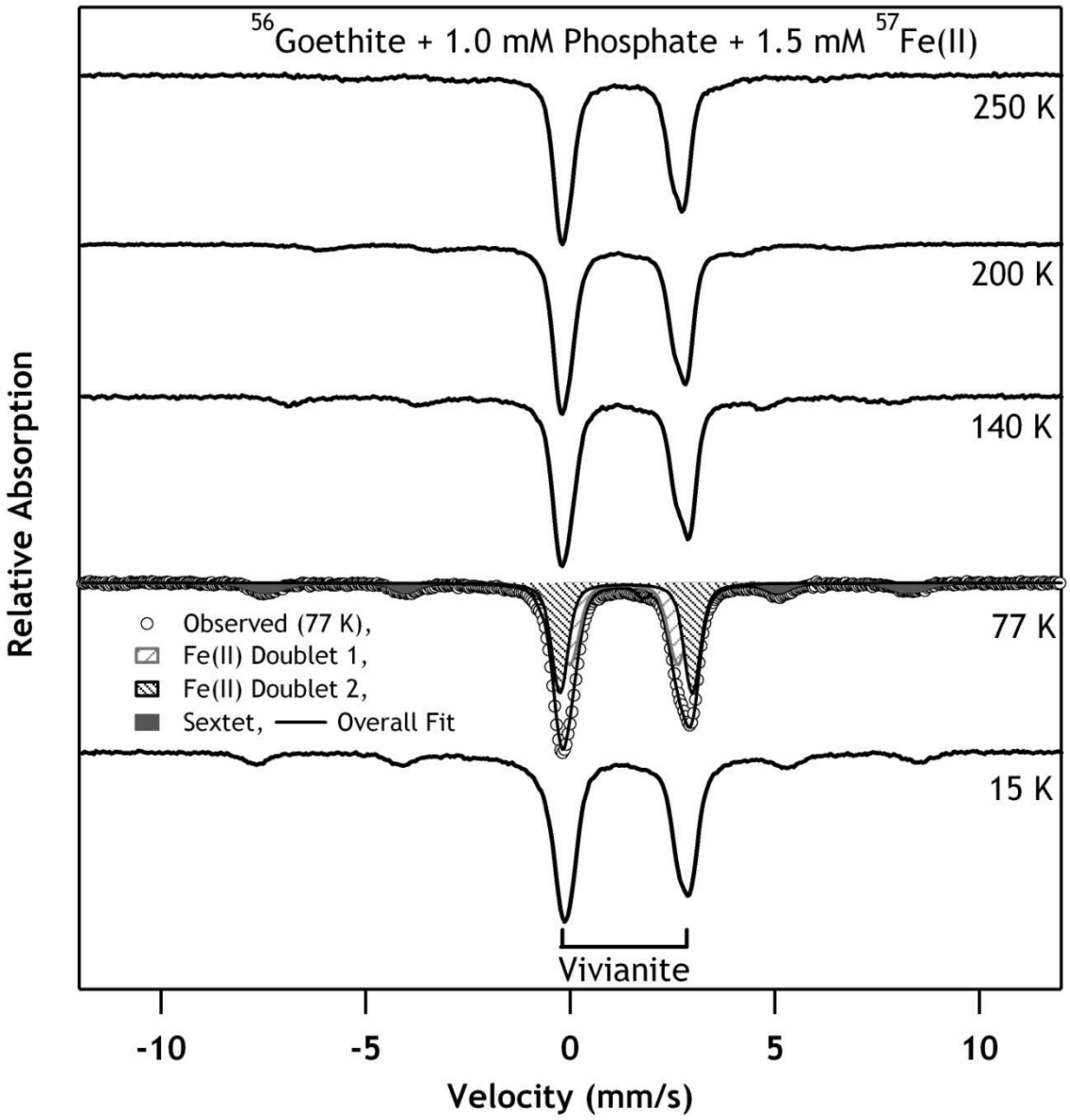

Figure 5.13. Temperature profiles of Mösssbauer spectra of ^{56}Fe goethite reacted with 1.0 mM P and 1.5 mM ^{57}Fe(II). Reactions were carried out in a 2 g L^{-1} suspension of goethite in 10 mM KCl background electrolyte (further solution details are in Table 5.4). We have fit the 77 K spectra with two Fe(II) doublets corresponding to vivianite and a sextet corresponding to goethite. Spectral parameters are reported in Table 5.5.

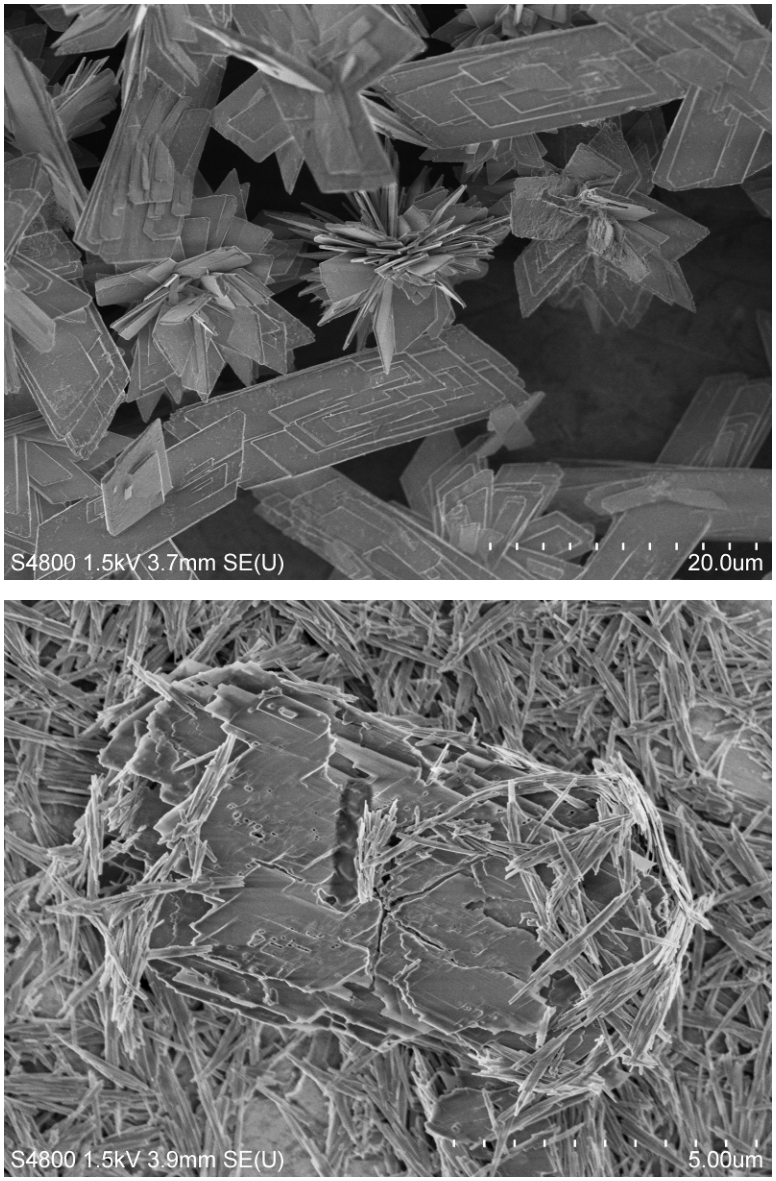

Figure 5.14. Scanning electron micrographs (SEMs) of vivianite homogeneously precipitated from solution (top) and vivianite precipitated in the presence of ^{56}Fe goethite in the High P/High Fe experiment (bottom).

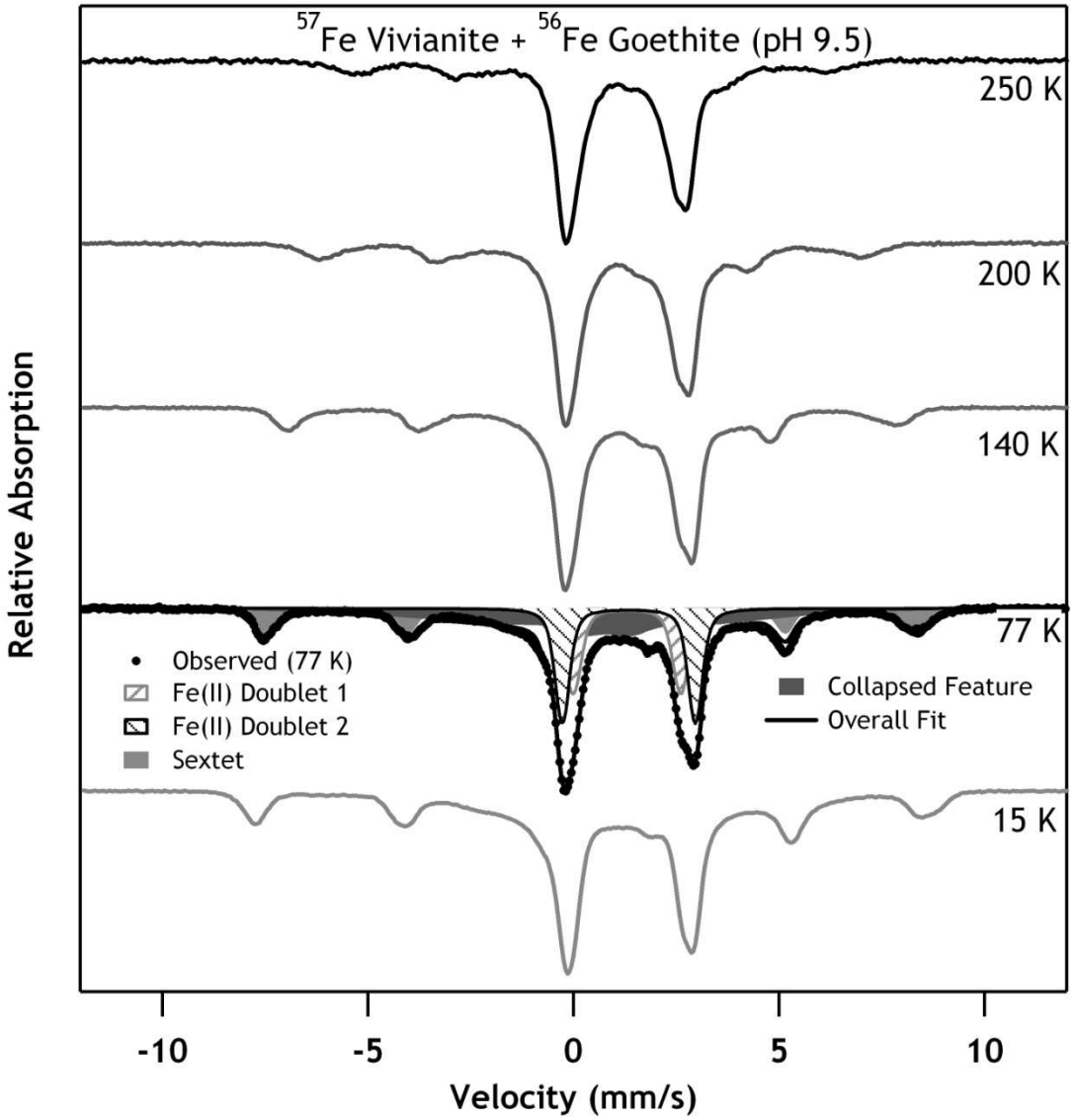

Figure 5.15. Temperature profiles of Mösssbauer spectra of ^{56}Fe goethite reacted with ^{57}Fe vivianite (1.5 mM ^{57}Fe(II) and 1.5 mM P). Reactions were carried out in a 2 g L^{-1} suspension of goethite in 10 mM KCl background electrolyte (further solution details are in Table 5.4). We have fit the 77 K spectra with two Fe(II) doublets corresponding to vivianite and a sextet corresponding to goethite, as well as a collapsed feature. Spectral parameters are reported in Table 5.5.

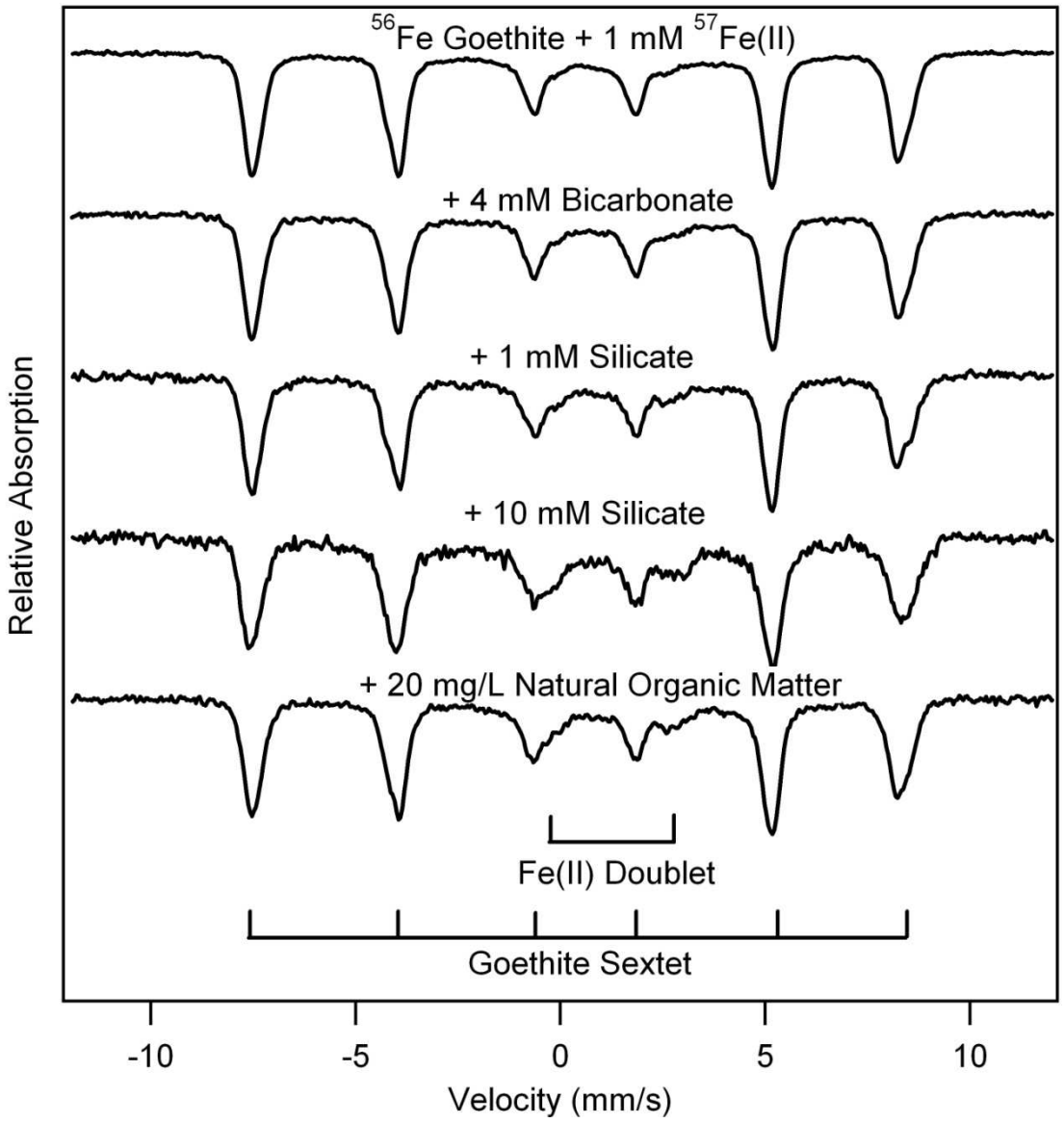

Figure 5.16. Mössbauer spectra of ^{57}Fe(II) reacted with ^{56}Fe goethite in the presence of several sorbed anions, including 4 mM bicarbonate, 1 and 10 mM silicate, and 20 mg/L natural organic matter (Aldrich humic acid). Bars are shown for a goethite sextet and an Fe(II) doublet for comparison to the measured spectra. Formation of a goethite sextet in all cases indicates that ^{57}Fe(II) has undergone electron transfer to Fe(III) in goethite and has been oxidized.

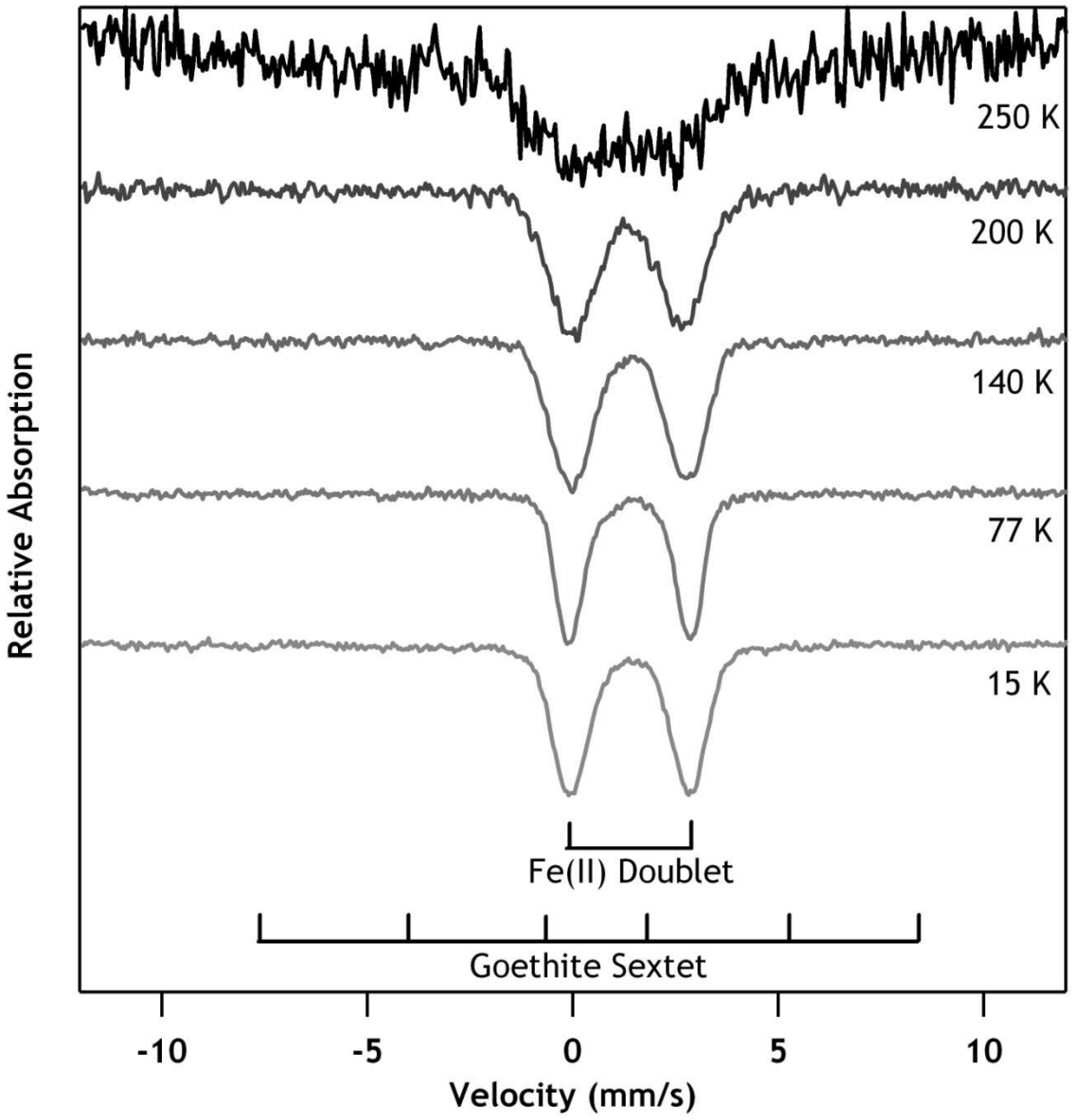

Figure 5.17. Mössbauer spectra of 1 mM ^{57}Fe(II) reacted with 2 g L^{-1} goethite in the presence of the phospholipid DOPA (1,2-dioleoyl-sn-glycero-3-phosphate). Only an Fe(II) doublet is observed in the spectra, indicating that the presence of the phospholipid has blocked Fe(II) from transferring an electron to Fe(III) in goethite. Bars are shown for an Fe(II) doublet and a goethite sextet for reference.

CHAPTER 6: IMPLICATIONS OF THE REDOX DRIVEN CONVEYOR BELT FOR CONTAMINANT TRANSFORMATIONS

Abstract

Recent work indicates that a series of reactions occurs when iron oxides are exposed to aqueous Fe(II). These reactions result in oxidation of Fe(II) at the surface of the oxide followed by oxide growth, electron transport through the bulk, and reductive dissolution of Fe(II) at a spatially separated site. When exposed to Fe(II), goethite and the aqueous Fe(II) undergo complete atom exchange. We have hypothesized that this atom exchange has an effect on contaminant transformations, which may lead to release or sequestration of trace metals or metalloids during Fe(II) induced atom exchange. We have exposed goethite synthesized to contain manganese (Mn-goethite) to solutions containing aqueous Fe(II) and measured Fe(II) uptake from solution and Mn release to solution. Our results indicate that Mn is released during reductive dissolution of the goethite, suggesting that metals may be released during atom exchange between Fe(II) and goethite. In addition, we have investigated whether uranium (U) is incorporated from solution into goethite during exposure to goethite and aqueous Fe(II). This work indicates that U^{VI} is reduced to U^{IV} by Fe(II) in the presence of goethite, but not incorporated into the goethite structure. Finally, we have begun to develop a method that allows for measurement of atom exchange between aqueous Fe(II) and Fe oxides using quadrupole-ICP-MS by using highly enriched ^{57}Fe(II) solutions and Fe oxides with natural compositions of Fe isotopes.

Introduction

Ferrous iron (Fe(II)) associated with iron oxides and oxyhydroxides (Fe oxides) is commonly considered an important reductant for many oxidized contaminants in the environment (*6-8, 242, 243*). The reactivity of Fe(II) with contaminants and its importance as a product of dissimilatory metal reduction of Fe(III) oxides (*82, 123, 187,*

244) has led to a variety of mechanistic studies on the interaction of Fe(II) with Fe oxides. These mechanistic studies have shown that there are dynamic redox reactions that occur between aqueous Fe(II) and the oxide (*17-25, 132*). These redox dynamics include oxidation of Fe(II) at the surface of an Fe oxide followed by growth of the oxide, electron conduction through the oxide, and reductive dissolution at a spatially separated site, a process that has been termed the "redox driven conveyor belt" (*24*). The atom exchange that occurs between aqueous Fe(II) and Fe oxides results in the complete mixing of the aqueous and solid phase Fe in goethite suspensions over short time scales of less than 1 month (*24, 25*). This mixing raises questions about the fate of metals and metalloids commonly associated with Fe oxides during atom exchange.

There are several studies that indicate contaminants may be strongly associated with iron oxides during redox transformations. One such study investigated the fate of arsenate (As(V)) during the Fe(II) catalyzed transformation of ferrihydrite to more crystalline Fe oxides and As(V) bound to goethite and lepidocrocite in the presence of Fe(II). Results from this study indicated that radioactive ^{73}As was so strongly bound to ferrihydrite recrystallization products (lepidocrocite, goethite, and/or magnetite) and to goethite exposed to Fe(II) that it could not be desorbed from the surface when exposed to an addition of unlabeled As (*245*). Another study investigating the fate of uranium during Fe(II) catalyzed recrystallization of ferrihydrite uses structural data from U x-ray absorption spectroscopy to argue that U may be incorporated into the products of ferrihydrite recrystallization (goethite and magnetite) (*246*).

Based on these studies as well as mechanistic studies that show redox driven dynamics between Fe(II) and Fe oxides, we have been compelled to explore the fate of metals during atom exchange between Fe(II) and goethite. We have explored the release of manganese (Mn) from goethite synthesized to have Mn-for-Fe substitution in the strucuture. We have also probed whether U is incorporated into goethite when the goethite is exposed to Fe(II) using both x-ray absorption spectroscopy (XANES and

EXAFS) as well as by measuring U and Fe release to solution during dissolution by acid. Finally, we have begun to develop a method for measuring Fe isotopes using a newly acquired Thermo X-Series 2 quadrupole-ICP-MS.

Experimental Approach

Mn-substituted Goethite

Manganese substituted goethite (Mn-goethite) was synthesized using a previously described procedure known to result in formation of Mn-substituted goethite (*161*). Briefly, goethites with Mn contents of 0.02 and 0.05 as Mn/(Mn+Fe) were synthesized to avoid the formation of Mn-Fe spinel phases at higher Mn contents (*161*). To make goethite with an Mn/(Mn+Fe) content of 0.02 (Mn2), 7.05 g $FeCl_3 \cdot 6H_2O$ and 0.105 g $MnCl_2 \cdot 4H_2O$ were mixed in 50 mL deionized water and 175 mL 2 M NaOH was added to precipitate the metals as a Mn-ferrihydrite gel. For a Mn/(Mn+Fe) content of 0.05 (Mn5) 0.262 g $MnCl_2 \cdot 4H_2O$ and 6.805 g $FeCl_3 \cdot 6H_2O$ were mixed together in 50 mL and 175 mL 2 M NaOH was added to precipitate the metals. The ferrihydrite gels were centrifuged and washed once and then resuspended in 0.3 M NaOH and heated at 60 °C for 15 days. The product was centrifuged and washed with deionized water 3 times and dried in the oven at 60 °C overnight. The dried product was ground and passed through a 150 µm sieve. The product was analyzed by powder x-ray diffraction using Co Kα radiation (Rigaku MiniFlex II), and found to be solely goethite with no detectable spinel phase. Work investigating Mn substitution in goethite suggests Mn is substituted as Mn(III) into the goethite structure (*247-249*).

The Mn-substituted goethite was reacted with Fe(II) to determine if Mn(III) could be reductively dissolved during redox reactions with Fe(II). Here duplicate reactors containing 15 mL of 25 mM HEPES (4-(2-Hydroxyethyl)piperazine-1-ethanesulfonic acid) buffer with 25 mM KBr electrolyte adjusted to pH 7.5 were spiked with 1 mM $FeCl_2$. The initial concentration of Fe(II) was measured, and 30 mg of Mn-goethite was

added to initiate the reaction. The loss of Fe(II) from solution and accumulation of Mn was measured over time up to 96 h. Controls without Fe(II) were done to determine if left over Mn(II) from synthesis could explain the Mn release. In addition, we added 5 M HCl to lower the pH of the suspension to a value of 2.0 to desorb any Fe(II) or Mn(II) at the end of the experiment. Fe(II) was measured colorimetrically using 1,10-phenanthroline (*139, 250*). Dissolved Mn was measured by modifying the formaldoxime method outlined in Morgan and Stumm (*251*) and Abel (*252*), using phenanthroline to complex interfering aqueous Fe.

Uranium Reaction with Goethite and Fe(II)

We have explored whether U is incorporated into goethite during redox interaction between Fe(II) and Fe(III) in goethite. We have reacted nominal concentrations of U^{VI} of 250 µM (uranyl acetate in 0.1 M HCl), with 1 and 2 g L^{-1} goethite in the presence of 1 mM Fe(II). Samples of 140 mL solution containing 4 mM $NaHCO_3$, 250 µM U^{VI}, and 1 mM Fe(II) were prepared and initial aliquots of solution were removed for Fe(II) and U analysis. To this solution 140 or 280 mg goethite or Al-substituted goethite was added and the pH was adjusted with KOH to a value near 7.50. A control was done without Fe(II). For the 1 g L^{-1} reactors, aqueous U and Fe(II) concentrations were measured as a function of time. The 0.5 M HCl extractable Fe(II) was measured for these reactors by mixing 0.1 mL of the suspension into 10 mL total 0.5 M HCl. In addition, 50 mM $NaHCO_3$ extractable U was measured in the same way. In the 2 g L^{-1} system a final aqueous Fe(II) and U measurement was taken at 17 hours. The 2 g L^{-1} reactors were sent to Argonne National Laboratory for x-ray absorption spectroscopic analysis of U valence state. A 1 g L^{-1} goethite reactor was sacrificed and extracted first with a 0.5 M HCl extraction, then subjected to complete dissolution with 6 M HCl. Uranium was measured in these experiments using ICP-MS (Thermo X-Series 2) by

following ^{238}U. Fe(II) and total Fe was measured using the 1,10-phenanthroline colorimetric method.

Isotope Exchange Experiments using Quadrupole-ICP-MS Measurements

We have begun to develop a method for measuring Fe isotopes with quadrupole-inductively coupled plasma-mass spectrometry (q-ICP-MS). The instrument is a Thermo X-Series 2 q-ICP-MS with a H_2/Ar collision cell capable of removing $^{40}Ar^{16}O$ interferences at mass 56 (^{56}Fe). A series of standards were prepared by adding isotopically enriched ^{57}Fe(II) (0.01 % ^{54}Fe, 0.96% ^{56}Fe, 97.82% ^{57}Fe, and 1.22% ^{58}Fe, Chemgas, Inc.) and ^{56}Fe(II) (99.77% ^{56}Fe) made by dissolving enriched Fe(0) 0.1 M HCl solutions to each other to achieve a range of isotope concentrations. These standards were used to evaluate whether ^{56}Fe and ^{57}Fe could be resolved from one another with the instrument and to see if quantitative recovery of known isotope compositions was possible. Mixtures were made with 90, 75, 50, 25, and 5% ^{56}Fe with the balance as ^{57}Fe, and recovery is compared with the expected value in Figure 6.6.

For isotope exchange experiments we have followed the experimental conditions of Handler et al. (*24*) to try and reproduce their data collected with high resolution multicollector ICP-MS (MC-ICP-MS). Briefly suspensions of 2 g L^{-1} natural isotopic composition goethite were made by suspending 30 mg goethite in 15 mL of 25 mM HEPES buffer with 25 mM KBr electrolyte. Prior to addition of the goethite a spike of Fe(II) highly enriched in ^{57}Fe was added to the solution to get a concentration of Fe(II) of 1 mM. An initial aliquot was withdrawn and acidified with trace metals grade HCl for later Fe(II) analysis with 1,10-phenanthroline and isotope analysis with q-ICP-MS. We also measured aqueous Fe isotopic composition and goethite isotopic composition with time. Aqueous Fe isotopes were measured by filtering an aliquot of solution (~100 mL) and acidifying it prior to analysis. Goethite isotopic composition was measured in two

ways, one way involved a 0.5 M HCl extraction of the whole solution to remove sorbed Fe(II), centrifugation to pellet the solids, followed by decanting of the supernatant prior to complete dissolution with concentrated HCl. In a second method, the solution containing Fe(II) and goethite was centrifugated and the pelleted goethite was dissolved in concentrated HCl without an 0.5 M HCl extraction.

We attempted to make samples for analysis on the q-ICP-MS such that the expected total Fe concentration would be around 30 ppb by addition of an aliquot of the sample to 10 mL of 0.1 M trace metals grade HCl. This concentration is below the threshold (~50-100 ppb) where the instrument detector mode switches from pulse counting to analog counting. Maintaining concentrations of Fe below the threshold of the detector mode ensures no detector cross calibration is necessary, which could add error to the measurements. However, the detector cross calibration routine was run to ensure measurements of concentrations could be made for other analytes of interest over a wider range (simultaneous determination of U in other experiments). We have also spiked an internal standard of ^{59}Co (100% natural abundance) at 10 ppb to track instrument drift with time. Isotopic fractions of the Fe isotopes were calculated by summing the total counts from the q-ICP-MS detector over ^{54}Fe, ^{56}Fe, and ^{57}Fe. We neglected ^{58}Fe due to its low concentration and potential for interference with ^{58}Ni (68.1% abundant).

Results and Discussion

Reductive Dissolution of Mn from Mn-Goethite by Fe(II)

We have investigated whether electron transfer between Fe(II) and Mn-substituted goethite might also cause reduction of Mn(III) in the goethite structure and dissolution of Mn(II) into solution. We have exposed goethites with Mn contents of 0.02 and 0.05 on a Mn/(Mn+Fe) basis (referred to as Mn2 and Mn5) to a 1.2 mM Fe(II) solution and measured the loss of Fe(II) from solution and the release of Mn (putatively Mn(II)) into solution (Figure 6.1). We found that Fe(II) uptake from solution is relatively

rapid over the first 4 hours, and continues to increase with time. In concert, Mn release to solution is very rapid, with the majority released to solution in the first 5 minutes of the experiment, but the concentration continues to rise with time out to 96 hours. Final concentrations after 96 hours were 60 µM and 107 µM Mn in the Mn2 and Mn5 reactors, respecitively. We observed no realease of Mn to solution in controls without Fe(II), suggesting that all Mn in the goethite structure is Mn(III) and released by reductive dissolution in the presence of Fe(II). The greater total uptake of Fe(II) from solution by the Mn5 goethite relative to the Mn2 goethite was consistent with a higher total amount of Mn added during the synthesis, if Fe(II) is oxidized by Mn(III). In addition, the Mn released to solution was greater in the Mn5 reactors than in the Mn2 reactors, again consistent with the higher amount of Mn substitution. However, we do not have surface area data for these two Mn-goethites, although visual inspection of the particles with SEM indicates similar sizes and morphologies. Surface area differences might also explain the observed release of Mn. Desorption of Mn and Fe(II) at pH 2.0 was done after 96 hours. In the Mn2 system, an extra 34 µM Mn was released by the desorption (94 µM Mn total), and in the Mn5 system, an extra 48 µM Mn was released (155 µM total). Fe(II) recovery was 810 and 635 µM in the Mn2 and Mn5 systems. This indicates that not all the added Fe(II) was recovered, and that Fe(II) lost was in excess of the amount of Mn released if Fe(II) reduced Mn(III) to Mn(II). We note under similar conditions that Fe(II) was recoverable in unsubstituted goethite suspensions even without acidification, but just by resuspending the goethite in a more dilute Fe(II) concentration (*20*).

We have shown that Mn is released from Mn-substituted goethite upon exposure of the goethite to aqueous Fe(II) and that Fe(II) appears to be irreversibly lost. Both of these lines of evidence suggest that net Fe(II) is oxidized to Fe(III) by Mn(III) in the structure of goethite, resulting in the reductive dissolution of Mn(II) from the goethite. Next, we have calculated whether the release of Mn to solution is just from the surface of goethite, or whether it occurs from the bulk of the particle due to redox driven Fe and Mn

atom exchange. We have used site densities reported by Villalobos et al. (*253*) for the (101) face, which comprises the majority of the goethite surface area, to calculate the surface Fe site concentration. We calculated that 12.1 Fe sites nm^{-2} are present on goethite (101) faces, and assume a goethite surface area of 30 m^2 g^{-1}. At 2 g L^{-1} solids loading this corresponds to 0.0012 moles surface Fe L^{-1}. Assuming congruent incorporation of Mn into the structure of goethite we arrive at a surface Mn concentration of 24 µmoles L^{-1} and 60 µmoles L^{-1} for the Mn2 and Mn5 samples respectively. In both cases, the amount of Mn dissolved at the end of the experiment corresponds to a release of Mn from approximately 3 monolayers of goethite.

Our observed release of Mn from goethite during redox induced atom exchange may have implications for the release of contaminants if they are incorporated into the goethite structure. While Mn is generally not considered to be a concerning contaminant, some evidence exists that suggests at elevated concentrations it could have deleterious effects to human health (*254*). Another metal that has been proposed to be substituted into goethite is Pb, which may be substituted as Pb(IV) in goethite (*255*). Pb(IV) substitution in goethite could be hypothesized to occur in pipe scale if a water distribution system contains both lead and iron distribution pipes. Reduction of Pb(IV) to Pb(II) by Fe(II) should be relatively facile ($E(PbO_2/Pb^{2+}$, pH 7.0) = 0.63 V) (*256*).

Reaction of Uranium with Fe(II) and Goethite

Uranium is rapidly removed from solution in the presence of 1 g L^{-1} goethite and 1 mM Fe(II) at pH 7.5. After 30 minutes, the aqueous U concentration drops from 217 µM to 0.12 µM (99.95% removal) (Figure 6.2). After 30 minutes nearly all (80%) of the U is recovered by 50 mM $NaHCO_3$ extraction, and the bicarbonate extractable U decreases to near 1 µM after 46 hours and stays at this level throughout the experiment, indicating that reduction of U may occur within 2 days. Similar results are seen for 0.5 M HCl extractable Fe(II), which decreases to 0.77 mM after 46 hours, and is constant over

time after this. Curiously, this 0.5 M HCl extractable Fe(II) concentration is higher than would be expected if all of the U^{VI} added to the system was reduced (0.58 mM is expected); however, caution must be taken in interpreting this result, as acidic conditions are expected to promote the oxidation of UO_2 by goethite (*257*). Aqueous Fe(II) concentrations also continue to drop with time out to 11 days, which would be unexpected if U^{VI} in the system was reduced after 2 days. After this period of time, an aliquot of concentrated HCl was added to make a 0.5 M HCl solution in the bottle and the solids were treated for 90 minutes. The 0.5 M HCl extracted concentration of U was measured to be 208 µM. This suspension was centrifuged and the solids were harvested and dissolved completely in 6 M HCl. U and Fe release was measured with time (Figure 6.3).

The results from the 6 M HCl extraction show that the U remaining after 0.5 M HCl extraction is immediately dissolved in 6 M HCl. This suggests the U is either in a separate phase that is easily dissolved in both 0.5 M HCl and 6 M HCl or sorbed onto the goethite. The U is not congruently incorporated into the goethite during Fe(II) induced atom exchange for the conditions studied here (1 g L^{-1} goethite and 1 mM Fe(II)). It is likely that U^{VI} was reduced to $U^{IV}O_2$ and thus not available for incorporation into the goethite.

In order to investigate whether U^{VI} is reduced by Fe(II) in the presence of goethite, we have used U-L_3 x-ray absorption spectroscopy to measure valence state (XANES) and the coordination environment of the U in the sample (EXAFS). In this set of experiments we explored whether Al-substitution in goethite (2Al, 4Al, and 10Al-Goethite described in Chapter 5) had any effect on reduction of U^{VI} by Fe(II). In these suspensions, we added 288 ± 4 µM U and after 17 hours the aqueous concentration U was reduced to 0.05 ± 0.03 µM (11 ± 6 ppb) in the Fe(II) containing suspensions, whereas U was only removed to 79 µM (19 ppm) in the 10Al-goethite control without Fe(II). The edge position of the control without Fe(II) in the XANES spectrum is near

that of the U^{VI} standard, and contains a post-edge feature indicative of U^{VI} in the uranyl (UO_2^{2+}) geometry (vertical arrow), indicating that all the U associated with the solid phase remained oxidized as U^{VI} (Figure 6.4). The edge position of the U XANES spectra of all the samples containing Fe(II) is near the U^{IV} standard, and lacks the post-edge feature indicative of U^{VI}, suggesting that nearly all of the added U has been reduced to U^{IV}. The EXAFS spectra of the goethite and Al-goethite reacted with U in the presence of Fe(II) indicate the reduced U product is consistent nanoparticulate uraninite ($U^{IV}O_2$) with a spectrum close to that of biogenically produced nanoparticulate uraninite (Figure 6.5) (*47*).

Formation of stable Fe(II) species on goethite (see discussion in Chapter 5) may have promoted U^{VI} reduction in the goethite + Fe(II) system. We note that in a study using insulating beads functionalized with carboxylate groups capable of binding U and Fe(II), that formation of Fe(II) polymers was required for the reduction of U^{VI} to U^{IV} (*111*). In contrast, some U^{VI} reduction has been noted in systems where Fe(II) concentrations were less than what would be expected to cause surface saturation of Fe(II). In addition, total Fe(II) loading in that system was less than that required to reduce all the added U^{VI} (*57*). Currently, we cannot conclude whether U^{VI} reduction might also be mediated by electron conduction through the bulk of goethite. Further study of this mechanism is warranted.

Isotope Exchange between Fe(II) and Goethite

We have begun to develop a method to measure isotope exchange between goethite and aqueous Fe(II) using a quadrupole-ICP-MS and highly enriched ^{57}Fe(II) solutions exposed to goethite with natural isotopic composition. We have started with determining whether ^{56}Fe and ^{57}Fe could be determined in mixtures using the q-ICP-MS using highly enriched isotope solutions (Figure 6.6). We have used spiked 2 g L^{-1} goethite suspensions with a natural abundance of Fe isotopes (5.8% ^{54}Fe, 91.8% ^{56}Fe,

2.1% ^{57}Fe, and 0.3% ^{58}Fe), with highly enriched (97.82%) ^{57}Fe(II) stock. We tracked the aqueous and solid phase ^{57}Fe fraction (denoted F, Equation 6.1) with time (Figure 6.7). We note that the ^{57}Fe content in the aqueous phase decreases and the ^{57}Fe content in the solids decreases. Over the ~12 days we followed the reaction we saw the goethite come to nearly complete mass balance of ^{57}Fe fraction in the solids of 0.058 to 0.061, whereas the aqueous phase did not, with ^{57}Fe fractions after 12 days of 0.31 to 0.36.

$$^{57}\text{Fe fraction} = \frac{^{57}\text{Fe}_{\text{counts}}}{^{54}\text{Fe}_{\text{counts}} + {}^{56}\text{Fe}_{\text{counts}} + {}^{57}\text{Fe}_{\text{counts}}} \quad (6.1)$$

$$^{57}\text{Fe fraction(system)}[\text{Fe}_{\text{total}}] = {}^{57}\text{Fe fraction(aq)}[\text{Fe(II)}] + {}^{57}\text{Fe fraction(s)}[\text{Fe}_{\text{goethite}}] \quad (6.2)$$

The difference between the aqueous phase ^{57}Fe fraction and the solid phase fraction indicates that we do not have mass recovery of ^{57}Fe in these systems. The most likely cause of this is the fact that aliquots of the goethite/Fe(II) suspension were removed with time. We note that Handler et al. set up many reactors in parallel and sacrificed them at each time point (*24*). This experimental method should be followed in further studies using the q-ICP-MS, but was not done here due to the exploratory nature of this work. While the lack of mass balance precludes any conclusions from this work, we note that the 10Al-goethite reacted with Fe(II) exchanged less ^{57}Fe between the aqueous and solid phase, suggesting that perhaps Al substitution in goethite has an effect on atom exchange between Fe(II) and goethite. Such a result would not be surprising considering that Al(III) is unlikely to dissolve from goethite during reduction in the absence of a ligand to promote its detachment (as is the case when dithionite-citrate-bicarbonate is used, as in Chapter 5). The presence of Al in goethite might make isotope exchange between Fe(II) and goethite in the environment quite variable, as Al contents of goethite in the environment are likely to vary significantly (*26*).

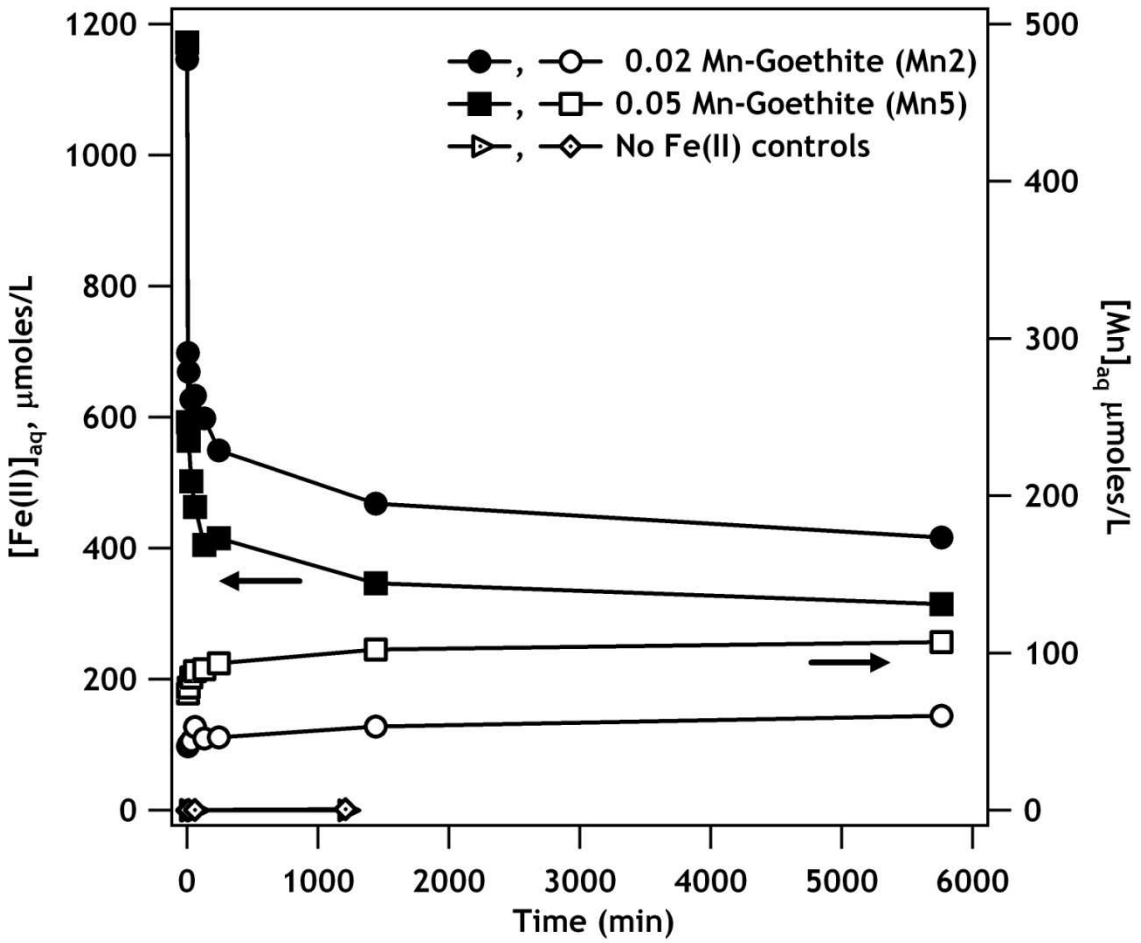

Figure 6.1. Loss of Fe(II) from solution (closed markers – left axis) and release of Mn into solution (open markers – right axis) when 2 g L^{-1} suspensions of Mn2 and Mn5-substituted goethites are exposed to 1.2 mM Fe(II). Controls without added Fe(II) are shown, and no Mn realease was observed.

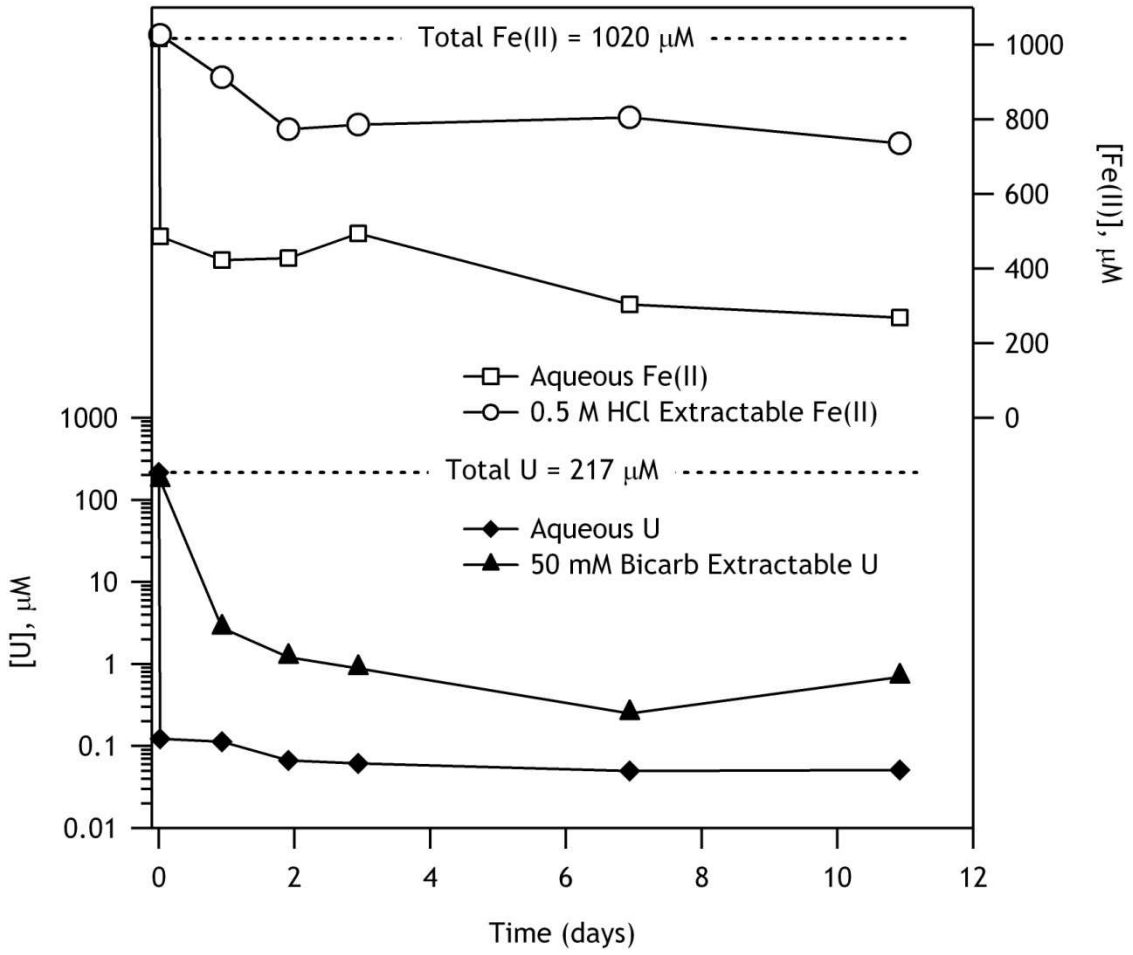

Figure 6.2. Measured aqueous concentrations of Fe(II) and U in a suspension of 217 μM U, 1 mM Fe(II), and 1 g L^{-1} goethite. In addition, 0.5 M HCl extractable Fe(II) and 50 mM bicarbonate extractable U were measured over 11 days.

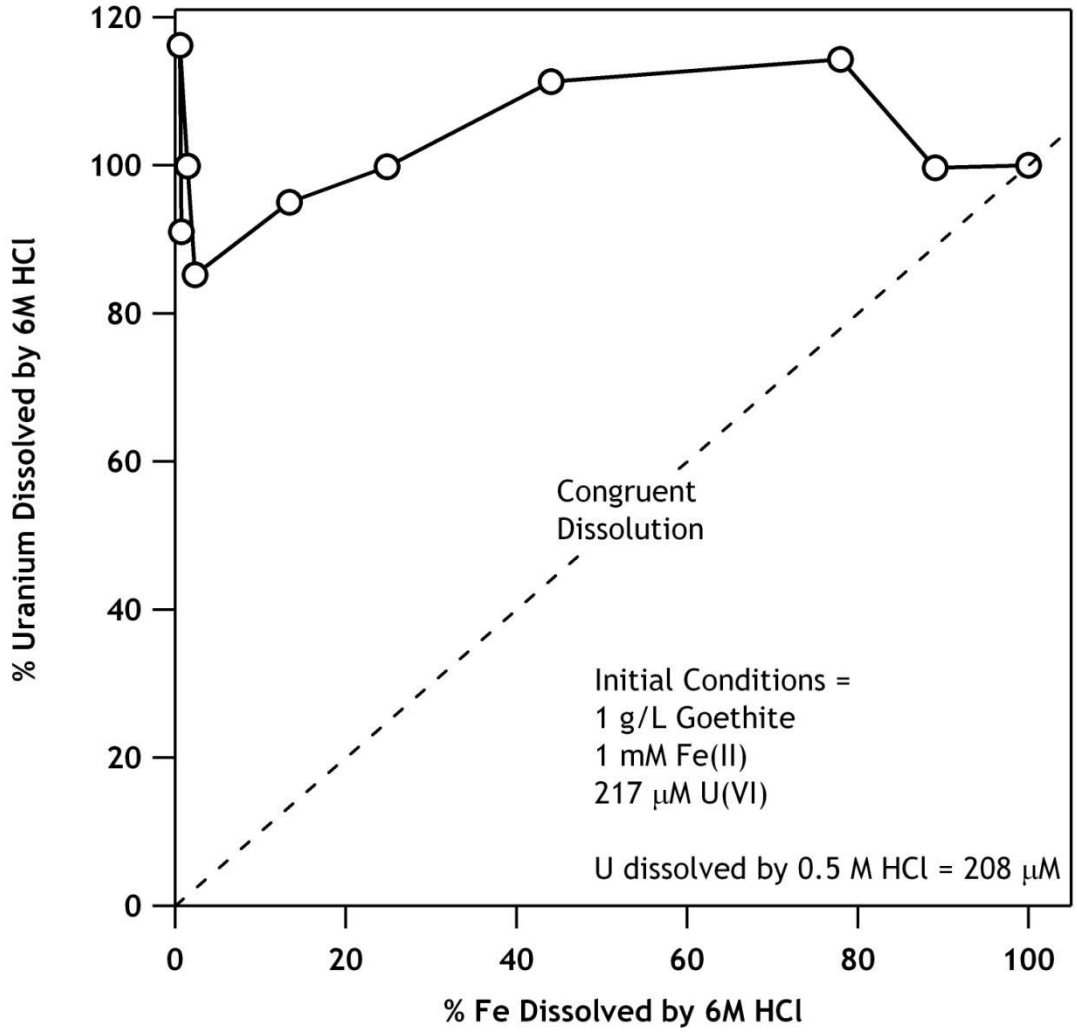

Figure 6.3. Dissolution of the remaining U associated with goethite after reaction with Fe(II) and 0.5 M HCl extraction. The solids were dissolved in 6 M HCl and the release of Fe and U were monitored with time. Dissolution along the dotted line would indicate that uranium was incorporated congruently into the goethite structure. All U remaining was either in a separate phase or associated with the surface.

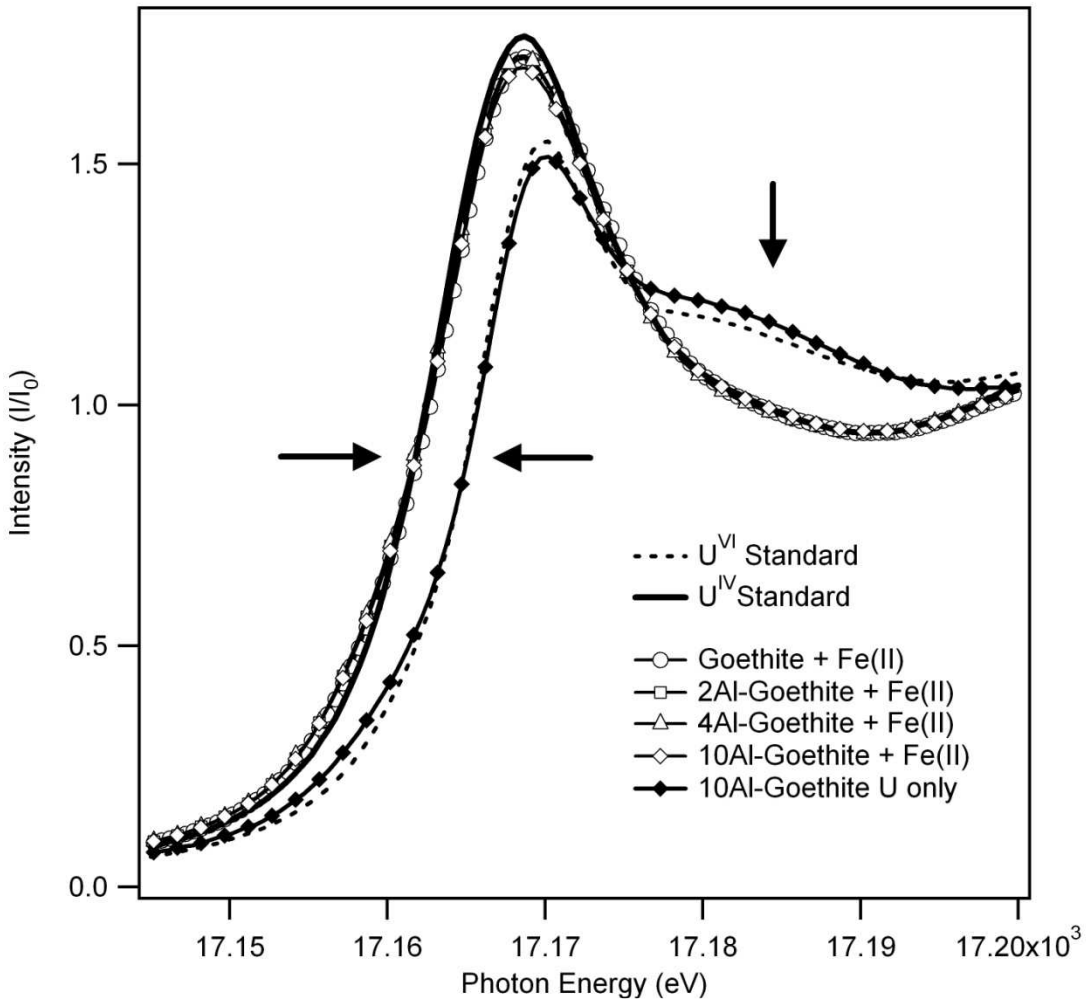

Figure 6.4. Uranium L_3 XANES spectra of U^{VI} reacted with goethite and Al-goethite in the presence of Fe(II). The horizontal arrows highlight the edge position, which is sensitive to U valence state with U^{IV} to the left and U^{VI} to the right. The vertical arrow points out the higher intensity post-edge feature for U^{VI} indicative of U in the uranyl (UO_2^{2+}) geometry. In all cases where Fe(II) is present U^{VI} is reduced to U^{IV}. U^{VI} remains in the 10Al-goethite sample without Fe(II).

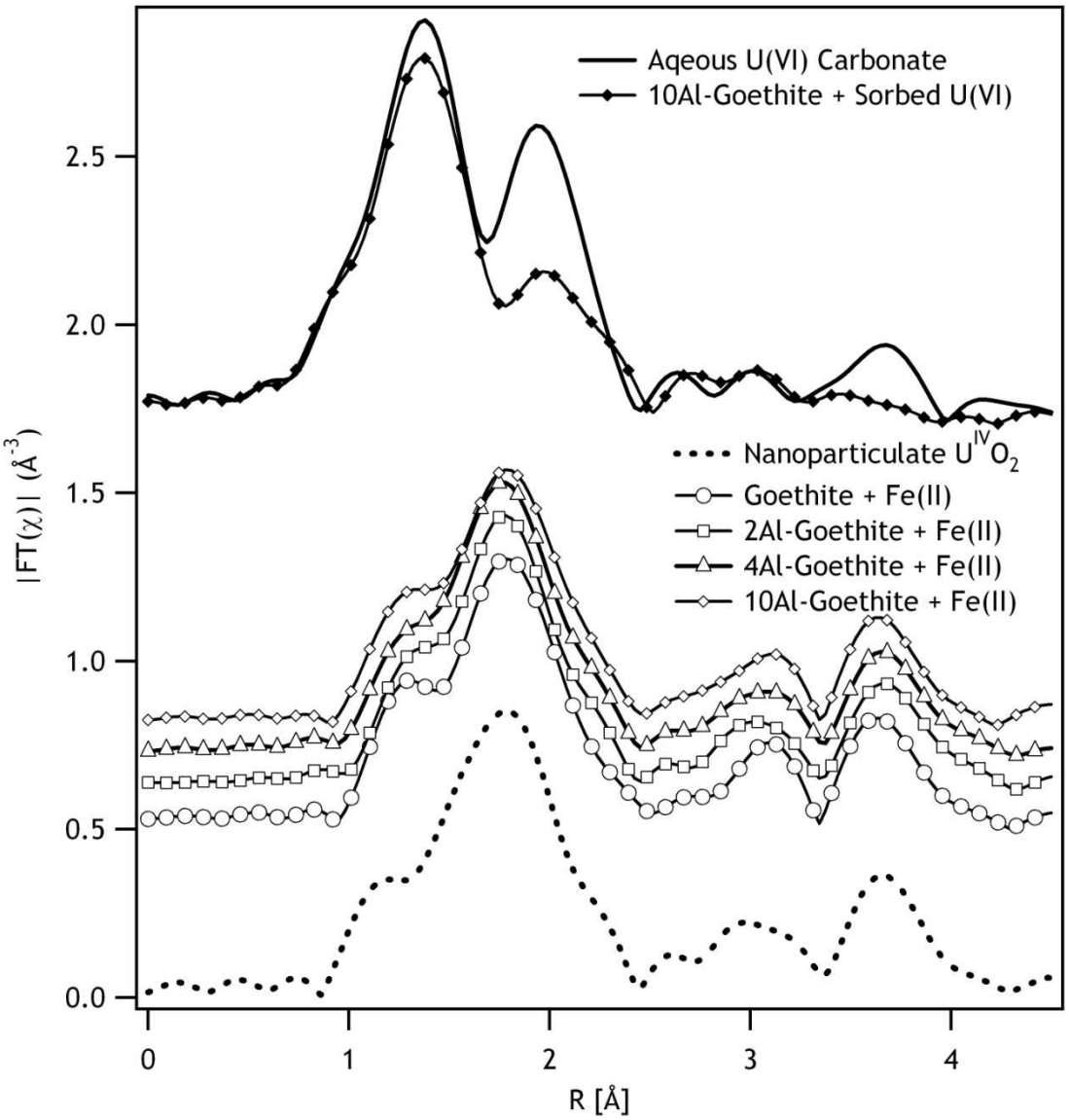

Figure 6.5. Uranium L_3 EXAFS spectra of U^{VI} reacted with goethite and Al-goethite in the presence of Fe(II). The EXAFS spectra of the U after reactions with Fe(II) and goethite are all consistent with a nanoparticulate $U^{IV}O_2$ (uraninite) product. The U^{VI} reacted with the 10Al-goethite control without Fe(II) is consistent with a uranyl species (UO_2^{2+}) sorbed to a Fe-O site on goethite.

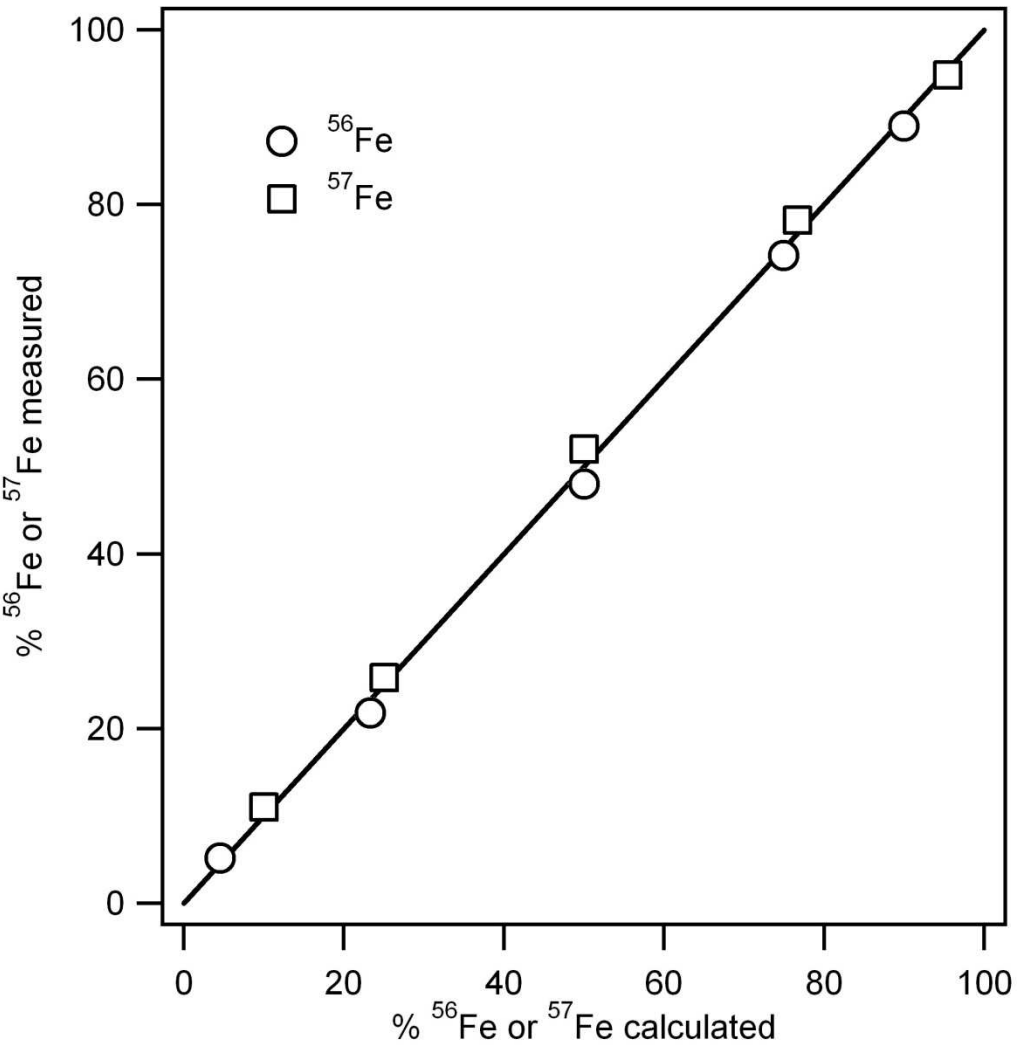

Figure 6.6. Plot showing agreement between ^{56}Fe and ^{57}Fe amounts added to several standards and their measured amounts with q-ICP-MS. The data suggest that ^{56}Fe and ^{57}Fe can be resolved from one another and quantified.

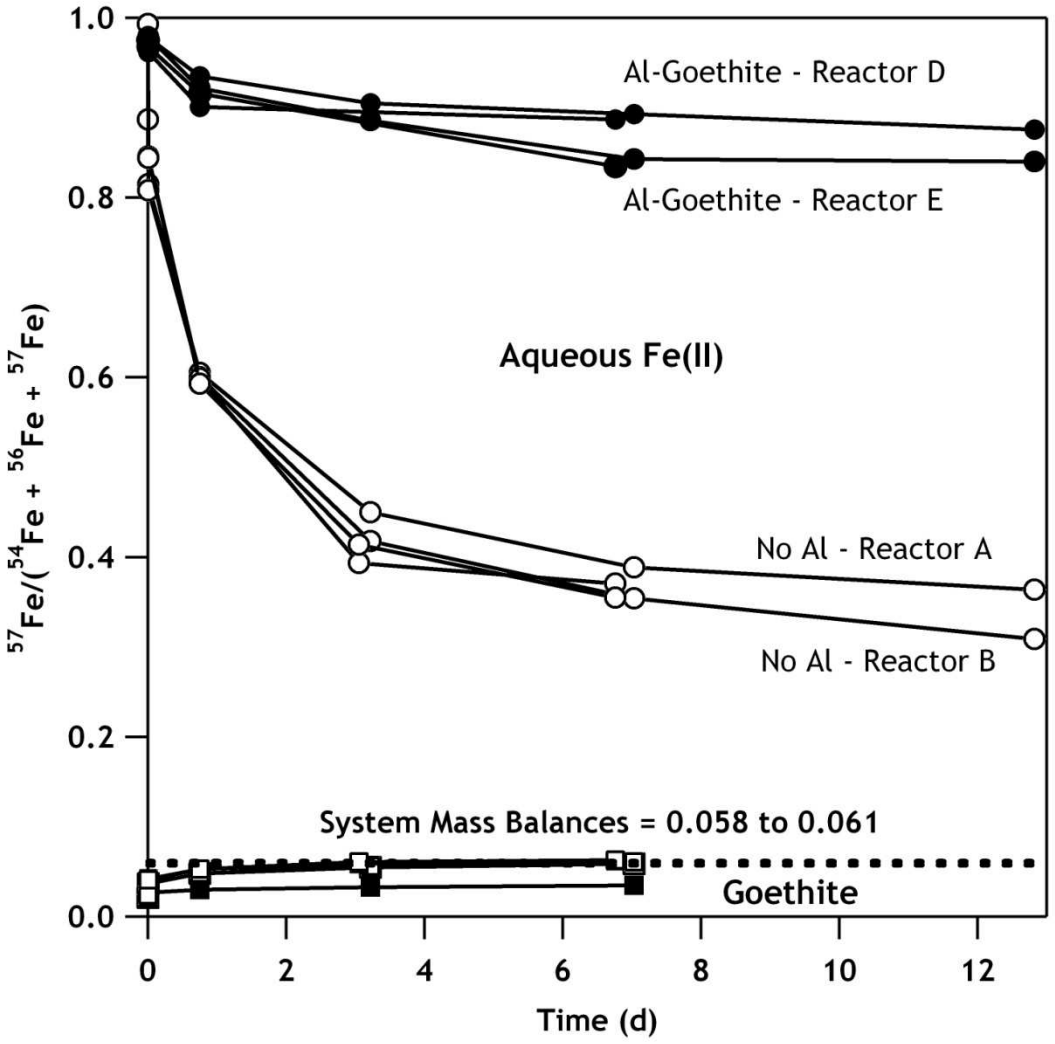

Figure 6.7. Measured ^{57}Fe fraction in the aqueous phase and goethite over time. The dashed line represents the mass balance of ^{57}Fe fraction in the system described in equation 6.2 in the text.

CHAPTER 7: ENGINEERING AND SCIENTIFIC SIGNIFICANCE

Summary

This work provides new evidence for the reactivity of iron minerals that have Fe(II) in their structure or have been exposed to Fe(II) in the aqueous phase. While the approach to all of the studies presented here has been reductionist in philosophy, we have used carefully selected and characterized systems to understand fundamental processes that occur between aqueous Fe(II), structural Fe(II), Fe oxides, and contaminants. This work provides compelling evidence to show that processes previously observed in the laboratory under minimal complexity are relevant in more complex biogeochemical systems.

In Chapter 2 we have provided evidence that green rusts are facile sorbents and reductants for U^{VI}, which is commonly found as a contaminant at U.S. Department of Energy sites where U was mined or refined. We have found that green rusts containing chloride, sulfate, and carbonate in their structure all reduce U^{VI} and that environmentally relevant carbonate concentrations do not greatly affect the reduction process. Because of their affinity for carbonate, green rusts are likely to be found with structural carbonate in most natural geochemical systems where dissimilatory metal reducing microbes use carbon as an electron donor and Fe oxides as electron acceptors. The chloride and sulfate forms of green rust may be important in engineered geological radioactive waste confinement settings, where sulfate or chloride containing brines may be present and in contact with corroding steel containment canisters. This work also provides a cautionary tale to future researchers on the importance of carefully selecting a buffer that does not complex the metal of interest, as TAPS was found to do with UO_2^{2+}.

Our work with a naturally reduced soil from Hedrick, Iowa, further indicates that abiotic reduction of U may be important under conditions where structural Fe(II) is present in the mineralogical matrix of soil or sediment. Our results appear to be the first

to demonstrate such an abiotic process in natural material. We have found that U is sequestered by soil as a mixture of reduced U^{IV}, oxidized uranyl U^{VI}, and U^{V} or U^{VI} in a non-uranyl coordination environment. The U^{IV} did not form uraninite nanoparticles, further indicating the diversity of U^{IV} products that might occur in natural sytems. Production of structural Fe(II) in soil and sediment minerals may serve as a long term redox buffer that allows for continued U reduction and removal from groundwater after biostimulation of microbial reduction is halted and microbial metabolism returns to background levels. In addition, we have circumstantial evidence that green rust is present as part of the Fe mineral assemblage in this soil. The presence of green rust is supported by wet chemical extraction and Mössbauer spectroscopy of both the reduced material and its behavior upon oxidation. Our work provides further validation that green rusts are an important part of the Fe biogeochemical cycle.

We have also shown that magnetite stochiometry is important to uranium reduction, with the redox properties of the magnetite that are influenced by the stoichiometry dictating whether U^{VI} is reduced by magnetite. Our work with U is consistent with the hypothesis that magnetite reducing power is capable of being recharged by aqueous Fe(II) (*132*). In the environment, magnetite may be regenerated by input of sufficient reducing power, such as aqueous Fe(II), or by microbial reduction making it a renewable reductant for various contaminants, like uranium.

Chapter 5 has evaluated whether electron transfer between sorbed Fe(II) and Fe(III) in Fe oxides occurs under more complex biogeochemical conditions relevant to natural aquifers and soils. We have used goethite due to its abundance in natural systems. This study indicates that interfacial Fe(II) to Fe(III) electron transfer occurs under a wide variety of conditions including when goethite has Al-for-Fe substitution in its structure, a phenomenon known to be common for goethite and many other iron oxides formed in low-temperature geochemical environments. We have also found that even when common aqueous anions like phosphate, silicate, carbonate, and natural organic matter

are present in solution and sorb onto goethite electron transfer between Fe(II) and goethite still occurs. At the concentrations of Fe(II) used in this study, there is evidence for the formation of a stable Fe(II) species sorbed on the surface or within the goethite. Electron transfer between Fe(II) and goethite was inhibited when we sorbed long-chain phospholipids to the surface of goethite, which potentially suggests other large macromolecules like extracellular polymeric substances produced by microbes might do the same. Such a mechanism might hinder or shut down Fe(II) to Fe oxide electron transfer in eutrophic biological systems where biofilms or high biomass densities occur.

Finally, we have begun to explore the implications of Fe(II)-Fe(III) interfacial electron transfer, as well as the redox driven conveyor belt of Fe atom exchange that it drives, on contaminant transformations. We have found it induces reductive dissolution and release of manganese (Mn) from Mn-substituted goethite, suggesting that atom exchange could potentially drive release of contaminant metals and metalloids like arsenic from Fe oxides. Under the conditions of this study, however, we found no incorporation of U into goethite, but rather that it was reduced by Fe(II), perhaps due to the formation of a stable Fe(II) phase associated with the goethite. We have also just begun to develop a method to use a newly acquired quadrupole-ICP-MS for tracking large (%) variations in aqueous and solid Fe isotope compositions during atom exchange, that allows this work to be done at The University of Iowa.

Recommendations for Future Work

Our finding that interfacial electron transfer between Fe(II) and Fe oxides occurs under a variety of more complex biogeochemical conditions, opens up many new and interesting avenues for research. First and foremost of these is: Do cation substitution and anion sorption in/on Fe oxides change whether Fe atom exchange occurs? Is the overall rate and extent of atom exchange influenced by structural cations other than Fe(III) and sorbed anions? For example, one might envision the presence of Al in an iron oxide

hindering the rate and extent of atom exchange, as the solubility of Al is low at near neutral pH. The detachment rate of Al from the oxide should be slower than that of Fe(II) (*206*); this would hinder dissolution Fe and Al from the bulk of the goethite particle. One might envision sorbed anions acting in either a similar way by blocking Fe detachment from the surface or by speeding it up by complexing Fe(II) and removing it from the surface. Fe atom exchange experiments will be important for answering these questions. Since atom exchange is likely driven by a thermodynamic potential difference between two sites, either at a distance as is the case for hematite (*22*), or possibly between near-neighbor sites, it is also worth considering whether changing Fe(II) concentrations change the rate of isotope exchange, or whether anionic ligands for Fe(II) or Fe(III) cause changes atom exchange rate/extent due to modification of redox potential. Studies probing atom exchange under advective flow conditions should also be explored, as we are interested in redox reactions occurring in groundwater.

We have begun to probe whether atom exchange between Fe(II) and Fe oxides influences contaminant cycling. Atom cycling can be envisioned to either promote release of contaminants (or environmentally benign elements) to a relatively pure aqueous phase, or sequester contaminants from a relatively contaminated aqueous phase. A better way to think of this is as a potentially dynamic equilibrium between contaminant X, Fe(II), and Fe oxide Y under the influence of a variety of geochemical parameters, including concentration of Fe(II), concentration of X, redox potential, pH, presence of ligands, and the Fe oxide. The downside is that this provides an infinite space to work in, and gives little predictive power. Conceptually, a model based on thermodynamic driving force would give more predictive power as to whether incorporation or release of X is to be expected. Here, the potential for X to be incorporated into the structure of an Fe oxide could be determined by the free energy gained by incorporation of X into the Fe oxide structure relative to it staying in solution or being sorbed. Recent work using *ab initio*

modeling, has been used to make a case that Tc(IV) may be incorporated into hematite based on calculated thermodynamics (*258*).

At this point, perhaps the best predictions for whether metals will be incorporated into Fe oxides during atom exchange may be those that can be incorporated congruently into the oxide structure during synthesis conditions. Of commonly studied contaminants, one that might be considered is Cr(VI), which is known to be reduced by Fe(II) in aqueous solution and the reaction is catalyzed by the presence of an oxide surface (*243*). Cr(III) is also known to substitute into the Fe oxide structure (*128, 161*) and to form Cr(III) substituted goethite after reduction of Cr(VI) by green rust (*259*).

Further work into the reactivity of common soil and sediment minerals containing structural Fe(II) with uranium could explain our results encountered with the soil samples reacted with U. Clay minerals containing structural Fe(II) may be responsible for the reduction of U in the soil and Fe(II) in clays could represent a fixed reductant that might not undergo reductive dissolution and mobilization during dissimilatory metal reduction. This Fe(II) could easily be regenerated. In addition, the Fe(II) content and the redox potential it imposes might also be important for contaminant reduction by clay minerals as it is for magnetite.

REFERENCES

1. Lloyd, J. R., Microbial reduction of metals and radionuclides. *Fems Microbiology Reviews* **2003,** 27, (2-3), 411-425.

2. Lack, J. G.; Chaudhuri, S. K.; Chakraborty, R.; Achenbach, L. A.; Coates, J. D., Anaerobic biooxidation of Fe(II) by Dechlorosoma suillum. *Microbial Ecology* **2002,** 43, (4), 424-431.

3. Murray, G. C.; Hesterberg, D., Iron and phosphate dissolution during abiotic reduction of ferrihydrite-boehmite mixtures. *Soil Science Society of America Journal* **2006,** 70, (4), 1318-1327.

4. Posth, N. R.; Hegler, F.; Konhauser, K. O.; Kappler, A., Alternating Si and Fe deposition caused by temperature fluctuations in Precambrian oceans. *Nature Geoscience* **2008,** 1, (10), 703-708.

5. Schaetzl, R.; Anderson, S., *Soils: Genesis and Geomorphology*. Cambridge University Press: Cambridge, UK, 2005; p 817.

6. Strathmann, T. J.; Stone, A. T., Mineral surface catalysis of reactions between Fe-II and oxime carbamate pesticides. *Geochimica Et Cosmochimica Acta* **2003,** 67, (15), 2775-2791.

7. Klausen, J.; Trober, S. P.; Haderlein, S. B.; Schwarzenbach, R. P., Reduction of substituted nitrobenzenes by Fe(II) in aqueous mineral suspensions. *Environmental Science and Technology* **1995,** 29, (9), 2396-2404.

8. Charlet, L.; Silvester, E.; Liger, E., N-compound reduction and actinide immobilisation in surficial fluids by Fe(II): the surface Fe(III)OFe(II)OH degrees species, as major reductant. *Chemical Geology* **1998,** 151, (1-4), 85-93.

9. Nano, G. V.; Strathmann, T. J., Ferrous iron sorption by hydrous metal oxides. *Journal of Colloid and Interface Science* **2006,** 297, (2), 443-454.

10. Dixit, S.; Hering, J. G., Sorption of Fe(II) and As(III) on goethite in single- and dual-sorbate systems. *Chemical Geology* **2006,** 228, (1-3), 6-15.

11. Hiemstra, T.; van Riemsdijk, W. H., Adsorption and surface oxidation of Fe(II) on metal (hydr)oxides. *Geochimica et Cosmochimica Acta* **2007,** 71, (24), 5913-5933.

12. Boclair, J. W.; Braterman, P. S., Layered double hydroxide stability. 1. Relative stabilities of layered double hydroxides and their simple counterparts. *Chemistry of Materials* **1999,** 11, (2), 298-302.

13. Delacaillerie, J. B. D.; Kermarec, M.; Clause, O., Impregnation of Gamma-Alumina with Ni(Ii) or Co(Ii) Ions at Neutral Ph - Hydrotalcite-Type Coprecipitate Formation and Characterization. *Journal of the American Chemical Society* **1995,** 117, (46), 11471-11481.

14. Tronc, E.; Belleville, P.; Jolivet, J. P.; Livage, J., Transformation of ferric hydroxide into spinel by Fe(II) adsorption. *Langmuir* **1992,** 8, (1), 313-319.

15. Tamura, Y.; Saturno, M.; Yamada, K.; Katsura, T., The Transformation of γ-FeOOH to Fe_3O_4 and Green Rust II in an Aqueous Solution. *Bulletin of the Chemical Society of Japan* **1984,** 57, (9), 2417-2421.

16. Hansel, C. M.; Benner, S. G.; Fendorf, S., Competing Fe(II)-induced mineralization pathways of ferrihydrite. *Environmental Science and Technology* **2005,** 39, 7147-7153.

17. Pedersen, H. D.; Postma, D.; Jakobsen, R.; Larsen, O., Fast transformation of iron oxyhydroxides by the catalytic action of aqueous Fe(II). *Geochimica Et Cosmochimica Acta* **2005,** 69, (16), 3967-3977.

18. Williams, A. G. B.; Scherer, M. M., Spectroscopic evidence for Fe(II)-Fe(III) electron transfer at the Fe oxide-water interface. *Environmental Science and Technology* **2004,** 38, (18), 4782-4790.

19. Larese-Casanova, P.; Scherer, M. M., Fe(II) sorption on hematite: New insights based on spectroscopic measurements. *Environmental Science & Technology* **2007,** 41, (2), 471-477.

20. Cwiertny, D. M.; Handler, R. M.; Schaefer, M. V.; Grassian, V. H.; Scherer, M. M., Interpreting nanoscale size-effects in aggregated Fe-oxide suspensions: reaction of Fe(II) with goethite. *Geochimica Et Cosmochimica Acta* **2008,** 72, (5), 1365-1380.

21. Silvester, E.; Charlet, L.; Tournassat, C.; Gehin, A.; Greneche, J.-M.; Liger, E., Redox potential measurements and Mössbauer spectrometry of Fe^{II} adsorbed onto Fe^{III} (oxyhdr)oxides. *Geochimica Et Cosmochimica Acta* **2005,** 69, (20), 4801-4815.

22. Yanina, S. V.; Rosso, K. M., Linked Reactivity at Mineral-Water Interfaces Through Bulk Crystal Conduction. *Science* **2008,** 320, (5873), 218-222.

23. Rosso, K. M.; Yanina, S. V.; Gorski, C. A.; Larese-Casanova, P.; Scherer, M. M., Connecting Observations of Hematite (alpha-Fe2O3) Growth Catalyzed by Fe(II). *Environmental Science & Technology* **2010,** 44, (1), 61-67.

24. Handler, R. M.; Beard, B. L.; Johnson, C. M.; Scherer, M. M., Atom exchange between aqueous Fe(II) and goethite: An Fe isotope tracer study. *Environmental Science & Technology* **2009,** 43 (4), 1102–1107.

25. Jang, J. H.; Mathur, R.; Liermann, L. J.; Ruebush, S.; Brantley, S. L., An iron isotope signature related to electron transfer between aqueous ferrous iron and goethite. *Chemical Geology* **2008,** 250, (1-4), 40-48.

26. Schwertmann, U.; Carlson, L., Aluminum Influence on Iron-Oxides .17. Unit-Cell Parameters and Aluminum Substitution of Natural Goethites. *Soil Science Society of America Journal* **1994,** 58, (1), 256-261.

27. Norrish, K.; Taylor, R. M., Isomorphous Replacement of Iron by Aluminium in Soil Goethites. *Journal of Soil Science* **1961,** 12, (2), 294-&.

28. Trolard, F.; Bourrie, G.; Jeanroy, E.; Herbillon, A. J.; Martin, H., Trace-Metals in Natural Iron-Oxides from Laterites - a Study Using Selective Kinetic Extraction. *Geochimica Et Cosmochimica Acta* **1995,** 59, (7), 1285-1297.

29. Weng, L. P.; Van Riemsdijk, W. H.; Koopal, L. K.; Hiemstra, T., Adsorption of humic substances on goethite: Comparison between humic acids and fulvic acids. *Environmental Science & Technology* **2006,** 40, (24), 7494-7500.

30. Villalobos, M.; Trotz, M. A.; Leckie, J. O., Variability in goethite surface site density: evidence from proton and carbonate sorption. *Journal of Colloid and Interface Science* **2003,** 268, (2), 273-287.

31. Hiemstra, T.; Barnett, M. O.; van Riemsdijk, W. H., Interaction of silicic acid with goethite. *Journal of Colloid and Interface Science* **2007,** 310, (1), 8-17.

32. Strauss, R.; Brummer, G. W.; Barrow, N. J., Effects of crystallinity of goethite .2. Rates of sorption and desorption of phosphate. *European Journal of Soil Science* **1997,** 48, (1), 101-114.

33. Parfitt, R. L.; Atkinson, R. J., Phosphate Adsorption on Goethite (Alpha-FeOOH). *Nature* **1976,** 264, (5588), 740-742.

34. Stachowicz, M.; Hiemstra, T.; van Riemsdijk, W. H., Multi-competitive interaction of As(III) and As(V) oxyanions with Ca2+, Mg2+, PO43-, and CO32- ions on goethite. *Journal of Colloid and Interface Science* **2008,** 320, (2), 400-414.

35. Garrett, R. G., Relative spatial soil geochemical variability along two transects across the United States and Canada. *Applied Geochemistry* **2009,** 24, (8), 1405-1415.

36. Ahearne, J. F., Radioactive waste: The size of the problem. *Physics Today* **1997,** 50, (6), 24-29.

37. Gavrilescu, M.; Pavel, L. V.; Cretescu, I., Characterization and remediation of soils contaminated with uranium. *Journal of Hazardous Materials* **2009,** 163, (2-3), 475-510.

38. Langmuir, D., Uranium solution-mineral equilibria at low temperatures with applications to sedimantary ore deposits. *Geochimica et Cosmochimica Acta* **1978,** 42, (6), 547-569.

39. Grenthe, I.; Ferri, D.; Salvatore, F.; Riccio, G., Studies on Metal Carbonate Equilibria .10. a Solubility Study of the Complex-Formation in the Uranium(Vi) Water Carbon-Dioxide (G) System at 25-Degrees-C. *Journal of the Chemical Society-Dalton Transactions* **1984**, (11), 2439-2443.

40. Barnett, M. O.; Jardine, P. M.; Brooks, S. C., U(VI) Adsorption to Heterogeneous Subsurface Media:â€‰ Application of a Surface Complexation Model. *Environmental Science & Technology* **2002,** 36, (5), 937-942.

41. Hiemstra, T.; Van Riemsdijk, W. H.; Rossberg, A.; Ulrich, K. U., A surface structural model for ferrihydrite II: Adsorption of uranyl and carbonate. *Geochimica Et Cosmochimica Acta* **2009,** 73, (15), 4437-4451.

42. Wazne, M.; Korfiatis, G.; Meng, X., Carbonate effects of hexavalent uranium adsoprtion by iron oxyhydroxide. *Environmental Science and Techonology* **2003,** 37, 3619-3624.

43. Wu, W. M.; Carley, J.; Gentry, T.; Ginder-Vogel, M. A.; Fienen, M.; Mehlhorn, T.; Yan, H.; Caroll, S.; Pace, M. N.; Nyman, J.; Luo, J.; Gentile, M. E.; Fields, M. W.; Hickey, R. F.; Gu, B. H.; Watson, D.; Cirpka, O. A.; Zhou, J. Z.; Fendorf, S.; Kitanidis, P. K.; Jardine, P. M.; Criddle, C. S., Pilot-scale in situ bioremedation of uranium in a highly contaminated aquifer. 2. Reduction of U(VI) and geochemical control of U(VI) bioavailability. *Environmental Science & Technology* **2006,** 40, (12), 3986-3995.

44. Qafoku, N. P.; Kukkadapu, R. K.; McKinley, J. P.; Arey, B. W.; Kelly, S. D.; Wang, C. M.; Resch, C. T.; Long, P. E., Uranium in Framboidal Pyrite from a Naturally Bioreduced Alluvial Sediment. *Environmental Science & Technology* **2009,** 43, (22), 8528-8534.

45. Kelly, S. D.; Kemner, K. M.; Carley, J.; Criddle, C.; Jardine, P. M.; Marsh, T. L.; Phillips, D.; Watson, D.; Wu, W. M., Speciation of uranium in sediments before and after in situ biostimulation. *Environmental Science & Technology* **2008,** 42, (5), 1558-1564.

46. Ulrich, K. U.; Singh, A.; Schofield, E. J.; Bargar, J. R.; Veeramani, H.; Sharp, J. O.; Bernier-Latmani, R.; Giammar, D. E., Dissolution of biogenic and synthetic UO2 under varied reducing conditions. *Environmental Science & Technology* **2008,** 42, (15), 5600-5606.

47. Burgos, W. D.; McDonough, J. T.; Senko, J. M.; Zhang, G. X.; Dohnalkova, A. C.; Kelly, S. D.; Gorby, Y.; Kemner, K. M., Characterization of uraninite nanoparticles produced by Shewanella oneidensis MR-1. *Geochimica Et Cosmochimica Acta* **2008,** 72, (20), 4901-4915.

48. Suzuki, Y.; Kelly, S. D.; Kemner, K. M.; Banfield, J. F., Radionuclide contamination - Nanometre-size products of uranium bioreduction. *Nature* **2002,** 419, (6903), 134-134.

49. Fletcher, K. E.; Boyanov, M. I.; Thomas, S. H.; Wu, Q. Z.; Kemner, K. M.; Loffler, F. E., U(VI) Reduction to Mononuclear U(IV) by Desulfitobacterium Species. *Environmental Science & Technology* **2010,** 44, (12), 4705-4709.

50. Lovley, D. R.; Stolz, J. F.; Gordon, L. N.; Phillips, E. J. P., Anaerobic production of magnetite by dissimilatory iron-reducing microarganism. *Nature* **1987,** 330, 252-254.

51. Kostka, J. E.; Stucki, J. W.; Nealson, K. H.; Wu, J., Reduction of structural Fe(III) in smectite by a pure culture of Shewanella putrefaciens strain MR-1. *Clays and Clay Minerals* **1996,** 44, (4), 522-529.

52. Fredrickson, J. K.; Zachara, J. M.; Kennedy, D. W.; Dong, H. L.; Onstott, T. C.; Hinman, N. W.; Li, S. M., Biogenic iron mineralization accompanying the dissimilatory reduction of hydrous ferric oxide by a groundwater bacterium. *Geochimica Et Cosmochimica Acta* **1998,** 62, (19-20), 3239-3257.

53. O'Loughlin, E. J.; Larese-Casanova, P.; Scherer, M.; Cook, R., Green rust formation from the bioreduction of gamma-FeOOH (lepidocrocite): Comparison of several Shewanella species. *Geomicrobiology Journal* **2007,** 24, (3-4), 211-230.

54. O'Loughlin, E. J.; Kelly, S. D.; Kemner, K. M., XAFS Investigation of the Interactions of U-VI with Secondary Mineralization Products from the Bioreduction of Fe-III Oxides. *Environmental Science & Technology* **2010,** 44, (5), 1656-1661.

55. Regenspurg, S.; Schild, D.; Schafer, T.; Huber, F.; Malmstrom, M. E., Removal of uranium(VI) from the aqueous phase by iron(II) minerals in presence of bicarbonate. *Applied Geochemistry* **2009,** 24, (9), 1617-1625.

56. Chakraborty, S.; Favre, F.; Banerjee, D.; Scheinost, A. C.; Mullet, M.; Ehrhardt, J.-J.; Brendle, J.; Vidal, L. c.; Charlet, L., U(VI) Sorption and Reduction by Fe(II) Sorbed on Montmorillonite. *Environmental Science & Technology* **2010,** 44, (10), 3779-3785.

57. Fredrickson, J. K.; Zachara, J. M.; Kennedy, D. W.; Duff, M. C.; Gorby, Y. A.; Li, S. M. W.; Krupka, K. M., Reduction of U(VI) in goethite (alpha-FeOOH) suspensions by a dissimilatory metal-reducing bacterium. *Geochimica Et Cosmochimica Acta* **2000,** 64, (18), 3085-3098.

58. Jeon, B. H.; Dempsey, B. A.; Burgos, W. D.; Barnett, M. O.; Roden, E. E., Chemical reduction of U(VI) by Fe(II) at the solid-water interface using natural and synthetic Fe(III) oxides. *Environmental Science & Technology* **2005,** 39, (15), 5642-5649.

59. Behrends, T.; Van Cappellen, P., Competition between enzymatic and abiotic reduction of uranium(VI) under iron reducing conditions. *Chemical Geology* **2005,** 220, (3-4), 315-327.

60. Jang, J.-H.; Dempsey, B. A.; Burgos, W. D., Reduction of U(VI) by Fe(II) in the presence of hydrous ferric oxide and hematite: Effects of solid transformation, surface coverage, and humic acid. *Water Research* **2008,** 42, (8-9), 2269-2277.

61. O'Loughlin, E. J.; Kelly, S. D.; Cook, R. E.; Csencsits, R.; Kemner, K. M., Reduction of uranium(VI) by mixed iron(II)/iron(III) hydroxide (green rust): Formation of UO_2 nanoparticies. *Environmental Science & Technology* **2003,** 37, (4), 721-727.

62. Scott, T. B.; Allen, G. C.; Heard, P. J.; Randell, M. G., Reduction of U(VI) to U(IV) on the surface of magnetite. *Geochimica Et Cosmochimica Acta* **2005,** 69, (24), 5639-5646.

63. Senko, J. M.; Istok, J. D.; Suflita, J. M.; Krumholz, L. R., In-Situ Evidence for Uranium Immobilization and Remobilization. *Environmental Science & Technology* **2002,** 36, (7), 1491-1496.

64. N'Guessan, A. L.; Vrionis, H. A.; Resch, C. T.; Long, P. E.; Lovley, D. R., Sustained removal of uranium from contaminated groundwater following stimulation of dissimilatory metal reduction. *Environmental Science & Technology* **2008,** 42, (8), 2999-3004.

65. Finneran, K. T.; Anderson, R. T.; Nevin, K. P.; Lovley, D. R., Potential for Bioremediation of uranium-contaminated aquifers with microbial U(VI) reduction. *Soil & Sediment Contamination* **2002,** 11, (3), 339-357.

66. Gorski, C. A.; Nurmi, J. T.; Tratnyek, P. G.; Hofstetter, T. B.; Scherer, M. M., Redox Behavior of Magnetite: Implications for Contaminant Reduction. *Environmental Science & Technology* **2010,** 44, (1), 55-60.

67. Lustig, H., The Mossbauer Effect. *American Journal of Physics* **1961,** 29, (1), 1-18.

68. Dyar, M. D.; Agresti, D. G.; Schaefer, M. W.; Grant, C. A.; Sklute, E. C., Mossbauer Spectroscopy of Earth and Planetary Elements. *Annual Review of Earth and Planetary Sciences* **2006,** 34, 83-125.

69. Long, G. J., *Mossbauer Spectroscopy Applied to Inorganic Chemistry*. Plenum Press: New York, 1984; Vol. 1.

70. Rancourt, D. G., Mossbauer spectroscopy in clay science. *Hyperfine Interactions* **1998,** 117, 3-38.

71. Evans, R. J.; Rancourt, D. G.; Grodzicki, M., Hyperfine electric field gradients and local distortion environments of octahedrally coordinated Fe2+. *American Mineralogist* **2005,** 90, (1), 187-198.

72. Evans, R. J.; Rancourt, D. G.; Grodzicki, M., Hyperfine electric field gradient tensors at Fe2+ sites in octahedral layers: Toward understanding oriented single-crystal Moessbauer spectroscopy measurements of micas. *American Mineralogist* **2005,** 90, (10), 1540-1555.

73. Rancourt, D. G.; Ping, J. Y., Voight-based methods for arbitrary-shape static hyperfine parameter distributions in Mössbauer spectroscopy. *Nuclear Instruments and Methods in Physics Research* **1991,** B58, 85-97.

74. Koningsberger, D. C.; Prins, R., *X-Ray Absorption: Principles, Applications, Techniques of EXAFS, SEXAFS and XANES*. John Wiley & Sons: New York, 1988; Vol. 92, p 673.

75. Denecke, M. A., Actinide speciation using X-ray absorption fine structure spectroscopy. *Coordination Chemistry Reviews* **2006,** 250, (7-8), 730-754.

76. Taylor, R. M., Formation And Properties Of Fe(II)-Fe(III) Hydroxy-Carbonate And Its Possible Significance In Soil Formation. *Clay Minerals* **1980,** 15, (4), 369-382.

77. Taylor, R. M.; McKenzie, R. M., The influence of aluminum on iron oxides. VI. The formation of Fe(II)-Al(III) hydroxy-chlorides, -sulfates, and -carbonates as new members of the pyroaurite group and their significance in soils. *Clays and Clay Min.* **1980,** 28, (3), 179-187.

78. Koch, C. B., Structures and properties of anionic clay minerals. *Hyperfine Interactions* **1998,** 117, (1-4), 131-157.

79. Evans, D. G.; Slade, R. C. T., Structural aspects of layered double hydroxides. In *Layered Double Hydroxides*, 2006; Vol. 119, pp 1-87.

80. Refait, P.; Drissi, S. H.; Pytkiewicz, J.; Genin, J.-M. R., The anioic species competition in iron aqueous corrosion: Role of various green rust compounds. *Corrosion Science* **1997,** 39, (9), 1699-1710.

81. Génin, J. M. R.; Dhouibi, L.; Refait, P.; Abdelmoula, M.; Triki, E., Influence of phosphate on corrosion products of iron in chloride-polluted-concrete-simulating solutions: Ferrihydrite vs green rust. *Corrosion Science* **2002,** 58, (6), 467-478.

82. Hansel, C. M.; Benner, S. G.; Neiss, J.; Dohnalkova, A.; Kukkadapu, R.; Fendorf, S., Secondary mineralization pathways induced by dissmilatory iron reduction of ferrihydrate under advective flow. *Geochimica et Cosmochimica Acta* **2003,** 67, (16), 2977-2992.

83. Chevrier, V.; Mathe, P. E.; Rochette, P.; Grauby, O.; Bourrie, G.; Trolard, F., Iron weathering products in a CO2+(H2O or H2O2) atmosphere: Implications for weathering processes on the surface of Mars. *Geochimica Et Cosmochimica Acta* **2006,** 70, (16), 4295-4317.

84. Kuma, K.; Paplawsky, W.; Gedulin, B.; Arrhenius, G., Mixed-Valence Hydroxides As Bioorganic Host Minerals. *Origins Of Life And Evolution Of The Biosphere* **1989,** 19, (6), 573-602.

85. Williams, A. G. B.; Scherer, M. M., Kinetics of Cr(VI) reduction by carbonate green rust. *Environmental Science & Technology* **2001,** 35, (17), 3488-3494.

86. Chun, C. L.; Hozalski, R. M.; Arnold, W. A., Degradation of disinfection byproducts by carbonate green rust. *Environmental Science & Technology* **2007,** 41, (5), 1615-1621.

87. Hansen, H. C. B.; Koch, C. B.; Nancke-Kroge, H.; Borggaard, O. K.; Sørensen, J., Abiotic nitrate reduction to ammonium: key role of green rust. *Environmental Science & Technology* **1996,** 30, 2053-2056.

88. Myneni, S. C. B.; Tokunaga, T. K.; Brown, G. E., Jr., Abiotic selenium redox transformations in the presence of Fe(II,III) oxides. *Science* **1997,** 278, 1106-1109.

89. Larese-Casanova, P.; Scherer, M. M., Abiotic transformation of hexahydro-1,3,5-trinitro-1,3,5-triazine (RDX) by green rusts. *Environmental Science & Technology* **2008,** 42, (11), 3975-3981.

90. Abdelmoula, M.; Trolard, F.; Bourrie, G.; Genin, J. M. R., Evidence for the Fe(II)-Fe(III) Green Rust "Fougerite" mineral occurrence in a hydromorphic soil and its transformation with depth. *Hyperfine Interactions* **1998,** 112, (1-4), 235-238.

91. Genin, J.-M. R.; Bourrie, G.; Herbillon, A.; Abdelmoula, M.; Jaffrezic, A.; Refait, P.; Maitre, V.; Humbert, B.; Herbillon, A., Thermodynamic equilibria in aqueous suspensions of synthetic and natural Fe(ll)-Fe(lll) green rusts: Occurrences of the mineral in hydromorphic soils. *Environmental Science and Technology* **1998,** 32, (8), 1058-1068.

92. Genin, J. M. R.; Aissa, R.; Gehin, A.; Abdelmoula, M.; Benali, O.; Ernstsen, V.; Ona-Nguema, G.; Upadhyay, C.; Ruby, C., Fougerite and FeII-III hydroxycarbonate green rust; ordering drprotonation and/or cation substitution; structure of hydrotalcite-like compounds and mythic ferrosic hydroxide Fe(OH)((2+x)). *Solid State Sciences* **2005,** 7, (5), 545-572.

93. Genin, J. M. R.; Refait, P.; Olowe, A. A.; Abdelmoula, M.; Fall, I.; Drissi, S. H., Identification of green rust compounds in the aqueous corrosion processes of steels; the case of microbially induced corrosion and use of 78 K CEMS. *Hyperine Interactions* **1998,** 112, (1-4), 47-50.

94. Fredrickson, J. K.; Kota, S.; Kukkadapu, R. K.; Liu, C. X.; Zachara, J. M., Influence of electron donor/acceptor concentrations on hydrous ferric oxide (HFO) bioreduction. *Biodegradation* **2003,** 14, (2), 91-103.

95. Kukkadapu, R. K.; Zachara, J. M.; Fredrickson, J. K.; Kennedy, D. W., Biotransformation of two-line silica-ferrihydrite by a dissimilatory Fe(III)-reducing bacterium: Formation of carbonate green rust in the presence of phosphate. *Geochimica Et Cosmochimica Acta* **2004,** 68, (13), 2799-2814.

96. Ona-Nguema, G.; Carteret, C.; Benali, O.; Abdelmoula, M.; Genin, J. M. R.; Jorand, F., Competitive formation of hydroxycarbonate green rust 1 versus hydroxysulphate green rust 2 in *Shewanella putrefaciens* cultures. *Geomicrobiology Journal* **2004,** 21, (2), 79-90.

97. Ona-Nguema, G.; Abdelmoula, M.; Jorand, F.; Benali, O.; Gehin, A.; Block, J. C.; Genin, J. M. R., Iron(II,III) hydroxycarbonate green rust formation and stabilization from lepidocrocite bioreduction. *Environmental Science & Technology* **2002,** 36, (1), 16-20.

98. Chaudhuri, S. K.; Lack, J. G.; Coates, J. D., Biogenic magnetite formation through anaerobic biooxidation of Fe(II). *Applied and Environmental Microbiology* **2001,** 67, (6), 2844-8.

99. Cui, D. Q.; Spahiu, K., The reduction of U(VI) on corroded iron under anoxic conditions. *Radiochimica Acta* **2002,** 90, (9-11), 623-628.

100. Bond, D. L.; Fendorf, S., Kinetics and Structural Constraints of Chromate Reduction by Green Rusts. *Environmental Science & Technology* **2003,** 37, (12), 2750-2757.

101. Morris, D. E., Redox energetics and kinetics of uranyl coordination complexes in aqueous solution. *Inorganic Chemistry* **2002,** 41, (13), 3542-3547.

102. Genin, J. M. R.; Ruby, C.; Upadhyay, C., Structure and thermodynamics of ferrous, stoichiometric and ferric oxyhydroxycarbonate green rusts; redox flexibility and fougerite mineral. *Solid State Sciences* **2006,** 8, (11), 1330-1343.

103. Bocher, F.; Gehin, A.; Ruby, C.; Ghanbaja, J.; Abdelmoula, M.; Genin, J. M. R., Coprecipitation of Fe(II-III) hydroxycarbonate green rust stabilised by phosphate adsorption. *Solid State Sciences* **2004,** 6, 117-124.

104. Ferreira, O. P.; Alves, O. L.; Gouveia, D. X.; Souza, A. G.; de Paiva, J. A. C.; Mendes, J., Thermal decomposition and structural reconstruction effect on Mg-Fe-based hydrotalcite compounds. *Journal of Solid State Chemistry* **2004,** 177, (9), 3058-3069.

105. Hansen, H. C. B.; Koch, C. B., Synthesis and Characterization of Pyroaurite. *Applied Clay Science* **1995,** 10, (1-2), 5-19.

106. Hansen, H. C. B., Composition, stabilization, and light-absorption of Fe(II)Fe(III) hydroxy-carbonate (green rust). *Clay Minerals* **1989,** 24, (4), 663-669.

107. Gustafsson, J. P. *Visual MINTEQ*, 2.51; 2006.

108. Teixeira, L. S. G.; Costa, A. C. S.; Ferreira, S. L. C.; Freitas, M. D.; de Carvalho, M. S., Spectrophotometric determination of uranium using 2-(2-thiazolylazo)-p-cresol (TAC) in the presence of surfactants. *Journal of the Brazilian Chemical Society* **1999,** 10, (6), 519-522.

109. Hua, B.; Xu, H. F.; Terry, J.; Deng, B. L., Kinetics of uranium(VI) reduction by hydrogen sulfide in anoxic aqueous systems. *Environmental Science & Technology* **2006,** 40, (15), 4666-4671.

110. Debeer, H.; Coetzee, P. P., Ion Chromatographic Separation and Spectrophotometric Determination of U(Iv) and U(Vi). *Radiochimica Acta* **1992,** 57, (2-3), 113-117.

111. Boyanov, M. I.; O'Loughlin, E. J.; Roden, E. E.; Fein, J. B.; Kemner, K. M., Adsorption of Fe(II) and U(VI) to carboxyl-functionalized microspheres: The influence of speciation on uranyl reduction studied by titration and XAFS. *Geochimica Et Cosmochimica Acta* **2007,** 71, (8), 1898-1912.

112. Kelly, S. D.; Kemner, K. M.; Fein, J. B.; Fowle, D. A.; Boyanov, M. I.; Bunker, B. A.; Yee, N., X-ray absorption fine structure determination of pH-dependent U-bacterial cell wall interactions. *Geochimica Et Cosmochimica Acta* **2002,** 66, (22), 3855-3871.

113. Webb, S. M., SIXpack: a graphical user interface for XAS analysis using IFEFFIT. *Physica Scripta* **2005,** T115, 1011-1014.

114. Hansen, H. C. B.; Guldberg, S.; Erbs, M.; Koch, C. B., Kinetics of nitrate reduction by green rusts - effects of interlayer anion and Fe(II):Fe(III) ratio. *Applied Clay Science* **2001,** 18, 81-91.

115. Lazaridis, N. K.; Asouhidou, D. D., Kinetics of sorptive removal of chromium(VI) from aqueous solutions by calcined Mg-Al-CO3 hydrotalcite. *Water Research* **2003,** 37, (12), 2875-2882.

116. Litten, G. R., Quality of ground water used for selected municipal water supplies in Iowa, 1997-2002 water years: USGS Open File Report 2004-1048. In USGS, Ed. 2004; p 36.

117. Trainer, F. W.; Heath, R. C., Bicarbonate Content of Groundwater in Carbonate Rock in Eastern North-America. *Journal of Hydrology* **1976,** 31, (1-2), 37-55.

118. Hou, W. G.; Su, Y. L.; Sun, D. J.; Zhang, C. G., Studies on zero point of charge and permanent charge density of Mg-Fe hydrotalcite-like compounds. *Langmuir* **2001,** 17, (6), 1885-1888.

119. Yu, Q.; Kandegedara, A.; Xu, Y.; BRorabacher, E. B., Avoiding Interferances from Good's Buffers: A Contiguous Series of Noncomplexing Tertiary Amine Buffers Covering the Entire Range of pH 3-11. *Analytical Biochemistry* **1997,** 253, 50-56.

120. He, J.; Wei, M.; Li, B.; Kang, Y.; Evans, D. G.; Duan, X., Preparation of layered double hydroxides. In *Layered Double Hydroxides*, 2006; Vol. 119, pp 89-119.

121. Christiansen, B. C.; Balic-Zunic, T.; Petit, P. O.; Frandsen, C.; Mørup, S.; Geckeis, H.; Katerinopoulou, A.; Stipp, S. L. S., Composition and structure of an iron-bearing, layered double hydroxide (LDH) - Green rust sodium sulphate. *Geochimica et Cosmochimica Acta* **2009,** 73, (12), 3579-3592.

122. Anderson, R. T.; Vrionis, H. A.; Ortiz-Bernad, I.; Resch, C. T.; Long, P. E.; Dayvault, R.; Karp, K.; Marutzky, S.; Metzler, D. R.; Peacock, A.; White, D. C.; Lowe, M.; Lovley, D. R., Stimulating the in situ activity of Geobacter species to remove uranium from the groundwater of a uranium-contaminated aquifer. *Applied and Environmental Microbiology* **2003,** 69, (10), 5884-5891.

123. O'Loughlin, E. J.; Gorski, C. A.; Scherer, M. M.; Boyanov, M. I.; Kemner, K. M., Effects of Oxyanions, Natural Organic Matter, and Bacterial Cell Numbers on the Bioreduction of Lepidocrocite (gamma-FeOOH) and the Formation of Secondary Mineralization Products. *Environmental Science & Technology* **2010,** 44, (12), 4570-4576.

124. Lovely, D. R.; Stolz, J. F.; Gordon, L. N.; Phillips, E. J. P., Anaerobic production of magnetite by dissimilatory iron-reducing microarganism. *Nature* **1987,** 330, 252-254.

125. Carlson, L.; Karnland, O.; Oversby, V. M.; Rance, A. P.; Smart, N. R.; Snellman, M.; Vähänen, M.; Werme, L. O., Experimental studies of the interactions between anaerobically corroding iron and bentonite. *Physics and Chemistry of the Earth, Parts A/B/C* **2007,** 32, (1-7), 334-345.

126. Missana, T.; Maffiotte, C.; Garcia-Gutierrez, M., Surface reactions kinetics between nanocrystalline magnetite and uranyl. *Colloid and Interface Science* **2003,** 261, 154-160.

127. White, A. F.; Peterson, M. L.; Hochella, M. F., Electrochemistry and Dissolution Kinetics of Magnetite and Ilmenite. *Geochimica Et Cosmochimica Acta* **1994,** 58, (8), 1859-1875.

128. Cornell, R. M.; Schwertmann, U., *The Iron Oxides: Structure, Properties, Reactions, Occurrences and Uses* 2nd ed.; Wiley-VCH: Weinheim, Germany, 2003; p 664.

129. Verwey, E. J. W.; Haayman, P. W., Electronic Conductivity and Transition Point of Magnetite ("Fe3O4"). *Physica* **1941,** 8, (9), 979-987.

130. Itai, R.; Shibuya, M.; Matsumura, T.; Ishi, G., Electrical resistivity of magnetite anodes. *Journal of the Electrochemical Society* **1971,** 118, (10), 1709-11.

131. Castro, P. A.; Vago, E. R.; Calvo, E. J., Surface electrochemical transformations on spinel iron oxide electrodes in aqueous solutions. *Journal of the Chemical Society-Faraday Transactions* **1996,** 92, (18), 3371-3379.

132. Gorski, C. A.; Scherer, M. M., Influence of magnetite stoichiometry on Fe(II) uptake and nitrobenzene reduction. *Environmental Science & Technology* **2009,** In press.

133. Dodge, C. J.; Francis, A. J.; Gillow, J. B.; Halada, G. P.; Eng, C.; Clayton, C. R., Association of uranium with iron oxides typically formed on corroding steel surfaces. *Environmental Science & Technology* **2002,** 36, (16), 3504-3511.

134. Duro, L.; El Aamrani, S.; Rovira, M.; de Pablo, J.; Bruno, J., Study of the interaction between U(VI) and the anoxic corrosion products of carbon steel. *Applied Geochemistry* **2008,** 23, (5), 1094-1100.

135. El Aamrani, S.; Gimenez, J.; Rovira, M.; Seco, F.; Grive, M.; Bruno, J.; Duro, L.; de Pablo, J., A spectroscopic study of uranium(VI) interaction with magnetite. *Applied Surface Science* **2007,** 253, (21), 8794-8797.

136. Missana, T.; Garcia-Gutierrez, M.; Fernndez, V., Uranium(VI) sorption on colloidal magnetite under anoxic environment: Experimental study and surface complexation modelling. *Geochimica Et Cosmochimica Acta* **2003,** 67, (14), 2543-2550.

137. Ilton, E. S.; Boily, J.-F. o.; Buck, E. C.; Skomurski, F. N.; Rosso, K. M.; Cahill, C. L.; Bargar, J. R.; Felmy, A. R., Influence of Dynamical Conditions on the Reduction of UVI at the Magnetite-Solution Interface. *Environmental Science & Technology* **2009,** 44, (1), 170-176.

138. Gorski, C. A.; Scherer, M. M., Determination of nanoparticulate magnetite stoichiometry by Mossbauer spectroscopy, acidic dissolution, and powder X-ray diffraction: A critical review. *American Mineralogist* **2010,** 95, (7), 1017-1026.

139. Tamura, H.; Goto, K.; Yotsuyan.T; Nagayama, M., Spectrophotometric Determination of Iron(II) with 1,10-Phenanthroline in Presence of Large Amounts of Iron(III). *Talanta* **1974,** 21, (4), 314-318.

140. Grenthe, I.; Stumm, W.; Laaksuharju, M.; Nilsson, A.-C.; Wikberg, P., Redox potentials and redox reactions in deep groundwater systems. *Chem. Geol.* **1992,** 98, 131-150.

141. Zeng, H.; Singh, A.; Basak, S.; Ulrich, K. U.; Sahu, M.; Biswas, P.; Catalano, J. G.; Giammar, D. E., Nanoscale Size Effects on Uranium(VI) Adsorption to Hematite. *Environmental Science & Technology* **2009,** 43, (5), 1373-1378.

142. Sherman, D. M.; Peacock, C. L.; Hubbard, C. G., Surface complexation of U(VI) on goethite (alpha-FeOOH). *Geochimica Et Cosmochimica Acta* **2008,** 72, (2), 298-310.

143. Coker, V. S.; Pearce, C. I.; Lang, C.; van der Laan, G.; Pattrick, R. A. D.; Telling, N. D.; Schuler, D.; Arenholz, E.; Lloyd, J. R., Cation site occupancy of biogenic magnetite compared to polygenic ferrite spinels determined by X-ray magnetic circular dichroism. *European Journal of Mineralogy* **2007,** 19, (5), 707-716.

144. Carvallo, C.; Sainctavit, P.; Arrio, M.-A.; Menguy, N.; Wang, Y.; Ona-Nguema, G.; Brice-Profeta, S., Biogenic vs. abiogenic magnetite nanoparticles: A XMCD study. *American Mineralogist* **2008,** 93, (5-6), 880-885.

145. Kukkadapu, R. K.; Zachara, J. M.; Fredrickson, J. K.; Kennedy, D. W.; Dohnalkova, A. C.; McCready, D. E., Ferrous hydroxy carbonate is a stable transformation product of biogenic magnetite. *American Mineralogist* **2005,** 90, 510-515.

146. Komlos, J.; Peacock, A.; Kukkadapu, R. K.; Jaffe, P. R., Long-term dynamics of uranium reduction/reoxidation under low sulfate conditions. *Geochimica Et Cosmochimica Acta* **2008,** 72, (15), 3603-3615.

147. Senko, J. M.; Kelly, S. D.; Dohnalkova, A. C.; McDonough, J. T.; Kemner, K. M.; Burgos, W. D., The effect of U(VI) bioreduction kinetics on subsequent reoxidation of biogenic U(IV). *Geochimica Et Cosmochimica Acta* **2007,** 71, (19), 4644-4654.

148. Moon, H. S.; Komlos, J.; Jaffe, P. R., Uranium reoxidation in previously bioreduced sediment by dissolved oxygen and nitrate. *Environmental Science & Technology* **2007,** 41, (13), 4587-4592.

149. Nielsen, L. P.; Risgaard-Petersen, N.; Fossing, H.; Christensen, P. B.; Sayama, M., Electric currents couple spatially separated biogeochemical processes in marine sediment. *Nature* **2010,** 463, (7284), 1071-1074.

150. Revil, A.; Mendonca, C. A.; Atekwana, E. A.; Kulessa, B.; Hubbard, S. S.; Bohlen, K. J., Understanding biogeobatteries: Where geophysics meets microbiology. *Journal of Geophysical Research-Biogeosciences* **2010,** 115.

151. Grenthe, I.; Fuger, J.; Lemire, R. J.; Muller, A. B.; Nguyen-Trung, C.; Wanner, H., *Chemical Thermodynamics of Uranium*. Nuclear Energy Agency: 2004.

152. Catalano, J. G.; Heald, S. M.; Zachara, J. M.; Brown, G. E., Spectroscopic and diffraction study of uranium speciation in contaminated vadose zone sediments from the Hanford site, Washington state. *Environmental Science & Technology* **2004,** 38, (10), 2822-2828.

153. Krupka, K. M.; Schaef, H. T.; Arey, B. W.; Heald, S. M.; Deutsch, W. J.; Lindberg, M. J.; Cantrell, K. J., Residual waste from Hanford tanks 241-C-203 and 241-C-204. 1. Solids characterization. *Environmental Science & Technology* **2006,** 40, (12), 3749-3754.

154. Liger, E.; Charlet, L.; Van Cappellen, P., Surface catalysis of uranium(VI) reduction by iron(II). *Geochimica Et Cosmochimica Acta* **1999,** 63, (19-20), 2939-2955.

155. Ilton, E. S.; Haiduc, A.; Cahill, C. L.; Felmy, A. R., Mica surfaces stabilize pentavalent uranium. *Inorganic Chemistry* **2005,** 44, (9), 2986-2988.

156. Ilton, E. S.; Haiduc, A.; Moses, C. O.; Heald, S. M.; Elbert, D. C.; Veblen, D. R., Heterogeneous reduction of uranyl by micas: Crystal chemical and solution controls. *Geochimica Et Cosmochimica Acta* **2004,** 68, (11), 2417-2435.

157. Zhang, G. X.; Senko, J. M.; Kelly, S. D.; Tan, H.; Kemner, K. M.; Burgos, W. D., Microbial reduction of iron(III)-rich nontronite and uranium(VI). *Geochimica Et Cosmochimica Acta* **2009,** 73, (12), 3523-3538.

158. Prior, J. C., *Landforms of Iowa*. 1 ed.; University of Iowa Press: Iowa City, Iowa, 1991; p 153.

159. Biscaye, P. E., Mineralogy and Sedimentation of Recent Deep-Sea Clay in Atlantic Ocean and Adjacent Seas and Oceans. *Geological Society of America Bulletin* **1965,** 76, (7), 803-&.

160. Feder, F.; Trolard, F.; Klingelhofer, G.; Bourrie, G., In situ Mossbauer spectroscopy: Evidence for green rust (fougerite) in a gleysol and its mineralogical transformations with time and depth. *Geochimica Et Cosmochimica Acta* **2005,** 69, (18), 4463-4483.

161. Schwertmann, U.; Cornell, R. M., *Iron Oxides in the Laboratory: Preparation and Characterization*. 2nd ed.; Wiley-VCH: New York, 2000; p 188.

162. Kostka, J.; Nealson, K. H., *Techniques in Microbial Ecology*. Oxford University Press: New York, 1998.

163. Burns, P. C.; Ewing, R. C.; Hawthorne, F. C., The crystal chemistry of hexavalent uranium: Polyhedron geometries, bond-valence parameters, and polymerization of polyhedra. *Canadian Mineralogist* **1997,** 35, 1551-1570.

164. Belai, N.; Frisch, M.; Ilton, E. S.; Ravel, B.; Cahill, C. L., Pentavalent Uranium Oxide via Reduction of [UO2](2+) Under Hydrothermal Reaction Conditions. *Inorganic Chemistry* **2008,** 47, (21), 10135-10140.

165. Ikeda, A.; Hennig, C.; Tsushima, S.; Takao, K.; Ikeda, Y.; Scheinost, A. C.; Bernhard, G., Comparative study of uranyl(VI) and -(V) carbonato complexes in an aqueous solution. *Inorganic Chemistry* **2007,** 46, (10), 4212-4219.

166. Trolard, F.; Abdelmoula, M.; Bourrie, G.; Humbert, B.; Genin, J. M. R., Evidence of the occurrence of a "Green Rusts" component in hydromorphic soils. Proposition of the existence of a new mineral: "Fougerite". *Comptes Rendus De L Academie Des Sciences Serie Ii Fascicule a- Sciences De La Terre Et Des Planetes* **1996,** 323, (12), 1015-1022.

167. Mehra, O. P.; Jackson, M. L., Iron oxide removal from soils and clays by a dithionite-citrate system buffered with sodium bicarbonate. *Clays, Clay Minerals, Proc. Natl. Conf. Clays Clay Minerals, 7th, Washington* **1960**, 317-27.

168. Soil Survey Staff. National Soil Survey Characterization Data. Accessed via http://ssldata.nrcs.usda.gov/sumReport.aspx?p=1439&c=a&a=52&t=ped&tt=&submit1=Get+Report

169. Drissi, S. H.; Refait, P.; Abelmoula, M.; Genin, J. M. R., The preparationand thermodynamic properties of Fe(II)-Fe(III) hydroxide carbonate (Green Rust 1); Pourbaix diagram of iron in carbonate -containing aqueous media. *Corrosion Science* **1995,** 37, (12), 2025-2041.

170. Trolard, F.; Genin, J.-M. R.; Abdelmoula, M.; Bourrie, G.; Humbert, B.; Herbillon, A., Identification of a green rust mineral in a reductomorphic soil by Mössbauer and Raman spectroscopies. *Geochim. Cosmo. Acta.* **1997,** 61, (5), 1107-1111.

171. Sawicki, J. A.; Brown, D. A., Investigation of microbial-mineral interactions by Mossbauer spectroscopy. *Hyperfine Interactions* **1998,** 117, 371-382.

172. Miyamoto, H.; Shinjo, T.; Takada, T., Mossbauer effect of the ^{57}Fe in $Fe(OH)_2$. *Journal of the physical society of Japan* **1967,** 23, 1421.

173. Miyamoto, H., The magnetic properties of $Fe(OH)_2$. *Materials Research Bulletin* **1976,** 11, (329-335).

174. Murad, E.; Cashion, J., *Mossbauer Spectroscopy of Environmental Materials and their Industrial Utilization*. Kluwer Academic Publishers: 2004.

175. McCammon, C. A.; Burns, R. G., The Oxidation Mechanism of Vivianite as Studied by Mossbauer-Spectroscopy. *American Mineralogist* **1980,** 65, (3-4), 361-366.

176. Russell, J. D.; Goodman, B. A.; Fraser, A. R., Infrared and Mossbauer Studies of Reduced Nontronites. *Clays and Clay Minerals* **1979,** 27, (1), 63-71.

177. Seabaugh, J. L.; Dong, H. L.; Kukkadapu, R. K.; Eberl, D. D.; Morton, J. P.; Kim, J., Microbial reduction of Fe(III) in the Fithian and Muloorina illites: Contrasting extents and rates of bioreduction. *Clays and Clay Minerals* **2006,** 54, (1), 67-79.

178. Dong, H. L.; Kukkadapu, R. K.; Zachara, J. M.; Kennedy, D. W.; Kostandarithes, H. M., Microbial reduction of structural Fe(III) in illite and goethite. *Environmental Science and Technology* **2003,** 37, (7), 1268-1276.

179. Root, R. A.; Dixit, S.; Campbell, K. M.; Jew, A. D.; Hering, J. G.; O'Day, P. A., Arsenic sequestration by sorption processes in high-iron sediments. *Geochimica Et Cosmochimica Acta* **2007,** 71, (23), 5782-5803.

180. Genin, J. M. R.; Ruby, C., Anion and cation distributions in Fe(II-III) hydroxysalt green rusts from XRD and Mossbauer analysis (carbonate, chloride, sulphate,...); the "fougerite" mineral. *Solid State Sciences* **2004,** 6, (7), 705-718.

181. van der Zee, C.; Roberts, D. R.; Rancourt, D. G.; Slomp, C. P., Nanogoethite is the dominant reactive oxyhydroxide phase in lake and marine sediments. *Geology* **2003,** 31, 993-996.

182. Murad, E.; Schwertmann, U., The Influence of Aluminum Substitution and Crystallinity on the Mossbauer-Spectra of Goethite. *Clay Minerals* **1983,** 18, (3), 301-312.

183. Komadel, P.; Madejova, J.; Stucki, J. W., Structural Fe(III) reduction in smectites. *Applied Clay Science* **2006,** 34, (1-4), 88-94.

184. Anthony, J. W.; Bideaux, R. A.; Bladh, K. W.; Nichols, M. C., *Handbook of Mineralogy.* Mineral Data Publishing: Tucson, Arizona, 1990.

185. Christiansen, B. C.; Balic-Zunic, T.; Dideriksen, K.; Stipp, S. L. S., Identification of Green Rust in Groundwater. *Environmental Science & Technology* **2009,** 43, (10), 3436-3441.

186. Murad, E.; Taylor, R. M., The Mössbauer spectra of hydroxycarbonate green rust. *Clay Minerals* **1984,** 19, 77-83.

187. Lovely, D. R., Microbial Fe(III) reduction in subsurface environments. *FEMS Microbiology Reviews* **1997,** 20, 305-313.

188. Lovley, D. R.; Phillips, E. J. P., Organic Matter Mineralization with Reduction of Ferric Iron in Anaerobic Sediments. *Appl. Environ. Microbiol.* **1986,** 51, (4), 683-689.

189. Hansen, H. C. B.; Koch, C. B., Reduction of nitrate to ammonium by sulphate green rust: activation energy and reaction mechanism. *Clay Minerals* **1998,** 33, (1), 87-101.

190. Larese-Casanova, P.; Scherer, M. M., Morin transition suppression in Polycrystalline (57)Hematite (alpha-Fe2O3) exposed to Fe-56(II). *Hyperfine Interactions* **2007,** 174, 111-119.

191. Schulze, D. G., The Influence of Aluminum on Iron-Oxides .8. Unit-Cell Dimensions of Al-Substituted Goethites and Estimation of Al from Them. *Clays and Clay Minerals* **1984,** 32, (1), 36-44.

192. Ainsworth, C. C.; Sumner, M. E., Effect of aluminum substitution in goethite on phosphorus adsorption: II. Rate of adsorption. *Soil Science Society of America Journal* **1985,** 49, (5), 1149-53.

193. Ainsworth, C. C.; Sumner, M. E.; Hurst, V. J., Effect of aluminum substitution in goethite on phosphorus adsorption: I. Adsorption and isotopic exchange. *Soil Science Society of America Journal* **1985,** 49, (5), 1142-9.

194. Torrent, J.; Schwertmann, U.; Barron, V., Fast and Slow Phosphate Sorption by Goethite-Rich Natural Materials. *Clays and Clay Minerals* **1992,** 40, (1), 14-21.

195. Kwon, K. D.; Kubicki, J. D., Molecular orbital theory study on surface complex structures of phosphates to iron hydroxides: Calculation of vibrational frequencies and adsorption energies. *Langmuir* **2004,** 20, (21), 9249-9254.

196. Persson, P.; Nilsson, N.; Sjoberg, S., Structure and bonding of orthophosphate ions at the iron oxide aqueous interface. *Journal of Colloid and Interface Science* **1996,** 177, (1), 263-275.

197. Parfitt, R. L.; Russell, J. D.; Farmer, V. C., Confirmation of the surface structures of goethite (a-FeOOH) and phosphated goethite by infrared spectroscopy. *J.Chem. Soc. Fara. Trans. I* **1975,** 72, 1082-1087.

198. Lewis, D. G.; Schwertmann, U., Influence of Aluminum on the Formation of Iron-Oxides .4. Influence of [Al], [Oh], and Temperature. *Clays and Clay Minerals* **1979,** 27, (3), 195-200.

199. Mehra, O. P.; Jackson, M. L., Iron oxide removal from soils and clays by a dithionate-citrate system buffered with sodium bicarbonate. *Clay and Clay Minerals* **1960,** 7, 317-327.

200. Xu, J.; Stevens, M. J.; Oleson, T. A.; Last, J. A.; Sahai, N., Role of Oxide Surface Chemistry and Phospholipid Phase on Adsorption and Self-Assembly: Isotherms and Atomic Force Microscopy. *Journal of Physical Chemistry C* **2009,** 113, (6), 2187-2196.

201. Oleson, T. A.; Sahai, N., Oxide-dependent adsorption of a model membrane phospholipid, dipalmitoylphosphatidylcholine: Bulk adsorption isotherms. *Langmuir* **2008,** 24, (9), 4865-4873.

202. Patterson, A. L., The Scherrer formula for X-ray particle size determination. *Physical Review* **1939,** 56, 978-982.

203. Prelot, B.; Villieras, F.; Pelletier, M.; Gerard, G.; Gaboriaud, F.; Ehrhardt, J. J.; Perrone, J.; Fedoroff, M.; Jeanjean, J.; Lefevre, G.; Mazerolles, L.; Pastol, J. L.; Rouchaud, J. C.; Lindecker, C., Morphology and surface heterogeneities in synthetic goethites. *Journal of Colloid and Interface Science* **2003,** 261, (2), 244-254.

204. Madsen, D. E.; Cervera-Gontard, L.; Kasama, T.; Dunin-Borkowski, R. E.; Koch, C. B.; Hansen, M. F.; Frandsen, C.; Morup, S., Magnetic fluctuations in nanosized goethite (alpha-FeOOH) grains. *Journal of Physics-Condensed Matter* **2009,** 21, (1).

205. Torrent, J.; Schwertmann, U.; Barron, V., The Reductive Dissolution of Synthetic Goethite and Hematite in Dithionite. *Clay Minerals* **1987,** 22, (3), 329-337.

206. Gonzalez, E.; Ballesteros, M. C.; Rueda, E. H., Reductive dissolution kinetics of Al-substituted goethites. *Clays and Clay Minerals* **2002,** 50, (4), 470-477.

207. Jang, J. H.; Brantley, S. L., Investigation of Wustite (FeO) Dissolution: Implications for Reductive Dissolution of Ferric Oxides. *Environmental Science & Technology* **2009,** 43, (4), 1086-1090.

208. Peretyazhko, T.; Zachara, J. M.; Heald, S. M.; Jeon, B. H.; Kukkadapu, R. K.; Liu, C.; Moore, D.; Resch, C. T., Heterogeneous reduction of Tc(VII) by Fe(II) at the solid-water interface. *Geochimica Et Cosmochimica Acta* **2008,** 72, (6), 1521-1539.

209. Sorensen, J.; Thorling, L., Stimulation by Lepidocrocite (Gamma-Feooh) of Fe(Ii)-Dependent Nitrite Reduction. *Geochimica Et Cosmochimica Acta* **1991,** 55, (5), 1289-1294.

210. Beard, B. L.; Handler, R. M.; Scherer, M. M.; Wu, L.; Czaja, A. D.; Heimann, A.; Johnson, C. M., Iron isotope fractionation between aqueous ferrous iron and goethite. *Earth and Planetary Science Letters* **2010,** 295, (1-2), 241-250.

211. Amstaetter, K.; Borch, T.; Larese-Casanova, P.; Kappler, A., Redox Transformation of Arsenic by Fe(II)-Activated Goethite (Î±-FeOOH). *Environmental Science & Technology* **2009,** 44, (1), 102-108.

212. Fysh, S. A.; Clark, P. E., Aluminous Goethite - a Mossbauer Study. *Physics and Chemistry of Minerals* **1982,** 8, (4), 180-187.

213. Golden, D. C.; Bowen, L. H.; Weed, S. B.; Bigham, J. M., Mossbauer studies of synthetic and soil occuring aluminum-substituted goethites. *Soil Science Society of America Journal* **1979,** 43, (4), 802-808.

214. Pollard, R. J.; Pankhurst, Q. A.; Zientek, P., Magnetism in Aluminous Goethite. *Physics and Chemistry of Minerals* **1991,** 18, (4), 259-264.

215. Hirt, A. M.; Lanci, L.; Dobson, J.; Weidler, P.; Gehring, A. U., Low-temperature magnetic properties of lepidocrocite. *J. Geophys. Res.* **2002,** 107, (B1), 2011.

216. Larese-Casanova, P.; Cwiertny, D. M.; Scherer, M. M., Nanogoethite Formation from Oxidation of Fe(II) Sorbed on Aluminum Oxide: Implications for Contaminant Reduction. *Environmental Science & Technology* **2010,** 44, (10), 3765-3771.

217. Gehin, A.; Greneche, J. M.; Tournassat, C.; Brendle, J.; Rancourt, D. G.; Charlet, L., Reversible surface-sorption-induced electron-transfer oxidation of Fe(II) at reactive sites on a synthetic clay mineral. *Geochimica et Cosmochimica Acta* **2007,** 71, (4), 863-876.

218. Vertes, A.; Nagy, D. L., *Mossbauer Spectroscopy of Frozen Solutions*. H. Stillman Publishers: Boca Raton, FL, 1990.

219. Besser, P.; Morrish, A.; Searle, C., Magnetocrystalline anisotropy of pure and doped hematite. *Physical Review* **1966,** 153, (2), 632-640.

220. Lamykin, E.; Fabrichnyi, P.; Babeshkin, A.; Nesmeyanov, A., Influence of small amounts of tin on the Morin transition temperature in hematite (alpha-Fe2O3). *Sov. Phys. Solid State* **1972,** 15, (3), 874-877.

221. Rosso, K. M.; Smith, D. M. A.; Dupuis, M., An *ab initio* model of electron transport in hematite (α-Fe_2O_3) basal planes. *Journal of Chemical Physics* **2003,** 118, (14), 6455-6466.

222. Kerisit, S.; Rosso, K. M., Computer simulation of electron transfer at hematite surfaces. *Geochimica Et Cosmochimica Acta* **2006,** 70, (8), 1888-1903.

223. Kerisit, S.; Rosso, K. M., Kinetic Monte Carlo model of charge transport in hematite (α-Fe_2O_3) *Journal of Chemical Physics* **2007,** 127.

224. Iordanova, N.; Dupuis, M.; Rosso, K. M., Charge transport in metal oxides: A theoretical study of hematite alpha-Fe2O3. *Journal Of Chemical Physics* **2005,** 122, (14).

225. Kaneko, K.; Inoue, N.; Ishikawa, T., Electrical and Photoadsorptive Properties of Valence-Controlled Alpha-FeOOH. *Journal of Physical Chemistry* **1989,** 93, (5), 1988-1992.

226. Guskos, N.; Papadopoulos, G. J.; Likodimos, V.; Patapis, S.; Yarmis, D.; Przepiera, A.; Przepiera, K.; Majszczyk, J.; Typek, J.; Wabia, M.; Aidinis, K.; Drazek, Z., Photoacoustic, EPR and electrical conductivity investigations of three synthetic mineral pigments: hematite, goethite and magnetite. *Materials Research Bulletin* **2002,** 37, (6), 1051-1061.

227. Berry, F. J.; Helgason, O.; Bohorquez, A.; Marco, J. F.; McManus, J.; Moore, E. A.; Morup, S.; Wynn, P. G., Preparation and characterisation of tin-doped alpha-FeOOH (goethite). *Journal of Materials Chemistry* **2000,** 10, (7), 1643-1648.

228. Vikesland, P. J.; Valentine, R. L., Iron oxide surface-catalyzed oxidation of ferrous iron by monochloramine: Implications of oxide type and carbonate on reactivity. *Environmental Science & Technology* **2002,** 36, (3), 512-519.

229. Schwertmann, U., Some properties of soil and synthetic iron oxides. In *Iron in Soils and Clay Minerals*, Stucki, J. W., Ed. D. Reidel Publishing Co.: Dordrecht, Holland, 1988; Vol. 217, pp 203-250.

230. Al-Borno, A.; Tomson, M. B., The Temperature-Dependence of the Solubility Product Constant of Vivianite. *Geochimica Et Cosmochimica Acta* **1994,** 58, (24), 5373-5378.

231. Refait, P.; Reffass, M.; Landoulsi, J.; Sabot, R.; Jeannin, M., Role of phosphate species during the formation and transformation of the Fe(II-III) hydroxycarbonate green rust. *Colloids and Surfaces a-Physicochemical and Engineering Aspects* **2007,** 299, (1-3), 29-37.

232. Cumplido, J.; Barron, V.; Torrent, J., Effect of phosphate on the formation of nanophase lepidocrocite from Fe(II) sulfate. *Clays and Clay Minerals* **2000,** 48, (5), 503-510.

233. Forsyth, J. B.; et al., The magnetic structure of vivianite, Fe 3 (PO 4) 2 .8H 2 O. *Journal of Physics C: Solid State Physics* **1970,** 3, (5), 1127.

234. Rouzies, D.; Millet, J. M. M., Mossbauer Study of Synthetic Oxidized Vivianite at Room-Temperature. *Hyperfine Interactions* **1993,** 77, (1-2), 19-28.

235. Wu, L. L.; Beard, B. L.; Roden, E. E.; Kennedy, C. B.; Johnson, C. M., Stable Fe isotope fractionations produced by aqueous Fe(II)-hematite surface interactions. *Geochimica Et Cosmochimica Acta* **2010,** 74, (15), 4249-4265.

236. Jones, A. M.; Collins, R. N.; Rose, J.; Waite, T. D., The effect of silica and natural organic matter on the Fe(II)-catalysed transformation and reactivity of Fe(III) minerals. *Geochimica Et Cosmochimica Acta* **2009,** 73, (15), 4409-4422.

237. Singer, S. J.; Nicolson, G. L., The Fluid Mosaic Model of the Structure of Cell Membranes. *Science* **1972,** 175, (4023), 720-731.

238. Cagnasso, M.; Boero, V.; Franchini, M. A.; Chorover, J., ATR-FTIR studies of phospholipid vesicle interactions with alpha-FeOOH and alpha-Fe2O3 surfaces. *Colloids and Surfaces B-Biointerfaces* **2010,** 76, (2), 456-467.

239. Li, T. T.; Weaver, M. J., Intramolecular electron transfer at metal surfaces. 4. dependence of tunneling probability upon donor-acceptor separation distance. *J. Am. Chem. Soc.* **1984,** 106, 6107-6108.

240. Wigginton, N. S.; Rosso, K. M.; Stack, A. G.; Hochella, M. F., Long-Range Electron Transfer across Cytochrome-Hematite (alpha-Fe2O3) Interfaces. *Journal of Physical Chemistry C* **2009,** 113, (6), 2096-2103.

241. Omoike, A.; Chorover, J., Adsorption to goethite of extracellular polymeric substances from Bacillus subtilis. *Geochimica Et Cosmochimica Acta* **2006,** 70, (4), 827-838.

242. Stone, A. T.; Coughlin, B. R., Nonreversible adsorption of divalent metal ions (Mn-II, Co- II, Ni-II, Cu-II, and Pb-II) onto goethite: Effects of acidification, Fe-II addition, and picolinic acid addition - Response. *Environmental Science & Technology* **1996,** 30, (4), 1412-1412.

243. Buerge, I. J.; Hug, S. J., Influence of mineral surfaces on chromium(VI) reduction by Iron(II). *Environmental Science and Technology* **1999,** 33, (23), 4285-4291.

244. Kukkadapu, R.; Zachara, J. M.; Smith, S. C.; Frederickson, J. K.; Liu, C., Dissimilatory bacterial reduction of Al-substituted goethite in subsurface sediments. *Geochimica et Cosmochimica Acta* **2001,** 65, (17), 2913-2924.

245. Pedersen, H. D.; Postma, D.; Jakobsen, R., Release of arsenic associated with the reduction and transformation of iron oxides. *Geochimica Et Cosmochimica Acta* **2006,** 70, (16), 4116-4129.

246. Nico, P. S.; Stewart, B. D.; Fendorf, S., Incorporation of Oxidized Uranium into Fe (Hydr)oxides during Fe(II) Catalyzed Remineralization. *Environmental Science & Technology* **2009,** 43, (19), 7391-7396.

247. Vempati, R. K.; Morris, R. V.; Lauer, H. V.; Helmke, P. A., Reflectivity and Other Physicochemical Properties of Mn-Substituted Goethites and Hematites. *Journal of Geophysical Research-Planets* **1995,** 100, (E2), 3285-3295.

248. Scheinost, A. C.; Stanjek, H.; Schulze, D. G.; Gasser, U.; Sparks, D. L., Structural environment and oxidation state of Mn in goethite-groutite solid-solutions. *American Mineralogist* **2001,** 86, (1-2), 139-146.

249. Ebinger, M. H.; Schulze, D. G., Mn-Substituted Goethite and Fe-Substituted Groutite Synthesized at Acid Ph. *Clays and Clay Minerals* **1989,** 37, (2), 151-156.

250. Fortune, W. B.; Mellon, M. G., Determination of iron with o-phenanthroline - A spectrophotometric study. *Industrial and Engineering Chemistry-Analytical Edition* **1938,** 10, 0060-0064.

251. Morgan, J. J.; Stumm, W. S., Analytical chemistry of aqueous manganese. *Journal of the American Water Works Association* **1965,** 57, (1), 107-119.

252. Abel, R. Scavenging of particulate and dissolved lead compounds by coprecipitation with manganese oxyhydroxides. Electronic M.S. thesis, Virginia Tech, 1998.

253. Villalobos, M.; Cheney, M. A.; Alcaraz-Cienfuegos, J., Goethite surface reactivity: II. A microscopic site-density model that describes its surface area-normalized variability. *Journal of Colloid and Interface Science* **2009,** 336, (2), 412-422.

254. Ljung, K.; Vahter, M., Time to re-evaluate the guideline value for manganese in drinking water? *Environmental Health Perspectives* **2007,** 115, 1533-1538.

255. Kaur, N.; Grafe, M.; Singh, B.; Kennedy, B., SIMULTANEOUS INCORPORATION OF Cr, Zn, Cd, AND Pb IN THE GOETHITE STRUCTURE. *Clays and Clay Minerals* **2009,** 57, (2), 234-250.

256. Bard, A. J.; Faulkner, L. R., *Electrochemical Methods. Fundamentals and Applications*. Second Edition ed.; Wiley: New York, 2001; p 833.

257. Ginder-Vogel, M.; Criddle, C. S.; Fendorf, S., Thermodynamic constraints on the oxidation of biogenic UO2 by Fe(III) (hydr) oxides. *Environmental Science & Technology* **2006,** 40, (11), 3544-3550.

258. Skomurski, F. N.; Rosso, K. M.; Krupka, K. M.; McGrail, B. P., Technetium Incorporation into Hematite (α-Fe2O3). *Environmental Science & Technology* **2010,** 44, (15), 5855-5861.

259. Skovbjerg, L. L.; Stipp, S. L. S.; Utsunomiya, S.; Ewing, R. C., The mechanisms of reduction of hexavalent chromium by green rust sodium sulphate: Formation of Cr-goethite. *Geochimica Et Cosmochimica Acta* **2006,** 70, (14), 3582-3592.